The Characterisation of an Openwork Block Deposit, Northern Buttress, Vesleskarvet, Dronning Maud Land, Antarctica

A thesis submitted in fulfilment of the requirements for the degree of

MASTER OF SCIENCE

of

Rhodes University

by

Christel Dorothee Hansen

February 2013

Supervisor

Professor K.I. Meiklejohn (Department of Geography, Rhodes University)

Co-Supervisor

Professor W. Nel (Department of Geography and Environmental Science, University of Fort Hare)

Abstract

Investigating openwork block accumulation has the potential to further our understanding of rock weathering, the control of geological structure on landforms, the production of substrates for biological colonisation and the impacts of climate change on landform development and dynamics. Various models for the development of these landforms have been proposed. This includes *in situ* weathering, frost heave and wedging. Furthermore, it has been suggested that cold-based ice has the potential to preserve these features rather than to obliterate them. Blocky deposits are also frequently used as proxy evidence for interpreting palaeoclimates. The morphology and processes acting on a blockfield located on the Northern Buttress of the Vesleskarvet Nunataks, Dronning Maud Land, Antarctica (2°W, 71°S) were investigated and characterised. Given block dimensions and orientations that closely resembled the parent material and only small differences in aspect related characteristics observed, the blockfield was found to be autochthonous with *in situ* block production and of a young (Holocene) age. Small differences in rock hardness measurements suggest some form of aspect control on rock weathering. South-facing sides of clasts were found to be the least weathered. In comparison, consistently low rock hardness rebound values for the north-facing aspects suggest that these are the most weathered sides. Additional indicators of weathering, such as flaking and pitting, support analyses conducted for rock hardness rebound values. Solar radiation received, slope gradients and snow cover were found to influence weathering of clasts across the study site. Furthermore, ambient temperatures and wind speed significantly influenced near-surface ground temperatures dynamics. However, the lack of a matrix and paucity of fine material in textural analyses suggest a limited weathering environment. It is suggested that the retreat of the Antarctic ice sheet during the last LGM led to unloading of the surface, causing dilatation and subsequent fracturing of the bedrock along pre-existing joints, leading to *in situ* clast supply. Subsequent weathering and erosion along other points or lines of weakness then yielded fines and slight edge rounding of clasts.

Keywords: autochthonous blockfield, openwork block deposit, Vesleskarvet, Western Dronning Maud Land, Antarctic

Acknowledgements

The author would like to express her gratitude and sincere appreciation to Professor Ian Meiklejohn of Rhodes University, as well as Professor Werner Nel of the University of Fort Hare, for their guidance and support throughout the two years of study undertaken to complete this dissertation. Funding by the NRF (National Research Foundation) is appreciated, without whose financial support the M.Sc. studies would not have been possible. DEA (Department of Environmental Affair) and SANAP (South African National Antarctic Programme) are thanked for providing logistical support during the fieldwork seasons conducted in the Antarctic. SAWS (South African Weather Service) and NGI (National Geo-Spatial Information) are thanked for the provision of data, as are those members of the 2009/10, 2010/11 and 2011/12 Austral summer relief voyage teams to SANAE IV that assisted during the fieldwork data collection process. Lodewyk van den Berg, Ian Meiklejohn and Carol Jacobs are thanked for giving permission to use their photographs for analyses and display purposes. Finally, Rhodes University is thanked for their support throughout the M.Sc. studies.

Table of Contents

Table of Figures

Table of Tables

Table of Equations

List of Abbreviations

ADD – Antarctic Digital Database

ANOVA – Analysis of Variance

BP – Before Present

C – Celsius

c – coefficient of variation

CF – Correction Factor

CSDA- Confirmatory Spatial Data Analysis

DEA – Department of Environmental Affairs

DEM – Digital Elevation Model

DML – Dronning Maud Land

ESDA – Exploratory Spatial Data Analysis

ESRI – Environmental Systems Research Institute

GIS – Geographical Information Systems

GPS – Global Positioning System

GST – Ground near-Surface Temperature

H_0 – Null Hypothesis

H_a – Alternate Hypothesis

HL – Leeb Hardness

hPa – hecto Pascal

ISRM – International Society of Rock Mechanics

LGM – Last Glacial Maxima

LIGT – Last Interglacial Transition

LSD –Least Significance Difference

M – Microporosity

Ma – Mega-annum (1 000 000 years)

MASL – Meters Above Sea Level

mb – millibar (1 mb = 1 hPa)

mPa – mega Pascal (1 000 000 Pa)

NGI – National Geo-Spatial Information

NRF – National Research Foundation

P – Porosity

PCA – Principal Components Analysis

QQ plot – Quantile-Quantile plot

r – Pearson's product-moment coefficient of linear correlation

RMS – Rock Mass Strength

R-values – Rock hardness rebound values

S – Saturation Coefficient

s – standard deviation

SANAE – South African Antarctic Expedition

SANAP – South African National Antarctic Programme

SAWS – South African Weather Service

SCAR – Scientific Committee on Antarctic Research

t-test – Student's *t*-test

UK – United Kingdom of Great Britain and Northern Ireland

USA – United States of America

WA – Water Absorption Capacity

WDML – Western Dronning Maud Land

α – level of significance

CHAPTER 1: Introduction

1.1 Background, Context and Motivation

Openwork block accumulations (*e.g.* Figure 1 & Figure 2) in cold environments are the subject of considerable academic debate and have generated much interest (Ballantyne, 1984; Rea *et al.*, 1996; Whalley *et al.*, 2004; Rea, 2007; Wilson, 2007). Blockfields have been shown to exist in a variety of settings, generally at high altitudes, such as mountaintops, summits, ridges and plateaus (Rea *et al.*, 1996; Rea, 2007), and mid to high latitudes (Rea, 2007). They have been well documented for Scandinavia and Arctic Canada and occur in areas previously glaciated or never glaciated (Nesje *et al.*, 1988; Rea *et al.*, 1996, Boelhouwers, 2004; Goodfellow *et al.*, 2008). Blocky deposits have been described for Namibia (Boelhouwers and Sumner, 2003; Boelhouwers, 2004), mainland South Africa (Boelhouwers, 1993), the Lesotho Highlands (Boelhouwers, 1999; Boelhouwers and Meiklejohn, 2002; Boelhouwers *et al.*, 2002; Sumner, 2004), Marion Island (Sumner and Meiklejohn, 2004), Svålbard (Rea, 2007), Scotland (Ballantyne, 1998; Hall and Phillips, 2006), Norway (Whalley *et al.*, 2004), Quebec-Labrador (Marquette *et al.*, 2004), Greenland, Fennoscandia and Iceland (Rea, 2007), the Laramide Ranges of the United States of America (Small *et al.*, 1999, Rea, 2007), Australia, Tasmania (Caine, 1983), the Falkland Islands (André *et al*., 2008) and Antarctica (Serrano and López-Martínez, 2000; Boelhouwers, 2004).

Figure 1: A blockfield on the Vesleskarvet Nunataks, Western Dronning Maud Land, Antarctica. The widest part of the blockfield is app. 340m and it is app. 695m long along the north-south axis. North is toward the bottom left portion of the image (Photo: Meiklejohn, 2007).

Figure 2: The Vesleskarvet blockfield looking to the south-west. Note the person for scale.

Various models for these landforms have been proposed. Autochthonous deposits are thought to develop following *in situ* weathering and frost heave, whereas allochthonous block streams result from the movement of blocks over an active layer (Ballantyne, 1984; Boelhouwers *et al.*, 2002;

Sumner, 2004; Sumner and Meiklejohn, 2004; Whalley *et al.*, 2004; Rea, 2007; Wilson, 2007; Grab *et al.*, 2012). Blocky deposits are also frequently used as proxy evidence for interpreting palaeoclimates, with their various aspects and characteristics providing a timeline for glacial or periglacial climates (Ballantyne, 1984; Rea *et al.*, 1996; Boelhouwers *et al.*, 2002; Sumner and Meiklejohn, 2004; Whalley *et al.*, 2004; Rea, 2007; Andre *et al.*, 2008). The interaction between glacial ice and landforms creates an interesting conundrum; in certain cases it has been suggested that ice has the potential to alter and destroy landforms through quarrying and abrasion and in others, cold-based ice has been argued to preserve blocky deposits (Rea *et al.*, 1996; Sumner and Meiklejohn, 2004; Whalley *et al.*, 2004; Kleman and Glasser, 2007). In addition, it has been argued that the presence of blocky deposits may lead to lower temperatures being maintained deeper within the soil than if these deposits were not present (Harris and Pedersen, 1998). This has implications for the depth and dynamics of the active layer and permafrost.

The aim of this dissertation is to improve our knowledge of blockfields in a cold desert environment using a variety of methods. In addition, although blockfields have been described for Antarctica (Rea, 2007; Ballantyne, 2010), only one such feature has been investigated within the specific study area at Basen (Boelhouwers, 2004). The project involves an investigation into the morphology and characterisation of the blockfield located on the Northern Buttress of the Vesleskarvet Nunataks, WDML (Western Dronning Maud Land), Antarctica (71°40'S, 2°51'W), in the vicinity of SANAP's (South African National Antarctic Programme's) base, SANAE IV (South African National Antarctic Expedition IV) (SANAP, 2009). Research conducted on such openwork block deposits can greatly improve our understanding on how these landforms develop and how they are being moulded by the current environment. Interrelationships are present in any landscape and investigating all processes, agents and factors is crucial to our understanding of landform and landscape development (Briggs, 1977a). Examining openwork block deposits, their development and role in the landscape, requires a holistic approach (Whalley *et al.*, 2004). This has the potential to further our understanding of rock weathering, the control of geological structure on landforms, the production of substrates for biological colonisation and the impacts of climate change on landforms (Rea *et al.*, 1996; Meiklejohn and Hall, 1997; Andre, 2003; Rea, 2007). The main component of the research is to characterise the blockfield and to determine the current processes acting on it, with a specific focus on the role that aspect has on rock weathering, material wasting and disintegration. Furthermore, to understand the local weathering regimes, local lithologies and their response to freeze-thaw cycles with regard to temperature and moisture dynamics need to be understood and investigated (Boelhouwers *et al.*, 2002). A holistic process is followed, identifying the various interactions and controls on blockfield development (Whalley *et al.*, 2004), including the developmental stage(s) of the blockfield, near-surface temperature dynamics, climate and weather regimes, topographical controls, lithology, clast

characteristics, various erosional agents (such as aeolian agents) as well as biological presence. The resulting dissertation provides valuable information on the control that aspect, rock structure and ice or snow-cover has on weathering and the development of openwork block deposits. The research is of global significance, as the study is taking place in an environment ideal for investigating permafrost and active layer processes and landforms. It can, therefore, be a useful proxy for similar, palaeo-landforms elsewhere. Additionally, the research forms part of a longer-term investigation into geomorphology and climate change in this region.

The project falls within the discipline of physical geography, in particular the sub-field of geomorphology. Geomorphology as a system science focuses on landform studies, landscape studies and landscape change (Murray *et al.*, 2009; Church, 2010). Periglacial geomorphology, as sub-discipline of geomorphology, consists of the examination of diurnal, seasonal and perennial ground ice (permafrost) and their impact on landform and landscape development (Thorn, 1992). A focus is made on past, present and future processes and environments. Furthermore, snowpacks, fluvial, lacustrine and marine ice may also be investigated. The periglacial environment is one in which frost-action dominates and permafrost-related processed occur (French, 1996). Freeze-thaw weathering is recognised as an integral part to the periglacial environment, as well as frost wedging, heaving, sorting and similar processes (Washburn, 1980). Weathering and erosion processes are investigated in terms of how these have, and are currently affecting the blockfield on the Northern Buttress of the Vesleskarvet Nunataks. In particular, their impact on landscape development through synergistic or competing processes is investigated. The research is not hypothesis driven, but rather uses an exploratory and investigative approach. It makes use of the deductive scientific method and falls within the Newtonian paradigm (Church, 2010). The approach is objective and quantitative in nature and utilises a variety of mathematical and statistical analyses, comprises a large fieldwork component and makes use of empiricism (Kitchin and Tate, 2000; Murray *et al.*, 2009). Where deemed necessary, methodologies are adapted to local conditions and project requirements.

This dissertation is divided into six chapters. The current chapter provides background information on the topic under investigation, the study area as well as the aims and objectives of this project. Chapter 2 gives a more in-depth and detailed discussion on the topic under investigation; Chapter 3 details data requirements as well as the methodologies employed, whereas Chapter 4 deals with the analyses and discussion of findings. Chapter 5 briefly discusses further areas of research and limitations to the study. The dissertation concludes with Chapter 6, which summarises the findings of the project and how these may contribute to our knowledge of openwork block deposits and blockfield development.

1.2 Study Site

South Africa, together with the governments of Argentina, Australia, Belgium, Chile, the French Republic, Japan, New Zealand, Norway, the Union of Soviet Socialist Republics (Russia), the UK (United Kingdom of Great Britain and Northern Ireland), and the USA (United States of America) signed the Antarctic Treaty on December 1st 1959 (ATS, 1959). South Africa committed to utilising its presence in the Antarctic for scientific enquiry (Article II) (ATS, 1959), further committing to scientific enquiry by being one of the founding and a current full member of SCAR (Scientific Committee on Antarctic Research) (SCAR, 2010; SANAP, 2012c). South Africa has maintained a permanent presence in Antarctica since 1959 and its most recent base (SANAE IV) was opened on January 19, 1997 on the Vesleskarvet Nunataks (Stewart, 2011; SANAP, 2012b), the Northern Buttress of which is the site of the blockfield under investigation. The study site falls within a Scientific Exclusion Zone as designated by the DEA (Department of Environmental Affairs) of South Africa, ensuring human impact on the site is minimal and maintaining the integrity of the site (SANAP, 2009). The study area for the project is located in DML (Dronning Maud Land), Antarctica (Figure 3). DML lies between 20°W and 45°E and consists of four coasts: Princess Martha, Princess Astrid, Princess Ragnhild and Prince Harald (SANAP, 1992).

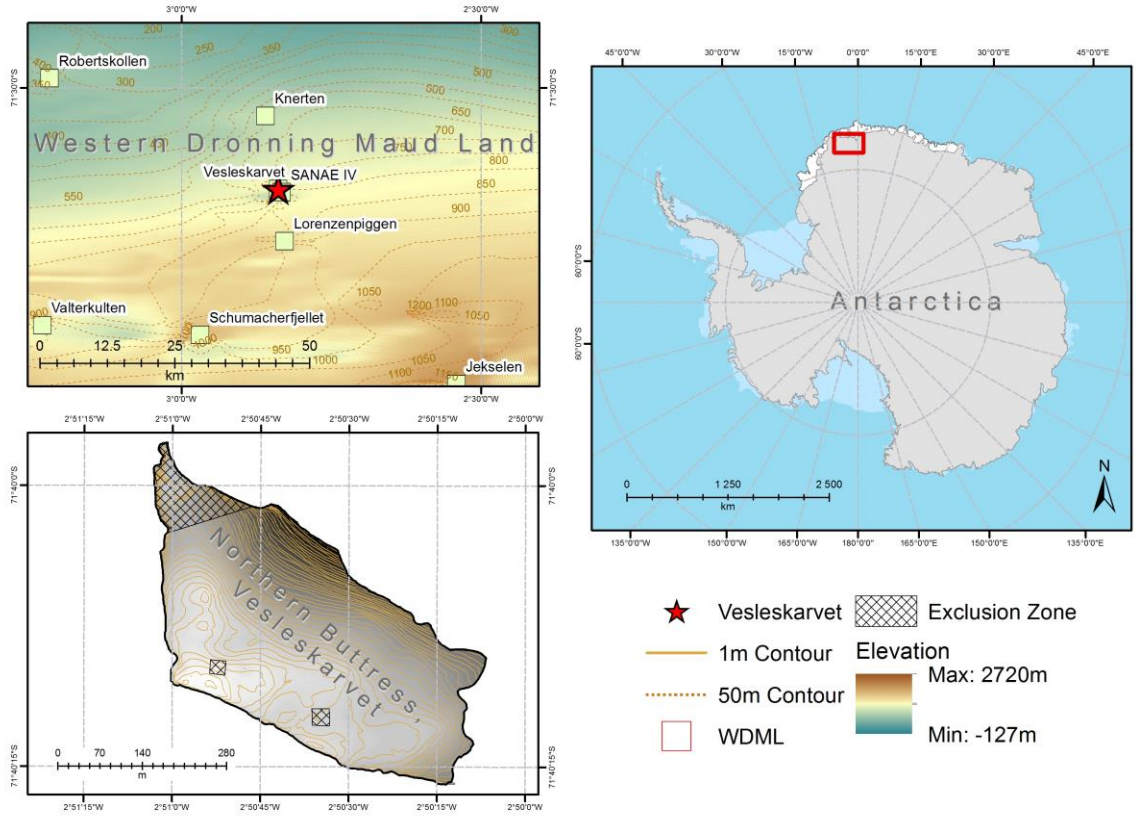

Figure 3: Location of the Vesleskarvet Nunataks and Western Dronning Maud Land in Antarctica.

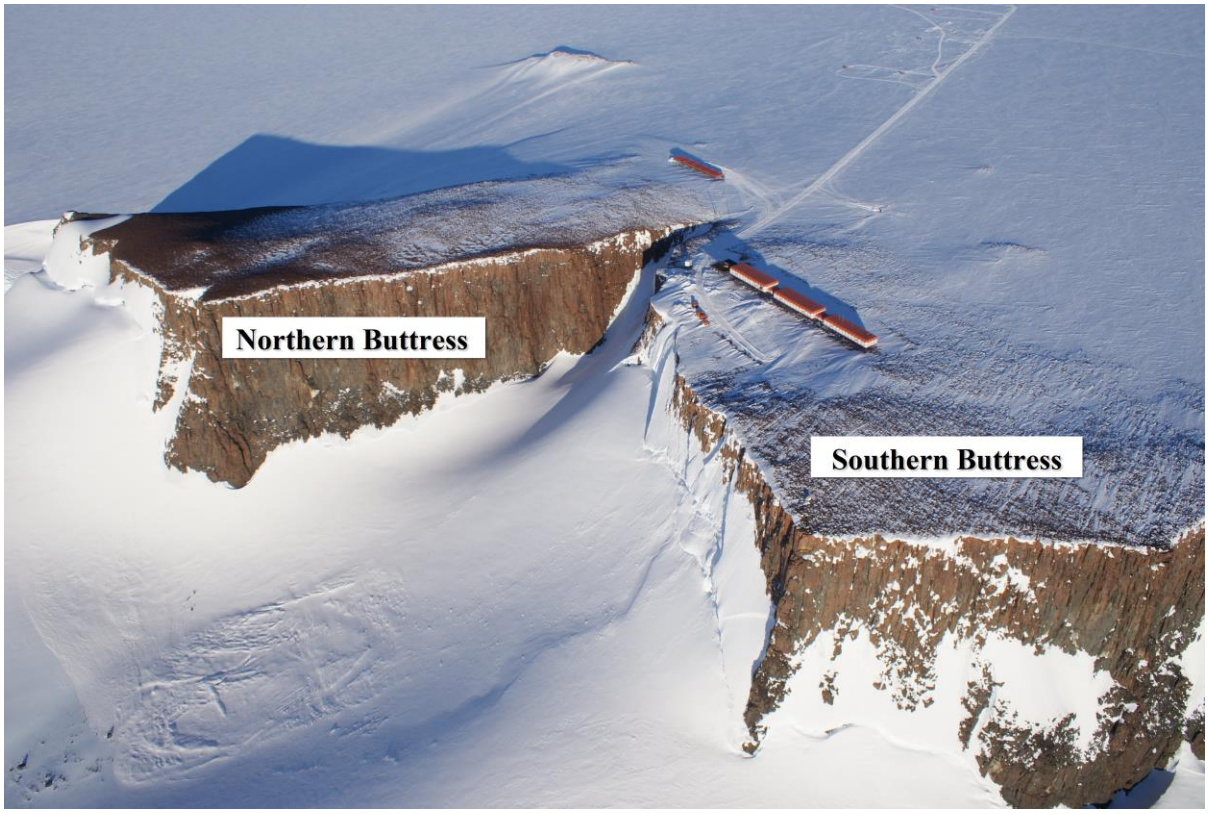

Figure 4: The Northern and Southern Buttress of the Vesleskarvet Nunataks. The blockfield under investigation is located on the Northern Buttress (Photo: Meiklejohn, 2007).

SANAE IV (the South African research base) and the study site for this project, the Northern Buttress (Figure 4) of the Vesleskarvet Nunataks (71°40'S, 2°51'W) are located inland of the Princess Martha coast in the north-eastern part of Maudheimvidda (Stewart, 2011). The region is characterised by the Ahlmannryggen-Borgmassivet Mountains (Figure 5, pg. 6) with scattered rocky outcrops (nunataks) (SANAP, 1992). These nunataks form part of the approximately ten percent of the Borgmassivet intrusive, such as Vesleskarvet, that is exposed at the surface (SANAP, 1992). In comparison, two percent of the Ahlmannryggen Mountains are exposed at the surface (SANAP, 1992). Overall approximately two percent of the underlying bedrock is accessible (Ravindra and Chaturvedi, 2011). The Vesleskarvet Nunataks, as a Borgmassivet intrusive, are of Mesoproterozoic origin (Republic of South Africa, 1981). The mafic Borgmassivet sill intruded into the Ritscherflya Supergroup at 1107 Ma (mega-annum); with mafic sills intruding into the north-eastern and south-western part of the Maud belt at 600 Ma (Grosch *et al.*, 2007).

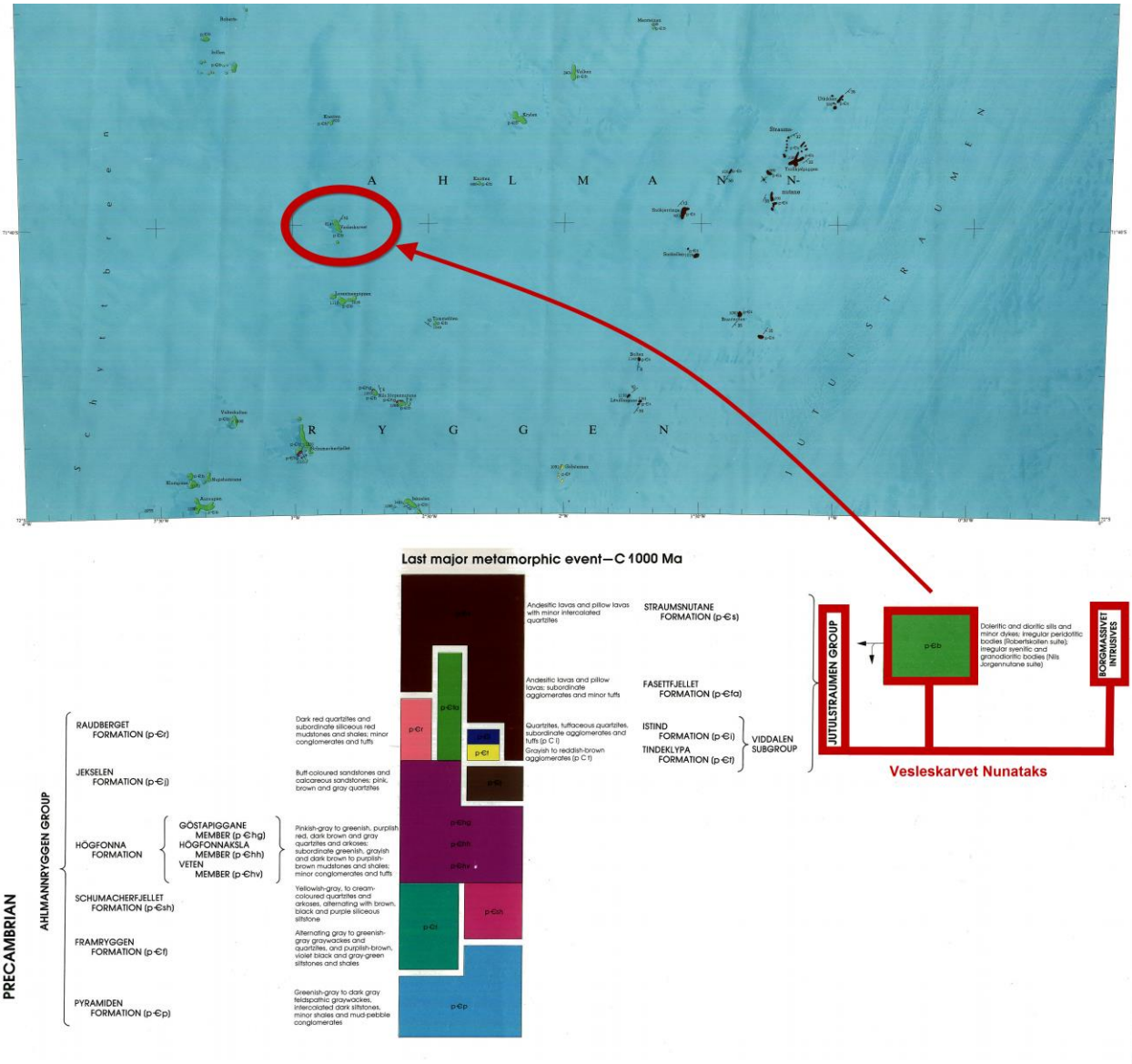

Figure 5: The top section of the figure shows a portion of the Borgmassivet intrusive with Vesleskarvet indicated by the red circle. The bottom part of the figure details the geological group (Adapted from Republic of South Africa, 1981).

A blockfield located on the Northern Buttress of the Vesleskarvet Nunataks consists of doleritic and dioritic sills and minor dykes with a strike and dip of the bedding at approximately ten degrees (Republic of South Africa, 1981; McCarthy and Rubidge, 2005). Diorite is a plutonic rock, of intermediate composition and is coarse grained, exhibiting crystals up to one centimetre in size (Weinert, 1980; McCarthy and Rubidge, 2005). Dolerite, on the other hand, is hypabyssal, of basic composition and is medium-grained, exhibiting smaller crystals than diorite (Weinert, 1980; McCarthy and Rubidge, 2005). Both dolerite and diorite are massive rocks, which are generally resistant to mechanical weathering processes (Briggs, 1977a). However, their large crystal sizes make them susceptible to both mechanical and chemical weathering. Examples of mechanical weathering

active for the study site include thermal stress and/or fatigue, granular disintegration, salt weathering, and freeze-thaw action. Examples of chemical weathering include hydration and hydrolysis, solution weathering, salt weathering, and oxidation (French, 1996). In particular, freeze-thaw weathering has long been thought to play a significant role in cold environments (Fahey, 1973; Sumner *et al.*, 2004). However, the role of freeze-thaw weathering in periglacial environments has been much debated (*e.g.* Hall, 2002). Furthermore, although rates of chemical weathering are slower for cold climates, it is still present and at best it may be said that mechanical weathering has a more dominant role in these environments (French, 1996). Chemical weathering of the large crystals leads to the solution of individual minerals within the matrix, whereas granular disintegration of individual grains occurs from mechanical processes (Briggs, 1977a). Dolerite contains equal portions of pyroxene (iron, calcium and magnesium silicates) and calcium feldspar [plagioclase] (potassium, sodium and aluminium silicates). Diorite contains equal portions of alkali feldspar (calcium aluminium silicate), calcium feldspar [plagioclase] (calcium aluminium silicate) and amphibole (calcium, iron, aluminium and magnesium silicate) (McCarthy and Rubidge, 2005). The greater the amounts of pyroxene present the darker the rock; dolerite is, therefore, darker than diorite. Diorite, unlike dolerite, may also occasionally contain some quartz (Weinert, 1980). In its non-weathered state dolerite is dark grey, whereas diorite appears medium grey. Rock surfaces for the study site, however, appear red in colour, indicating weathering of metallic minerals, such as iron, after exposure (Weinert, 1980). They are also metamorphosed and exhibit case hardening (*e.g.* Mol and Viles, 2012). This, together with the origin and length of exposure of the surface all has implications on the susceptibility of the rock to weathering and erosion as well as the formation of the blockfield.

The current climate is that of a cold desert and the continent is the coldest and driest on earth, receiving very little precipitation (SANAP, 1992; Ravindra and Chaturvedi, 2011). Average temperatures in the Antarctic coastal regions are approximately 5°C for the summer months and -35°C for the winter months, whereas the Antarctic plateau experiences approximately -25°C for the summer months and -70°C for the winter months (Ravindra and Chaturvedi, 2011). The average annual temperature for the study site is -16.4°C, the average lowest temperature is -24°C and the average highest temperature is -14°C. The highest recorded temperature is 6°C and the lowest recorded temperature is -27.8°C. Average relative humidity is 63%. Precipitation throughout the year is negligible, with only 150-200 mm of precipitation in the form of snowfall being received annually in the coastal areas (Ravindra and Chaturvedi, 2011). WDML receives between 55-81 mm annually (Reijmer and van den Broeke, 2001). The study site also experiences a dominant wind direction from the east and average wind speed approximates 11 $m.s^{-1}$. Due to the current climate chemical weathering, although present, occurs at a slower rate than in more humid climates and physical weathering is thought to have the greatest impact. Evidence also shows that the current extent of the

Antarctic ice sheet can be traced back to the LIGT (Last Interglacial Transition), approximately 8 000 years BP (Before Present), following the ice sheet's retreat after the LGM (Last Glacial Maxima) about 18 000 years BP (Ravindra and Chaturvedi, 2011). Accordingly, the Vesleskarvet Nunataks have been exposed for approximately 8 000 years and all surfaces may be considered to have been exposed to erosional and weathering processes since the Holocene. Nunataks, rising above the ice, have been exposed to the elements longer than areas still covered by snow (Ballantyne, 1984) and are, therefore, more likely to exhibit periglacial landforms than areas still covered by ice and snow (Rea, 2007). It has also been suggested that nunataks are examples of blockfields (Paasche *et al.*, 2006; Rea, 2007). Blockfields are known to occur in glacial or periglacial environments and, regardless of their environment, exhibit common features (Boelhouwers, 1999; Sumner, 2004; Sumner and Meiklejohn, 2004; Rea, 2007). These include angular to sub-angular clasts on gentle to undulating surfaces (less than 25°) (Rea, 2007; Ballantyne, 2010; Grab *et al*., 2012). Furthermore, although sediment and soil may be sparse, it is not uncommon and sandy to silt/clay matrices have been observed (Ballantyne, 2010). Blockfields also commonly have clasts whose surfaces exhibit edge-rounding (Ballantyne, 1998; Hall *et al.*, 2002; Boelhouwers, 2004), pitting and hollowing, friable surfaces, rough surfaces or flaking (Rea *et al.*, 1996; Whalley *et al.*, 1997; Ballantyne, 1998; Goodfellow *et al.*, 2008). The characterisation of the blockfield located on the Vesleskarvet Nunataks (Figure 6) contribute to our knowledge of these landforms, the processes acting on them, the length of exposure of the surface as well as the role of biological organisms across the landform. Additionally, an autochthonous blockfield, also occurring on dolerite, has been described for Basen, WDML, Antarctica by Boelhouwers (2004). Both the Basen blockfield and the blockfield under investigation are of similar geology. Clasts for the autochthonous Basen blockfield consist of rounded blocks of medium-grained dolerite. Furthermore, both blocky deposits occur in the same geographical region. This offers the unique opportunity to contrast and compare the two openwork blocky deposits.

Figure 6: View of the blockfield looking north. Note the person for scale.

Weathering and erosion processes and rates on the Vesleskarvet nunataks are affected by the dry, cold and periglacial conditions of the study site. The angular nature and distinct faces of the doleritic and dioritic clasts (Republic of South Africa, 1981) allow for investigating the role that parameters such as aspect have on weathering across the study site. Additionally, the small amounts of exposed bedrock, as discussed above, underlie the rarity of accessible research sites on the continent. The site under investigation is not only exposed but also accessible, located on the same nunatak as the current South

African research base. All these factors, as discussed above, make the selection of the site for the project suitable. Science on the Antarctic continent is both exciting and valuable and research in the earth sciences has the potential to further our understanding of the earth and earth systems (SANAP, 2012a). This project contributes to such knowledge and may be used as a baseline for further studies.

1.3 Aims and Objectives

The aim of the project is to characterise the openwork block deposit on the Northern Buttress of the Vesleskarvet Nunataks and to identify any environmental processes currently active across the blockfield. The overall aim may be broken down into six key objectives. These are listed below.

1. To determine whether or not the blockfield is allochthonous or autochthonous and to identify the blockfield matrix;
2. To investigate the morphology and clast characteristics of the blockfield;
3. To determine if any aspect control on weathering across the blockfield exists;
4. To identify soil moisture and temperature regimes across the blockfield;
5. To identify the susceptibility of moisture uptake of clasts in different environments; and
6. To determine how long the blockfield surface has been exposed to weathering processes and erosional agents using proxies such as sediment clay content and climate record.

CHAPTER 2: Background

The following chapter is divided into two parts. First, blockfields, their occurrence, development and formation, where they are found, as well as current research into these landforms are discussed. Second, an introduction into weathering and possible glacial influence on the study area is examined.

2.1. Blockfields

Landforms known as blockfields are also described by terms such as blockmeer, felsenmeer, stone fields, boulder fields or mountain top detritus (Rea *et al.*, 1996; Rea, 2007). For the purpose of this study, the term '*blockfield'* is used to describe these features.

A blockfield consists of regolith boulders and angular to sub-angular clasts, on a gentle or undulating surface (less than 25°) in present-day or former periglacial environments (Rea, 2007; Ballantyne, 2010; Grab *et al*., 2012). However, these periglacial or glacial settings are not always the case (Boelhouwers and Sumner, 2003). Blockfields are thought to form under tectonically stable conditions (Rea, 2007) and are described as either openwork deposits or consist of clasts embedded in a matrix of fines (Ballantyne, 2010). These landforms may be grouped into different types depending on the matrix they occur on. Ballantyne (1998) suggests that Type I is clast supported and consists of an openwork blocky deposit with fines forming a matrix at some depth below the surface. A Type II blockfield consists of blocks set in a cohesionless sandy matrix, whereas a blockfield of Type III has blocks set in a silt/clay matrix exhibiting no evidence of frost sorting. Autochthonous deposits, characterised by *in situ* weathering and limited downslope displacement of debris, may exhibit abrupt clast changes at geological boundaries. Allochthonous blocky deposits, such as block streams or blockruns, are characterised by mass movement downslope (Ballantyne, 1998; Ballantyne, 2002; Boelhouwers, 2004; Paasche *et al.*, 2006; Goodfellow *et al.*, 2008). As previously described (Background, Context and Motivation, pg. 1), they are found at high altitudes and mid to high latitudes (*e.g*. Rea *et al.*, 1996; Rea, 2007). Blockfields are generally associated with highly metamorphosed and resistant lithologies such as Palaeozoic quartzite, fine to medium grained basalts, granites or gneisses (Boelhouwers, 2004). All of these lithologies have clasts with low porosities (non-frost susceptible) and a crystalline structure (Ballantyne, 2010). Soil is often absent, or if present, horizons are poorly developed (Ballantyne, 2010). Lozinski in 1909 (in Boelhouwers, 2004) first proposed that blockfields indicate the presence of periglacial environments. Furthermore, Ballantyne and Matthews (1982) imply blockfields postdate deglaciation. In contrast, Whalley *et al.* (2004) argue that cold-based ice may preserve these landforms and suggest blockfields can predate glaciation. The presence of angular clasts and the absence of chemical weathering support the

argument of post-deglaciation (Boelhouwers, 2004). However, blockfields are increasingly thought to be the result of complex and azonal processes acting over a long period of time, including stress release, chemical and mechanical weathering as well as biogenic weathering (Meiklejohn and Hall, 1997; Andre, 2003; Boelhouwers, 2004). Hall (2002) suggests that the size and shape of blocks found in blockruns on the Falkland Islands relates to the joint-determined blocks of rock outcrops. The influence of geological and lithological control on such landforms may not be underestimated (Briggs, 1977a). Consequently, the angular nature of clasts may not solely be used as an indicator of periglacial environments and one single linear process or control cannot be ascribed to blockfield development.

Rea (2007) assigns blockfields to various ages: the recent (Holocene), of Pleistocene origin or to pre-Pleistocene age. The different ages yield specific blockfield characteristics and are described by Rea (2007) as follows; recent blockfields, younger than 10 000 years old (10 000 BP), require rapid development under cold climatic conditions. This would have an impact on particle size ranges, quantity of fines, clay mineralogy and clast angularity found at these sites. Processes such as granular disintegration control particle size ranges. Furthermore, clay minerals should be absent or if present, represent limited chemical alteration of clast surfaces. For these blockfields a Type I openwork structure is expected. Blockfields of Pleistocene origins have developed over the last 1.8 Ma. The Pliocene-Pleistocene boundary has recently been adjusted to 2.58 Ma (Gibbard *et al.*, 2010) and Rea's age description of blockfields is adjusted accordingly. The longer period of exposure yields more fines. However, the sediment range will be significantly controlled by the local lithology and bedrock grain size. The greater quantity of fines and the role of frost action yield structures of Type II or Type III. The most likely structure to be expected is Type II. However, Type III openwork structures may be found if blockfield development is lithology controlled. Blockfields of pre-Pleistocene origin have formed for more than 2.58 Ma and have been exposed to cold (periglacial and glacial) as well as warm climates. Both Type II and Type III structures are expected, unless fines have been removed through erosional processes. Both Pleistocene and pre-Pleistocene era blockfields may have survived glacial-interglacial periods as ice-free nunataks. Alternatively they might have survived glaciation, if glaciers were cold-based and non-erosive (Whalley *et al.*, 2004). It is, however, problematic to assign blockfields to these different ages. Furthermore, various developmental models have been proposed for blockfield development, increasing the complexity of assigning blockfields to a specific age.

Two general models, the Neogene and periglacial model of blockfield development have been suggested. Ballantyne (2010) suggests an alternate model that combines the two previous models into one. The Neogene model proposes that pre-Quaternary chemical weathering, *i.e.* deep weathering

leads to long-term regolith production (Boelhouwers, 2004; Ballantyne, 2010). A lowering of blockfield mantles occurs during the Quaternary, tor emergence during the Pleistocene and a subsequent renewal of regolith cover. Depending on the depth of the original regolith and the surface-lowering rate during the Quaternary a blockfield may retain Neogene characteristics. Assuming surface lowering is greater than the original depth of the regolith; mechanical weathering becomes the main mechanism acting on the blockfield. Throughout these stages frost action (if present) is restricted to the sorting and alteration of the Neogene deposits and it is not seen as an active mechanism in blockfield development (Ballantyne, 2010). Rea *et al.* (1996) and Kleman and Glasser (2007) also suggest that blockfields may survive glaciations intact, such as the blockfield on Bouvetøya (Hall, 2002). A blockfield remains intact if glaciations are cold-based and frozen to the substrate (*e.g.* Whalley *et al.*, 2004; Kleman and Glasser, 2007). Holmlund and Näslund (1994) argue that no significant increase in ice thickening during the Quaternary occurred for DML. Instead they suggest that the glacial landscape was moulded by temperate glaciers of a warmer Antarctica and that the Maudheimvidda ice sheet in DML is cold-based and frozen to the substrate. Consequently, blockfields may have remained intact during glaciation and pre-date glaciation for the region.

Blockstreams and blockfields, as sedimentary evidence of periglacial activity, allow for the quantitative analyses of palaeoclimates (Boelhouwers *et al.*, 2002.) Relative-age dating (quantifying the change to rock surfaces due to exposure over time) may be used to determine the time since deglaciation (Sumner *et al*., 2002). This includes weathering rind development (thickness), increase in surface roughness, lichen presence, depth of weathering pits and decrease in rock hardness. Clast angularity may also be used as a relative-age dating technique, due to *in situ* grain-to-grain physical and chemical weathering resulting in a decrease of angularity (Sumner *et al*., 2002). However, a loss in angularity may also be due to attrition during transport (Sumner *et al*., 2002). Older surfaces tend to be more weathered, whereas younger active sites tend to be more blocky and angular (Sumner *et al*., 2002). Furthermore, older and well-structured blockfields exhibit blocky material that is disassociated from the bedrock (Sumner and Meiklejohn, 2004). The relict nature of blockfields and the fact that post-glacial surfaces may exhibit pre-glacial erosional features (Boelhouwers, 2004), lends support to the Neogene model. This is further supported by blockfield surfaces exhibiting features dating back to the Tertiary, as described by *e.g.* Rea *et al.* (1996), Whalley *et al.* (2004), Sumner and Meiklejohn (2004) and Paasche *et al.* (2006). High clay content of fines (Rea *et al.*, 1996; Whalley *et al.*, 2004; Paasche *et al.*, 2006), evidence of pitting and etching (Whalley *et al.*, 1997) and blockfield surfaces showing no evidence of postglacial frost action (Andre, 2002) all lend evidence to the Neogene model. On the other hand, clay minerals are not a definite indicator of certain climates, such as humid ones, and the Neogene surface is not likely to remain intact (Meiklejohn and Hall, 1997; Andre, 2003; Boelhouwers, 2004; Ballantyne, 2010). Chemical weathering has also been shown to play a role in

cold environments, even if rates of decomposition are slower. Furthermore, it has been shown to be important for joint widening and matrix development (Boelhouwers, 2004). The importance of temperature cycles and regimes may also not be underestimated as hourly, diurnal and seasonal cycles contribute to thermal stress and fatigue. It is also thought that thermal stress may lead to bedrock fracturing (Boelhouwers, 2004), although the inherent tensile strength of the rock still needs to be overcome. Nevertheless, thermal differences due to hourly, diurnal and seasonal temperature cycles occur for the regions blockfields are found in. Stress due to these cycles is found to be highest on intact bedrock and lower on already fractured clasts, indicating that the clasts most non-susceptible to frost action are most suited to thermal fatigue (Boelhouwers, 2004). The temperature threshold of 70°C suggested by Yong and Wang (1980) furthermore indicates that temperature ranges for thermal stress may be less than the required 2°C.min^{-1} referred to by Richter and Simmons (1974). This supports thermal fatigue and stress in blockfield development.

The periglacial model, on the other hand, suggests that blockfields developed during the colder Quaternary, with the main mechanisms being frost wedging, sorting and weathering (Ballantyne, 2010). Blockfields on South Georgia are thought to be the result of frost shattering of the fissile bedrock (Stone, 1974 in Hall, 2002). Frost wedging is thought to be active in the jointed bedrock at the boundary of the active layer and impermeable permafrost, where seasonal freeze-thaw cycles are strongest (Ballantyne, 1998; Boelhouwers, 2004; Paasche *et al.*, 2006; Ballantyne, 2010). Matsuoka (2008) and Murton *et al.* (2006) provide evidence for the role of freeze-thaw weathering in blockfield development. Angular sub-surface clasts overlying non-weathered jointed bedrock, microgelivation in porous bedrock (Dredge, 1992) and the fact that clay minerals are not necessarily the result of the humid Neogene climate, as suggested above, all support this model (Ballantyne, 2010). Blockfields may, therefore, be impacted by periglacial processes and features such as lateral and vertical sorting profiles and their associated clast fabrics, sorted circles and stripes, needle ice, thúfur mounds, sorted ground and gelifluction lobes have been found on blockfields (Whalley *et al.*, 1997; Boelhouwers, 2004; Goodfellow, 2008; Ballantyne, 2010). However, Rea *et al.* (1996) and Boelhouwers (1999; 2004) suggest that these features are secondary and not responsible for block production. Instead, thermal stress, chemical weathering and pre-existing bedrock jointing have all been suggested as mechanisms of block production (Boelhouwers, 2004). Boelhouwers (2004) suggests that frost weathering requires pre-existing jointing and cracks to widen and extend joint spaces, rather than frost weathering being a mechanism of block production. This suggests that periglacial controls take a secondary role in blockfield development. Pre-existing jointing and fracturing are thought to be the result of stress release (for example dilatation), tectonic stress or the unloading of surfaces (Boelhouwers, 2004; Goodfellow *et al.*, 2008), or as a result of thermal fatigue (Boelhouwers, 2004). Pre-existing cracks and joints are zones of preferential weathering where water infiltrates, freezes and

exerts pressure, leading to granular disintegration. However, the angularity of clasts, previously thought to support periglacial origins, doesn't necessarily indicate an absence of chemical weathering (Boelhouwers, 2004) or prescribe periglacial conditions (Hall *et al.*, 2002). Blockfields have also been shown to exist in areas never glaciated (Boelhouwers and Sumner, 2003). Hall *et al.* (2002) also suggest a diminished role of freeze-thaw weathering in blockfield evolution. Furthermore, cold regions also exhibit rounded clasts (Boelhouwers, 2004). Here the rounding of clasts is partly ascribed to mechanical weathering (Boelhouwers, 2004). Clasts are, therefore, predominantly influenced by the underlying lithology, joint structure and inherent mineralogy, (Ballantyne, 1998; Boelhouwers, 2004; Whalley *et al.*, 2004, French, 2011).

With both models having proponents for and against them, Ballantyne (2010) suggests an alternate model (Figure 7). The general model of blockfield development can be divided into four stages, incorporating both the Neogene and periglacial models. Stage 1 applies to pre-Pleistocene chemical weathering of bedrock; Stage 2 applies to stripping of regolith by ice masses during the cooler Pleistocene; in Stage 3 frost wedging becomes the dominant mechanism of rock disintegration and in Stage 4 the (now) periglacial blockfield exhibits no Neogene characteristics, chemical weathering is diminished and mechanically weathered clasts overlie a matrix of fines. For this model to apply certain assumptions have to be made. Ballantyne (2010) assumes a lowering of approximately ten meters of the original Neogene saprolite cover during the Quaternary. This threshold may be exceeded if local circumstances allow for it. Surface lowering may be due to glacial erosion, mass movement or *in situ* weathering and erosion. Glacial erosion strips the regolith due to the overlying ice masses. However, in a region that has not experienced glaciation this cannot be assumed to be the reason for surface lowering. This, for example, applies to the blockfield described by Boelhouwers and Sumner (2003) for Namibia. Mass movement (the second mechanism of surface lowering) is thought to be the reason for surface lowering when frost creep is balanced by the production of debris under periglacial conditions (Ballantyne, 2010). High pore-water pressure during the seasonal thaw of

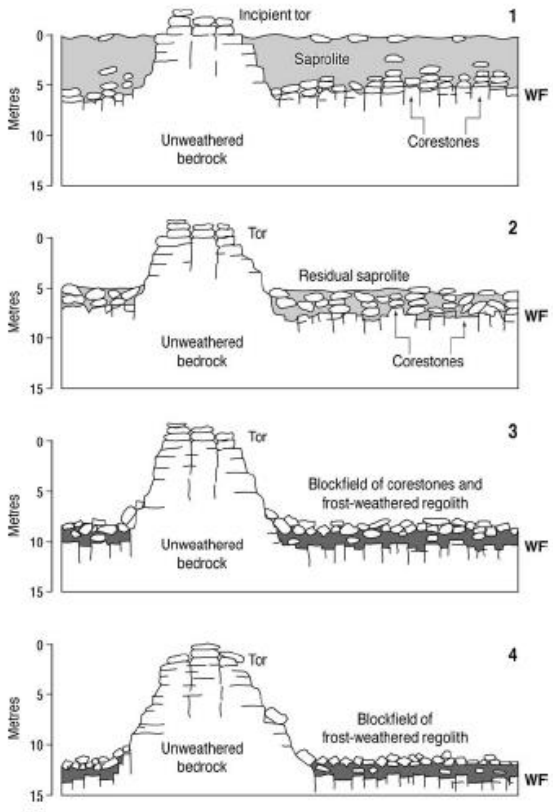

Figure 7: The general model of blockfield development (Ballantyne, 2010).

underlying sediment leads to gelifluction or sliding failing (Wilson, 2007). However, excavations of autochthonous blockfields show little evidence of mass movement (Ballantyne, 1998; Paasche *et al.*, 2006). Mass movement as an instrument of surface lowering also fails to explain sudden changes in blockfield composition at geological boundaries (Ballantyne, 2010). Finally, the third mechanism of surface lowering is *in situ* weathering and erosion. The gradual weathering of clasts and subsequent removal of fines by either wind or water action causes the surface to lose material. Weathering and erosion occurs due to freeze-thaw cycles, thermal fatigue and stress as well as chemical and biological weathering, albeit at slower rates (Ballantyne, 1998). The surfaces of clasts found on blockfields also exhibit specific features such as edge-rounding (Ballantyne, 1998; Hall *et al.*, 2002; Boelhouwers, 2004), pitting and hollowing, friable surfaces, rough surfaces or flaking (Rea *et al*., 1996; Whalley *et al.*, 1997; Ballantyne, 1998; Goodfellow *et al.*, 2008). The mechanisms for surface lowering can, therefore, be said to be a combination of the three mechanisms mentioned above.

Blockstreams in the Western Cape Mountains of South Africa appear to have developed following mechanical weathering of Neogene deposits during the Late Pleistocene, followed by further clast accumulation due to a periglacial environment (Boelhouwers, 1993; Boelhouwers and Meiklejohn, 2002). Similar to this are blockfields described by Grab (1999) and Boelhouwers *et al.* (2002). These deposits, therefore, support Ballantyne's (2010) proposed model of blockfield development. However, blockfields elsewhere support the Neogene, periglacial or Ballantyne's composite model. Blockfields described by Boelhouwers and Sumner (2003) speak against periglacial origin. The notion that blockfields are the exclusive result of periglacial conditions is a contentious and much debated one (Boelhouwers and Sumner, 2003; Boelhouwers, 2004; Whalley *et al.*, 2004). Similarly contentious is the argument that blockfields are an indication of current or previous periglacial environments (Boelhouwers and Sumner, 2003; Boelhouwers, 2004).

2.2. Weathering and Erosion

Retreating and advancing ice masses of past ice ages have shaped the region under investigation. During the Pleistocene epoch the most recent ice age ended approximately 10 000 years BP (McCarthy and Rubidge, 2005). Ravindra and Chaturvedi (2011) suggest the Antarctic ice sheet reached its current extent approximately 8 000 years BP, during the LIGT. The milder climate of the Holocene opened up areas previously glaciated, in some areas creating periglacial environments (McCarthy and Rubidge, 2005). Indications of these environments include, for example, patterned ground (Grab *et al.*, 2012). Miniature sorted patterned ground such as sorted circles occurs for the study site. Sorted circles are characterised by fine material surrounded by a border of coarse stones (Ballantyne and Matthews, 1982) and may be the result of frost heave (Grab, 1997) and/or freeze-

thaw processes (Boelhouwers, 1995). Patterned ground is also found on other nunataks in the region. The current periglacial environment also influences the development and form of blockfields on the continent.

As discussed under Study Site (pg. 6) the current climate of Antarctica is that of a dry and cold desert (SANAP, 1992; Ravindra and Chaturvedi, 2011). Average temperatures are less than 5°C and -35°C in the coastal regions for the summer and winter months respectively. In comparison, the average temperatures for the Antarctic plateau are approximately 35°C less for the same seasons (Ravindra and Chaturvedi, 2011). Cold temperatures, low relative humidity and a low average dew point of -21°C result in only a small amount of precipitation (150-200 mm) falling annually in the coastal areas (Ravindra and Chaturvedi, 2011), with 55-81 mm for WDML (Reijmer and van den Broeke, 2001). Mean annual permafrost temperatures for DML range from -8.3°C to -17.8°C and increasing altitude is correlated with lower temperatures. Active layers in the coastal regions have average depths of 0.7 m (Vieira *et al.*, 2010). At high elevations the active layer is generally between 0.1 m and 0.25 m deep (Vieira *et al.*, 2010). Both elevation and latitude have been shown to control active layer thickness with an increase in latitude and altitude resulting in a decrease in active layer thickness (Adlam *et al.*, 2010). Coastal regions also have deeper active layers than the interior (Adlam *et al.*, 2010). The glacial environment, furthermore, impacts soil and sediment properties. Glacial sediment is generally unsorted, comprised of coarse and fine sediment (Briggs, 1977a). For these sediments the sorting value will be large, as the sorting process is generally inefficient and sediment tends to be local (Briggs, 1977a). Consequently, a high sorting value is expected for sediment analyses for the study site.

Local geology and lithology as well as relief and topography influence the energy of and type of erosional agents (Alsharhan and El-Sammak, 2004). Similarly, the parent rock, which dictates mineralogy, and the environment influence the type and rate of weathering (Weinert, 1980; Grotzinger *et al.*, 2007; Rea, 2007). Climate influences the rate of weathering (Grotzinger *et al.*, 2007) and chemical weathering is dominant in hot and humid climes. Local climate (precipitation and temperature), topography, the presence or absence of soil as well as time all play important roles in the weathering process (Weinert, 1980; Grotzinger *et al.*, 2007; Rea, 2007). In particular, microclimates are important drivers to weathering processes, as are rock temperatures and moisture (Sumner *et al.*, 2002). Nevertheless, the role of general climatic conditions may not be overlooked. Climate influences reaction rates and cold conditions may, as opposed to enhancing detritus formation, preserve existing layers (Sumner and Meiklejohn, 2004). Snow cover also influences weathering rates (Shakesby *et al.*, 2006), providing an insulating layer or being a source of moisture

(Ishikawa, 2003; Hedding, 2008). Local topography influences drainage and the water to rock contact, whereas the age of the deposit controls the length of time the deposit has been exposed to weathering processes (Rea, 2007). Lithology and geology exert significant control on landform development and weathering rates (Weinert, 1980). Microbiota have been shown (*e.g.* Weinert, 1980; Büdel *et al.*, 2004; Shakesby *et al.*, 2006; Matthews and Owen, 2008; Church, 2010; Mol and Viles, 2012) to influence weathering rates as well as rock properties (Briggs, 1977a; Cooke, 1979). The susceptibility of rock to weathering is to a large extent influenced by properties such as microporosity, water absorption capacity and porosity (Briggs, 1977a; Cooke, 1979). However, porosity and permeability is low in material such as igneous rock, common to the study area (Grotzinger *et al.*, 2007). Vesleskarvet, a Borgmassivet intrusive, is of Precambrian origin (Republic of South Africa, 1981) and intruded at approximately 1107 Ma into the Ritscherflya Supergroup (Grosch *et al.*, 2007). The current extent of the Antarctic ice sheet can be traced back to the last LIGT, approximately 8 000 years BP (Ravindra and Chaturvedi, 2011), indicating that the current surface of the nunatak has only been exposed for approximately 8 000 years. Consequently, weathering processes and erosional agents are considered to have been acting on the nunatak's surface only since the Holocene. The absence and scarcity of soil, the cold and dry climate and the massive structure of the rock suggest slow weathering rates for the study site (Grotzinger *et al.*, 2007). The presence of plagioclase, pyroxene and amphibole in the rock, furthermore, suggests low weathering intensities for the study site (Grotzinger *et al.*, 2007). The mineral solubility of pyroxene and feldspar as well as the fractured nature of clasts, on the other hand, suggest moderate weathering rates (Grotzinger *et al.*, 2007).

The Northern Buttress of the Vesleskarvet Nunataks consists of doleritic and dioritic sills and minor dykes (Republic of South Africa, 1981). Joints develop from the cooling, contracting and cracking of lava (Grotzinger *et al.*, 2007). Similarly, the cooling of magma leads to joint development, which exert control on the blockfield under investigation. This is of particular importance, as block supply on the blockfield is largely due to preferential weathering along pre-existing joints within the deposit. An area covered by glaciers, once deglaciated may undergo dilatation and stress release (Boelhouwers *et al.*, 2003; Boelhouwers *et al.*, 2008). The removal of country rock through erosional agents or isostatic uplift results in fracturing of the intrusive rock following stress release along bonded discontinuities (Briggs, 1977a; Weinert, 1980; Boelhouwers *et al.*, 2003). Fractures and joints become zones of weakness and areas of preferential weathering (Weinert, 1980; Grotzinger *et al.*, 2007) for ice and frost (Boelhouwers *et al.*, 2008). A more dense network of fractures are found closer to the surface and rocks that are foliated, as some metamorphosed rock, fail along planes of foliation (Weinert, 1980). Homogeneous rock tends to fail perpendicular to the plane of unloading, such as the surface of the earth. However, little evidence of foliation is present for the study site and block supply is predominantly due to the pre-existing joint structure of the deposit. Furthermore, minerals such as

olivine become unstable under lower temperatures (Weinert, 1980). As the country rock is unloaded rock temperatures decrease, allowing the mineral to transform into serpentine, further fracturing the rock due to volumetric differences (Weinert, 1980).

Rocks for the study site appear angular in nature (*e.g.* Figure 8 to Figure 11). The shape and size of a clast is not only dependent on its original shape, lithology, its physical and chemical properties (Ballantyne, 1998; Boelhouwers, 2004; Whalley *et al.*, 2004, French, 2011) but also the type and extent of weathering it has been exposed to (Briggs, 1977a). A blockfield in the Skeleton Coast of Namibia also displays angular clasts (Boelhouwers and Sumner, 2003). The common factor between the blockfield under investigation and the Namibian openwork block deposit appears to be the fine-grained dolerite regolith; suggesting angularity of clasts for the study site may be partly ascribed to the nature of the underlying bedrock, as already discussed on pg. 14.

Figure 8: Angular nature of Sample 9. A measuring rod of 50 cm length is used for scale.

Figure 9: Angular nature of Sample 14. A measuring rod of 50 cm length is used for scale.

Figure 10: Angular nature of Sample 20. A measuring rod of 50 cm length is used for scale.

Figure 11: Angular nature of Sample 22. A measuring rod of 50 cm length is used for scale.

The network of fractures present in the original bedrock initially determines clast shape and size after dilatation (*e.g.* Ballantyne, 1998; Boelhouwers, 2004; Whalley *et al.*, 2004, French, 2011). Subsequent weathering and erosional processes cause the formation to break into large columns of rocks along joint intersections, rounding clasts and further disintegrating and decomposing the rock (Grotzinger *et al*., 2007). The type of weathering not only leads to mineralogical and textural changes but also influences the sediment produced (Briggs, 1977a; Weinert, 1980; Hall, 2002; Grotzinger *et al.*, 2007). Weathering and erosional processes active on the nunatak include thermal stress and/or fatigue, solution weathering, granular disintegration, hydration and hydrolysis, freeze-thaw action and oxidation. Biological agents are also thought to play a role.

Dolerite and diorite, hypabyssal and plutonic respectively (McCarthy and Rubidge, 2005), are crystalline rocks (Weinert, 1980). The hypabyssal nature of dolerite yields a medium-grained rock, whereas plutonic rocks are characterised by coarse crystals (Grotzinger *et al*., 2007). Both classed as massive, dolerite is a basic and diorite an intermediate rock (Weinert, 1980; Grotzinger *et al*., 2007). Massive rock is more resistant to mechanical weathering than well-structured rock and basic (mafic) rocks, such as dolerite, are prone to solution (Briggs, 1977a; Grotzinger *et al.*, 2007). The large crystals of the rock are susceptible to both chemical (solution) weathering, weakening the rock, as well as mechanical (granular) disintegration (Briggs, 1977a). Diorite consists of plagioclase and amphibole, whereas dolerite consists of plagioclase and pyroxene (Weinert, 1980; McCarthy and Rubidge, 2005). Calcium feldspar, a calcium aluminium silicate, occurs as isolated crystals in the rock (Grotzinger *et al*., 2007). Its structure is that of a framework of silicates and it has a hardness of six on the Moh hardness scale. In addition, crystals faces are commonly not developed, increasing the strength of the rock (Grotzinger *et al.*, 2007). Pyroxene consists of calcium, magnesium and iron silicate minerals (Grotzinger *et al.*, 2007). A structure of single chains and four- to eight-sided prismatic crystals yield a hardness of five to six (Grotzinger *et al*., 2007). Amphibole (hornblende), consist of calcium, aluminium and iron/magnesium silicate (Grotzinger *et al.*, 2007). Its pale to deep green colour (Grotzinger *et al*., 2007) allows for differentiation between dolerite and diorite for the study site. The double-chain structure and six-sided prismatic crystals give it the same hardness as pyroxene (Grotzinger *et al*., 2007).

The type of bond also has implications on weathering of minerals (Klein and Dutrow, 2008). Relatively weak bonds exist between the stronger bonds of the chains of feldspar, pyroxene and amphibole minerals. These result in the blocky habit of feldspar and the prismatic habit and cleavage of pyroxene and amphibole (Klein and Dutrow, 2008). Consequently, the weaker bond between the chains is dissolved more easily, yielding individual mineral crystals. Overall, the rock for the study site is fairly hard (six on the Moh hardness scale) and fairly resistant to weathering and erosional processes (Grotzinger *et al.*, 2007). The ophitic texture of dolerite, consisting of the interlocking of plagioclase and pyroxene, also yields a strong interlock (Weinert, 1982). This interlock, together with the hiding of plagioclase crystal faces, makes dolerite resistant to weathering (Weinert, 1980; McCarthy and Rubidge, 2005; Grotzinger *et al.*, 2007). Nevertheless, amphibole and pyroxene of these mafic rocks initially weather to chlorite, eventually decomposing to montmorillonite, (Weinert, 1980). In particular, the highly modal calcium feldspar (plagioclase) of the rock (Grosch *et al.*, 2007) decomposes easily (in the presence of sufficient moisture) into secondary minerals such as kaolinite (Briggs, 1977a; Weinert, 1980; Grotzinger *et al.*, 2007). The solution of susceptible feldspar weakens the rock and promotes mechanical disintegration (Briggs, 1977a). Water is an essential component in the weathering of feldspar to kaolinite as solid feldspar undergoes hydrolysis when being converted to

kaolinite (Grotzinger *et al.*, 2007). In polar deserts feldspar remains largely non-weathered, due to the lack of water to the weathering process (Grotzinger *et al.*, 2007). Nevertheless, moisture does become available following snow- and ice-melt. The availability of moisture is, therefore, a key component of chemical weathering, wetting-drying and frost-action (Briggs, 1977a; Weinert, 1980; Matthews and Owen, 2008). Local lithology as well as climate point to physical weathering having the greatest impact on the study and clasts appear more suited to disintegration than decomposition. Nevertheless, decomposition of rock remains present in cold environments, albeit at much slower rates (Hall, 2002).

Freeze-thaw action, in particular, is seen as one of the main geomorphic agents in periglacial and cold environments (*e.g.* Fahey, 1973; Sumner *et al.*, 2004), resulting in angular clasts. However, frost cycles are also known to occur in hot-desert environments (Sumner *et al.*, 2004) and angular clasts don't necessarily indicate frost weathering. Instead they may be attributed to salt weathering, thermal stress, hydration, dilatation and fire-induced spalling (Boelhouwers *et al.*, 2002). Environmental conditions favourable to chemical weathering, such as high rainfall and temperatures, are not present for the area under investigation (Sumner *et al.*, 2004). Nevertheless, mechanical weathering due to wetting and drying is present in cold regions (Hall, 2002). Snow cover, seen as a limiting factor in mechanical disintegration of bedrock by *e.g.* Sumner and Meiklejohn (2004), is also a source of moisture to the deposit. Moisture becomes available during periods of sunshine when the warmer rocks melt adjacent snow and ice, wetting clast surfaces. Melting snow results in prolonged wetting of rocks, promoting chemical weathering (Hedding, 2008) and provides a favourable environment for hydration (Weinert, 1980). When freeze-thaw cycles occur, the increase of hydraulic pressure of water causes joints to fracture (Grotzinger *et al.*, 2007). Enhanced weathering along joints, such as frost wedging during the summer months, leads to an increase in stress and possible blockfield development (Boelhouwers *et al.*, 2008). Snowmelt in spring also allows for deeper thawing of the ground (Vieira *et al.*, 2010) and contributes to soil moisture (Adlam *et al.*, 2010). Furthermore, melt-out processes are seen as effective erosional agents in periglacial environments (Hedding, 2008). Surface hydration often precedes hydrolysis, which further weathers the rock, with oxidation leading to further mineralogical changes of the mafic rock (Weinert, 1980; Grotzinger *et al.*, 2007). The medium and dark grey colour of diorite and dolerite respectively indicates the amount of pyroxene present in the rock (McCarthy and Rubidge, 2005). The greater the amounts of pyroxene present the darker the rock. The rocks of the Northern Buttress appear red in colour (*e.g.* Figure 12 & Figure 13, pg. 21), indicating weathering after exposure. The red surfaces of the clasts signify oxidation processes, with a vermillion red colour indicating the anhydrous Fe_2O_3 (hematite) mineral (Weinert, 1980). They are also metamorphosed and exhibit case hardening (*e.g.* Mol and Viles, 2012).

Figure 12: Oxidised surface and weathering rind observed on a sample rock for the blockfield. Note the red surface compared to the grey rock.

Figure 13: A thin weathering rind is observed for a clast on the blockfield. The outer surface is red, indicating oxidation weathering.

Diurnal differences in temperature may lead to surficial stress and granular disintegration (Weinert, 1980). Thermally induced weathering occurs when rock expands and contracts (compression and tensile stresses) under short- or long-term oscillating temperatures, resulting in thermal stress fatigue and ultimately granular disintegration (Sumner *et al.*, 2004). Thermal stress or fatigue is known to occur in cold environments (Hall, 2002). During the day the warmer temperatures on a clast surface (compared to its centre) lead to stress along the warm-cold material interface. This stress results in parallel micro fissures (Weinert, 1980). During the night this process is reversed, yielding vertical micro fissures. These micro fissures become zones of preferential weathering and areas of weakness, along which the rock may fail. Thermal shock occurs when rapid temperature changes result in rock failure. These are processes commonly ascribed to hot deserts; however, research has suggested that they also play a large role in cold alpine and high-altitude environments where high rock-to-air temperature gradients are achieved during rock cooling cycles (Sumner *et al.*, 2004). Supporting this argument are highly-similar fracture patterns, resulting from thermal stress, and the angularity of clasts, due to mechanical rock breakdown (Sumner *et al.*, 2004). A temperature change of 2°C.min^{-1} is required for thermal stress fatigue (Richter and Simmons, 1974). However, this figure may be lower in the presence of differing tensile stress over the surface of a rock (Sumner *et al.*, 2004). Research from the sub-Antarctic (Sumner *et al.*, 2004) indicates rock temperature changes (Δ54.9°C) similar to that observed in the hot desert of Namibia (Δ64.4°C). Thermally induced weathering may, therefore, be underestimated in cold environments (Sumner *et al.*, 2004).

Weathering rinds, sediment evidence, surface pitting and tafoni indicate chemical weathering cannot be excluded as a process acting on the blockfield. Nevertheless, chemical weathering is thought to occur at slowed rates with mechanical weathering dominating. Block production appears to be as a result of dilatation, followed by mechanical production of clasts along pre-exiting zones of weakness in blocks. The weathering environment of the study site, although colder, windier and drier than

Marion Island, may be compared to the periglacial environment described by Sumner and Meiklejohn (2004) for Marion Island. The azonal nature of processes acting over a long period of time (Meiklejohn and Hall, 1997; Andre, 2003; Boelhouwers, 2004) and nonlinear weathering rates (Sumner *et al*., 2009) are parameters that must be taken under consideration when investigating the blockfield on the Northern Buttress of the Vesleskarvet Nunataks.

CHAPTER 3: Materials and Methods

Openwork block deposits are found in a variety of locations (*e.g.* Ballantyne, 1998; Small *et al.*, 1999; Boelhouwers and Sumner, 2003; Hall and Phillips, 2006) and environments (*e.g.* Rea *et al.*, 1996; Boelhouwers, 2004; Goodfellow *et al.*, 2008). Their worldwide high altitude and latitude distribution has generated much interest and debate and an improved understanding of such landforms is needed. The project is the first detailed study of an openwork block deposit in the region and contributes to our understanding and knowledge of such landforms in terms of aspect-controlled weathering in high latitudes, active layer dynamics and estimating the age of the surface of the deposit using indicators such as rock hardness and clay mineral ratios of the fine earth fraction. Furthermore, the characterisation of the blockfield under investigation has the potential to add to our knowledge of the role of rock weathering in cold climates, the control of geological structure on landforms, the production of substrates for biological colonisation and the impacts of climate change on landforms (Rea *et al.*, 1996; Meiklejohn and Hall, 1997; Andre, 2003; Whalley *et al.*, 2004; Rea, 2007).

The project focused on the characterisation of a blockfield located on the Northern Buttress of the Vesleskarvet Nunataks. The scientific method and empiricism were used throughout to achieve each individual objective. Being quantitative in nature it comprised a large fieldwork component and was explorative, rather than hypotheses driven. In addition, all main branches (field observations, laboratory observations, office observations) of geomorphological enquiry (Anderson and Burt, 1981) were followed. The majority of data were collected during the 2010/11 and 2011/12 Austral summer fieldwork seasons. An additional small portion of fieldwork was undertaken during the 2009/10 Austral summer season. The fieldwork component was supplemented by a number of statistical and mathematical analysis methods. Large datasets on a number of parameters were required and variables included the study area geology, climate, clast location, characteristics and surface hardness, soil characteristics as well as soil moisture and soil temperature regimes. The majority of data were acquired through fieldwork, followed and supplemented by laboratory analyses. GIS (Geographical Information Systems) were employed to conduct analyses and to process data. The Analysis Tool Pak plug-in of Microsoft® Excel was utilised to do the majority of statistical analyses. OpenStereo (Instituto de Geociências– Universidade de São Paulo, 2010) and GEOrient (Holcombe, 2011) was used to draw rose diagrams. All methods employed in the field were adapted to local conditions and project requirements where deemed necessary. However, accepted methods as described in the literature were closely followed throughout the project in order to minimise bias and subjectivity. These methods are described in greater detail in Field Methods (pg. 27). Furthermore, laboratory and statistical methods were selected following an extensive literature review and may be perused in the

sections titled Laboratory Methods (pg. 53) and Statistical Analyses and Preparation (pg. 57) respectively.

In order to achieve Objectives 1 (the autochthonous nature and matrix of the deposit, pg. 9), 2 (morphology and characteristics of clasts, pg. 9) and 3 (aspect control on weathering, pg. 9) data on clast morphology, location, angle and slope were required. Additional data found to be of interest or pertinent to the study were also collected. Harris and Pedersen (1998) argue that block deposits may lead to lower temperatures being maintained deeper within the soil, influencing the depth and dynamics of the active layer and permafrost. Objective 4 (pg. 9) attempts to improve our understanding of these soil temperature dynamics and required the collection of soil temperature and moisture dynamics using appropriate loggers in the field. Objective 5 (rock properties and moisture uptake of clasts, pg. 9) required the collection of clasts for subsequent laboratory analyses to be conducted in South Africa. Particle size analysis gives an indication of the age of the deposit and impact of chemical weathering on clasts (Biggs, 1977b; Rea *et al.*, 1996; Whalley *et al.*, 2004). In order to achieve Objective 6 (pg. 9) soil samples were collected from a number of locations on the blockfield. These samples underwent subsequent laboratory analyses in South Africa. Climate and geological data were obtained from SAWS (South African Weather Service) and the South African Scientific Committee for Antarctic Research respectively. NGI (National Geo-Spatial Information) provided aerial imagery. Large datasets were collected during the various field seasons and Figure 14 (pg. 25) provides an overview of all sample points at which data were collected. Data collection is discussed in greater detail in the relevant sections of this chapter.

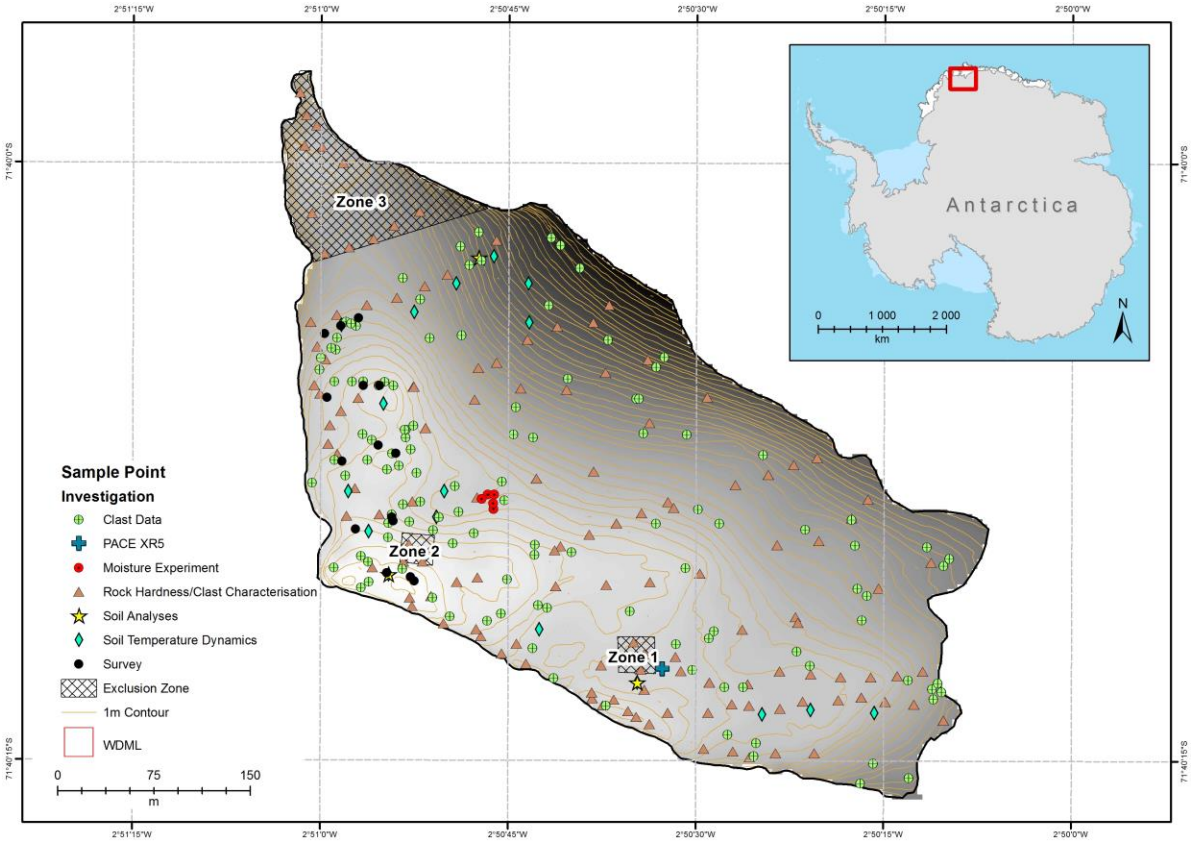

Figure 14: Sample points (n = 525) for all data collected across the Northern Buttress. Equotip: n = 234. Schmidt Hammer: n = 140. Soil samples: n = 3. Moisture samples: n = 5. Survey: n = 120. iButtons (thermochrons): n = 22. PACE XR5 data logger: n = 1.

Table 1 lists the data collected during fieldwork as well as the instruments used throughout the project. The purpose of the data in terms of which objective was addressed by their collection is also indicated. A detailed description of instruments used may be viewed in Appendix A: Instruments (pg. 165).

Table 1: A list of data requirements and instruments used during field- and laboratory work is given in the table below. The period of each field season or when laboratory work was done is also indicated.

Measurement/ Observation	Instrument	Date/Season	Objective	Source	Scale of Measurement
CLAST CHARACTERISATION AND SURVEY					
Location	GIS and GPSmart 60CSx GARMIN	2009/10, 2010/11 and 2011/12	1, 2	Fieldwork	Ratio
Axes (cm): A, B and C	WEBCO measuring tape	2010/11 and 2011/12	2	Fieldwork	Ratio
Top plane	Visual inspection	2010/11 and 2011/12	1, 2	Fieldwork	Nominal

Measurement/ Observation	Instrument	Date/Season	Objective	Source	Scale of Measurement
Top orientation (true bearing)	SILVA Sight Master magnetic compass	2010/11 and 2011/12	1, 2	Fieldwork	Ratio
Dip (degrees): north-, east-, south-, west-, top-facing aspect	SILVA Clino Master clinometer	2010/11 and 2011/12	1, 2	Fieldwork	Ratio
Block/ice supported	Visual inspection	2010/11 and 2011/12	1, 2	Fieldwork	Nominal
Snow cover	Visual inspection	2011/12	2, 3	Fieldwork	Nominal
Evidence of flaking	Visual inspection	2010/11 and 2011/12	2, 3	Fieldwork	Nominal
Evidence of pitting	Visual inspection	2010/11 and 2011/12	2, 3	Fieldwork	Nominal
Roughest face	Visual inspection	2010/11 and 2011/12	2, 3	Fieldwork	Nominal
Lichen presence	Visual inspection	2009/10; 2010/11 and 2011/12	2, 3	Fieldwork	Nominal
Lichen sheltered	Visual inspection	2010/11 and 2011/12	2, 3	Fieldwork	Nominal
Rock Hardness: north-, east-, south-, west-, top-facing aspect	Proceq N-34 SH, Proceq Equotip with impact device D-type	2009/10; 2010/11 and 2011/12	3	Fieldwork	Ratio
Picture	SONY Cyber-shot	2010/11 and 2011/12	1, 2, 3, 4	Fieldwork	N/a
SOIL TEMPERATURE AND MOISTURE REGIMES					
Near-surface soil temperature dynamics	iButton thermochrons (DS1922L)	2010/11 and 2011/12	4	Fieldwork	Ratio
Permafrost-active layer dynamics	PACE & XR5 data logger	2006-2012	4	Fieldwork	Ratio
ROCK PROPERTIES					
Clast moisture susceptibility	N/a	2011/12	5	Fieldwork	Ratio
Clast properties	Labcon forced radiation oven FSOE	2012	5	Laboratory analysis	Ratio
Clast properties	Scaltec Scale SBA 41	2012	5	Laboratory analysis	Ratio
SOIL PROPERTIES					

Measurement/ Observation	Instrument	Date/Season	Objective	Source	Scale of Measurement
Particle size analysis	Mettler PF3000 scale	2012	6	Laboratory analysis	Ratio
Particle size analysis	Endecott test sieve shaker; SediGraph 5100	2012	6	Laboratory analysis	Interval
Particle size analysis	Labotec Ultrasonic LC130H	2012	6	Laboratory analysis	N/a
OTHER DATA					
Climate data (wind direction and speed, ambient temperatures, humidity, pressure)	N/a	2012	4	SAWS	Ratio
Geology data	N/a	1981	1, 2, 3	South African Scientific Committee for Antarctic Research; NGI	Nominal
Aerial imagery	N/a	1981	1-6	NGI	N/a

This chapter is divided into three sub-sections. The first sub-section details methods employed in the field, the second sub-section explains laboratory methods used and the final sub-section deals with statistical and geostatistical techniques applied. These sections may be found under Field Methods (see below), Laboratory Methods (pg. 53), and Statistical Analyses and Preparation (pg. 57) respectively. All methods utilised are explained in detail in each respective section.

3.1 Field Methods

Fieldwork constituted a large portion of the study and a variety of methods were followed and/or adapted in the field. Accuracy of statistical analyses depends largely on the accuracy of data collected during fieldwork (Till, 1985). Consequently, methods were standardised, equipment calibrated every few days to reduce collection error (Briggs, 1977a) and fieldwork was conducted with great care. Methodologies employed used random selection methods in an effort to remove bias and to ensure representative sampling (Biggs, 1977b; Till, 1985). However, random, systematic as well as judgement sampling was employed in the field depending on local conditions and when certain parameters had to be met. These parameters, where applicable, are explained in greater detail in their relevant sections. Fieldwork, which forms part of a larger investigation into geomorphology and

climate change, was undertaken during the 2009/10, 2010/11 and 2011/12 Austral summer seasons to SANAE IV.

3.1.1 Blockfield Survey

The matrix of the deposit may indicate palaeoclimates, current weathering agents and processes active within the matrix. The location of the clasts, their support (such as block or ice support), as well as data on soil characteristics indicates the matrix of a deposit. An autochthonous deposit consists of clasts weathering *in situ*, whereas an allochthonous deposit consists of clasts that exhibit preferential orientation and/or dip. The presence of mass movement or slope processes yields preferential orientation in clasts (Doornkamp and King, 1971). Preferential orientation of clasts has also been observed on some glacial deposits (Doornkamp and King, 1971). Blocks in juxtaposition to each other indicate no discernible movement, whereas blocks overlying different lithologies indicate movement (Hall, 2002). Any movement and observable dip of clasts across the blockfield, especially along a slope, indicates an allochthonous deposit (Ballantyne, 1998). In contrast, an autochthonous deposit, taking the original joint structure into consideration, yields a random orientation of clasts. The first objective (Objective 1, pg. 9) required the determination of the allochthonous or autochthonous nature of the deposit, as well as the blockfield matrix. Observations on the location of the clasts, whether or not clasts were ice, block or ice and block supported and data on soil characteristics were collected in the field. Furthermore, data on clast shape, orientation and dip indicate the nature of the deposit and observations on these were recorded during fieldwork. The following section describes methods employed to achieve Objective 1 (pg. 9).

The Vesleskarvet Nunataks rise to an elevation of about 814 m (Republic of South Africa, 1981). However, only approximately 200 m are visible above the ice (see Figure 15, pg. 29). The blockfield under investigation, as indicated in Study Site (pg. 4), is located on the Northern Buttress of the Vesleskarvet Nunataks and mapping its extent was required for the purpose of the study. To determine the extent of the blockfield on the buttress, the visible blockfield was mapped by walking around its extent with a handheld GPS (Global Positioning System) whilst tracking the route. Exclusion zones and areas of permanent snow cover were also recorded. In addition, GIS were used to delineate the outline of the blockfield using aerial imagery and the recorded GPS points.

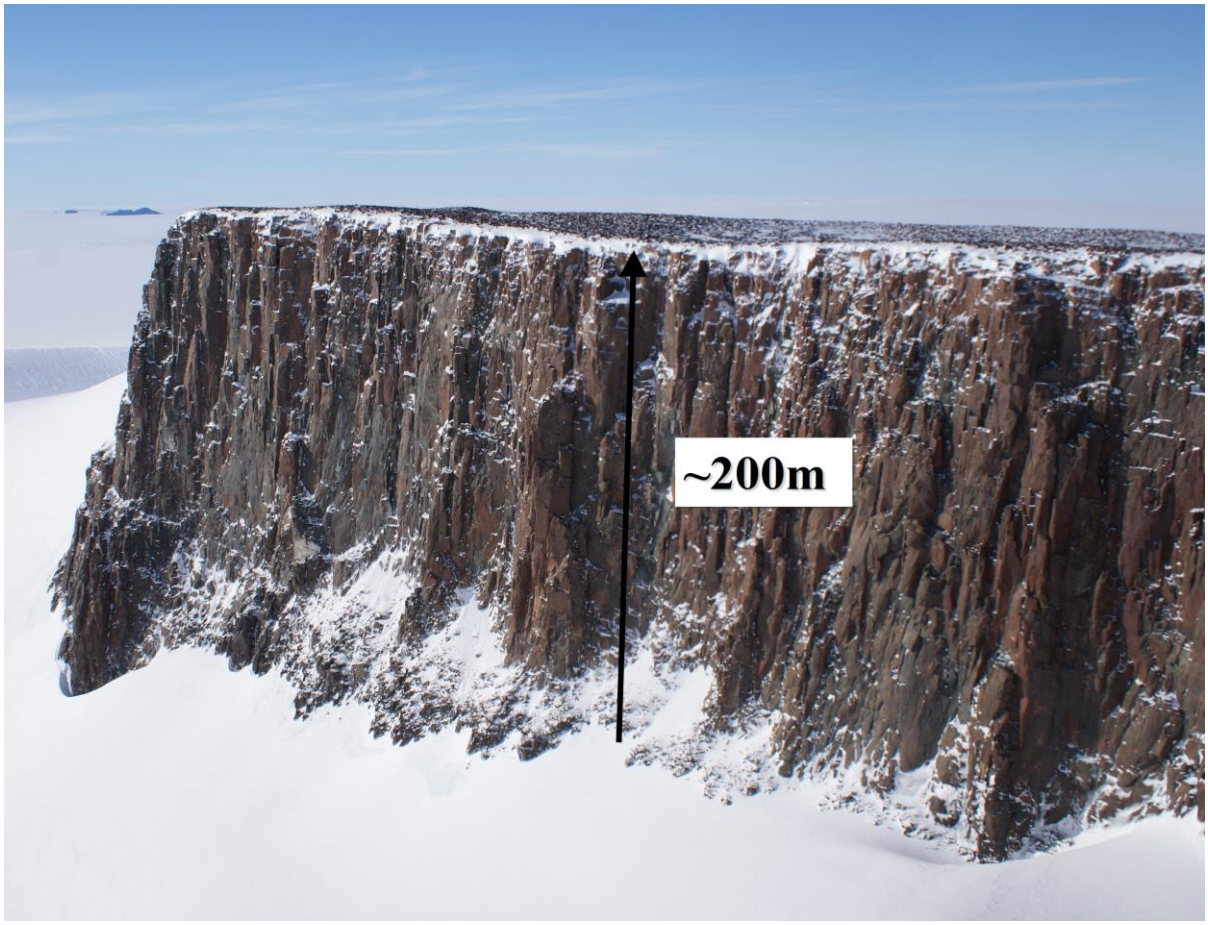

Figure 15: The Northern Buttress seen from the Southern Buttress. Only 200 m of the approximately 800 m high landform rise above the surrounding ice plain (Photo: Meiklejohn, 2007).

A survey, focusing on the general characteristics of the clasts present on the blockfield, was conducted by traversing the blockfield along transects. Three transects of 200 m lengths were sampled along the north-south extent of the blockfield (Figure 16, pg. 30). Each transect was sampled in 50 m sections, with one rock being sampled systematically every five meters. This yielded 120 rock samples (n = 120) in total. The two eastern transects were close to each other for the last 50 m, due to the presence of an exclusion zone. Entry into this area is restricted (SANAP, 2009) and sampling had to occur around the zone.

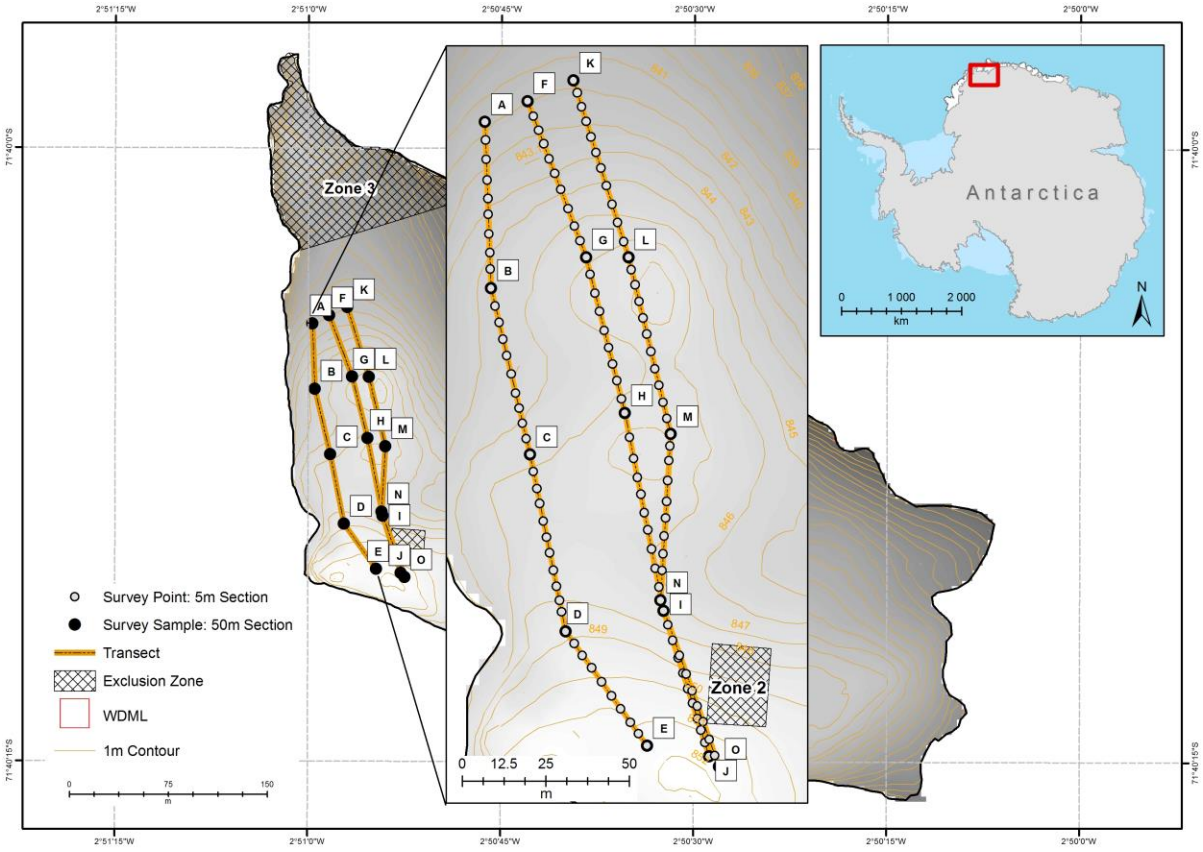

Figure 16: The location of data points along the three 200 m long transects. Samples points occur every five metres along each transect (n = 120).

Data collected during the blockfield survey represented cross-sectional measurements. The location of each sample was recorded using a handheld GPS and the a-, b- and c-axis lengths (longest, intermediate and shortest axis respectively) of each clast recorded (Doornkamp and King, 1971; Briggs, 1977a). Axis measurements were taken in such a way that the three respective axes intersected at a 90° angle to each other (Briggs, 1977a; Aydin, 2008). The a-axis and ab-plane orientation, as well as dip were measured. Other data recorded included whether or not the clast was ice, block or ice and block supported, the roughest observable face, presence of flaking, snow cover and lichen and whether or not the lichen were sheltered as well as other general notes on edge rounding (angularity of clast) and any other specific features. The profile of each transect was determined by taking a backward sighting from one transect starting point to the appropriate transect end point, in both degrees and percentage. Data collected were statistically analysed using Microsoft® Excel and GIS. Refer to Statistical Methods (pg. 59) and Geostatistical Methods and GIS (pg. 71) for a detailed explanation of methods employed.

3.1.2 Clast Characterisation

The aim of the second objective (Objective 2, pg. 9) was to investigate and define the morphology and characteristics of clasts. Data on clast dimensions, axes orientations, evidence of pitting or flaking, lichen presence and if lichen was sheltered, whether or not the clast was block, ice or block/ice supported as well as snow were recorded. Clast dimensions were used to plot the relative dimensions of the long, short, and intermediate axes of the clasts. This allowed clast shapes to be classified as blades, rods, spheres or discs (Briggs, 1977a). In addition, it allowed for the cataloguing of clast shapes and their distributions. Objective 3 (pg. 9) attempts to identify the role that aspect has on the weathering of surfaces of clasts. Rock hardness values were recorded using both the SH (Schmidt Hammer) and Equotip (Equotip® 3) devices (*e.g.* Sumner *et al.,* 2002; Shakesby *et al.*, 2006), using the methods described under the sections titled Schmidt Hammer (pg. 38) and Equotip (pg. 40). Hardness tests are quick and useful indicators of mechanical characteristics of a material. Hardness is the ability of a material to resist deformation when exposed to an indenter (Kompatscher, 2004) such as the SH or Equotip. The SH measures *R*-values (rock hardness rebound values), whereas the Equotip measures L-values or HL (Leeb Hardness). Hard rocks yield higher *R*- and L-values and these values have been shown to correlate with rock properties (Goudie, 2006). Such rock properties include hardness, smoothness, density and cementation (Katz *et al.*, 2000) and indicate the degree of weathering a surface has undergone (Sumner and Nel, 2002; Goudie, 2006). As material weathers, its mechanical strength decreases, which in turn decreases surface hardness and the elastic recovery of the surface (Ericson, 2004), yielding lower *R*- and L-values. Rock hardness was, therefore, used as an indicator of weathering across clast surfaces in order to achieve the third objective (Objective 3, pg. 9). The following section describes methods employed to achieve both Objective 2 and 3 (pg. 9).

Sample sites were determined by randomly generating 100 points (n = 100) using the *'Create Random Points'* tool in ArcGIS®. This tool made use of a random number generator and seed and placed generated points in the specified extent (the study site) using a standard polygon-partitioning algorithm. The algorithm initially divided the study site into triangles and proceeded to randomly select triangles from this population. Sample points were then placed at random within each selected triangle (ESRI, 2012). Each generated point was set to be a minimum of three meters from any other point. This corresponded to the three-meter accuracy of the hand-held GPS used to navigate to sample points in the field. In addition to the randomly generated points, data were recorded for 40 samples (n = 40) by traversing the blockfield systematically in transects. These transects ran parallel to transects employed for the blockfield survey. As for the 100 points described above, samples had to be a minimum of three meters apart. Figure 17 shows locations of samples used to achieve Objective 2 and 3 (pg. 9).

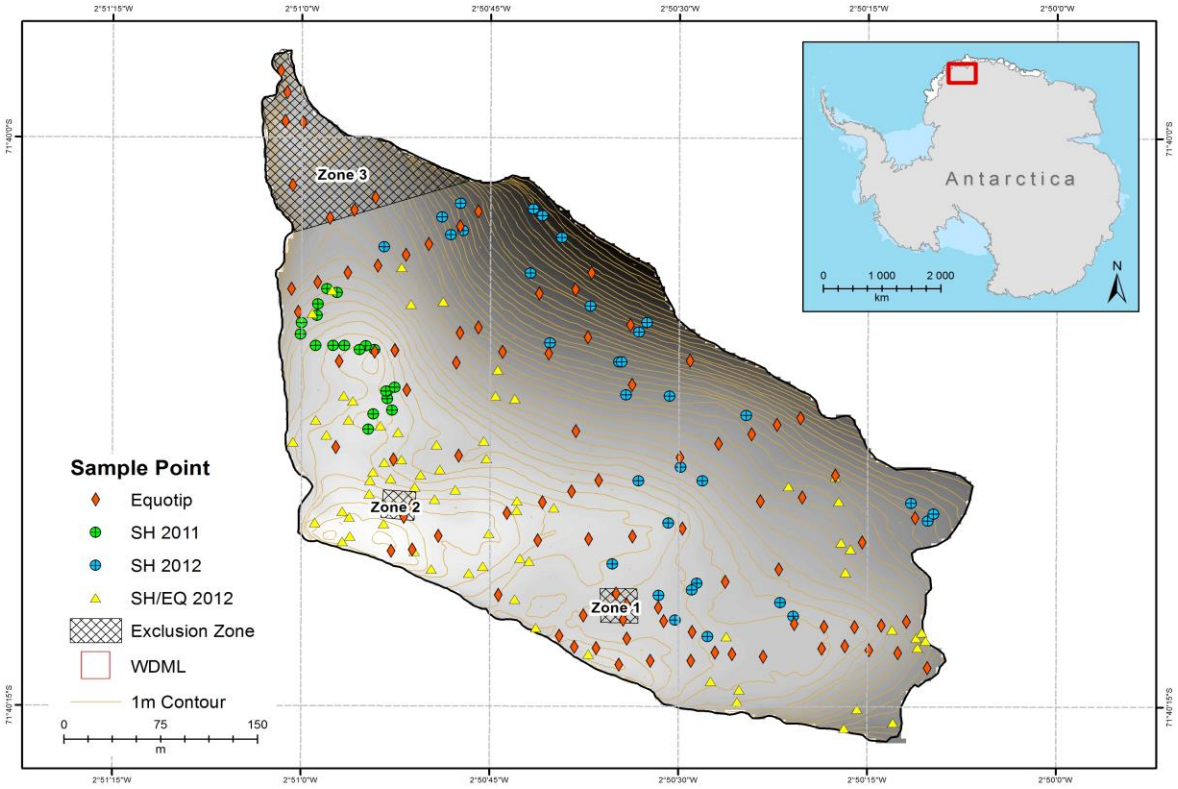

Figure 17: Sample points for the Equotip (2009/10 and 2011/12 field season) and Schmidt Hammer (2010/11 and 2011/12 field season) measurements. Equotip measurements: n = 234. Schmidt Hammer: n = 140.

For both randomly generated points and points within transects, clasts were selected based on specific criteria (judgement sampling) as detailed below.

- Rocks had to exceed 25 kg in weight (Sumner and Nel, 2002), have a minimum thickness of 100 mm and a minimum radius of 54.7 mm to ensure reliable N-type SH readings (Aydin, 2008);
- Clast dimensions had to be measured (Aydin, 2008). Therefore, axes had to be accessible and clasts blocked by surrounding rocks were not considered;
- Rock faces had be accessible enough to allow for SH readings perpendicular to the surface (Ericson, 2004; Basu and Aydin, 2004; Matthews and Owen 2008), *i.e.* no other boulders were allowed to block faces to such an extent the SH plunger was at non-perpendicular angle to the surface being investigated; and
- Rocks had to have five accessible faces: four side faces and a top face. This criterion was deemed necessary to ensure comparison amongst samples (*e.g.* Figure 18 & Figure 19, pg. 33).

Figure 18: Sample 7, with all aspects accessible. A 50 cm long measuring rod gives an indication of scale.

Figure 19: Sample 27, with all aspects accessible. A 50 cm long measuring rod gives an indication of scale.

As indicated above, rock hardness was used as an indicator of weathering across clast surfaces. This was based on the premise that non-weathered surfaces of similar material exhibit higher rebound values to weathered surfaces (Aoki and Matsukura, 2007). Rebound values are, therefore, influenced by surface roughness, consolidation of mineral grains, compaction due to repeated impacts and the looseness of the original rock surface (Ericson, 2004; Goudie, 2006; Aoki and Matsukura, 2007; Gupta *et al.*, 2009). When taking rock hardness measurements using the SH and Equotip, field measurements should also include the dimensions of the tested clasts (Aydin, 2008). At each sampling location the dimensions of the a-, b- and c-axes were, therefore, measured, as well as the a-axis orientation, top orientation and the top aspect plane. Clasts were cleared of surrounding snow and allowed to air dry before measurements were taken (Aydin, 2008). Axes measurements were taken in such a way that the three respective axes intersected at a 90° angle to each other (Briggs, 1977a; Aydin, 2008). To take accurate dip measurements, a clinometer was fixed to a wooden support (Figure 20). The support was placed on each face when taking measurements, resulting in a more representative, *i.e.* average dip value being recorded. After a visual inspection, data on lichen presence, whether or not the lichen was sheltered from the elements, the roughest aspect, any flaking or pitting and whether or not the clast was ice, block or block and ice supported were recorded. In addition, 20 clasts were investigated for weathering pitting. The a-, b- and c-axes of ten weathering pits per clast were measured using a Vernier calliper.

Figure 20: Clinometer affixed to wooden support when taking dip measurements in the field (Photo: van den Berg, 2012).

Microbiotas are known to influence the weathering process (*e.g.* Church, 2010). Lichen has been shown to cause granular disintegration and dissolution of iron compounds in their colonised zone

(Friedmann, 1986). Matthews and Owen (2008) show how endolithic lichen on boulders in Norway decrease rock hardness values by 20 units within 30-40 years after exposure, highlighting the role that these organisms have in the reduction of *R*-values for pyroxene-granulite boulders in a periglacial environment. Studies in the Drakensberg (Mol and Viles, 2012) indicate that sub-surface microbial presence is often associated with thicker flakes. Similarly, Büdel *et al.* (2004) suggest the role cryptoendolithic cyanobacteria have on the flaking of sandstone. Their presence may, therefore, influence the weathering rind and rock surface (Shakesby *et al.*, 2006). However, lichen presence on the Northern Buttress is sparse and is not though to influence the weathering regime significantly. Instead, lichens are thought to colonise previously weathered areas, as these provide shelter and habitable zones for these organisms (Friedmann, 1986). Lichen was deemed sheltered if it grew in weathering rinds, fractures or joints, inside tafoni/pitting or was protected by surrounding rock. Figure 21 to Figure 26 illustrate sheltered locations. *'A'* indicates a sheltered location due to surrounding rocks; *'B'* indicates a sheltered location in a depression on a rock surface (such as flaked-off areas, weathering pitting or tafoni); *'C'* indicates a sheltered location due to fracturing on the rock surface. A circle indicates the extent of the area sheltered by the surrounding micro-landscape.

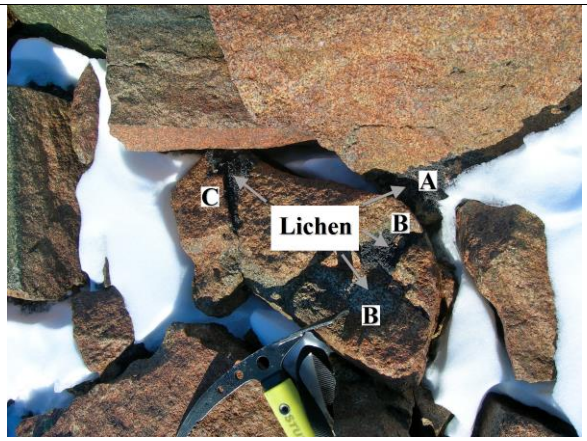

Figure 21: Lichen occurring in sheltered locations A, B and C. An ice axe gives an indication of scale.

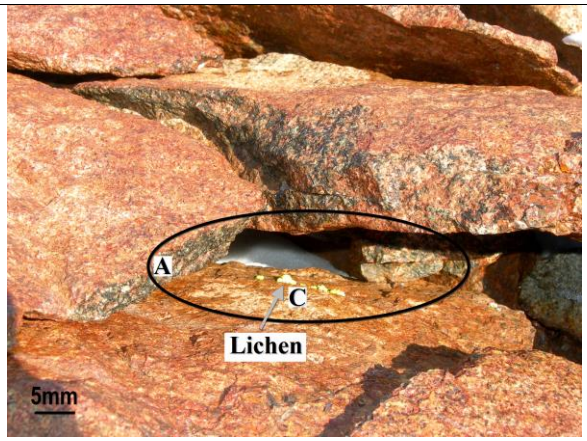

Figure 22: Lichen sheltered by locations A, indicated by a circle, and C.

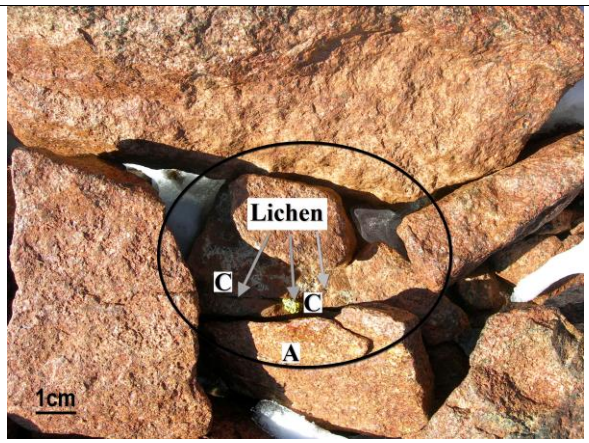

Figure 23: Lichen sheltered by locations A, indicated by a circle, and C.

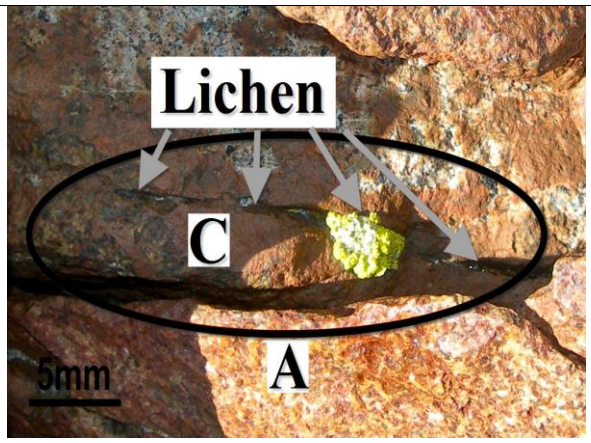

Figure 24: Zoomed-in view of Figure 23.

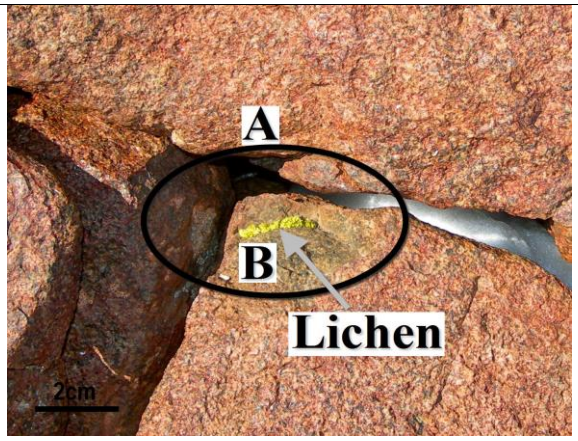

Figure 25: Lichen sheltered by locations A, indicated by a circle, and B.

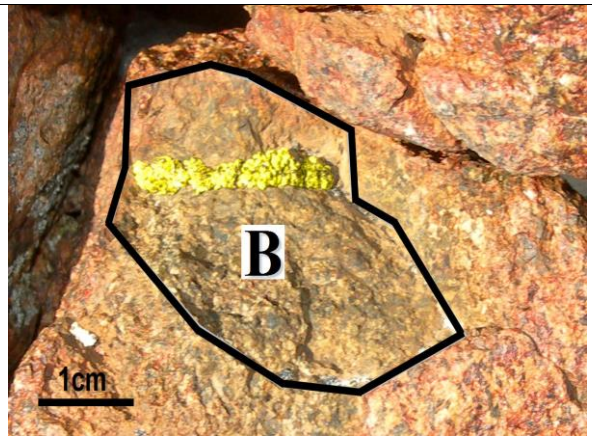

Figure 26: Zoomed-in view of Figure 25. The outline indicates where the surface has flaked off, creating a sheltered area.

Soil moisture has been shown to be significant to micro-organism distribution for the region (Lee *et al.*, 2013). In addition, Sumner and Nel (2002) argue that for sub-Antarctic Marion Island rock moisture influences *R*-values, with *R*-values negatively correlated to moisture content. Similarly, Viles *et al.* (2011) show that surface moisture influences comparative SH-Equotip rock hardness values, albeit not significantly. Snow cover also influences weathering rates (Shakesby *et al.*, 2006). Consequently, data on snow cover, as a source of moisture, was recorded. These data were compared to snow extents delineated in GIS (Geostatistical Methods and GIS, pg. 71). The roughest face was the most subjective data recorded and followed a visual inspection of each clast. To ensure a higher degree of objectivity, a consensus was reached between a minimum of two people on which aspect appeared the roughest. A field assessment of the clast surface in terms of weathering was conducted, as was a visual assessment of the angularity of clasts. Although this assessment was subjective, it did give an indication of the roundness of clasts for the blockfield.

3.1.3 Rock Hardness: Schmidt Hammer and Equotip Methods

Studies by Hall (1997 in Goudie, 2006) and Waragai (1999 in Goudie, 2006) reveal that aspect influences the degree and rate of weathering. Aspect plays a role in the observed variability of rock temperatures (Grab, 2007) and freeze-thaw cycles of earth hummocks (Grab 2005). On the South Shetland Islands research by Hall (1983, in Hall, 2002) shows that mechanical weathering (wetting-drying) is thought to be more prevalent on northern aspects and chemical weathering on southern aspects (higher moisture content, leeward sides). Near vertical and high angle faces in high latitudes receive greater solar incidence than horizontal faces (Sumner *et al.*, 2004). Friedmann (1986) suggests an optimal angle of 45° for the Antarctic region. These faces, therefore, experience a greater range in temperatures. In the higher latitudes of the southern hemisphere the north-facing slopes also receive

more sunshine and warmth than the south-facing slopes (Doornkamp and King, 1971; Friedmann, 1986; Mulder and Grab, 2002). Since incident solar radiation influences thermal regimes across clast surfaces, this has implications on weathering, freeze-thaw activity and similar processes (Doornkamp and King, 1971). Furthermore, relative-age dating techniques include weathering rind development (thickness), increase in surface roughness, lichen presence, depth of weathering pits and decrease in rock hardness (Sumner *et al*., 2002). These indications of weathering, if different for various orientations, would suggest aspect control on weathering processes. Increased lichen presence of northward facing aspects (Friedmann, 1986), also suggests possible aspect control on weathering. Mol and Viles (2012), in contrast, indicate that aspect has no clear correlation on rock hardness in the Drakensberg. Objective 3 (pg. 9) aimed to investigate the role that aspect has on weathering for the study site, contributing to this debate. In order to achieve Objective 3, rock hardness was used as a proxy for surface weathering. Studies (*e.g*. Sumner and Nel, 2002; Goudie, 2006; Aoki and Matsukura, 2007; Mol and Viles, 2012) show that rock hardness may be used as an indicator of weathering of rock surfaces. Ericson (2004) and Gupta *et al*. (2009) suggest that, using rock hardness values as proxy (Shakesby *et al*., 2006), surfaces affected by different geomorphological processes and of varying lithology, are statistically different to each other. *R*-values indicate the degree of weathering a surface has undergone (Sumner and Nel, 2002; Goudie, 2006). Hard rocks yield higher *R*-values and these values have been shown to correlate with rock properties (Goudie, 2006). As material weathers its mechanical strength decreases, decreasing surface hardness and the elastic recovery of the surface (Ericson, 2004). This is based on the premise that non-weathered surfaces of similar material will exhibit higher rebound values to weathered surfaces (Aoki and Matsukura, 2007). Assuming aspect control on weathering, clast rock hardness rebound values for the various aspects will (statistically) differ.

Both the Equotip and SH are rebound or impact hammers (Basu and Aydin, 2004). These sclerometer devices use an indenter of known geometry and mechanical properties (the Equotip D-type impact device and the SH's plunger) and rebound the indenter onto the measured surface to determine surface hardness (Katz, *et al*., 2000; Sumner and Nel, 2002; Ericson, 2004; Shakesby *et al*., 2006). The indenter is accelerated towards the measured surface in a controlled blow using a series of springs and a piston (Ericson, 2004; Kompatscher, 2004; Goudie, 2006; Aydin, 2008) (see Figure 27 & Figure 28, pg. 37). When placing the SH orthogonally against a surface the steel piston is released onto the plunger (Basu and Aydin, 2004; Goudie, 2006). Upon impact, the surface and the indenter are elastically and plastically deformed, transferring kinetic energy from the impact device onto the surface (Goudie, 2006; Aydin, 2008). For the Equotip the recorded hardness value is the residual energy of the rebound impact body (Kompatscher, 2004). The *R*-value of the SH piston is equal to the residual energy of the piston after impact and is equal to the percentage of the length of the string

before compared to after impact, *i.e.* the rebound height of the piston (Ericson, 2004; Basu and Aydin, 2004; Aydin, 2008). The rebound of the impact device is, therefore, considered an index of surface hardness as provides a relative value of the compressive strength of the surface under investigation (Ericson, 2004; Basu and Aydin, 2004).

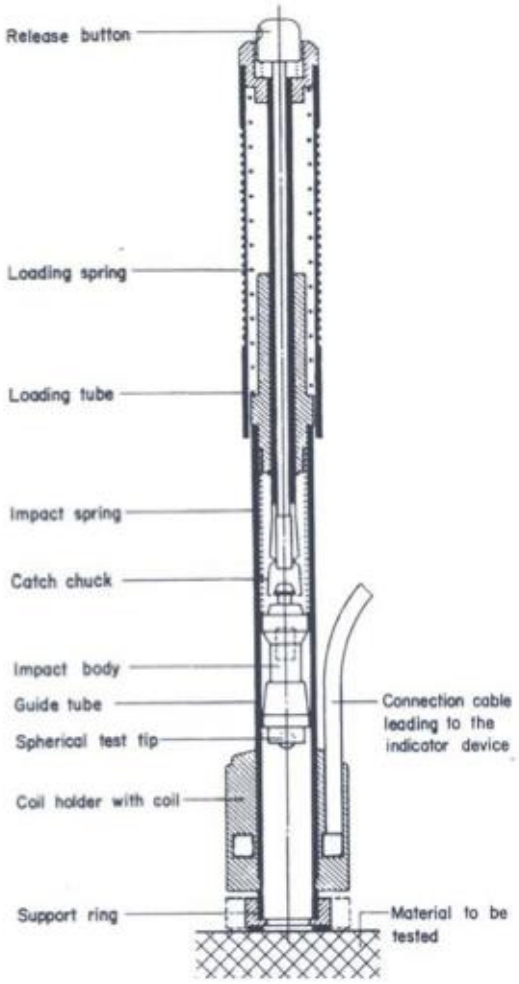

Figure 27: Schematic view of the Equotip impact device (Kompatscher, 2004).

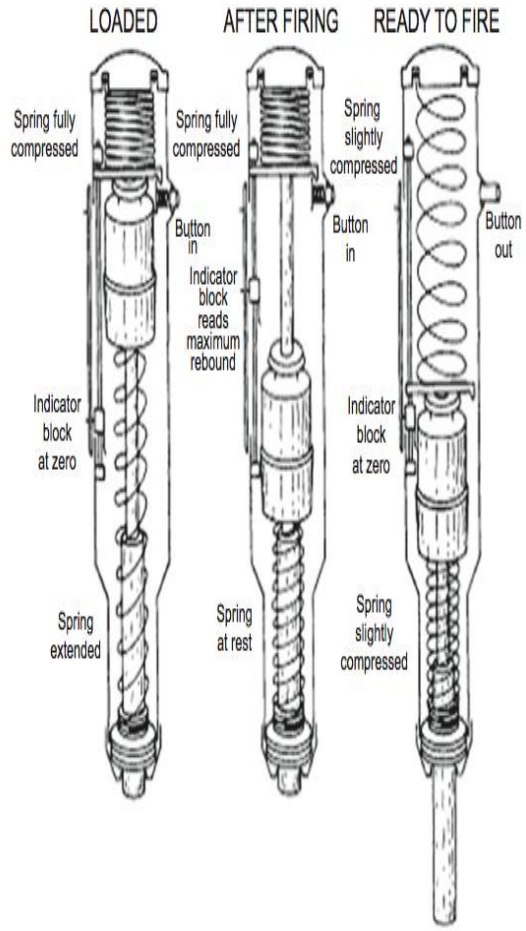

Figure 28: The working principle of the SH (McCarroll, 1994 in Aydin, 2008).

The SH has been employed in geomorphological studies since the 1960s (Goudie, 2006; Aoki and Matsukura, 2007). Specifically, it has been employed to determine RMS (Rock Mass Strength) (Viles *et al.*, 2011) in field conditions (Niedzielskie *et al.*, 2009). Applications of the SH include its use in structural geomorphology (Goudie, 2006) and quantifying the degree of weathering of a surface, due to weathering being associated with a decrease in surface rock strength (*e.g.* Ericson, 2004; Basu and Aydin, 2004; Goudie, 2006; Shakesby *et al.*, 2006; Aoki and Matsukura, 2007). Furthermore, SH readings are considered reproducible and consistent (Katz *et al.*, 2000). Although the instrument is light, easy to use in the field and classed as non-destructive (Basu and Aydin, 2004; Aoki and Matsukura, 2007; Aydin, 2008), the plunger has high impact energy and may cause damage to the

surface under investigation. Studies show (*e.g.* Aoki and Matsukura, 2007) that the thickness of the material being tested may impact the rebound value of the hammer, indicating that the rebound value represents weathered surface material, as well as internal non-weathered material, *i.e.* a broad near-surface zone (Viles *et al.,* 2011). In comparison, the Equotip records rock hardness in a narrow surface zone. It uses smaller impact energy (11 $N.mm^{-2}$) (Viles *et al.,* 2011) and may be used to measure the hardness of a wide range of materials, making it a suitable instrument for weathering research. It has been successfully applied in a number of weathering studies (*e.g.* Aoki and Matsukura, 2007; Mol and Viles, 2012). In particular, the lower impact energy ($\frac{1}{200}$ that of the N-type SH) means it may be employed in measuring relatively thin layers near a clasts' surface, compared to the SH whose values are more greatly influenced by the thickness of the layer (Aoki and Mastuoka, 2007; Viles *et al.,* 2011). With that in mind the SH is suitable for measuring rock hardness of material 20-250 mPa (mega Pascal) in strength (Aydin, 2008, Goudie, 2006). The Equotip is suitable for measuring surface hardness 0.03-1000 MPa in strength (Aoki and Matsukura, 2007). Although Viles *et al.* (2011) show that SH and Equotip readings are not necessarily comparable, for the purpose of this study the Equotip was used in conjunction with the SH to record the relative hardness of clast surfaces. Additional data on biological presence, flaking, pitting, roughness and snow cover were also considered.

3.1.3.1 Schmidt Hammer

The SH is easy to use, portable and relatively cheap (Ericson, 2004; Basu and Aydin, 2004; Aydin, 2008). The N-type SH, used throughout this study, is most suited to field applications (Goudie, 2006; Viles *et al.*, 2011), due to it being less susceptible to surface irregularities. It exerts approximately 2.207 $N.m^{-1}$ upon impact and is not suited to values less than 20 MPA, where the L- or P-type should be used instead (Basu and Aydin, 2004; Goudie, 2006; Aydin 2008). However, as *R*-values are strongly influenced by surface roughness (Ericson, 2004), the greater force exerted by the N-type makes this the most suitable type for conducting fieldwork. The SH scale ranges from 10-100 with two unit intervals (Goudie, 2006; Shakesby *et al.*, 2006), reflects a ratio and is dimensionless (Niedzielskie *et al.*, 2009). Before use in the field, the hammer must be calibrated with the supplied calibration anvil (Basu and Aydin, 2004; Shakesby *et al.*, 2006). If the rebound is outside of the predetermined rebound range, a CF (Correction Factor) (see Equation 1) must be applied to recorded values (Aydin, 2008).

Equation 1: CF applied to SH readings in the event SH rebound is outside of the expected range (Aydin, 2008).

CF = specific standard value of the anvil/average of ten readings on the anvil

Before commencing with fieldwork the SH was calibrated using the calibration block provide and no CF had to be applied to readings. A method adapted from Aoki and Matsukura (2007) and Aydin (2008) was employed in the field. Clasts had to have a minimum size and thickness, as described on pg. 32. To prevent impact energy dissipating through wave scattering and cracking, readings were taken six centimetres away from clast boundaries (Ericson, 2004), weathering bands, thin loose slabs, exfoliated surfaces and visible cracks (*e.g.* Aydin, 2008; Gupta *et al.*, 2009; Niedzielskie *et al*., 2009). This is due to the SH's sensitivity to slight heterogeneities within the rock (Niedzielskie *et al*., 2009). Readings had to be taken one radius away from other impact points and avoid surfaces covered by lichen or dust (Katz *et al*., 2000; Niedzielskie *et al*., 2009). The clast surface was allowed to air dry before measurements were taken. If the surface was not dry, the degree of moisture present (wet, damp, dry) was recorded. When taking impact readings, the hammer was held at 90° to the surface to prevent the influence of gravitational forces (Basu and Aydin, 2004; Goudie, 2006), frictional sliding, material removal by the plunger and partial transfer of energy to and from the hammer. Readings taken on rock aspects were taken in straight lines by rotating the core axis 90° at a time (Aydin, 2008). To minimise operator variation (Shakesby *et al.*, 2006; Viles *et al.*, 2011), all SH readings were taken by the same person (Gupta *et al.*, 2009).

For the purpose of this study the single impact method was utilised, *i.e.* no repeated impacts were recorded per sample point. This ensured that only surface roughness and concomitant degree of weathering was recorded. This is based on studies by Aoki and Matsukura (2007) and Viles *et al.*, (2011), who show that repeated rebound values increase in rebound strength due to compaction of the surface by the rebound device. Ericson (2004) and Matthews and Owen (2008) highlight the importance of measuring the naturally weathered surface, stressing randomly sampling across the surface and not polishing or grinding the surface in any way. Preparing the surface greatly reduces variability among data (Katz *et al.*, 2000), misrepresenting the weathered nature of a surface. Surfaces were, therefore, not ground down or polished in the field. Sufficient rock rebound values need to be recorded to ensure meaningful numerical mean rock strength (Niedzielskie *et al.*, 2009). However, there is no consensus in the literature in terms of how many rebound values should be taken per sample. SH readings are generally highly variable. As such, a higher sample set per clast is required to reduce this variability, yielding an average that may be used as an approximation of the sample surface hardness. Aydin (2008) suggests a minimum of 20 rebound values, as recommended by the ISRM (International Society of Rock Mechanics) (1978 in Goudie, 2006). Matthews and Shakesby (1984 in Goudie, 2006) propose 15 rebound values to be taken per sample, a method followed in many studies (*e.g*. Sumner and Nel, 2002; Sumner *et al.*, 2002). Niedzielskie *et al.* (2009) suggest a minimum sample size of 25 for weak (R = 34-40) and moderately strong rock (R = 40-50). A minimum sample size of 30 is recommended for strong rock (R = 50-60). Dolerite, common to the

study site, is defined as a very strong rock, with *R*-values exceeding 60 and a uniaxial compressive strength of more than 200 MPa (Goudie, 2006). This suggests a minimum sample size of 30 for measurements taken on dolerite. However, ten readings will suffice if the *R*-values differ by only four units (SH repeatability range of ±2). Niedzielskie *et al.* (2009) also show that the exclusion of extreme values, when investigating granite and gabbro, reduces the minimum sample size required. Working at a level of significance of 0.1 ($\alpha = 0.1$, $p < 0.1$) the minimum sample size, using the median, is eight. The higher the accuracy of data required, for example using rock rebound values as an indicator of relative age, the smaller the significance level needs to be and the larger the sample size required (Niedzielskie *et al.*, 2009). For the purpose of the study, a lower accuracy was required, reducing the minimum sample size by a third (⅓) (Niedzielskie *et al.*, 2009). Consequently, the minimum sample size of ten rebound values, as recommended by *e.g.* Katz *et al.* (2000), Ericson (2004), Aoki and Matsukura (2007) and Niedzielskie *et al.* (2009), was applied in the field to ensure the largest number of clasts was investigated.

3.1.3.2 Equotip

Similar to work done by Mol and Viles (2012), for the purpose of this study the Equotip with the D-type impact device was used. This device is the universal impact device and may be applied over a large range of hardness values (Kompatscher, 2004). Comparative to the SH, rock rebound values for the Equotip may be used as an indicator of surface weathering (Mol and Viles, 2012). High Equotip values indicate less weathered surfaces and *vice versa* (Mol and Viles, 2012). The Equotip was set to employ the dynamic Leeb scale, which ranges from 0-999 (Kompatscher, 2004). This scale is independent of test direction (orientation) and material surface and is suitable as a direct measure of material hardness (Kompatscher, 2004; Viles *et al.*, 2011). It makes use of the L-value or HL, where the L-value is the ratio of the impact velocity (v_t) to the rebound velocity (v_i) of the indenter, multiplied by 1 000 (Equation 2). A fully elastic surface yields an HL of 1000; a surface experiencing full plastic deformation will yield an HL of zero. The L-value or HL, being a ratio, is dimensionless, as is the SH scale. It must be noted, however, that Viles *et al.* (2011) indicate that Equotip and SH readings are not necessarily comparable. L- and *R*-values must, therefore, be analysed with care when compared to each other.

Equation 2: L (Leeb value) equation (Kompatscher, 2004).

$$L = \frac{v_t}{v_i}\ 1\ 000.$$

Reliable Equotip readings require a minimum clast weight of five kilogram and a recommended five to ten impacts should be used for determining average surface hardness (Kompatscher, 2004). The

Equotip may be used on smaller clast sizes and nearer to edges than the SH (Viles *et al.*, 2011). However, recorded Equotip rebound values reflect the susceptibility of the instrument to micro-scale variations in surface roughness (Viles *et al.*, 2011). An increased number of samples should be taken with the Equotip to get a representative sample (Viles *et al.*, 2011). For the purpose of this study a minimum of 15 impacts were used, compared to the ten values recorded with the SH. In the field the D-type impact device was held at the specified 90° angle when recording data. Nevertheless, to prevent accidental errors the Equotip was set to auto-adjust values to changes in orientation, ensuring maximum possible accuracy of recorded data. Before use in the field the Equotip was calibrated according to manufacturer's instructions. It was tested and calibrated using the calibration surface provided and the results analysed to determine incorrect or correct calibration (see Figure 29 & Figure 30). Furthermore, for each field season the same person measured all Equotip readings in order to minimise operator variation (Viles *et al.*, 2011).

Figure 29: Equotip calibration set-up. The impact device is seen toward the left of the image. The calibration block is seen in the centre of the image.

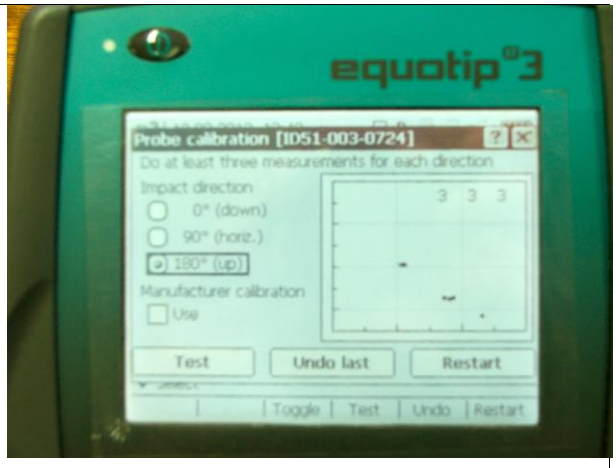

Figure 30: Equotip calibration screen for the Equotip with a D-type impact device. The impact device can be seen on Figure 29.

3.1.4 Near-Surface Ground Temperature Dynamics

Ninety percent (90%) of the global ice is found in Antarctica and the continent is crucial to global atmospheric and cryospheric systems. DML experiences cold permafrost with temperatures as low as -17.88°C on nunataks (Vieira *et al.*, 2010). However, our knowledge of permafrost-active layer dynamics in this region is poor, especially with regard to geomorphic dynamics (Vieira *et al.*, 2010). GST (Ground near-Surface Temperature) is measured in the uppermost centimetres of the soil and reflects temperatures of the top-most layer of the active layer (PermaNet, 2011). The active layer is subject to annual freeze-thaw cycles and overlies a layer of permafrost, ground that is below 0°C for a minimum of two years (*e.g.* Hedding, 2008; Adlam *et al.*, 2010). Active layer depth is determined by the intersection of the 0°C isotherm with the annual maximum soil temperature profile (Adlam *et al.*, 2010). GST provides an indication of the thermal regime of the ground and may be used as an

indicator of permafrost. A threshold of less than 3°C suggests the probable presence of permafrost (PermaNet, 2011). Warming climates may alter active layer dynamics (Adlam *et al.*, 2010), changing hydrological and ecological conditions (Vieira *et al.*, 2010). In particular, permafrost is the controlling factor on Antarctic terrestrial ecosystems and it is present in virtually all ice-free areas (Vieira *et al.*, 2010). Material high in insulation properties such as pyroclastic and pumice deposits may lead to a greater presence of ice-rich permafrost. Thermophysical properties of the ground must, therefore, be considered when determining spatial extent and distribution of permafrost (Vieira *et al.*, 2010). Harris and Pedersen (1998) argue that block deposits may lead to lower temperatures being maintained deeper within the soil. This impacts the depth and dynamics of the active layer and permafrost and has wide-ranging implications. In particular, this applies to our understanding of the active layer and permafrost within the region, the role that openwork block deposits have on these dynamics and the response of GST to *e.g.* a changing and warming climate. Furthermore, Vieira *et al.* (2010) have stressed the importance of monitoring ground temperatures in WDML. Relief is also thought to have a modifying influence on soil dynamics (Weinert, 1980), as active layer dynamics are related to topography (Vieira *et al.*, 2010) and microtopography (Ishikawa, 2003; PermaNet, 2011). Furthermore, an increase in altitude, due to environmental lapse rates, results in a decrease in active layer depth (Adlam *et al.*, 2010).

Moisture availability, sediment characteristics, snow cover depth and presence as well as topography and relief all influence ground temperature dynamics (Ishikawa, 2003; Grab *et al.*, 2012). Furthermore, mean summer and winter temperature, total summer radiation and mean summer wind speed influence active layer depth (Adlam *et al.*, 2010; PermaNet, 2011). Ambient temperature exerts the greatest influence on active layer dynamics, with high temperatures resulting in deep active layers. From spring to autumn, when snow cover decreases, GST is strongly influenced by ambient temperatures and diurnal cycles are observed (Ishikawa, 2003; PermaNet, 2011). Soil temperatures should respond to ambient temperatures within a 24-hour period. However, total annual solar radiation does not significantly affect active layer depth (Adlam *et al.*, 2010), due to the insulation effects of snow observed during winter months. Snow cover and depth influence ground temperature dynamics (Ishikawa, 2003; Grab *et al.*, 2012). A snow depth of 80-100 cm is required to provide the necessary insulation against ambient temperatures (PermaNet, 2011). During winter, when snow depth is highest, GST will stabilise and reach near-equilibrium values. In contrast, snowmelt during the warmer month percolates through the soil, resulting in heat transfer, increasing active layer depth through thermal conductivity and heat transfer via sub-surface flow (Adlam *et al.*, 2010). Strong winds also influence the ground response to ambient temperatures, having positive correlation to active layer depths (Adlam *et al.*, 2010). The aim of the fourth objective (Objective 4, pg. 9) was to identify near-surface soil moisture and temperature regimes and the implications this has on active

layer dynamics across the blockfield. The following section details methodologies employed to address Objective 4 (pg. 9).

iButtons were used to collect data on GST across the Northern Buttress. Data were collected during the 2010/11 and 2011/12 Austral summer season to SANAE IV. These included near-surface temperature regimes recorded with iButtons (thermochrons of type DS1922L), as well as climate variables recorded by the SANAE IV weather station and the PACE XR5 (or ACR) data logger. Thermochrons were placed in the field for ten days from the 18th to 28th of January 2011; and for 28 days from the 6th of January to the 3rd of February 2012. iButtons from Fairbridge Technologies (Pty) Ltd. were selected as their small size allows them to be used in many environments as an inexpensive method to record temperature regimes. Additionally, the mobility provided in the use of iButtons allows the sample size to be as large as deemed fit, depending only on the amount of sensors available (Ashcroft and Gollan, 2012). The ease of placing these sensors in the field also allows for spatial variable sampling, as sensors do not need to be fixed to permanent structures. Thermochrons were prepared to sample at 0.0625°C precision and placed in the field at suitable locations. A random placement of iButtons was not possible as sediment (soil) is scarce on the Northern Buttress. Instead, the area was systematically traversed in three second transects from east to west and iButtons placed in the ground whenever a suitable location was found (Figure 31, pg. 44).

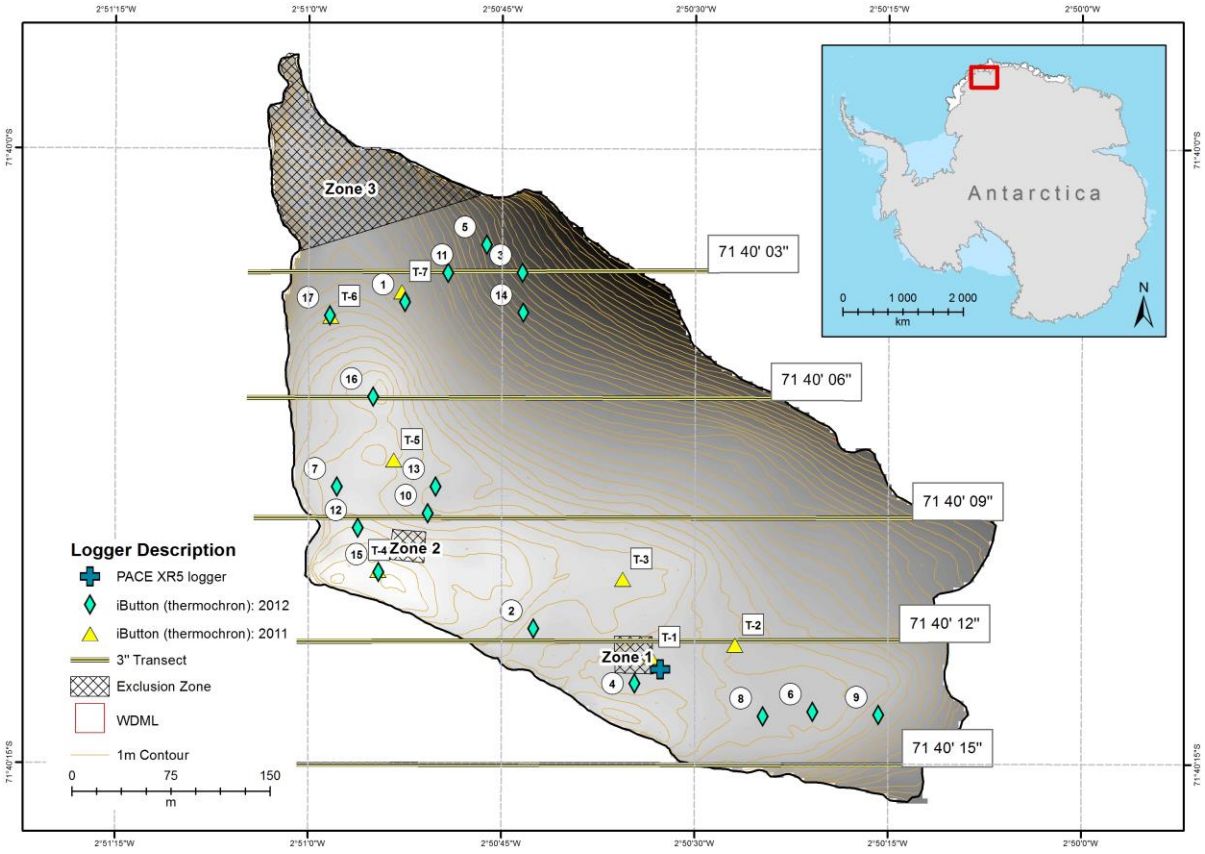

Figure 31: iButton (thermochron) sampling locations across the blockfield. Sample locations for the 2010/11 field season are indicated by triangles; diamonds indicate sample locations for the 2011/12 field season (2010/11: n = 6; 2011/12: n = 16).

iButtons were placed in snow-free areas as the lack of a snow cover removes the insulating effect of snow, resulting in a more dynamic thermally driven weathering environment (Hedding, 2008). A photo was taken of each site (*e.g.* Figure 32 & Figure 33), its latitude, longitude and elevation recorded. Each site was visited every few days to ensure iButtons remained covered by sediment.

Figure 32: Sampling site of Sample One (iB1).

Figure 33: Sampling site of Sample Six (iB6).

To ensure each iButton was placed at the same depth in the ground, iButtons were attached to 1 cm wide wooden supports, each marked with a unique number. Supports were marked at 7.5 cm and 5 cm along their lengths: the 5 cm mark corresponding to how much of the support would extend above the ground once buried, the 7.5 cm mark corresponding to where the iButtons were attached to each support. This ensured each iButton, once the poles were placed in the field, would be buried 2.5 cm in the ground. iButtons were attached to supports as detailed below.

- Each iButton, clearly marked the same way as its support, was attached to the pole 7.5 cm from the top of the support using a key tag and a cable tie (Figure 34). This ensured that iButtons didn't touch the support directly (to minimise influence of the wood on temperature measurements); and
- Each iButtons faced outward from the support, resulting in sampling in the vertical. Refer to Figure 35 for an overview of the set-up.

Note: The sampling set-up for iButtons was developed in conjunction with Barend van der Merwe (2012, personal communication).

Figure 34: iButton (thermochron) and key tags set-up.

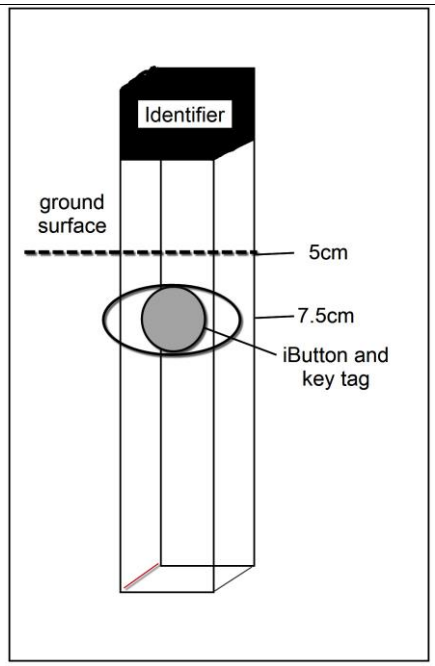

Figure 35: iButton field set-up.

During the 2010/11 field season seven iButtons were placed in the field. However, only six thermochrons were recovered at the end of the data observation period. iButtons were placed in the field on the 17th of January and set to record at midnight. This allowed temperatures within the ground to stabilise after the placement of iButtons. Data from this field season was recorded at hourly

intervals, yielding 242 data points per study site (n = 242) and a total number of 1533 data points (n = 1533). During the 2011/12 field season 17 iButtons were buried on January 5th. All iButtons were set to record a total of 4096 data points, recording every ten minutes until 10:29 on the 3rd of February. Similarly to the 2010/11 field season, thermochrons were buried at noon and set to start recording data at midnight. One iButton (sample 12) was found to be faulty and the final sample size was 16 (n = 16). Furthermore, only data recorded until midnight of the 2nd of February (n = 4 033 per site) were considered for this study. For this field season a total of 64 306 (n = 64 306) data points were used when combining data from all sample sites.

Data recorded by iButtons during the 2010/11 field season were compared to long-term temperature and moisture data collected for the Northern Buttress by a PACE XR5 data logger since 2006 (Vieira *et al.*, 2010). The PACE XR5 data logger records ground moisture and temperature at hourly intervals. The PACE XR5 logger forms part of the Antarctic permafrost borehole network and is located in a borehole less than two metres from the surface (Vieira *et al.*, 2010). The logger records ground temperatures at depths of 1 cm, 15 cm, 30 cm, 45 cm and 60 cm depths and ground moisture at a depth of one centimetre using a Decagon EC5 soil moisture sensor (Vieira *et al.*, 2010). In addition to temperatures and moisture recorded, the logger also monitors ambient air temperature at a height of one and a half metres above the ground and is protected by a radiation shield (Vieira *et al.*, 2010). The combination of ground and atmospheric data collection allows for the investigation of ground-atmosphere coupling (Vieira *et al.*, 2010). The setup of the logger may be viewed in Figure 36 on pg. 47.

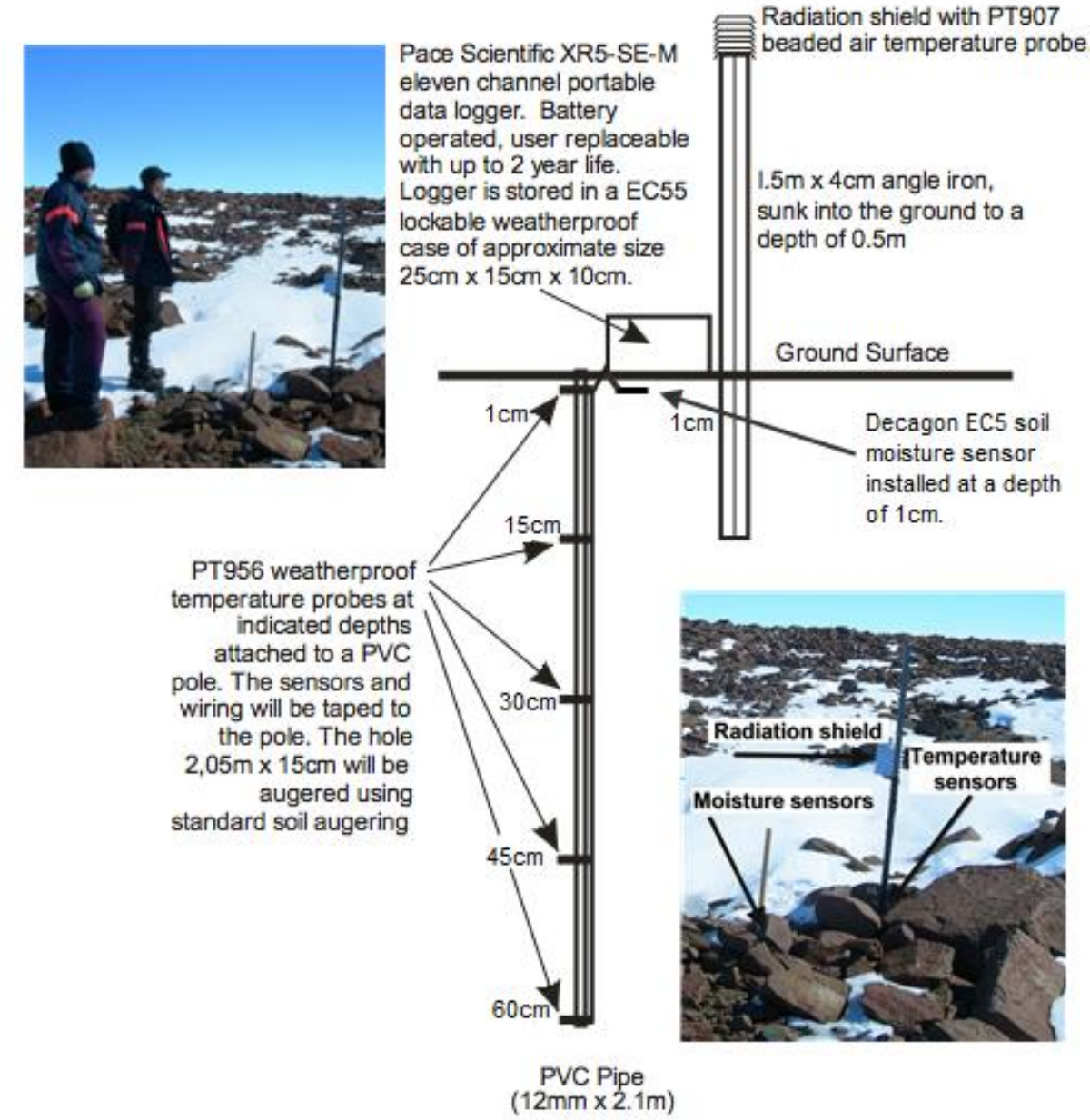

Figure 36: PACE XR5 logger system set-up for the Northern Buttress, Vesleskarvet (Adapted from Meiklejohn, 2012). Note the persons for scale.

Data recorded by iButtons during the 2011/12 field season were compared to climate parameters recorded during the same period by the SAWS weather station located at SANAE IV. Climate data analyses were conducted for relative humidity, pressure, temperature, wind direction and wind speed. Data on ambient temperature, relative humidity, wind direction and pressure were available for 12 years (n = 131 months, starting January 2000). Wind speed data were only available for 15 months (n = 15 months). The weather station parameters are listed in Table 2 (pg. 48).

Table 2: SANAE IV weather station description.

Description	Value
Climate Number	00000024
Latitude	71° 40’ 48” S
Longitude	02° 51’ 00” W
Height	849 m

Relative humidity was measured as a relative percentage (%), temperature in degrees Celsius (°C) and pressure in millibar (mb). One mb (1 mb) is equal to one hPa (hecto Pascal). Wind direction and wind speed were observed as degrees clockwise from north and in metres per second ($m.s^{-1}$) respectively. All parameters were observed on the hour. Table 3 gives provides a description of wind direction and associated bearing, as designated by SAWS.

Table 3: Orientation and assigned bearing for wind direction, as classified by and adapted from SAWS.

Bearing	Orientation
N	dir. >= 349° OR dir. < 11°
NNE	11°- 34°
NE	34°- 56°
ENE	56°-79°
E	79°-101°
ESE	101°-124°
SE	124° -146°
SSE	146°-169°
S	169° -191°
SSW	191°-214°
SW	214°-236°
WSW	236°- 259°
W	259°- 281°
WNW	281°-304°
NW	304°-349°

3.1.5 Rock Properties and Moisture Uptake

Rock lithology as well as rock shape and form influence weathering rates (Cooke, 1979). Individual properties such as microporosity, porosity and water absorption capacity of clasts are also known to influence rock weathering (Briggs, 1977a; Cooke, 1979). Rock weathering is directly proportional to microporosity, porosity and water absorption capabilities and inversely proportional to the rock’s saturation coefficient (Cooke, 1979). The igneous rock of the study area has low porosity and

permeability values (Grotzinger *et al.*, 2007). Furthermore, the highly metamorphosed and resistant lithologies found on many blockfields are associated with low porosities (non-frost susceptible) and crystalline structures (Ballantyne, 2010). Regardless of rock properties, moisture availability is known to influence weathering rates. In particular, this applies to chemical weathering. The ability of clasts to absorb moisture, therefore, has implications on clast weathering. Moisture absorption of rocks in different environmental settings, on the other hand, indicates moisture availability particular to each separate setting. Moisture availability, although low for the region, is largely influenced by microclimate and during the warmer Austral summer months, this availability increases (Lee *et al.*, 2013). The aim of the fifth objective (Objective 5, pg. 9) was to identify the role that different environmental settings have on the moisture uptake of rocks. These settings are related to snow and ice availability, being the source of moisture. The following section details methods employed to achieve the fieldwork component of Objective 5 (pg. 9). The laboratory component of this objective is discussed under Rock Properties (pg. 53).

Twenty rocks of similar weight but not exceeding 320 g were collected in the field, divided into five groups and clearly marked. Rocks had to be less than 320 g in weight due to restrictions placed on weight by the scale available. Rocks were collected in the field from one location in an attempt to obtain samples exposed for a similar amount of time, located on the same aspect and of the (presumably) same source. Each group of four rocks was assigned to a specific setting: Group 1 (Figure 37) was placed on ice; Group 2 (Figure 38) was placed on top of rock; Group 3 (Figure 39, pg. 50) was placed on soil; Group 4 (Figure 40, pg. 50) was placed on snow and Group 5 (Figure 41, pg. 50) was buried in snow.

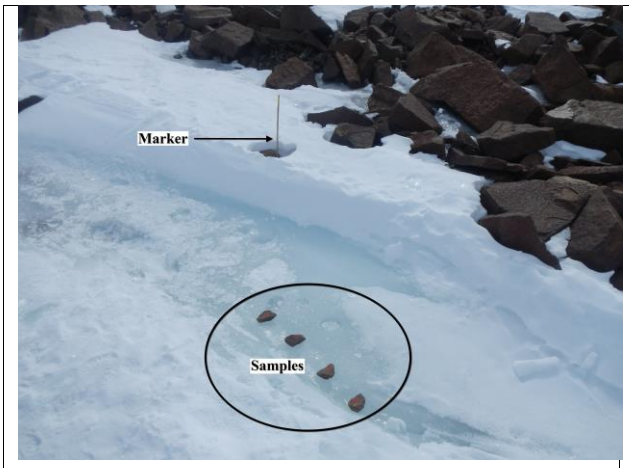

Figure 37: Samples (1-4) placed onto ice.

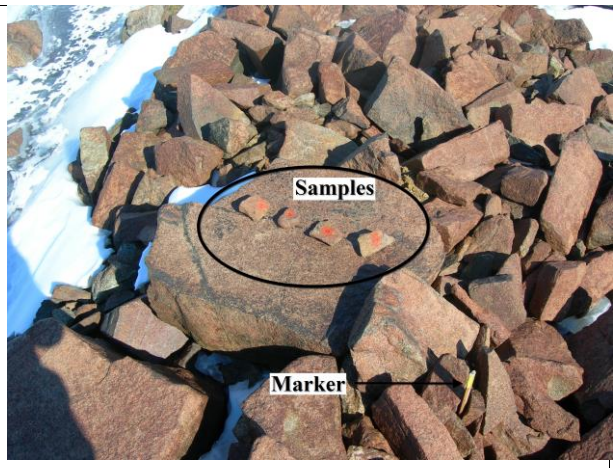

Figure 38: Samples (17-20) placed on rock.

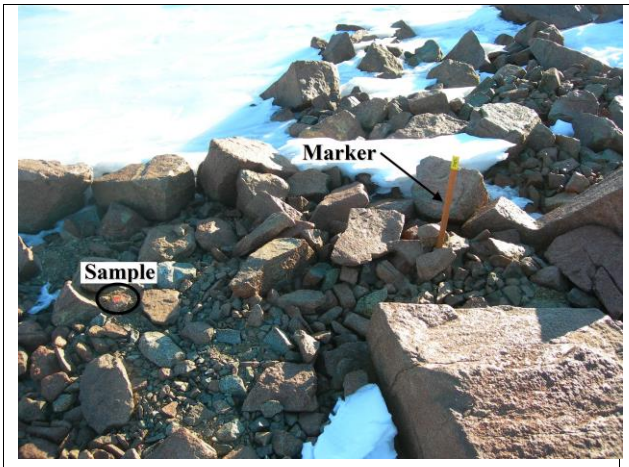

Figure 39: Samples (13-16) placed on soil.

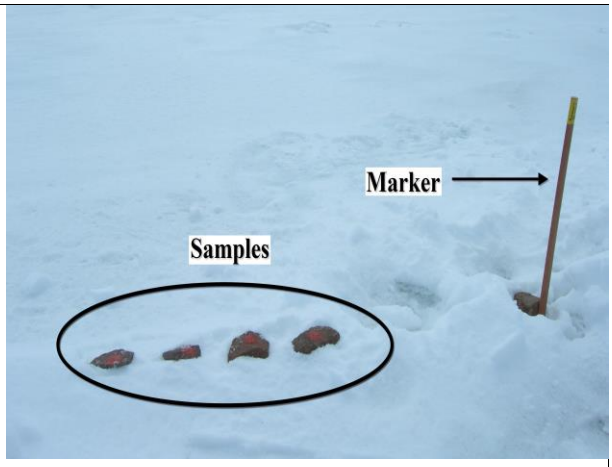

Figure 40: Samples (9-12) placed onto a snow surface.

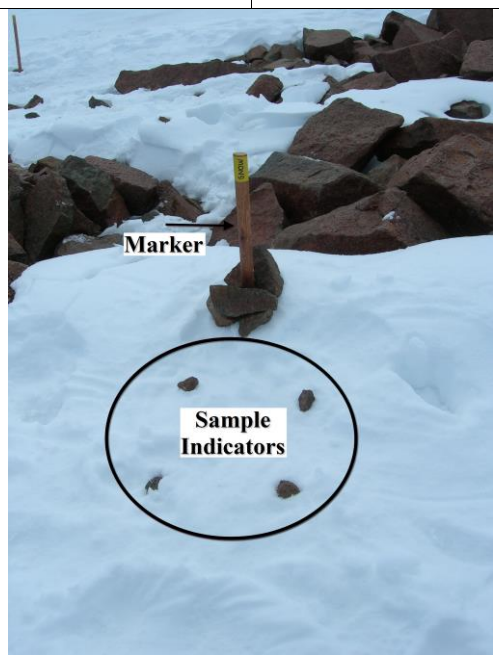

Figure 41: Samples (5-8) buried in snow. The small rocks indicate the location of buried samples.

In order to prepare samples for the field, rocks were dried in an IncoTherm Labotec oven at 105°C for three days. All samples were placed into the field at five different sites on January 9th 2012, a photo taken from each site and its latitude, longitude and elevation recorded. The field site was selected due to all the specific settings being available in close proximity to each other (Figure 42, pg. 51). This ensured that samples of all settings were exposed to similar weather, such as wind speed, wind direction and precipitation. Samples were also placed in the field in an east-west orientation. Samples were removed from the field every 24 hours, depending on local conditions, weighed and returned to the field, yielding time series data spanning four weeks. Samples were removed from the field on February 3rd 2012 and their physical properties, namely rock moisture content (percentage dry mass and percentage saturation), P (porosity), WA (water absorption capacity), S (saturation coefficient) and M (microporosity) determined during laboratory analyses using the method described by Cooke

(1979). The field weight used for each calculation was based on the weight of each rock upon final removal from the field. Subsequently, data were statistically analysed using Microsoft® Excel. Please refer to Statistical Methods (pg. 68) and Rock Properties (pg. 53) for a detailed explanation of statistical and laboratory methods used.

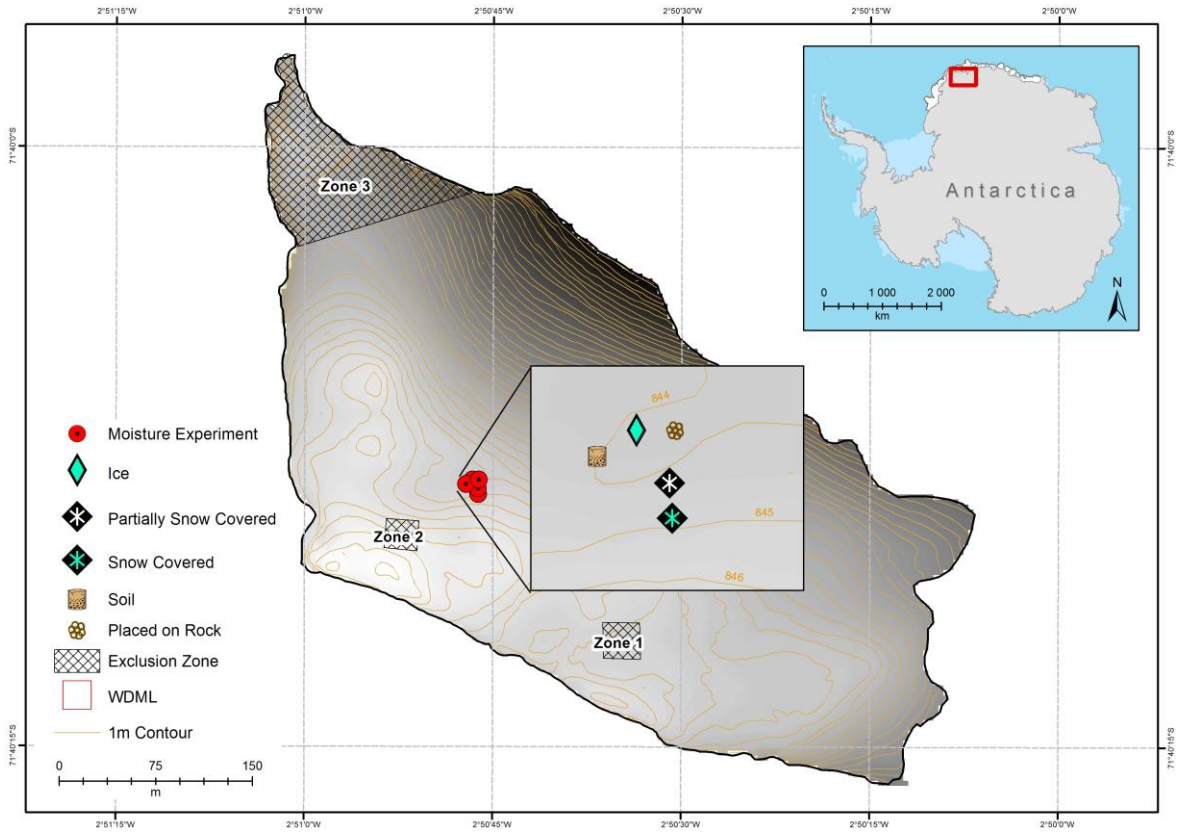

Figure 42: Location of clasts placed in the field to determine susceptibility to moisture uptake in various environments. A diamond indicates samples placed on ice; the round marker indicates samples placed on bare rock; a square indicates samples placed on soil; a two-tone (black-white) diamond indicates samples placed onto a snow surface; and a two-tone (blue-black) diamond indicates samples buried in snow.

3.1.6 Particle Size Analysis

The sixth objective (Objective 6, pg. 9) aimed to examine the impact chemical and physical weathering processes and erosional agents have had and are having on the blockfield. Soil formation is controlled by the nature and evolution of the landscape and gives an indication of the interrelationships between geographical phenomena and processes active within the landscape (Briggs, 1977a, 1977b). It is the result of weathering processes and controlled by the local climate and lithology (Grotzinger *et al.*, 2007). Clay minerals result due to the chemical weathering (alteration) of primary minerals (Briggs, 1977a). They give an indication of the age and stage of the deposit and impact of chemical weathering on clasts (Biggs, 1977b; Rea *et al.*, 1996; Whalley *et al.*, 2004; Rea, 2007). Both dolerite and diorite contain feldspar (McCarthy and Rubidge, 2005). Feldspar is susceptible to chemical weathering, which should indicate a presence of clay minerals in the soil

(Briggs, 1977a), as already discussed under Weathering and Erosion (pg. 15 onwards). The following section details the field method employed to achieve Objective 6 (pg. 9). For a description of laboratory methods used please refer to Particle Size Analysis (pg. 69).

In order to conduct particle size analysis and fine sediment analysis, sediment was collected from three sites (n = 3). An attempt was made to sample at more than three locations. However, the known scarcity of soils on blockfields made random site selection difficult, if not impossible. Consequently, three suitable sites were identified when placing iButtons in the field (Figure 43). Each site falls within its own three second transect, following an east-west orientation.

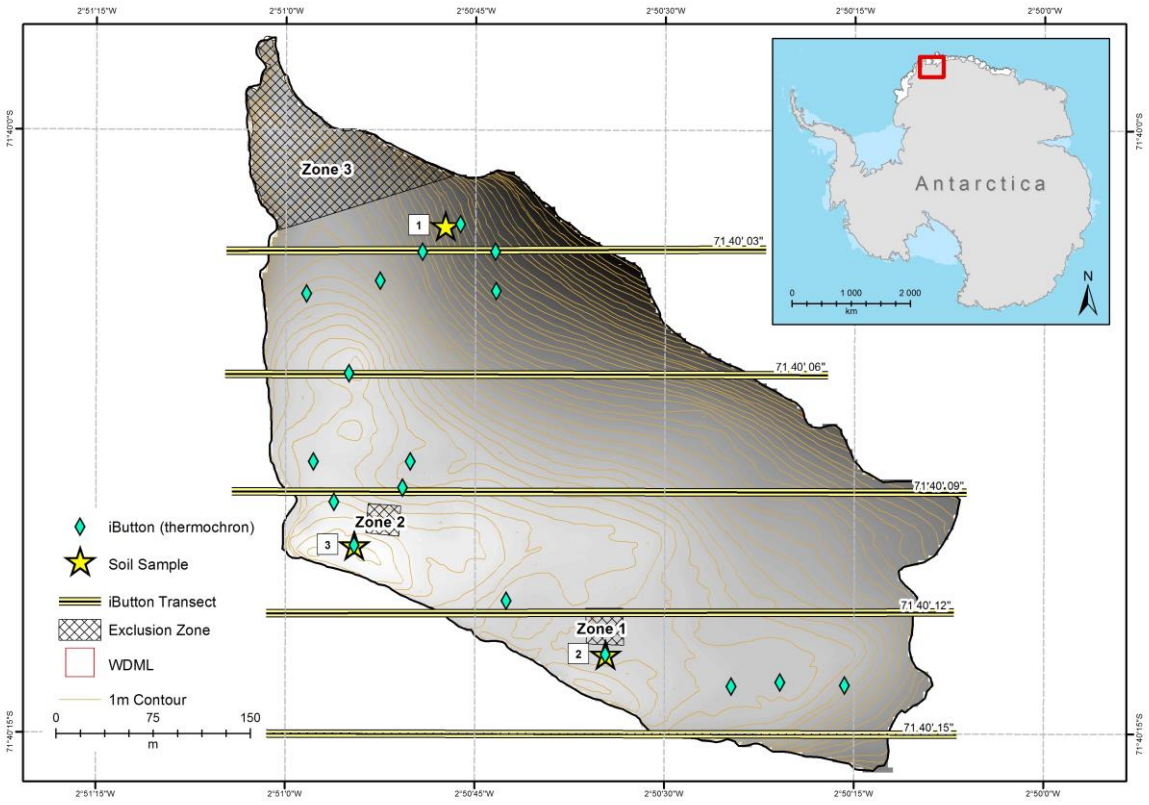

Figure 43: Location of sediment sample sites (n = 3) for the blockfield. Yellow stars indicate S1, S2 and S3. Diamonds represent iButton (thermochron) sampling locations. Note the proximity of soil sample locations to iButton sampling locations.

After removal of the thermochrons a bulk specimen of soil was collected at each site (Briggs, 1977b). Sandy samples require a minimum sample weight of 100 g (Briggs, 1977a). After a visual examination of the very coarse sediment found at the study site it was decided to collect samples exceeding one kilogram in weight to ensure a representative portion of the fine earth fraction was collected. Samples were sealed in airtight polythene bags and stored for transport to South Africa. To ensure maximum accuracy and precision, all samples were subjected to similar storage and transport

conditions (Briggs, 1977b). Samples subsequently underwent laboratory analyses in South Africa. These are described under Particle Size Analysis (pg. 54).

3.2 Laboratory Methods

Laboratory methods were employed to conduct particle size analyses (to determine the amount of weathering the surface of the deposit has been exposed to) and to determine rock properties. All laboratory methods were completed in the same laboratory, using the same equipment. All samples, when required, were weighed to the nearest 100^{th} of a gram (0.01 g). Each of these methods is explained in detail in the sections below.

3.2.1 Rock Properties

The aim of the fifth objective (Objective 5, pg. 9) was to determine the influence several environmental setting have on moisture susceptibility and uptake of rocks. This section details the laboratory component of Objective 5 (pg. 9), adapted after Cooke (1979). Rock properties in terms of moisture content and susceptibility are vital when interpreting the weathering process (Cooke, 1979). Rock moisture content is influenced by the rock mineral properties, environmental conditions and rock temperature (Briggs, 1977a). In addition, it is influenced by the rock's physical properties such as microporosity and porosity (Cooke, 1979). Field data (see Rock Properties and Moisture Uptake, pg. 48) consisted of sample weights, taken over a period of 25 days. Weight gain and loss was used as a proxy for moisture gain and loss. However, as rock properties influence rock moisture content (Cooke, 1979), field weights and rock properties were examined together. Individual rock properties from samples within groupings needed to represent the same populations, *i.e.* have similar sample variations. Otherwise, samples may have skewed field observations. Rock properties were determined during laboratory analyses, discussed in the section below, and subsequently statistically analysed to determine comparability of populations. For a detailed explanation of mathematical and statistical methods employed please refer to Rock properties (pg. 68).

All clasts collected in the field (n = 20) were lightly brushed, dried in a Labcon Forced Circulation oven for 24 hours at 105 ºC and weighed (W_0). Samples were saturated in deionised water for 24 hours, dabbed dry and weighed again (W_3). Subsequently, samples were oven dried for another 24 hours at 105 ºC. Samples were placed in a desiccator, left in vacuum for two hours and saturated under vacuum (20 mmHg) for 24 hours. Upon removal from the desiccator, samples were dabbed dry and weighed again (W_2). Following this, samples were weighed suspended in water (W_1), surface dried and placed in a partial vacuum (286 mmHg) for 24 hours. After 24 hours the samples were

weighed again (W_4). Clast field weight equalled the weight of rocks upon last removal from the field (W_5). Data collected during laboratory methods were used to determine rock moisture content (percentage dry mass and percentage saturation), P, WA, S and M. The percentage saturation of each clast gives an indication of the amount of moisture the clast can absorb, whereas the percentage dry mass indicates the amount of moisture absorbed in the field (Cooke, 1979). P is the volume of the clast pore space expressed as a percentage of bulk volume (Cooke, 1979), *i.e.* pore space as a portion of total volume. WA expresses, as a percentage, the amount of moisture absorbed in a specific time, *i.e.* a 24-hour period (Cooke, 1979). The time span for the various portion of the laboratory work equalled the approximately time span between the weighing of rocks in the field (24 hours). S is the amount of water absorbed in this same time span (24 hours) and indicates the fraction of available pore space of the sample (Cooke, 1979). M estimates the amount of water retained by the sample under a negative pore water pressure (Cooke, 1979).

3.2.2 Particle Size Analysis

The aim of the sixth objective (Objective 6, pg. 9) was to identify the impact of chemical weathering on the blockfield. Sediment production is influenced by the different types and rates of weathering processes active within a specific region (Briggs, 1977a). Clay minerals are the result of *in situ* chemical alteration of primary minerals (Briggs, 1977a; Weinert, 1980) and may be used as a proxy for chemical weathering on clasts for the study site (Biggs, 1977b; Rea *et al.*, 1996; Whalley *et al.*, 2004). Particle size analysis and the proportion of clay particles were determined during laboratory analyses. Particle size analyses (fine earth fraction analyses) give an indication of the depositional, erosional and weathering environment of a region (Alsharhan and El-Sammak, 2004), and allow for sediment classification (Weaver and Grobler, 1981). Assuming glacially and periglacially derived sediment; samples should be low in organic matter, poorly sorted and have low (if any) clay content (*e.g.* Briggs, 1977a). Nevertheless, the feldspar content of both dolerite and diorite (McCarthy and Rubidge, 2005), common to the study site, should yield clay minerals (montmorillonite) in sediment samples (Briggs, 1977a; Weinert, 1980). The longer the blockfield has been exposed to weathering processes, the greater this clay proportion is expected to be. The following section details the laboratory methods employed to achieve Objective 6 (pg. 9). These comprise sieving and sedimentation (settling) techniques after Briggs (1977a; 1977b) and Weaver and Grobler (1981).

Samples were oven-dried for 24 hours in a Labcon Forced Circulation oven at 60 ºC (Briggs, 1977b). The bulk density of each sample was determined to identify the nature of the soil (Briggs, 1977b). The organic component causes the bulk density of a soil to decrease. On average, mineral soils have a bulk density of 1.25 $g.cm^{-3}$ (Briggs, 1977b). Soil on the study site is assumed to have little or no

organic component and mineral soil should fall within the range of approximately 1.0-2.0 $g.cm^{-3}$. Fieldwork conditions did not allow for the exact volume of samples to be collected. As such an estimate of bulk density and volume was determined for each sample. Samples were weighed, put into a beaker of known weight, height and radius and their volume determined using Equation 3.

Equation 3: Volume equation (Briggs, 1977b).

$$V = h\pi r^2$$

Bulk density was calculated using Equation 4.

Equation 4: Bulk density equation, where W = weight of sample and V = volume of sample (Briggs, 1977b).

$$D_b = W.V^{-1}$$

Particle size analysis was done after the bulk density of sediment samples was determined. The three samples were weighed, disaggregated with a mortar and pestle and sieved in a sieve stack for ten minutes (Briggs, 1977b). Sediment in each sieve was weighed separately to determine the dry mass proportion of sediment within each size class. Sieving identifies the proportion of material between 0.05-5.0 mm (4ø – -1ø). A focus was on the fine earth fraction (coarse sand-clay), those particles smaller than 2 mm in diameter (Briggs 1977b). Refer to Table 4 for sedimentation grades and sizes.

Table 4: The three grades of the fine earth fraction, indicated in millimetres (mm) and micrometres (µm) (Briggs, 1977b).

Type	Millimetre	Micrometre
Sand	2-0.06	2000-60
Silt	0.06-0.002	60-2
Clay	< 0.002	< 2

Sieving techniques were used to identify particle sizes up to 63 µm in diameter. Particles smaller than 63µm in diameter underwent SediGraph analyses. The SediGraph, compared to the pipette method, hydrometer or sedimentation balance method, has been shown by *e.g.* Weaver and Grobler (1981) and Lara and Matthes (1986) to identify finer particle size distributions. Particles smaller than 2 mm, therefore, underwent sediment analysis using the SediGraph 5100. The SediGraph is an automated, quick and reproducible method for conducting fine particle size analysis (Weaver and Grobler, 1981; Lara and Matthes, 1986). Similar to the pipette method, it is based on Stokes' Law as well as the Beer-Lambert Law (Stein, 1985; Lara and Matthes, 1986; Cramp *et al.*, 1997). Stokes' Law (Equation 5, pg. 56) states that the velocity of a particle falling under its own weight in a viscous medium (such as water) is directly proportional to the diameter of the particle: the heavier the particle, the faster it

falls (Briggs, 1977a; 1977b). Sand sized particles will settle out of a liquid within approximately 50s, with clay taking up to eight hours to settle out of the liquid (Briggs, 1977b).

Equation 5: Stokes' Law. D = size of the particle; ν = terminal velocity of the particle; η = viscosity of the liquid; ρ = density of the particle material; ρ0 = density of the liquid; *g* = gravity (Briggs, 1977a).

$$D^2 = \frac{18\nu\eta}{(\rho-\rho 0)\, g}$$

The law incorporates the size of the particle (D), density of the particle material (ρ), gravity exerted on the particle (g), the buoyant force of the liquid (depending on terminal velocity [v]) as well as the density ($\rho 0$) and viscosity (η) of the liquid. Stokes' Law does not provide absolute size values for non-spherical particles (Lara and Matthes, 1986). Nevertheless, it may be used to create an index of particle size. The Beer-Lambert law describes how a ray of photons, for example X-rays, is attenuated when passing through matter, as a function of time and height in the medium (Stein, 1985; Micromeritics, 2012). The attenuation is directly proportion to the concentration, extinction coefficient and path length of the beam through the medium (see Equation 6 below).

Equation 6: Equation describing Beer-Lambert's Law. I_f = final beam; I_i = incident beam; ε = absorptivity of the medium; *c* = concentration of the medium; *d* = path length of beam (Stein, 1985).

$$\frac{I_f}{I_i} = \exp(-\varepsilon c d)$$

Combining the two laws allows for the determination of particle size distributions. The SediGraph automatically records the rate of sedimentation of particles (applying Stokes' Law) using a finely collimated beam of X-rays (applying Beer-Lambert's Law), where the intensity of the recorded X-rays is directly proportional to the density of the sediment (Weaver and Grobler, 1981; Lara and Matthes, 1986; Cramp *et al.*, 1997). Results are shown as a cumulative percentage graph of particle sedimentation rates and sizes (Stein, 1985; Lara and Matthes, 1986). The SediGraph method requires a minimum reading of 25µA on the X-ray intensity meter and a maximum concentration of five percent per volume per SediGraph cell. A concentration of two percent per volume, equivalent to two grams of sediment per 100 ml, is recommended (Stein, 1985; Cramp *et al.*, 1997).

A solution of sodium hexametaphosphate ($NaPO_4$) of 0.1% was prepared by adding one gram of sodium hexametaphosphate to one litre of deionised water (Stein, 1985; Cramp *et al.*, 1997). Sediment samples were prepared at a two percent volume to the sodium hexametaphosphate solution. This was achieved by adding one gram of sediment to 50 ml of the solution. The prepared sample was subsequently put into an ultrasonic bath to remove air bubbles. The X-ray intensity of the SediGraph was set to normal, pump control to auto and operating temperature to 32°C, with an error of ±0.2°C.

The sample density was determined by weighing 1 millilitre of sediment. Sediment densities can be seen in Table 5 below.

Table 5: Densities ($g.ml^{-1}$) of sediment samples (S1, S2, S3) determined during laboratory analyses.

Sample	Density
S1	1.2566
S2	1.1416
S3	1.3211

Before commencing with sediment analyses, a baseline sample was conducted by adding the sodium hexametaphosphate solution to the SediGraph cell. The baseline sample (refer to Appendix C: SediGraph 5100 Settings, Figure 77, pg. 170) allows for the calibration of subsequent data obtained using the instrument. Following this sample test, sodium hexametaphosphate, deionised water and the required sediment portion (two percent per volume) was added to the SediGraph cell. Sodium hexametaphosphate aids in the disaggregation of particles. Samples were, furthermore, agitated in the SediGraph cell to ensure a homogeneous dispersion of particles (Lara and Matthes, 1986). Once particles were allowed to settle, analyses using parallel X-ray beams commenced. Each sample underwent three analyses runs and the average of these was used in subsequent statistical analyses. Please refer to Particle size analysis (pg. 69) for results and discussion of these. Table 77 and Table 78 in Appendix C: SediGraph 5100 Settings (pg. 169) list the settings used during analyses.

3.3 Statistical Analyses and Preparation

Geographical data varies across space. However, items close to each other are often related or share similar attributes (Atkinson, 2001). Variation in data occurs over space, relationships are inherently different and relationships are non-stationary across space (Charlton *et al.*, 2006). This is known as spatial autocorrelation, forming the basis of Tobler's First Law of Geography (Miller, 2012). Classical statistical analyses assume data points are independent of each other. In terms of geographical data, statistical analyses assume that data points are dependent on each other, *i.e.* spatially autocorrelated (Doornkamp and King, 1971; Atkinson, 2001; Griffith, 2005). The use of both classical (for example non-spatial regression) and geographical (for example spatial regression) statistical methods allows for the comparison and validation of results (Miller, 2012). Autocorrelation in geographical statistics is similar to Markov chains of classical statistics (Till, 1985). The two statistical approaches complement each other (Griffith, 2005; Miller, 2012) and mean responses improve if autocorrelation is considered during spatial analyses (Griffith, 2005). In particular, physical geographers often investigate relationships and processes that vary from one place to another, requiring the use of non-stationary geostatistical models (Atkinson *et al.*, 2003). The combination of statistics, GIS and

geostatistics for analysing geographical data has, therefore, been found to be a powerful analytical combination (*e.g.* Burrough, 2001). The nature of the project required both classical and geographical statistical analyses to be employed and all three approaches (statistics, GIS and geostatistics) were applied when conducting analyses. The methods employed are detailed in the two sections titled Statistical Methods (pg. 59) and Geostatistical Methods and GIS (pg. 71).

Data were initially analysed in Microsoft® Excel using descriptive statistics as well as statistical inference. Data were examined to determine whether or not relationships existed between the data collected, such as ground temperature regimes and measurable external parameters, such as dominant wind speed and ambient temperature. Specifically, field data were statistically compared to short- and long-term temperature regimes as well as moisture profiles. In addition, data were analysed in GIS. GIS provide a powerful platform for creating, storing, manipulating and analysing data. They allow for the statistical exploration of spatial data and their visualisation and display (Burrough, 2001). ESDA (Exploratory Spatial Data Analysis), such as means, deviations, ranges and correlations were applied when conducting spatial data analysis. In particular, histograms, QQ (Quantile-Quantile) plots, trend analyses, semi-variance/covariance clouds were determined using ESDA. These tools all form part of the Geostatistical Analyst toolbar in ArcMap® 10. In addition, CSDA (Confirmatory Spatial Data Analysis) was used for the testing of hypotheses (Burrough, 2001). GIS were used to model the predominant direction and strength of wind over the surface of the blockfield and to allow for geographical statistical analysis in terms of climate control on rock-aspect characteristics. In addition, GIS were utilised to spatially extrapolate the data collected to a larger area. These extrapolation values, when compared to field measurements were used as data control points, giving a good indication of the accuracy of the analysed and calculated data points.

3.3.1 Data Preparation

Field data were processed and cleaned before statistical analyses could be carried out. Bearings taken in the field constituted magnetic bearing. These were adjusted to true bearing using magnetic declination and change per year. Magnetic declination was determined for the latitude (72°S) and time of year (January/February 2011 and 2012) when measurements were taken. SH and Equotip readings were assigned to their appropriate aspect (north-, east-, south-, west-, top-facing sides), as were measurements on lichen presence, flaking, pitting and the roughest face. Data were analysed for population means and *s* (standard deviations) to compute *z*-scores. Any values exceeding the value of two *z*-scores were deemed outliers and removed from the population. The remaining data were statistically and geostatistically analysed in Microsoft® Excel and the Esri ArcGIS suite of products.

An in-depth description of the methods used follows in the sections Statistical Methods (pg. 59) and Geostatistical Methods and GIS (pg. 71).

3.3.2 Statistical Methods

Descriptive statistics as well as statistical inference, using both parametric and non-parametric statistics (Till, 1985) were utilised throughout the project. All data collected represented time series data and spanned two years. Statistical inference requires the use of hypothesis testing, where H_0 (the null hypothesis), H_a (the alternate hypothesis), the test statistics, α (level of significance) and confidence interval are determined (Briggs, 1977a; Till, 1985). A level of significance of 0.05 ($\alpha = 0.05$) generally reflects a realistic level of certainty in physical geography and reflects the lowest acceptable level of significance for the purpose of this project (Briggs, 1977a). Furthermore, a confidence interval of 0.95 has been found (*e.g.* Till, 1985) to be the most suitable level to minimise both Type I (rejecting a true H_0) and II errors (accepting a false H_0). At this level there is a 5% probability of the result being wrong, *i.e.* rejecting or accepting H_0 incorrectly.

3.3.2.a Descriptive statistics

Descriptive statistics comprises measures of location, dispersion, shape and association (Williams *et al.*, 2006). Measures of location include the median, mode and mean (Williams *et al.*, 2006). The mean (average) is used as a measure of central location for the data set and is used when calculating *z*-scores. The median is the central value of the data set and the mode is the value that occurs with the greatest frequency. With highly skewed data the median is preferred over the mean and the mode is used as an indicator of the most common value. The median and mean can be used to identify the shape of the distribution. This is combined with skewness, an indication of the asymmetry of the dataset, with a value of zero indicating a symmetrical and normal distribution (Williams *et al.*, 2006). A skewness value exceeding 1.62 or -1.62 indicates a highly skewed distribution to the right or left respectively. Please refer to Appendix B: Statistical Descriptions, Ranges and Classes, Table 74 (pg. 167) for a description of classes of skewness. When the median and mean are close together and skewness values are near zero the data set is said to be symmetrical and normally distributed (Briggs, 1977a; Williams *et al.*, 2006). In order to identify the shape of the distribution of the data set, the median, mean and skewness were calculated for each data set. In addition, sample minimums, maximums and ranges were calculated.

Measures of variability apply to *s* and *c* (the coefficient or variation) (Till, 1985; Williams *et al.*, 2006). *C* expresses *s* as a percentage of the mean. *S* indicates the deviation of data about the mean and

is used when calculating *z*-scores. The shape of the distribution is of importance when applying *z*-scores and removal of outliers to the data set. Applying the empirical rule to a data set, standardised residuals are used to remove outliers from the data set (Williams *et al.*, 2006). Outliers (extreme values) represent data points that do not fit the trend of remaining data (Williams *et al.*, 2006). Field values were converted to standardised residuals using the data series mean and *s*. Outliers were identified using standardised residuals and removed from the data set. The literature (*e.g.* Williams *et al.*, 2006) recommends identifying *z*-scores (standardised values) more than ±3 as outliers (Williams *et al.*, 2006). However, Williams *et al.*, suggest removing *z*-values falling outside of two *s* as outliers. Assuming a normal distribution, values falling within two *s* from the mean represent 95% of the data (Till, 1985; Williams *et al.*, 2006). Consequently, standardised residuals should fall outside the set limit of two *s* only five percent (5%) of the time and values greater than ±2 were removed as outliers from the data sets.

3.3.2.b Statistical inference

Statistical inference used for the project comprises *r (*Pearson's product-moment coefficient of linear correlation, regression analyses, the *F*-test, *t*-test (Student's *t*-test), Kolmogorov-Smirnov two-sample test, Tukey Chi-square test, von Mises distribution as well as ANOVA (ANalysis Of VAriance) tests. Linear regression employs the least squares method to fit a line through a set of observations. It is used to identify relationships amongst data (Till, 1985). Predictor variables (independent variables) are modelled against response variables (dependent variables), assuming that the calculated relationship is constant across the study area (Doornkamp and King, 1971; Brunsdon *et al.*, 1998; Charlton *et al.*, 2006). This allows for determining the relative influence of independent variables, for example wind speed and precipitation, on dependent variables such as soil temperatures. Pearson's correlation coefficient (*r*) determines correlation between data sets when each data set has variable observations, *i.e.* n is variable (Till, 1985). Due to the coefficient being scaled, the final value is independent of the units of measurement for the separate populations (Williams *et al.*, 2006). It is used to determine whether or not two measurement variables tend to move together. When calculating *r* between more than two variables a correlation matrix is calculated (Doornkamp and King, 1971). The value of the coefficient indicates the strength of the relationship (Brunsdon *et al.*, 1998), and a value of approximately zero indicates not relationship or trend observed between populations (Williams *et al.*, 2006). The R^2-statistic indicates how much of the total variance is explained by the linear relationship (Till, 1985). However, classical linear regression does not take the location of geographical variables into account, *i.e.* the model is stationary (Brunsdon *et al.*, 1998; Charlton *et al.*, 2006). Instead, interpolation methods using a non-stationary approach should be applied. Please refer to Interpolation and geostatistical data analyses (pg. 72) for further discussion on this.

The *F*-test is used to determine the similarity of sample variances (Till, 1985; Williams *et al.*, 2006). A normal distribution is assumed and the test is performed before the parametric *t*-test (Doornkamp and King, 1971). When conducting an *F*-test, the sample distribution variances are calculated, to allow for the correct identification of the nominator (larger variance) and denominator (smaller variance) in the *F*-test statistic. The *t*-test may be used to determine whether or not two populations are statistically similar when population variance is not known (Doornkamp and King, 1971; Till, 1985). Similarity is tested using a homoscedastic two-sample *t*-test for the equality of means (n is variable; variance is similar). A normal distribution is assumed, however, the test may be applied for non-normal distributions (Till, 1985). Similar to the *t*-test, the non-parametric Kolmogorov-Smirnov test may be used to compare two data sets (Till, 1985). However, data sets do not have to approximate normal distributions and have to be arranged as cumulative percentages (Till, 1985). The Tukey Chi-square test is employed when testing for preferred orientation as well as significance (Middleton, 1965; Doornkamp and King, 1971). Like the *t*-test a normal distribution is assumed (Middleton, 1965) and the expected frequency within each class must exceed five (n = 5) (Doornkamp and King, 1971; Till, 1985). Von Mises distribution is used to determine the measure of orientation (Till, 1985). When testing on more than two populations, ANOVA is used. One-tailed tests test for significance in one direction, *i.e.* a difference in a particular direction whereas the two-tailed tests are non-directional and test for significance in either direction (Briggs, 1977a; Till, 1985). This is due to the fact that bias may be negative or positive (Till, 1985). Two-tailed tests were carried out for the majority of inferential statistics calculated for the project.

ANOVA is a statistical technique comparing more than two observed population sample means to determine whether or not populations are statistically similar (Doornkamp and King, 1971; Till, 1985). There are three assumptions for ANOVA: 1) for each population, the response variable is normally distributed, 2) the variance of the response variable is the same for all populations, and 3) observations are independent (Till, 1985; Williams *et al.*, 2006). Data were, therefore, tested for normal distributions (Ericson, 2004). ANOVA forms part of hypothesis testing and was carried out in Microsoft® EXCEL, using the Analysis Tool Pak plug-in. The method requires the definition of the factor (independent variable) and a response (dependent) variable. Furthermore, the values of a factor become the treatments of the analysis (Williams *et al.*, 2006). The test statistic (*F*), confidence interval and α are calculated during ANOVA analyses. Rejection of H_0 occurs when *F* exceeds the critical value or if the *p*-value is less than α. Fisher's LSD (Least Significance Difference) test is used to determine which population variances are different, in the case where H_0 of ANOVA is rejected (Till, 1985; Williams *et al.*, 2006). This test is based on a pair-wise comparison *t*-test and evaluates two populations at a time. Table 6 (pg. 62) summarises the inferential statistical methods employed for each of the study's relevant objectives.

Table 6: Inferential statistical methods employed during analyses.

Question	Investigation	Method	Description
Is the blockfield autochthonous or allochthonous?	Investigating a preferred/random orientation of clasts	Tukey Chi-square test	Clast survey (Objective 2, pg. 9)
Can SH and Equotip readings be used comparatively?	Determining if SH and Equotip sample variances are similar	*F*-test	Rock hardness (Objective 3, pg. 9)
Can SH and Equotip readings be used comparatively?	Comparing SH and Equotip readings	Student's *t*-test	Rock hardness (Objective 3, pg. 9)
Does aspect play a role in weathering of clasts?	Determining if rock hardness rebound values, lichen presence, observable surface flaking, pitting and roughness for all aspect are drawn from the same population	ANOVA	Rock hardness (Objective 3, pg. 9)
Which clast sides exhibit similar populations?	Determining if individual pairings of clast sides have similar population variances	Fisher's LSD test	Rock hardness (Objective 3, pg. 9)
Does topography influence near-surface soil temperatures?	Determining if soil temperature values for all sample points are drawn from the same population	ANOVA	GST dynamics (Objective 4, pg. 9)
Which sample sites exhibit similar populations?	Determining if individual pairings of sample sites have similar population variances	Fisher's LSD test	GST dynamics (Objective 4, pg. 9)
Which climate parameters have an influence on soil temperatures?	Identify relationships amongst climate parameters and GST	Pearson's product-moment coefficient of linear correlation	GST dynamics (Objective 4, pg. 9)
Are individual rock properties similar for all samples?	Determining if clast properties (porosity, microporosity, water absorption capability, saturation coefficient, percentage saturation) for all clasts are drawn from the same population	ANOVA	Rock properties and moisture uptake (Objective 5, pg. 9)
Does topography and degree of exposure influence soil characteristics?	Determining if particle size fractions for all sample sites are drawn from the same population	ANOVA	Particle size analysis (Objective 6, pg. 9)
Are soil samples similar?	Determining if particle size fractions for two-sample sets are drawn from the same population	Kolmogorov-Smirnov	Particle size analysis (Objective 6, pg. 9)

3.3.2.1 Blockfield survey

Observations on orientation of clasts (top orientations as well as a-axis orientations) were divided into nine classes of 20° each for a half-circle of 180°. A half-circle was used due to the non-directional and circular pattern of orientation (Doornkamp and King, 1971). The Tukey Chi-square test was applied to determine the randomness of observed orientation as well as dip. A random orientation indicates *in situ* weathering and may be used as a proxy for the autochthonous nature of a deposit. The hypotheses for the Tukey Chi-square test are listed below.

H_0 = *the observed and expected distributions are similar and can be considered part of the same population,* i.e. *orientation for clasts is random across the blockfield and shows no preferred pattern*
H_a = *orientation for clasts is ordered across the blockfield and a preferred orientation is observable*

Preferred orientation of clasts (if present) was determined using the von Mises distribution. A rose diagram of clast orientation and top face dip was drawn, as was the backward sighting of slope for each transect.

3.3.2.2 Clast characterisation

Clast characteristics were calculated for all 140 random samples as well as the 120 survey samples (n = 260). This included the dip of the various faces, the plane of the top aspect (ab, ac, bc) and the orientation (true bearing) of the top aspect. The shape of a clast is dependent on its original shape, its physical and chemical properties and the type and extent of weathering it has been exposed to (Briggs, 1977a). Its shape can, therefore, give an indication of weathering the clast has undergone. In glacial environments clasts may exhibit both rounding and angularity, due to the interaction of the various processes (attrition, grinding, splitting, chipping) (Briggs, 1977a). A Zingg diagram was drawn to determine the shape index of clasts and to determine the overall sample set (Doornkamp and King, 1971; Briggs, 1977a). The diagram is a simple means of grouping clast shape into four categories (spheres, discs, rods, and blades), based on ratios of clast axes. The b/a axis ratio is equivalent to the y-coordinate; the c/b axis ratio equates to the x-coordinate (Forbes, 2007). The Zingg diagram represents nominal data (Doornkamp and King, 1971), restricting statistical analyses. However, this diagram indicates the three dimensional shape, which is closely related to the structure of the material (Briggs, 1977a). Glacial debris generally has a low roundness index and varying flatness indices. The Krumbein Sphericity Index, an indication of the three-dimensional shape, was calculated to determine the sphericity of each sample. Sphericity refers to the ratio of the surface of the clast to that of an inscribed sphere (Briggs, 1977a). A value of one reflects that of a true sphere and most sedimentary particles have an index between 0.3 and 0.9. Krumbein's Sphericity Index

yields results on a continuous interval scale and is suited for a wide range of statistical analyses (Briggs, 1977a). The Cailleux Flatness Index was determined for each sample to determine the relative flatness of each sample to each other (Briggs, 1977a): the higher the flatness index, the flatter the sample. The minimum value of 100 reflects the index of a cube: a perfectly equi-dimensional particle. Bivariate scattergrams comparing sphericity and flatness were also generated. Furthermore, the mean size (diameter) of each sample was calculated (Briggs, 1977a). Equations employed for calculations may be viewed in Table 7.

Table 7: Equations used for rock property analyses (Doornkamp and King, 1971; Briggs, 1977a).

Parameter/Attribute	Equation
Sphere (equi-axial/spheroidal)	b/a > 0.67; c/b > 0.67
Disc (oblate/discoidal)	b/a > 0.67; c/b < 0.67
Rod (prolate/rod-shaped)	b/a < 0.67; c/b > 0.67
Blade (triaxial/bladed)	b/a < 0.67; c/b < 0.67
Mean Sample Diameter	$\frac{(a+b+c)}{3}$
Cailleux Flatness Index	$F = \left(\frac{(a+b)}{2c}\right) * 100$
Krumbein Sphericity Index	$\psi = \sqrt[3]{\frac{bc}{a^2}}$

Furthermore, totals were calculated and grouped per aspect for lichen presence and whether or not lichen was deemed sheltered. Percentages were calculated in terms of lichen presence for each aspect. Additionally, the percentage of sheltered lichen was calculated. Similar calculations were carried out for pitting, flaking and the roughest observable face, whether or not the clast was block, ice or both block and ice supported, as well as snow cover.

3.3.2.3 Rock hardness: Schmidt Hammer and Equotip methods

Statistical analyses used a method adapted from Ericson (2004). Rock hardness values were evaluated for each aspect to determine possible aspect control on weathering across the study site. The ISRM (1978 in Goudie, 2006), Matthews and Shakesby (1984 in Goudie, 2006), Katz *et al.* (2000) as well as Sumner *et al.* (2002) all suggest discarding some (predominantly low values) of the recorded *R*-values before conducting statistical analyses. However, studies (*e.g.* Ericson, 2004) show that using all *R*-values yields the most accurate results. Similarly, Niedzielskie *et al.* (2009) and Aoki and Matsukura (2007) have indicated that no readings should be discarded. This is due to low and high values reflecting the heterogeneity of the surface under investigation. Different rock forming minerals enhance granular heterogeneity (Aydin, 2008) and extreme values don't necessarily significantly alter the recorded mean (Ericson, 2004). Rather, these values are a reflection of the weathered rock surface

(Gupta *et al.*, 2009) and are often present in SH and Equotip readings (Niedzielskie *et al.*, 2009). Aoki and Matsukura (2007) propose to take the mean of all recorded values for statistical analyses, an approach adapted by Mol and Viles (2012) for Equotip values. Niedzielskie *et al.* (2009) suggest using the interquartile distance (one half of the distance between 40% and 60% quartiles) when conducting analyses. However, abnormally low values occur due to incorrect placement of the plunger or the plunger being placed on loose grains. Abnormally high values may be due to the plunger impacting on grains such as quartz, which may only occur selectively across the surface (Ericson, 2004). As such, the removal of outliers using standardised residuals (a method appropriate for statistical analyses) was employed for the purpose of this project. The statistical mean, median and *s* were calculated for SH and Equotip readings. This was done for each clast aspect individually (five aspects per clast,) as well as the total aspect measurements (data points for all five aspects in total) (Table 8).

Table 8: The number of sample points for the SH and Equotip are indicated, grouped per clast aspect. Total number of sample points is also indicated.

Aspect	**Number of Aspects**	**Number of Sample Points per Aspect**	**Number of Aspects**	**Number of Sample Points per Aspect**
North	128	1 383	151	3 592
East	134	1 410	158	3 694
South	131	1 462	166	4 040
West	127	1 359	146	3 200
Top	140	1 411	200	4 918
Total	**660**	**7 025**	**821**	**19 444**

The shape of the distribution was determined for each clast aspect individually, as well as for the aspects as a whole using the method described in Descriptive statistics (pg. 59). Calculations on total SH as well as Equotip sample points showed near symmetrical distributions per aspect. Calculations on SH and Equotip data points per clast per aspect showed an overall symmetric distribution. Consequently, a normal distribution was assumed for data collected using the SH and Equotip.

Outliers were removed using the method described by Williams *et al.* (2006) and described in Statistical Methods (pg. 59). Any values outside of two *z*-scores were removed from the data set. This was done until all values fell within two *s* of the mean. In order to use both SH and Equotip readings for determining aspect control, the similarity of their populations had to be determined. Sample variances for SH and Equotip values were calculated to correctly identify the denominator and nominator for determining the *F* test statistic. The *F*-test was used to test for sample variances at a confidence coefficient of 0.95 and $\alpha = 0.05$ ($p < 0.05$). In the event the data sets had the same variances, H_0 was accepted. The hypotheses for the *F*-test are listed on the following page.

H_0 = *SH and Equotip populations have the same variances*

H_a = *SH and Equotip variances are not the same*

Subsequently, the *t*-test was used to compare SH and Equotip readings at a confidence coefficient of 0.95 and $\alpha = 0.05$ ($p < 0.05$). This version of the *t*-test (variances assumed to be the same) does not require the number of sample points to be the same for all populations ($n_1 = n_2 = \ldots = n_i$). In the event the data sets were not comparable, H_0 was rejected. The hypotheses for the *t*-test are listed below.

H_0 = *SH and Equotip measurements are comparable to each other,* i.e. $\mu_1 = \mu_2 = \ldots = \mu_i$

H_a = *SH and Equotip measurements are drawn from different populations and are not comparable to each other,* i.e. $\mu_1 \neq \mu_2 \neq \ldots \neq \mu_i$

In addition, ANOVA was conducted on the data sets. Single factor ANOVA ($\alpha = 0.05$, $p < 0.05$) was calculated on rock hardness values to determine whether or not aspects belonged to different populations (Ericson, 2004; Viles *et al.*, 2011). Single factor ANOVA was selected as the preferred analysis method as only a single factor (aspect) was being investigated. Other possible factors such as geology and time of exposure were assumed to be similar across the blockfield. Lichen on the blockfield is found to prefer sheltered locations on clasts. These include flaked-off surfaces, joints, cracks or weathering pits. See CHAPTER 3: Materials and Methods, Field Methods (pg. 34) for a discussion on this. Furthermore, flaking and pitting occur as a result of weathering processes. Lichen, pitting and flake data were, therefore, used to support ANOVA analyses of *R*- and L-values. ANOVA was conducted for lichen presence per aspect, flaking, pitting as well as the roughest observable face per clast. The rejection of H_0 indicated aspect control on weathering for the study site. The hypotheses for ANOVA are listed below.

H_0 = *mean rock hardness rebound values/lichen presence/flaking/weathering pitting/roughest observable clast face are similar for all aspects*

H_a = *mean rock hardness rebound values/lichen presence/flaking//weathering pitting/roughest observable clast face is different for all aspects*

Aspect was identified as the factor and rock hardness/lichen presence/flaking/weathering pitting/roughest observable clast face, all indicators of weathering, as the response variables. For the purpose of the study there were five treatments. These were the north-, east-, south- west-and top-facing sides of clasts. For the instances when H_0 of ANOVA was rejected, Fisher's LSD test was run

to determine which population variances were different. The hypotheses for Fisher's LSD are listed below.

H_0 = *the two population variances are equal,* i.e. $\mu_1 = \mu_2$
H_a = *the two population variances are not equal,* i.e. $\mu_1 \neq \mu_2$

3.3.2.4 Near-surface ground temperature dynamics

GST and moisture regimes were recorded using iButton thermochrons and a Decagon EC5 soil moisture sensor. These data were compared to climate data (dominant wind direction, wind speed, pressure, humidity and ambient temperatures) for the same period. Outliers were removed from iButtons and climate data using *z*-scores after computing measure of skewness, median and mean for each data series (see Descriptive statistics, pg. 59). Invalid values such as negative values (observed for pressure and humidity) and null or missing values were excluded when conducting analyses. The mean, median, variance and *s* were computed for each series individually, as well as for the global data set. Statistical inference (*r*; linear regression) was used to identify correlations between ground and climate data (see Statistical inference, pg. 60) for each individual data series as well as the global data set. In addition, linear regression was used to determine the role/importance of individual climate parameters.

Simpsons' Paradox proposes that the subset of a data set may produce opposite results compared to analyses done on the entire data set (Miller, 2012). GIS and spatial interpolation may, therefore, yield results on the spatial scale that would have gone unnoticed in classical statistics. Accordingly, collected data were investigated with topographical control in mind. Topography has been shown to exert an influence on, for example, crop yield (Atkinson, 1999) and may influence soil temperature across the blockfield. Topographic effects, therefore, influence local climate (Church, 2010) and may have a modifying effect (Weinert, 1980). If topographic control can be excluded for the study site, data from all sample sites should be part of the same population. Accordingly, ANOVA was calculated to determine whether or not the various sample locations represented the same population. Single factor ANOVA was selected as the preferred analysis method as only a single factor was being investigated (sample location as a proxy for topography). The rejection of H_0 indicated that populations are dissimilar; suggesting other factors such as topography might play a role in determining soil temperature regimes. The hypotheses for ANOVA are listed below.

H_0 = *ground temperature values are similar for all sample points*
H_a = *ground temperature values vary across the nunatak*

Sample location was identified as the factor and soil temperature as the response variable. For the purpose of the study there were six treatments for 2010/11 and 16 treatments for 2011/12. These were the various sample locations. For the instances when H_0 of ANOVA was rejected, Fisher's LSD test was run to determine which population variances were different or similar. The hypotheses for Fisher's LSD are listed below.

H_0 = *the two population variances are equal,* i.e. $\mu_1 = \mu_2$
H_a = *the two population variances are not equal,* i.e. $\mu_1 \neq \mu_2$

Furthermore, data were spatially interpolated in GIS across the study site in order to identify topographical control on the observed values. Please refer to Interpolation and geostatistical data analyses (pg. 72) on an in-depth description of these methods.

3.3.2.5 Rock properties and Moisture Uptake

Data collected during laboratory analyses were used to determine rock moisture content (percentage dry mass and percentage saturation), P, WA, S, and M. Individual clast properties were compared to each other and to the rock weights recorded in the field. This was done to identify noticeable changes in water absorption related to the environmental settings the clasts were placed in. Please refer to Table 9 for the list of equations used to calculate rock properties.

Table 9: List of equations used during rock properties analyses (Cooke, 1979).

Parameter/Attribute	**Equation**
Percentage dry mass	$\frac{(W_5-W_0)}{(W_0)} * 100$
Percentage saturation	$\frac{(W_5-W_0)}{(W_3-W_0)} * 100$
P (Porosity)	$\frac{(W_2-W_0)}{(W_2-W_1)} * 100$
WA (Water absorption capacity)	$\frac{(W_3-W_0)}{(W_2-W_1)} * 100$
S (Saturation coefficient)	$\frac{(W_3-W_0)}{(W_2-W_0)}$
M (Microporosity)	$\frac{(W_4-W_0)}{(W_2-W_0)} * 100$

The calculated rock properties per grouping were statistically compared to each other using ANOVA to determine the comparability of samples within each group. Statistically different populations would

have affected field observation and these samples had to be excluded from the study. The hypotheses for ANOVA are listed below. The individual rock properties (P, M, WA, S or % saturation) were the factors and there were five treatments, representing the five groupings.

H_0 = samples are similar for P/M/WA/S/% saturation and can be used comparatively
H_a = samples represent different populations and should be excluded from the study

Field data were converted to percentage weight gain or loss per sample, averages taken for samples within each grouping and a linear graph drawn of these. Weather averages on wind speed, ambient temperature, relative humidity and pressure were calculated to allow for an evaluation of clast percentage weight gain or loss to external parameters. ANOVA was conducted on sample series within each grouping, as well as on the five separate data series to determine if they represented similar populations (refer to Statistical inference, pg. 60). ANOVA was calculated for samples within each group to ensure sample observations were comparable. Single factor ANOVA was selected as the preferred analysis method as only a single factor was being investigated (sample location). Due to the close proximity of sample locations, other possible factors such as geology, time of exposure and climate parameter were assumed to be similar. The rejection of H_0 indicated that moisture susceptibility of clasts was impacted by the different environmental settings. The hypotheses for ANOVA are listed below.

H_0 = moisture uptake is similar for all clasts for all environmental settings
H_a = environmental setting does influence moisture uptake of clasts

Sample location was identified as the factor and rock weight, as an indicator of moisture uptake, the response variable. For the purpose of the study there were four treatments for ANOVA calculated within each grouping. ANOVA calculated for all groups required five treatments. These were the different environmental locations of clasts (clasts placed on ice; clasts placed on top of other rock; clasts placed on soil; clasts placed on snow and clasts buried in snow). Please refer to Rock Properties and Moisture Uptake (pg. 48) for a detailed description of these. Additionally, data series were compared to laboratory data on rock properties in order to draw conclusions on the moisture-absorption capacity of rocks within each separate setting.

3.3.2.6 Particle size analysis

Particle size analysis, fine fraction (fine earth fraction) analysis as well as the samples' textural classes were determined. For particle size analyses the percentage dry mass for each class was

calculated in terms of the total mass of the sample, followed by plotting the values on a bar graph. In addition, the cumulative percentage (coarse to fine) of each sieve class was determined and plotted, as was the soil texture class per sample according to the triangular plot of particle size data (Briggs, 1977a). Refer to Appendix B: Statistical Descriptions, Ranges and Classes (pg. 166), Table 73 and Figure 76 for a list of sediment size grades and an example of a triangular plot respectively. The Phi (ø) scale also precluded the need for normalising data (Briggs, 1977a).

Particle sizes follow a lognormal distribution (Briggs 1977a; Till, 1985). The Phi (ø) median (average particle size) and Phi (ø) mean (arithmetic average particle size) were calculated to determine the central tendency of the distribution (Briggs, 1977a). Phi (ø) skewness, kurtosis and sorting are used to define the scatter or non-normal shape of a distribution (Briggs, 1977a), and were calculated for each sample. The Phi (ø) skewness is used to determine a coarse tail (negative skewness) or a fine tail (positive skewness). Phi (ø) sorting is an indication of the dispersion, *i.e. s* of the distribution (Briggs, 1977a). Well-sorted soils tend to have low *s* values. The sorting value may indicate the presence of geomorphic processes (that contribute to sorting). Glacial deposits, for example, are poorly sorted and will have a high sorting value, whereas fluvial sediment, which is normally well sorted, will have a low sorting value (Briggs, 1977a). Well-sorted sediment will have grain sizes in the fine sand range (Alsharhan and El-Sammak, 2004). Consequently, less well-sorted sediment will have coarser particles. This relationship is easily identified using graphical discrimination analyses, such as bivariate scatterplots (Briggs, 1977a; Alsharhan and El-Sammak, 2004; Onuigbo *et al.*, 2012). These plots were performed for Phi (ø) kurtosis- Phi (ø) skewness and Phi (ø) sorting- Phi (ø) mean. Bivariate scatterplots of kurtosis vs. skewness, by allowing for the identification of the shape of the distribution, are powerful tools for identifying the genesis of particles (Alsharhan and El-Sammak, 2004; Onuigbo *et al.*, 2012). Phi (ø) kurtosis measures the peakedness of a distribution compared to the Gaussian distribution. Poorly sorted sediment tends to be platykurtic (Briggs, 1977a). Please refer to Appendix B: Statistical Descriptions, Ranges and Classes, Table 74 and Table 75 (pg. 167) for a description of classes and ranges used. Equations used to achieve each point are given in Table 10.

Table 10: Equations used during particle size analyses (Briggs, 1977a).

Parameter/Attribute	Equation
Phi (ϕ) median	$\phi 50$
Phi (ϕ) mean	$\overline{\phi} = \frac{\phi 75 + \phi 50 + \phi 25}{3}$
Phi (ϕ) skewness	$\frac{(\phi 84 - \phi 50)}{(\phi 84 - \phi 16)} - \frac{(\phi 50 - \phi 10)}{(\phi 90 - \phi 10)}$
Phi (ϕ) sorting	$\frac{(\phi 90 - \phi 80 — \phi 70 - \phi 30 - \phi 20 - \phi 10)}{5.3}$
Phi (ϕ) kurtosis	$\frac{(\phi 90 - \phi 10)}{1.9\,(\phi 75 - \phi 25)}$

A SediGraph 5100 was used to conduct fine fraction analyses. Textural analyses determine the percentage of coarse silt, fine and medium silt, clay as well as sand per sample. Subsequently, the Kolmogorov-Smirnov test was conducted to determine if soil samples differed statistically from each other. This test was utilised as data were already in the required format, *i.e.* cumulative percentages (Till, 1985). Hypotheses for the test are given below.

H_0 = *particle size fractions are similar for two sample locations*
H_a = *particle size fractions are different for two sample locations*

3.3.3 Geostatistical Methods and GIS

GIS were used to create, modify, analyse and map data. This comprised spatial analysis, geostatistical, digitising as well as mapping techniques. The GIS process may be divided into Data preparation (see below), Interpolation and geostatistical data analyses (pg. 72) and Mapping (pg. 75). Each of these is described in greater detail in the respective sections below. Models created in Model Builder™ of ArcGIS are illustrated in Appendix D: GIS Models (pg. 171).

3.3.3.1 Data preparation

The majority of data were captured during fieldwork. NGI and ADD (Antarctic Digital Database) provided additional data such as aerial imagery and vector data. Raw data were captured in Microsoft® Excel spreadsheets and prepared for importing into the Esri ArcGIS suite of products, in particular ArcCatalog® and ArcMap®. ArcMap® was used exclusively for analysis and mapping purposes, whereas ArcCatalog® was used to prepare geographical data for analyses. All data were assigned the WGS84 datum and projected into a custom projection (Gauss Conformal) using the Transverse Mercator planar coordinate system (central meridian 3°W). This projection was selected based on the high accuracy within its 2° East to West extent: it preserves shape, while minimising distance and area distortion.

Dimensions for the blockfield located on the Northern Buttress of the Vesleskarvet Nunataks were calculated using GIS. The extent of the blockfield, as well as snow cover was delineated (digitised) using aerial imagery. Digitised data were assigned the projection described above. To ensure maximum accuracy in the digitising process, features were mapped at a constant scale of 1:500. All sample points were imported into ArcMap®, displayed using their respective X (longitude) and Y (latitude) coordinates, assigned the projection described above and displayed on the map. These points were used as input data to subsequent geostatistical and interpolation methods. In addition to

displaying sample points, the distance of each point to other sample points was calculated. The handheld GPS had an accuracy of approximately three meters. Accordingly, when navigating to randomly generated sample points in the field, a three-meter accuracy applied to identifying samples. In order to ensure all samples were more than three meters apart (ensuring clasts were not sampled twice), sample points were used to create a feature class using the '*Points to Line'* tool. The output of this tool was a polyline feature class, where all points were connected in all possible combinations using a linear feature. This feature class was subsequently split using the '*Split Line at Vertices'* tool in order to determine individual straight-line distances between sample points. An aspect as well as slope surface was calculated for the study site. Please refer to Figure 78 and Figure 79 (pg. 171) for the GIS model used to calculate aspect and slope surfaces respectively. Furthermore, GIS were used to determine annual solar radiation received for the study site, as well as radiation received during the 2011/12 field season (6th of January to 3rd of February 2012). The appropriate GIS model is shown in Figure 80 (pg. 172). A DEM (Digital Elevation Model) was also determined for the study site (Figure 81, pg. 172). Height values for the DEM are expressed as MASL (Metres Above Sea Level).

3.3.3.2 Interpolation and geostatistical data analyses

When working with spatial data Griffith (2005) suggests the following: 1) compute a spatial autocorrelation index; 2) estimate an auto-model keeping regression analysis in mind and 3) inspect local spatial autocorrelation statistics. This involves analyses of the spatial data and requires trend analysis to be calculated for each data set. Depending on the result, an appropriate interpolation technique is applied to the data. Interpolation involves the creation of a continuous surface using point data as the input (Burrough, 2001). Geostatistical techniques are based on stochastic theory and allow for the modelling of dynamic processes (Burrough, 2001). These powerful techniques use statistical variation combined with spatial autocorrelation as a source of information, improving the prediction of unsampled points (Atkinson, 2001; Burrough, 2001). Spatial autocorrelation, in particular, improves the estimation of unknown points (Griffith, 2005). In addition, certain geostatistical techniques such as Universal Kriging allow for local variation and not simply global variation, further increasing the accuracy of predicted points (Miller, 2012). Objectives 2, 3 and 4 (pg. 9) required data to be spatially interpolated across the blockfield's surface. Before data could be interpolated ESDA was calculated for the specific parameters. Histograms, trend analyses and QQ plots were determined for mean *R*-values for the SH and Equotip as well as for evidence of flaking, pitting, the roughest observable face per clast and lichen presence. Histograms and QQ plots were used to determine the shape of the various distributions. This was done in addition to and to confirm results of classical statistical analyses, described in Descriptive statistics (pg. 59). The histogram provided a visual representation of the shape, median, mean, skewness and kurtosis of the data. The QQ plot compared

the cumulative distribution of the data to a theoretical model (normal distribution). If the data was plotted on a straight line it followed the theoretical distribution. The semi-variogram/covariance cloud tool plotted the empirical semi-variogram for paired sample locations on a graph and was used to determine the lag size to a data set. The empirical semi-variogram provides information on the spatial autocorrelation of the datasets that allows the user to subsequently fit the data to the correct empirical semi-variogram (Chang, 2012). Trend analysis was used to identify inherent trends to datasets. If no trend is apparent the projected trend line of the graph approximates a horizontal/flat line; if a trend exists the line is drawn with a curve (Chang, 2012).

Depending on the result of ESDA data were spatially interpolated using IDW (Inverse Distance Weighted) (no trend) and Kriging (inherent trend/bias) methods. IDW is a deterministic (exact) interpolation technique that estimates cell values in a raster from a set of sample points (Chang, 2012), for example mean *R*-values, using distance as the defining parameter. The further an input point is from the cell being calculated, the less influence or weight it has on the value of that cell. Calculated values are the average of nearby points and the search radius was set to variable (n = 12), ensuring the same number of input points was used for the calculation of each raster cell. The power *k* was set to two, as rate of change was set to be higher near sample points than further away (Chang, 2012). This interpolation technique was used for interpolating *R*- and L-values for all aspects (north-, east-, south-, west-, top-facing sides), since these data showed no inherent trend. The GIS model utilised to interpolate data using this technique is shown on Figure 82 (pg. 173). Clast support, lichen presence, observable pitting, flaking and the roughest face per clast were interpolated across the study site using this analysis method (please refer to Figure 83, pg. 173 for the applicable GIS model). Furthermore, flatness and sphericity indices were interpolated across the study site using IDW. In addition to spatially interpolating rock hardness values, zonal statistics were performed (Please refer to Figure 84, pg. 173 for the applicable GIS model). The reclassified slope, snow and annual solar radiation surfaces created for the study site were used as the defining boundaries for conducting zonal statistics. The zonal statistic function summarises the values of the rock hardness value raster within slope and snow zones, reporting the results as a table of statistics. This table was used to determine differences in rock hardness values per slope, snow and radiation zones, in order to identify possible control of these parameters (such as the amount of snow cover) to observed clast surface hardness values.

Kriging is a geostatistical interpolation method, which incorporates autocorrelation in its calculations. It uses the least squares regression predictor (variance-covariance matrix) and a non-stationary mean to predict unknown values (Atkinson, 2001). It incorporates both stochastic and deterministic

elements (Chang, 2012) and was used for spatially interpolating near-surface soil temperatures. Assuming topographic control on recorded soil temperatures, positive spatial autocorrelation should occur. Points on the associated Moran scatterplot will reflect a straight line, sloping from the lower left corner to the high right-hand corner. If the scatterplot reflects a random pattern, negligible spatial autocorrelation is present (Griffith, 2005). In addition to spatially interpolating data, Kriging creates a prediction surface as well as giving an indication of the accuracy of the prediction (the error of interpolation or Kriging error) (Burrough, 2001; Chang, 2012). Furthermore, it allows for determining propagation of error, making it a powerful geostatistical interpolation technique (Burrough, 2001). Assuming these errors are normally distributed, there is a 95.5 % probability that the value predicted is the actual real-world value, plus/minus two times the square root of the value ($\pm 2\sqrt{x}$). Kriging fits a mathematical model (variography) to the number of input points specified within the search radius (Burrough, 2001), to determine the predicted raster cell value. The semi-variogram measures the spatially correlated component, with samples furthest apart having large semi-variances (Chang, 2012). To conduct Kriging, a spherical semi-variogram was used to fit a curve to the empirical semi-variogram. The spherical model is used to model a continuous decrease in spatial dependence until a threshold is reached, where autocorrelation remains level (Chang, 2012). The nugget (semi-variance at a distance of zero), range (the distance at which the semi-variance threshold is reached) and sill (threshold level) are required as inputs to Kriging (Chang, 2012) and were determined using GIS. In addition, a variable search radius was used ensuring the same number of input points was used for the calculation of each raster cell. Finally, Universal Kriging was selected as the preferred method for interpolating near-surface temperature dynamics (Figure 87, pg. 176) as it assumes an inherent overriding trend (linear with quadratic drift) within the dataset. Furthermore, it uses a non-stationary mean and a covariant structure that varies with location (Atkinson, 2001; Miller, 2012). In addition to spatially interpolating near-surface soil temperature regimes, the *'Identity'* tool was used to determine possible spatial relationships between datasets. The *'Identity'* tool overlays attributes of specified layers at a specific location. This enables the identification of similarities in attributes for sample points. Figure 85 and Figure 86 (pgs. 174 and 175 respectively) show the GIS models used to run the tool for GST samples and soil samples respectively. Table 11 summarises the geographical statistical methods used for each of the study's relevant objectives.

Table 11: Inferential statistical methods employed during GIS analyses.

Investigation	Method	Description
Interpolating clast support for all samples across the study site	IDW	Clast characterisation (Objective 2, pg. 9)
Interpolating rock hardness for SH and Equotip mean rebound values across the study site for each aspect	IDW	Rock hardness (Objective 3, pg. 9)
Interpolating lichen presence, flaking, observable weathering	IDW	Rock hardness (Objective 3, pg. 9)

Investigation	Method	Description
pitting and the roughest observed face per aspect across the study site		
Determining zonal statistics in terms of rock hardness for slope, snow cover and annual solar radiation received	Zonal Statistics	Aspect control on weathering (Objective 3, pg. 9)
Determining the amount of annual solar radiation received per aspect for the study site	Solar Radiation	Aspect control on weathering (Objective 3, pg. 9)
Determining the amount of solar radiation received for the study site during January and February	Solar Radiation	GST dynamics (Objective 4, pg. 9)
Interpolating GST values across the study site	Kriging	GST dynamics (Objective 4, pg. 9)

3.3.3.3 Mapping

The majority of data were collected in the field. Additional data were obtained from NGI, ADD and SAWS. All data used the WGS84 datum and Transverse Mercator planar projection centred on 3°W. This projection was selected based its high accuracy within its 2° East to West extent, preserving shape, while minimising distance and area distortion. Maps were standardised in terms of symbology, colour use, font type, size and weight as well as features such as the north arrow (ESRI North 3) and scale bar. Each map included a graticule set to intervals of 15”. Maps provided the visual output of statistical analyses.

CHAPTER 4: Results and Discussion of Findings

System science is by definition complex and comprises the interaction of a variety of synergistic or competing processes (Church, 2010). Processes act over different spatial and time scales and obtaining data at these scales is often problematic (Murray *et al.*, 2009). Furthermore, identifying local variations and the boundary conditions within which processes act, spatial localisation, non-linear feedback and self-organisation of processes and landforms is challenging (Murray *et al.*, 2009). Although a holistic investigation of the study site was implemented, a reductionist approach was applied. Processes currently acting on the blockfield were investigated, as was the character of the blockfield. However, no attempt was made to identify historic processes and large-scale processes. Results are represented in graphical and tabular format.

4.1 Blockfield Survey

The blockfield is approximately 2 000 m in circumference, with an approximately area of 16 ha. A straight line drawn across its longest extent has a length of approximately 700 m, whereas its breadth is approximately 340 m. The blockfield is, therefore, longer than it is wide and follows a north-south orientation. Exact dimensions for the blockfield are given in Table 12 below.

Table 12: Dimension of the blockfield under investigation, following fieldwork and GIS analyses. Perimeter, length and breadth of the blockfield are measured in metres (m). Area is measures in either metres squared (m^2) or hectares (ha).

Perimeter	Length	Breadth	Area: Metres Squared	Area: Hectares
1 911	694	340	16 0214	16

Backward sightings of slope of each transect were drawn as linear graphs and may be seen in Figure 44 (pg. 77) and Figure 45 (pg. 78). Figure 44 shows percentage rise and fall, as well as the equivalent in degrees. A topographic interpretation of each transect is given in Figure 45. As can be seen in both figures, the northern portions of the three transects are initially higher, sloping down toward the middle and rising again toward the southern portion of each transect. The western region of the area covered by each transect is also higher, sloping downward toward the east (see Figure 45, pg. 78).

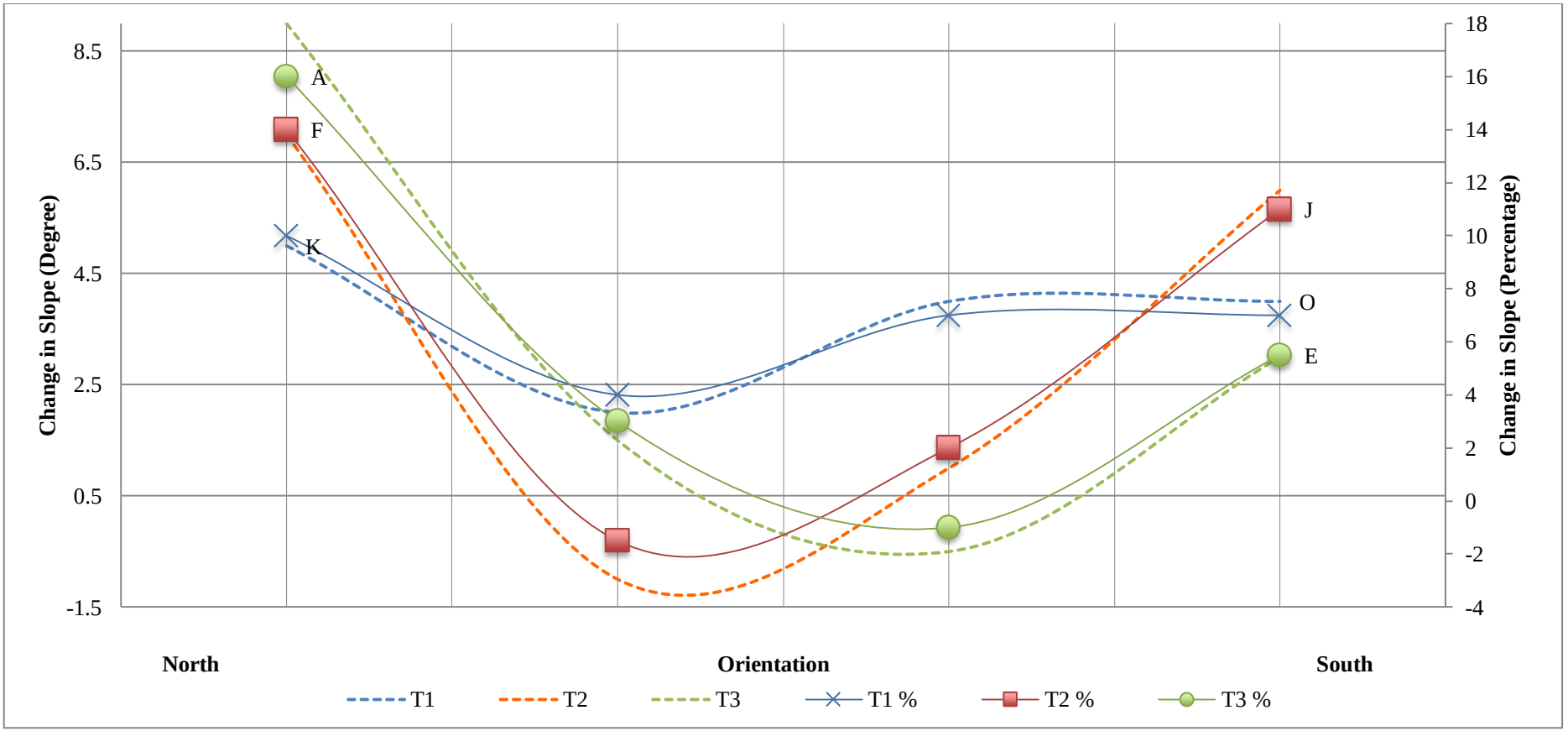

Figure 44: The slope of each transect (T1, T2, T3) is indicated in both percentage and degree rise or fall. Starting and end points of each transect are indicated by their corresponding letters. Slope, as a percentage, for T1 is indicated by cross hairs over the marker line; for T2 as squares overlying the marker line; and as circles for T3.

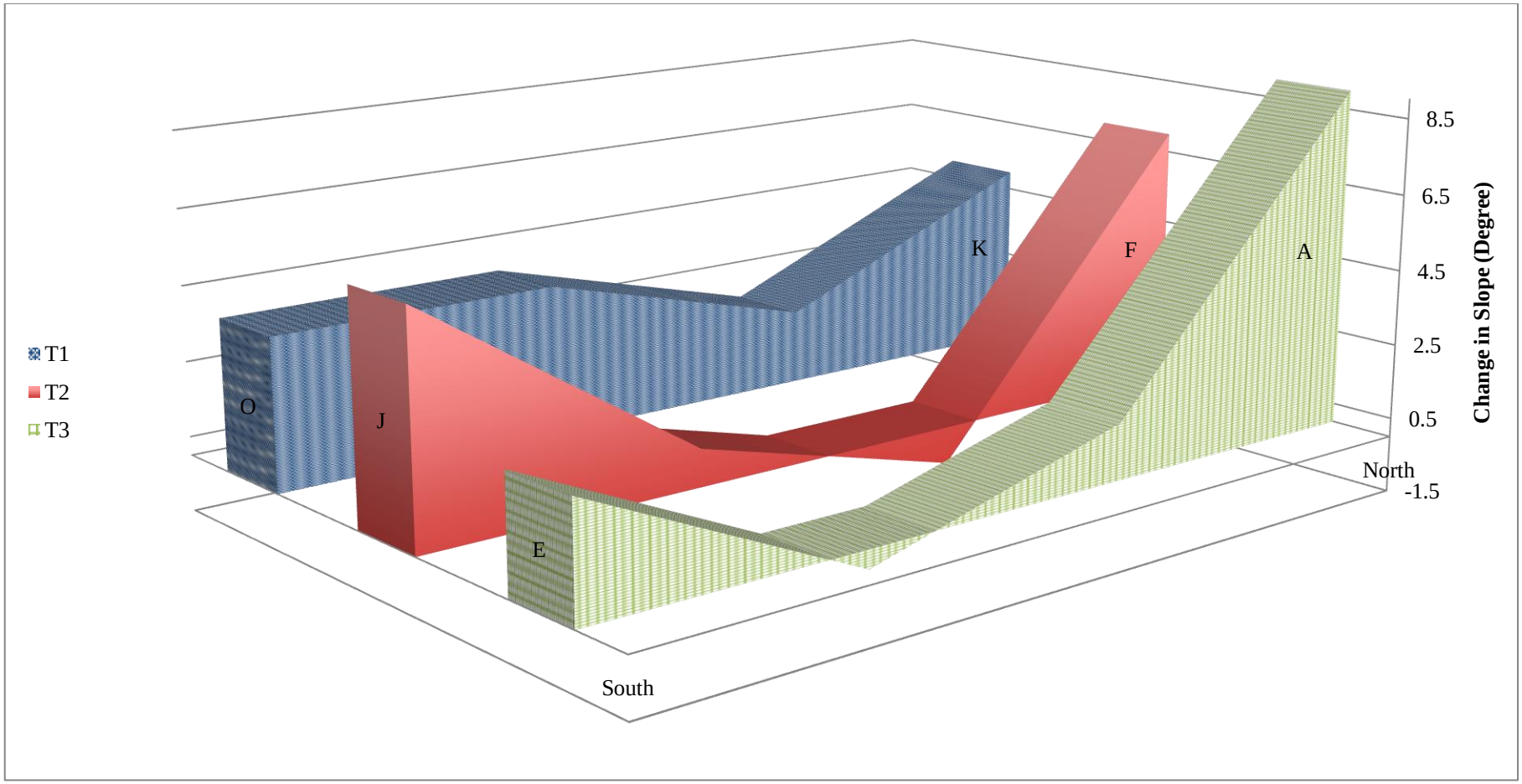

Figure 45: A topographic interpretation of each transect. Starting and end points of each transect are indicated by their corresponding letters.

Approximately 99.96% (15.96 ha) of the area of the blockfield occurs on a slope gradient of less than 25°. This measurement falls within the classification given by Rea (2007), where blockfields consist of regolith boulders on a gentle or undulating surface of less than 25°. A visual inspection of clasts suggests that clast shape is related to the underlying joint structure of the doleritic and dioritic intrusion. This is similar to the joint-determined blocks found in blockruns on the Falkland Islands (Hall, 2002). Clasts are predominantly (85.83%) supported by bedrock, with 12.50% supported by a combination of rock and ice and the remainder (1.67%) supported by ice (Table 13).

Table 13: The type of underlying support of clasts for the study site is indicated (n = 120). B indicates block support; I indicates ice support; and B/I indicates a combination of block and ice support.

Support	**B**	**I**	**B/I**
Count	103	2	15
% of Total	85.83	1.67	12.50

Soil, as already mentioned in Particle Size Analysis, (pg. 51) is scarce for the study site. Clasts are also not well disassociated from the underlying bedrock. The lack of soil and clast supported nature of the deposit points to a Type I matrix, where the openwork blocky deposit is supported by clasts and fines, if present, form a matrix at some depth below the surface (Ballantyne, 1998). However, the large amount of ice underlying clasts is of concern and its impact on the matrix, as well as its role in blockfield development, warrants further investigation. Please refer to CHAPTER 5: Considerations and Recommendations (pg. 149) for a discussion on this.

As discussed in Blockfield Survey (pg. 28), a random orientation of clasts suggests an autochthonous deposit. This may be determined by a statistical analysis of clast orientation and dip. The null and alternate hypotheses of the Tukey Chi-square are given below.

H_0 = *the observed and expected distributions are similar and can be considered part of the same population*, i.e. *orientation for clasts is random across the blockfield and shows no preferred pattern*

H_a = *orientation for clasts is ordered across the blockfield and a preferred orientation is observable*

A more detailed explanation of the Tukey Chi-square test and its application in the current context is given under Blockfield survey (Statistical Methods, pg. 63). Results of the Tukey Chi-square test for a-axes orientations as well as the top face orientations are presented in Table 14 (a-axis orientations, pg. 80) and Table 15 (top-facing side orientations, pg. 80) respectively. In both cases the values of 2.7 (a-axes) and 10.14 (top faces) of the test statistic (X^2) are below that of the critical value of 20.09 (p = 0.01). Even at $\alpha = 0.05$ ($X^2 = 15.51$), H_0 cannot be rejected, indicating that the orientation for clasts is random across the blockfield and no preferred pattern occurs. Consequently, at a confidence interval

of 0.99, the tests show that a random orientation of clasts for the study site is expected. A random orientation for glacially derived clasts has been observed (Doornkamp and King, 1971) and no preferred pattern is observable amongst the sample rocks for the study site. The lack of preferred orientation of clasts and clasts of the same mineralogy and geology overlying each other (Ballantyne, 1998; Hall, 2002), indicate an autochthonous deposit.

Table 14: Calculations for the Tukey Chi-square test on a-axis orientations for the study site.

Orientation Interval (°)	**Calculations** ($\sum \frac{(O-E)^2}{E}$)
0-20	0.13
21-40	0.03
41-60	0.03
61-80	0.03
81-100	1.01
101-120	0.01
121-140	0.41
141-160	0.21
161-180	0.83
X^2 (Test Statistic)	**2.70**
X^2 (Critical Value)	**20.09**
df = 8; p = 0.01; n = 120	

Table 15: Calculations for the Tukey Chi-square test for top-face orientations for the study site.

Orientation Interval (°)	**Calculations** ($\sum \frac{(O-E)^2}{E}$)
0-20	1.82
21-40	5.02
41-60	1.82
61-80	0.00
81-100	0.64
101-120	0.09
121-140	0.74
141-160	0.001
161-180	0.001
X^2 (Test Statistic)	**10.14**
X^2 (Critical Value)	**20.09**
df = 8; p = 0.01; n = 118	

Results of the Tukey Chi-square test on the dip of the top faces of clasts across the study site are shown in Table 16. The test statistic (X^2 = 67.93) exceeds the critical value of 13.28, yielding a rejection of H_0 at confidence interval of 0.99 (p = 0.01), indicating dip angles are not random for the study site. This preferred dip angle is related to the micro-topography of the blockfield, where clasts follow the change of relief of the surface.

Table 16: Calculations for the Tukey Chi-square test for the dip of top-facing sides across the study site.

Orientation Interval (°)	**Calculations** ($\sum \frac{(O-E)^2}{E}$)
0-10	12.04
11-20	26.86
21-30	1.54
31-40	12.95
41-50	14.53
X^2 (Test Statistic)	**67.93**
X^2 (Critical Value)	**13.28**
df = 8; p = 0.01; n = 109	

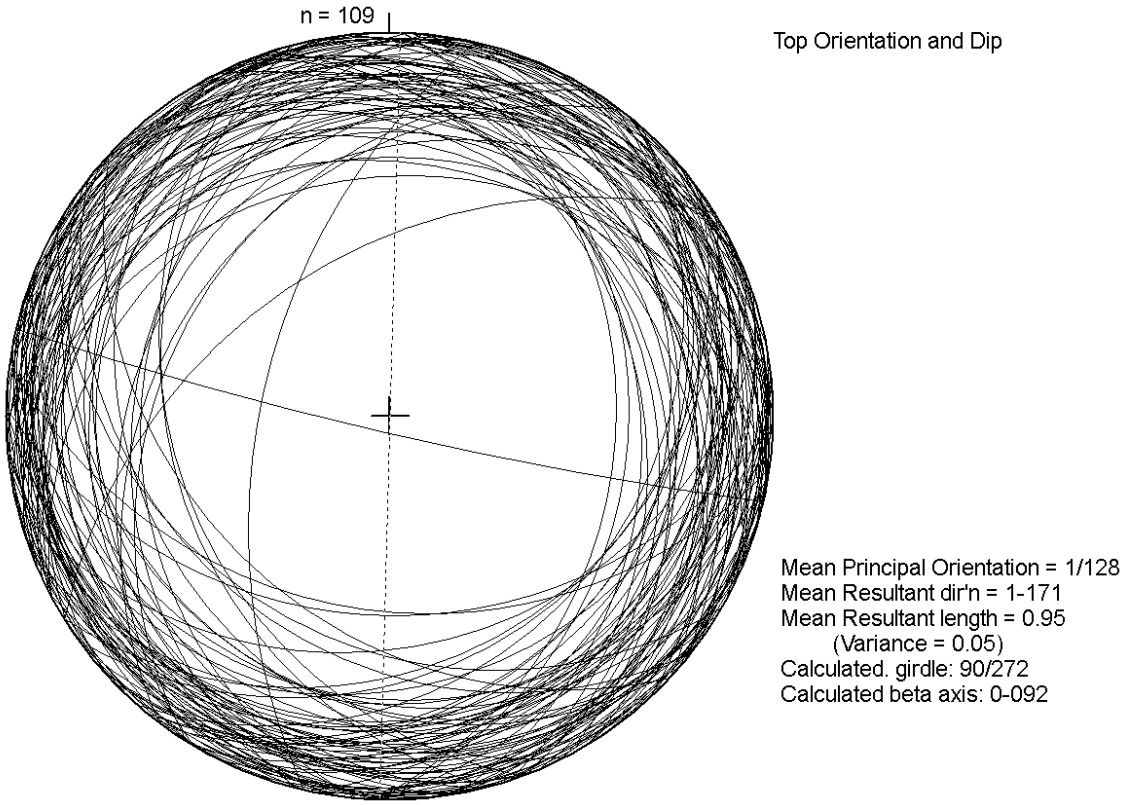

Figure 46: A stereographic projection of top-face orientations and dip (n = 109). An equal angle plot was used to draw the data.

An equal angle stereographic projection showing orientation of clasts (top faces) and their corresponding angle of inclination (dip) is shown in Figure 46. The figure shows that the majority of clasts have a shallow top facing aspect, with only a few steep dipping clasts observed. It is also clear from the image that there is no dominant orientation. This supports the argument that the blockfield is autochthonous, as an autochthonous blockfields should not have a predominant orientation observed amongst its clasts. Clasts having a top-facing dip of less than ten degrees are also predominantly (at 37%) found on level slopes (0-10°) (Table 17). A total of 58%, more than half of the samples, exhibit a top-face dip of less than 15° on slopes less than ten degrees. Similarly, clasts exhibiting a dip of 15-20° for their top-facing sides are found on slopes inclined between five and 15°. These values suggest that clast dip is affected by slope.

Table 17: Percentages calculated for observed clast dip vs. slope gradient. Both dip and slope gradient are measured in degrees (°).

	Slope			
Dip	**0-5**	**5-10**	**10-15**	**15-20**
0-5	8	6	1	1
5-10	10	13	4	1
10-15	12	9	2	0

	Slope			
Dip	**0-5**	**5-10**	**10-15**	**15-20**
15-20	0	4	4	0
20-25	0	0	0	0
> 25	7	11	6	0

Although orientation was determined random, von Mises distribution was nonetheless calculated to determine any modal orientation of clasts. Calculations for the von Mises distributions may be viewed in Table 18 (a-axis orientations) and Table 19 (top-facing side orientations) below. A comparison of values shows that both orientation parameters yield similar values, indicating a close relationship between a-axis and top-facing sides' orientations. This agrees with observations made in the field that a-axes often hold the same orientation as the top plane orientation of clasts. 32% of a-axes orientations were found to be the same to top-face orientations. Calculations for orientations of clasts for the study site show that the mean orientation vector has a direction of 83.68° (Table 18) for a-axes; and 90.00° for top faces (Table 19) respectively. This equates to an easterly direction. Values for *s* (mean angular deviation) show that approximately three quarters (¾) of the a-axes orientation angular measurements lie within an angle of 83.68°±76.84° (Table 18). Similarly, approximately seven tenths ($\frac{7}{10}$) of the top-faces orientation angular measurements lie within an angle of 90.00°±71.88° (Table 19).

Table 18: Results of von Mises distribution analysis on a-axes orientations for sample clasts.

Parameter	**Value**
$\bar{x}$	-0.10
$\bar{y}$	-0.01
r	0.10
$cos\bar{\theta}$	-0.99
$sin\bar{\theta}$	-0.11
$\mu_0\,(\bar{\theta})$	83.68
s	76.84
k	0.13
c	91.83
n	120

Table 19: Results of von Mises distribution analysis on top-face orientations for sample clasts.

Parameter	**Value**
$\bar{x}$	-0.21
$\bar{y}$	0.03
r	0.21
$cos\bar{\theta}$	-0.99
$sin\bar{\theta}$	0.12
$\mu_0\,(\bar{\theta})$	90.00
s	71.88
k	0.44
c	79.88
n	118

Coefficients of variation are 91.83% and 79.88% for a-axis and top-facing side orientations respectively. The high values for *c* and *s* for both orientation parameters indicate the large variability inherent in the data, further supporting the above conclusion that no preferred orientation exists for

clasts across the study site. These findings again suggest that the blockfield is autochthonous. Furthermore, a-axes show greater variability than top-face orientations, with the sample *s* of a-axes equalling approximately 92% of the sample mean. Von Mises distribution analyses also allow for the determination of the equation of the given distributions. These equations are given as Equation 7 and Equation 8.

Equation 7: Equation describing the distribution of clast a-axis orientations. The equation was determined using von Mises distribution analysis.

$$y_{a\ orientation} = \frac{1}{2\pi I_o(0{,}13)}^{0{,}13\cos(\theta - 1{,}46)}$$

Equation 8: Equation describing the distribution of clast top-face orientations. The equation was determined using von Mises distribution analysis.

$$y_{top\ orientation} = \frac{1}{2\pi I_o(0{,}44)}^{0{,}44\cos(\theta - 1{,}57)}$$

4.2 Clast Characterisation

Two hundred and sixty (n = 260) clasts were investigated for a variety of characteristics. These comprise identification of clast support, top-facing planes, shape indices, sphericity and flatness indices, clast mean diameter, lichen presence, pitting, flaking, roughest clast sides as well as a-axis and top-facing side orientations. Clasts were selected using random as well as systematic methods, as discussed in Clast Characterisation, (pg. 31). The handheld GPS used to navigate to randomly generated clast locations had an accuracy of three meters. GIS analyses (see Data preparation, pg. 72) showed that the smallest straight-line distance between clasts was 3.88 m. Consequently; the possibility of the same clast being sampled twice is excluded. Percentages of the type of support as well as the plane of top-facing sides are shown in Table 20. The majority of samples (75.38%) are supported by rock, with the minimum (10.77%) supported by a layer of ice. Approximately 14% (13.85%) of sample clasts are supported by a combination of ice and rock. The top-facing aspect is predominantly (86.54%) found to be the ab-plane, with less than 15% taken up by the ac-plane (11.15%) and bc-plane (2.31%). Consequently, less than 15% of the blocks are resting on their sides with the majority lying in a horizontal position (a- and b-axis parallel to the ground). Pie charts illustrating the type of support and dominant plane may be viewed in Appendix E: Pie Charts Accompanying Statistical Analyses of Clast Characterisation, Figure 88 and Figure 89 (pg. 177) respectively. Figure 47 (pg. 84) provides a view of the expected clast support across the study site.

Table 20: Percentages calculated for the matrix and support of clasts, as well as the plane of top-facing sides (n = 260).

Clast Support	**Block**	**Ice**	**Block/Ice**
Count	196	28	36
% of Total	75.38	10.77	13.85
Top Face Plane	**AB**	**AC**	**BC**
Count	225	29	6
% of Total	86.54	11.15	2.31

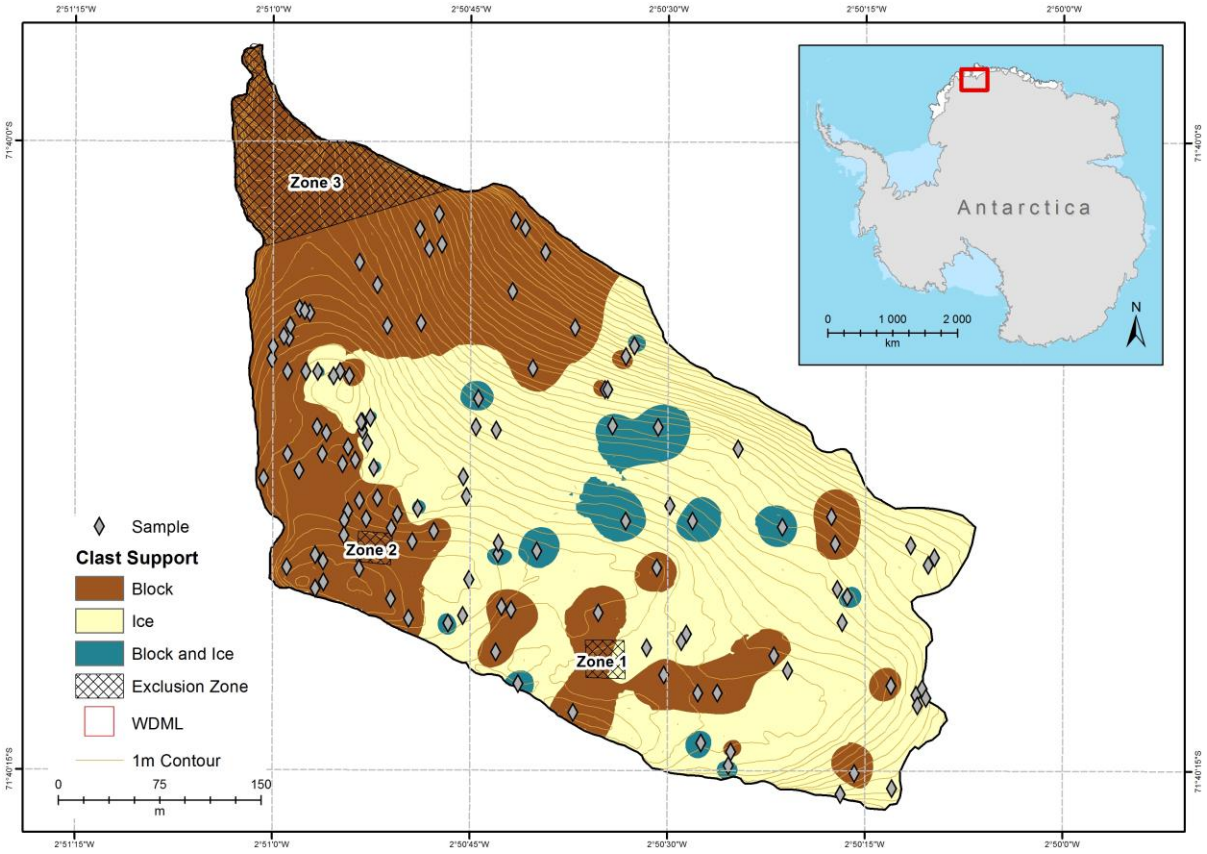

Figure 47: The type of support expected for clasts is shown (n = 118). Clasts supported by a combination of other blocks and ice occur predominantly toward the central and eastern section of the blockfield, whereas block supported clasts occur near Zones 2 and 3.

Clast shape depends on the original shape, inherent nature of the material (lithology, mineralogy, crystal habit, abrasional and fracture anisotropy), nature of weathering as well as nature of transport of the clasts. As discussed in Blockfields (pg. 10 onwards), block production is largely controlled by pre-existing joints and fractures of the parent material. Shape gives an indication of the source, transportation and deposition the particle or clast has undergone. Descriptive statistics calculated for b/a and c/b axes ratios using the total sample size of 260 (n = 260) are shown in Table 21 (pg. 85). The lowest c-axis/b-axis ratio is 0.264, with the highest value equalling one (1.000). The large range of 0.736 indicates high variability for this ratio. Similarly, the lowest b-axis/a-axis ratio equals 0.120 and the highest 0.987, also indicating high variability. The coefficients of variation for the two ratios (c-axis/b-axis; b-axis/a-axis) show similar values of approximately 30%, suggesting comparability (in terms of variability) for the two distributions. The b/c axes ratio shows a finely positively skewed distribution, indicating a tail (sub-population) toward the ratio of rods or spheres. The moderately negatively skewed distribution of the b/a axes ratio, in contrast, suggests a sub-population of blades or rods. Mean values calculated for the axes ratios equal 0.643 (b-axis/a-axis) and 0.667 (c-axis/b-axis). These ratios make the expected clast index for the study site that of rods.

Table 21: Descriptive statistics calculated for axes ratios of the Zingg classification.

Axes	Min	Max	Range	Mean	Median	Mode	Skew	*s*	*c*
b/a	0.264	1.000	0.736	0.643	0.635	0.727	0.139	0.172	26.709
c/b	0.120	0.987	0.867	0.639	0.667	0.500	-0.360	0.208	32.520

The Zingg diagram (Figure 48) shows that the most common form of clasts for the study site is that of rods (34.23%), followed by discs (27.31%) and blades (23.08%). Spheres take up the smallest proportion of 15.38%. Please refer to Table 22 for clast shape summations according to Zingg's classification.

Table 22: Percentage values for the four clasts shapes of the Zingg classification are indicated.

	Sphere	Disc	Rod	Blade
Count	40	71	89	60
% of Total	15.38	27.31	34.23	23.08

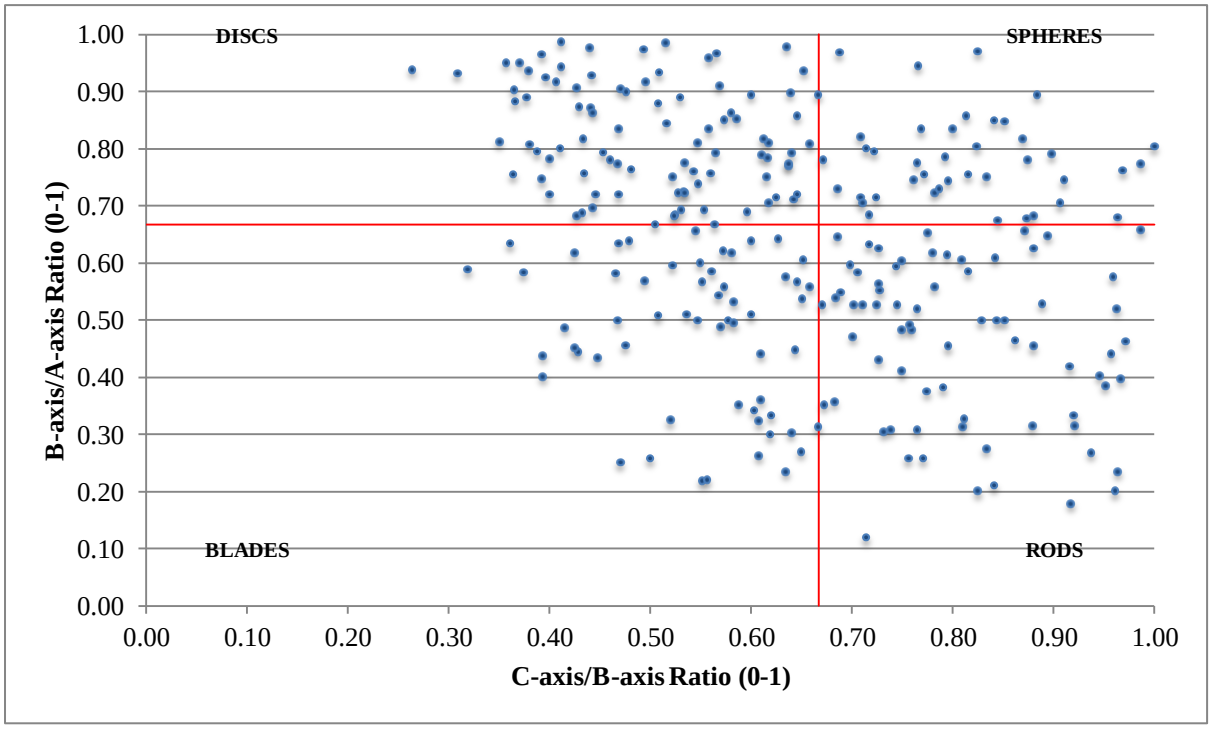

Figure 48: The Zingg diagram of sample clasts for the study site (n = 260).

Rods dominate the overall sample set. A discussed in Clast characterisation (pg. 63), the three-dimensional (3-D) shape of clasts is closely related to the structure of the source material (Briggs, 1977a). The predominant rod index indicates a jointed bedrock structure that yields clasts elongate and rectangular in nature. Furthermore, the small proportion of spherical shapes may be partly attributed to the lack of chemical weathering present for the study site. The visual assessment of the

angularity of clasts in the field gives a Powers' roundness index of 0.25-0.35. Clasts are, therefore, angular. In comparison to the blockfield under investigation, clasts for the blockfield described by Boelhouwers (2004) are rounded. This difference is ascribed to the flaking and granular disaggregation of the Basen blocks along conchoidal planes, distinct from grid-like cooling joints. However, other aspects of the two blockfields are similar. Both consist of dolerite, are autochthonous with *in situ* block production and occur in the same geographical setting. Angularity and rounding of clasts is, therefore, to a great extent controlled by the local lithology, mineralogy and geology.

The calculated Krumbein's Sphericity Index shows variable values (Table 23), with a minimum value of 0.38 and a maximum value of 0.93 recorded. Interestingly, this agrees with expected indices for sedimentary particles (Briggs, 1977a). The distribution for Krumbein's index approximates that of a normal distribution, as average (0.62) and median (0.61) sphericity values are almost identical and the skewness value (0.3) indicates a finely positively skewed distribution with a fine tail toward spherical clasts. The fairly large range of 0.55 indicates the variability of samples in terms of the sphericity index. A scatterplot of the sphericity values of all samples is shown in Figure 49 (pg. 87). The figure clearly shows the great range of indices observed.

Table 23: Descriptive statistics determined for clast sphericity and flatness indices of samples. A-, b-, c- axes as well as mean clast diameter are measured in centimetres (cm).

Sample	**A-axis**	**B-axis**	**C-axis**	**Sphericity Index**	**Flatness Index**
Min	19.00	11.00	3.00	0.38	9 000.00
Max	192.00	104.00	61.00	0.93	696 925.00
Range	173.00	93.00	58.00	0.55	687 925.00
Mean	62.07	37.84	23.72	0.62	133 663.22
Median	55.00	35.00	23.00	0.61	106 700.00
Mode	51.00	24.00	29.00	0.61	85 800.00
Skew	1.43	1.07	0.40	0.30	1.67
s	28.00	15.20	10.77	0.12	107 310.90
c	45.11	40.12	45.40	19.35	80.28

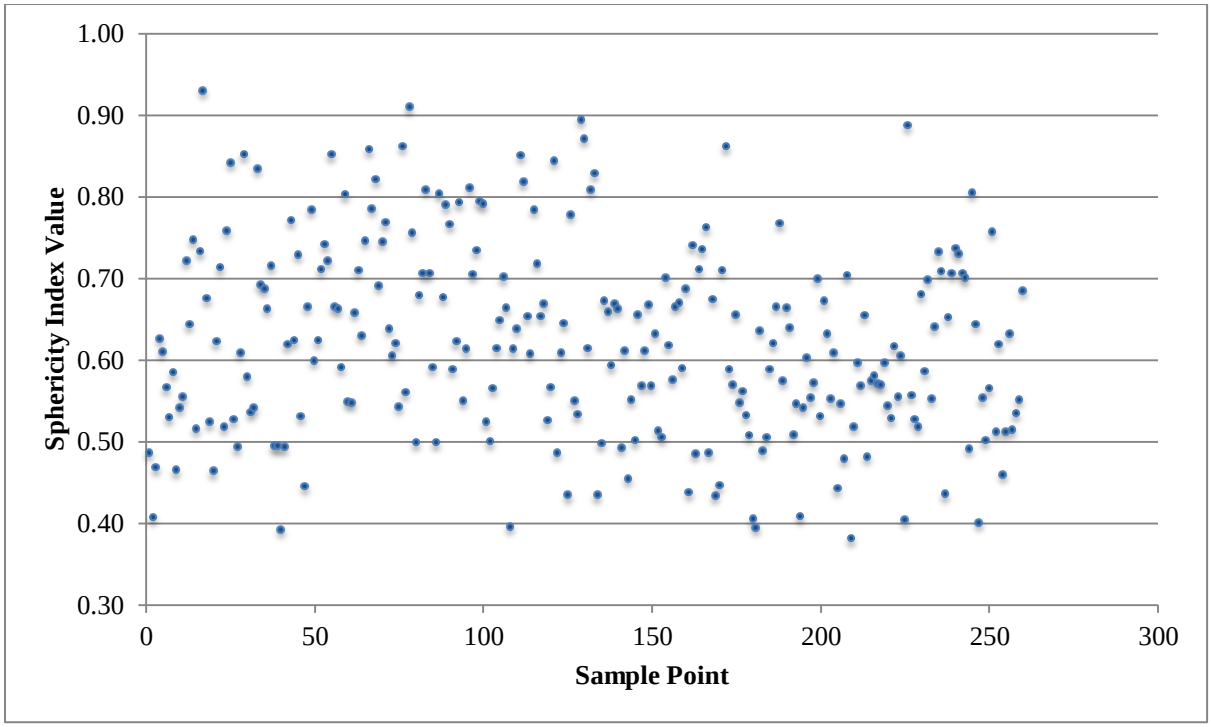

Figure 49: Krumbein's Sphericity Index for sample clasts (n = 260).

Values calculated for the Cailleux Flatness Index (Table 23, pg. 86) show variability in the dataset, as indicated by the high *s* of 107 310.90. The coefficient of variation (80.28%) shows that the sample *s* is approximately 80% of the sample mean. Calculated values support the argument discussed under Clast characterisation (pg. 63) that glacial debris generally exhibits varying Cailleux indices. Furthermore, the flatness index data distribution is highly positively skewed (skewness value of 1.67), corroborated by the dissimilar values for mean (133 663.22) and median (106 700.00) values. The skewness value also suggests a tail toward the non-cubic end of the index. Samples for the study site may be described as fairly flat, with the minimum recorded index of 9 000, well above the minimum flatness index value of 100. These values support results of the Zingg diagram, which shows a dominance of rods and discs (generally more flat than cubic). A scattergram of Caileux' fatness index is shown in Figure 50 (pg. 88). The range observed for the dataset is quite large (687 925) and this great variability on observed values is reflected in the figure. This supports the earlier statement of glacial debris having varying flatness indices. However, values are concentrated in the lower ranges (around the median and mean). Nevertheless, these values are still well above the minimum flatness value of 100.

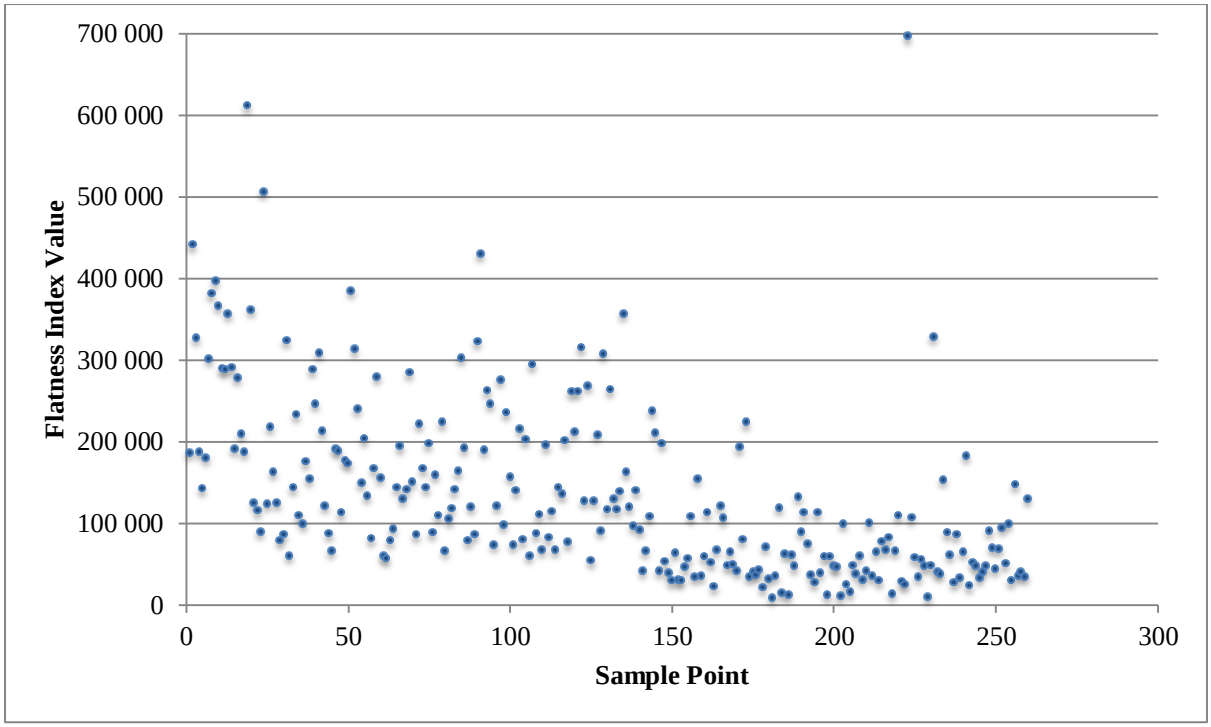

Figure 50: Cailleux Flatness Index for sample clasts (n = 260).

The bivariate scatterplot of Krumbein's Sphericity Index and Cailleux' Flatness Index is shown in Figure 51 (pg. 89). The R^2-statistic for the bivariate scatterplot approximates 40% (+0.37). This indicates that 37% (⅓) of the total variance of sphericity is explained by the linear relationship between sphericity and flatness indices. One dominant cluster (population) may be identified from the scatterplot. Consequently, all samples are classed into one main population, with a few outliers occurring. The main cluster (C1) occurs for the largest number of clasts (n = 227). This cluster ranges from 9 000 to approximately 400 000 for the flatness index and, in terms of the sphericity index, ranges from approximately 0.35 to approximately 0.90. There is also a concentration of samples within C1 falling within a fairly narrow flatness indices range of approximately 9 000-100 000. Sphericity values for these samples range from approximately 0.35 to 0.70. The concentration of samples within these ranges indicates that a large number of samples with low flatness indices have variable sphericity values. The first observable outlier (C2) comprises of the smallest number of clasts (n = 3) with a sphericity index of approximately 0.75 and a flatness index of approximately 500 000. These samples are, therefore, flatter compared to C1. The third class of outliers (C3; n = 5) exhibits the overall lowest sphericity values (least approximation of a sphere) with flatness indices between 0.50 and 0.60. These samples also have the highest flatness indices. Clasts exhibiting sphericity indices closest to that of a perfect sphere (1.000) all fall within C1.

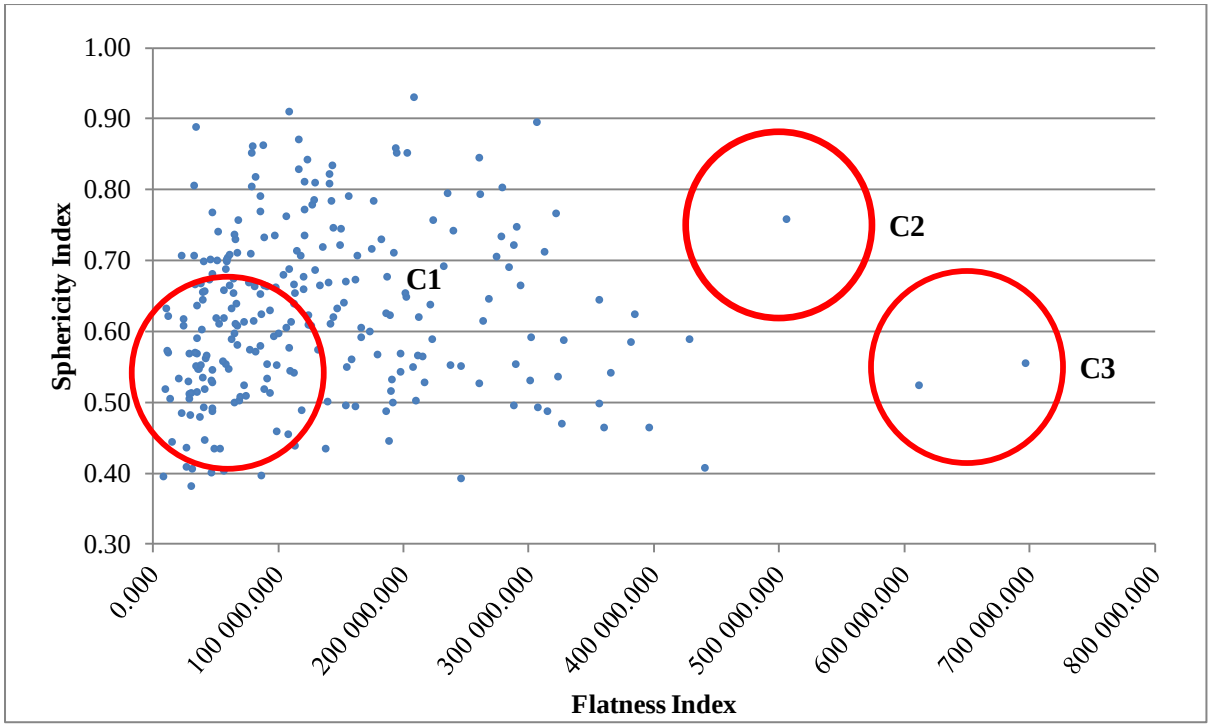

Figure 51: Bivariate scatterplot of Krumbein's Sphericity Index vs. Cailleux' Flatness Index (n = 260). The majority of samples cluster together (C1), with a few outliers observed (C2 and C3).

Table 24 shows that samples for C2 occur on even ground (slope < 6°) and only for the northern aspect. Members of C3 occur for even and gentle slopes (slope < 12°), for northern as well as eastern aspects. By far the majority of all samples (110) occur on even slopes (slope < °6) for the northern aspect. Only a few samples (6 out of 260) are found on slopes exceeding 12°, and none of these occur for the southern, western and top-facing aspects.

Table 24: Sample sub-populations (C1, C2, C3) grouped by aspect and slope gradient (°) (n = 235). The first value for slope and aspect combinations represents C1; a second value after the first semi-colon indicates C2; and a third value after the second semi-colon represents C3.

Aspect	**Slope**		
	0-6	6-12	12-18
North	103; 3; 2	50; 0; 2	4
East	29; 0; 1	12	2
South	20	6	0
West	0	0	0
Top	1	0	0

The high flatness indices combined with median sphericity values are indicated on Figure 52 (pg. 90). Low sphericity values (indicated by a yellow outline) overlie low flatness values. Clasts of sphericity indices between 055-0.60 as well as 0.60-0.65 take up a large portion of the area (indicated by blue and red outlines respectively). Samples closest to that of a cubic form, *i.e.* lowest sphericity indices

occur on the western extent of the blockfield with none occurring toward the eastern extent. Furthermore, clasts of sphericity indices between 0.70-0.75 occur scattered across the study site in isolated and small populations. The highest sphericity indices (0.75-0.91) occur for clasts in a small area on the eastern-most side of the blockfield. Flatness indices show that the most cubic samples occur in a north-south direction for two bands (the most western as well as in the extent approximate east of the central region) on the blockfield. The most flat samples occur in the approximate centre of the blockfield. Figure 52 shows discernible clustering for both sphericity as well as flatness indices.

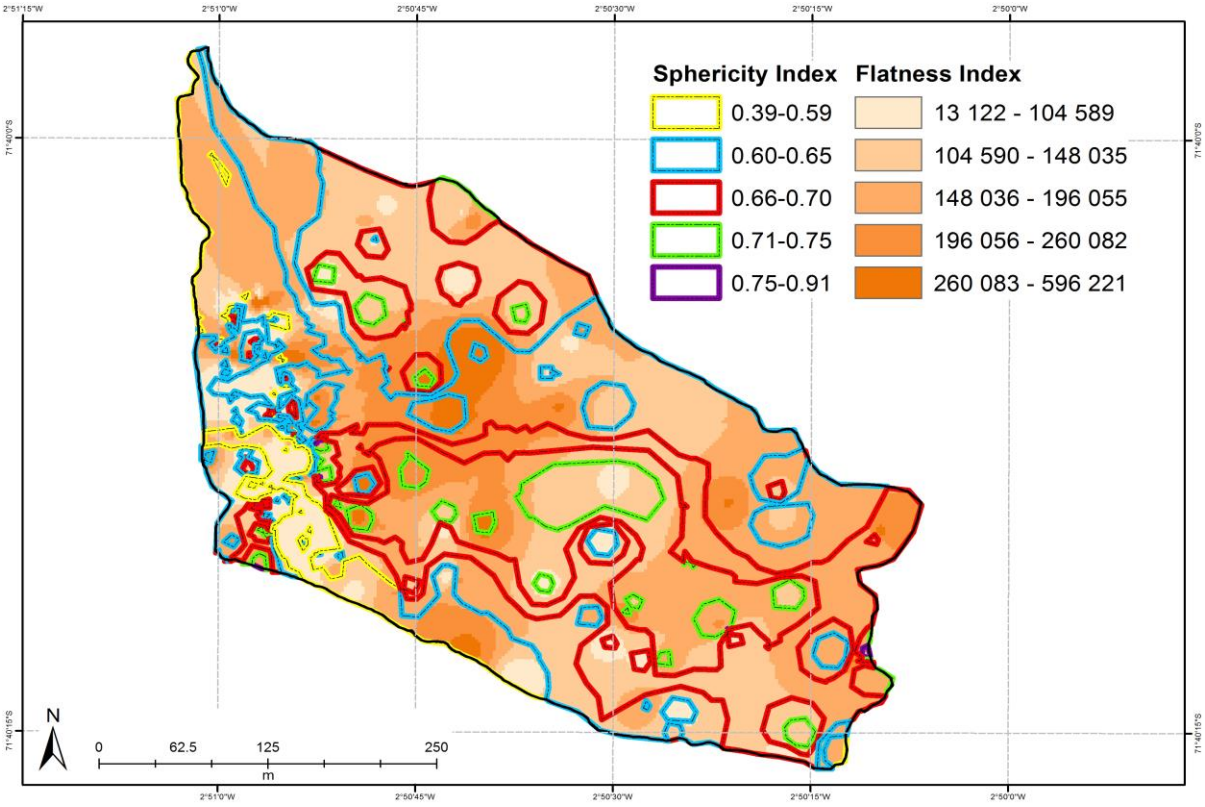

Figure 52: Cailleux' Flatness Index overlain with Krumbein's Sphericity Index. Darker (more intensely red) hues indicate higher flatness indices; lines of varying colours indicate sphericity values.

The mean diameter of clasts ranges from a minimum of 13 cm to a maximum of one meter (Table 25, pg. 91). The median clasts diameter is approximately 38 cm (37.67 cm). Mean diameter data indicates a skewed distribution, as mean (41.21 cm) and median (37.67 cm) are slightly dissimilar. Furthermore, the skewness value (0.97) indicates a positively skewed distribution with a tail toward larger clast diameters. The average clast diameter data distribution also shows moderate variability, with a median coefficient of variation value of 39.31%. This value is mirrored by coefficients calculated for a-, b- and c-axes lengths (45.11%, 40.12% and 45.40% respectively). Variation amongst the three axes populations, as well as mean diameter population, is, therefore comparable. Mean lengths recorded for the respective axes (a-, b- and c-axes) are 62.07 cm, 93.00 cm and 58.00

cm. The longest a-axis recorded is almost two meters (192 cm). In contrast, the shortest a-axes measurement is only 19 cm. These values clearly show the variety of clast sizes and shape (refer to Zingg's diagram, Figure 48, pg. 85) found at the study site, supporting the contention that the blockfield contains glacially derived debris. Nevertheless, this does not conclusively indicate glacially derived debris and the results should be analysed with a measure of caution. This is particularly of importance as the study site does not consist of mixed and varying lithologies, as would be expected for glacially derived debris. Furthermore, Holmlund and Näslund (1994) suggest that the Maudheimvidda ice sheet in DML is cold-based and frozen to the substrate. Blockfields are, therefore, thought to have remained intact during glaciation, suggesting little erosive and transportational power of ice sheets. The large variety of clast size and shape can, therefore, be ascribed to pre-existing jointing of the rock and subsequent weathering along these pre-existing lines of weakness.

Table 25: Descriptive statistics for mean diameter, as well as a-, b-, c-axis lengths for clasts from the study site (n = 260). A-, b-, c- axes as well as mean clast diameter are measured in centimetres (cm).

Sample	**A-axis**	**B-axis**	**C-axis**	**Mean Diameter**
Min	19.00	11.00	3.00	13.00
Max	192.00	104.00	61.00	100.17
Range	173.00	93.00	58.00	87.17
Mean	62.07	37.84	23.72	41.21
Median	55.00	35.00	23.00	37.67
Mode	51.00	24.00	29.00	48.00
Skew	1.43	1.07	0.40	0.97
s	28.00	15.20	10.77	16.20
c	45.11	40.12	45.40	39.31

Calculations on lichen presence and the sheltered nature of lichen are shown in Table 26 (pg. 92). The majority of lichen (26.43%) is observed on the west-facing sides. In contrast, the eastern faces show the lowest lichen presence (12.78%). The dominant wind direction is from the east (please refer to Near-Surface Ground Temperature Dynamics, pg. 112), making the eastern clast faces the most wind-exposed and least likely to be colonised by lichen. Please refer to Clast Characterisation (pg. 34) for a discussion on the colonisation of lichen in sheltered locations. Overall, 92.50% of lichen is found in sheltered locations, supporting the assumption made previously, that lichen prefers sheltered locations. Pie charts illustrating the amount of lichen observed may be viewed in Appendix E: Pie Charts Accompanying Statistical Analyses of Clast Characterisation, Figure 90 (pg. 177).

Table 26: Lichen presence and the sheltered or exposed nature of lichen colonisation per clast aspect, are indicated. Percentage values are grouped per aspect (Lichen count: n = 227).

	North	**East**	**South**	**West**	**Top**
Lichen Presence	55	29	44	60	39
% of Total	24.23	12.78	19.38	26.43	17.18
Lichen Sheltered	50	24	41	57	38
% Sheltered	90.90	82.76	93.18	95.00	18.10
% of Lichen Sheltered					**92.51**

A visual assessment of the weathering of clast surfaces on the blockfield shows clasts are moderately weathered with a discoloured surface and sporadic thin exfoliation occurring. Indications of weathering, such as weathering pitting, flaking and roughest sides, and calculations on these are shown in Table 27. The majority of flaking (26.90%) is observed for the top-facing sides, with the lowest percentage (15.24%) observed for the southern aspect. Similar values are observed for the roughest face (67.31% for the top-facing sides; 5.00% for south-facing sides) as well as pitting (65.00% for the top-facing sides; 17.31% for south-facing sides). These values suggest possible aspect control on weathering for clasts for the study site. Pie charts illustrating the amount of flaking, pitting and roughest observable face expressed as a percentage may be viewed in Appendix E: Pie Charts Accompanying Statistical Analyses of Clast Characterisation, Figure 91, Figure 92, Figure 93 (pg. 177) respectively. In addition, please refer to Rock Hardness (pg. 101) for analyses and an in-depth discussion on aspect control on weathering for clasts across the blockfield.

Table 27: Counts and percentages calculated for flaking, the roughest observed face and pitting for all samples, are indicated. Percentage values and counts are grouped per aspect (n = 260).

	North	**East**	**South**	**West**	**Top**
Flaking	90	74	64	79	113
% per Aspect	21.43	17.62	15.24	18.81	26.90
Roughest Face	21	31	13	20	175
% of Total	8.08	11.92	5.00	7.69	67.31
Pitting	65	63	45	48	169
% of Total	25.00	24.23	17.31	18.46	65.00

Thirty-three percent of samples exhibit pitting on only one of their sides. The next highest percentage (25%) occurs for clast with two of their sides showing evidence of pitting. Only seven percent of samples have four or five sides exhibiting weathering pitting. In contrast, 22% of clasts exhibit no pitting for the five aspects under investigation. Using evidence of pitting as an indicator of the amount or intensity of weathering a surface has undergone, clasts surfaces may be described as neither intensely weathered nor non-weathered. A column graph depicting the cumulative percentage of

pitting per side is shown in Figure 53. It is apparent from the figure that more than half of all samples (58%) have at least two or three sides exhibiting weathering pitting. This suggests a bi-or multimodal-weathering regime in terms of aspect and orientation. Figure 54 (pg. 94) depicts the number of sides exhibiting pitting, classed according to the five aspects under investigation (north-, east-, south-, west-, top-facing sides). It can be clearly seen from Figure 54 (pg. 94), that the top-facing sides show the greatest amount of pitting, as discussed previously. Possible aspect control on weathering, the extent of chemical weathering and subsequent analyses on surface length exposure is discussed in greater detail in Particle Size Analysis (pg. 134) and Rock Hardness: Schmidt Hammer and Equotip and Methods (pg. 145).

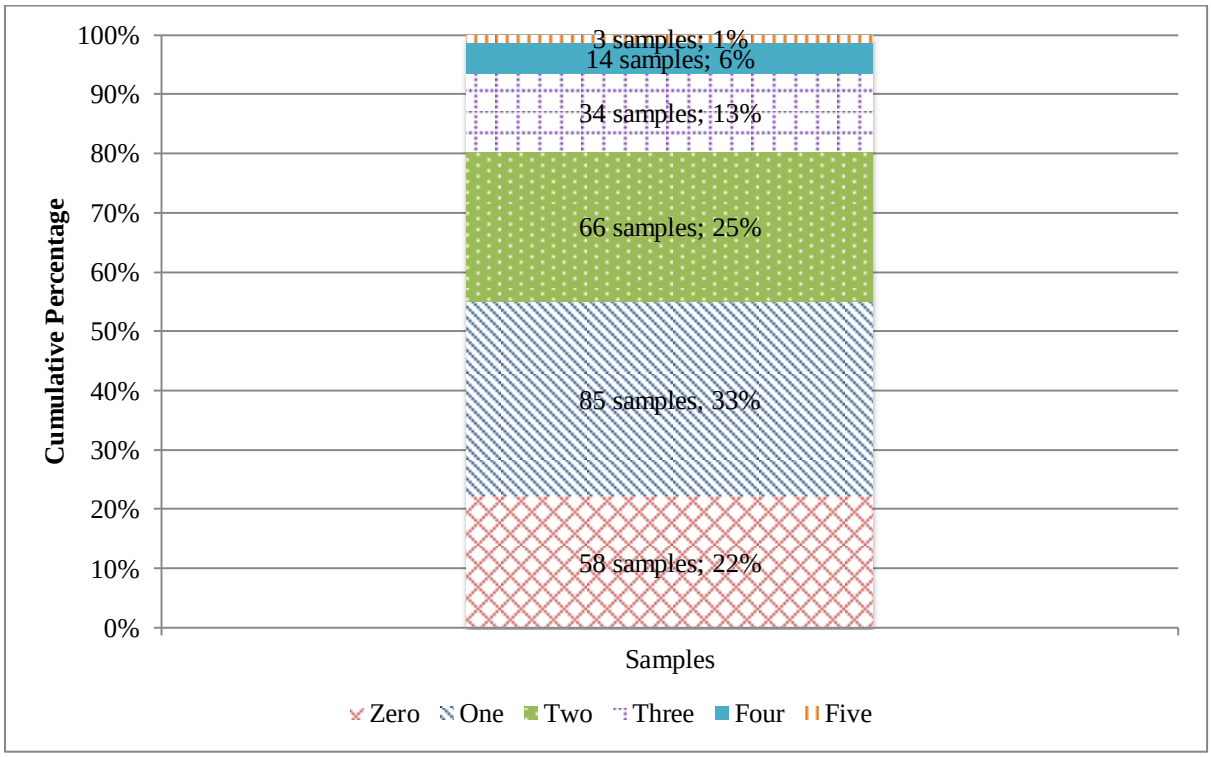

Figure 53: Column graphs of cumulative percentages of the number of pitted sides all clasts for the study site exhibit (n = 260).

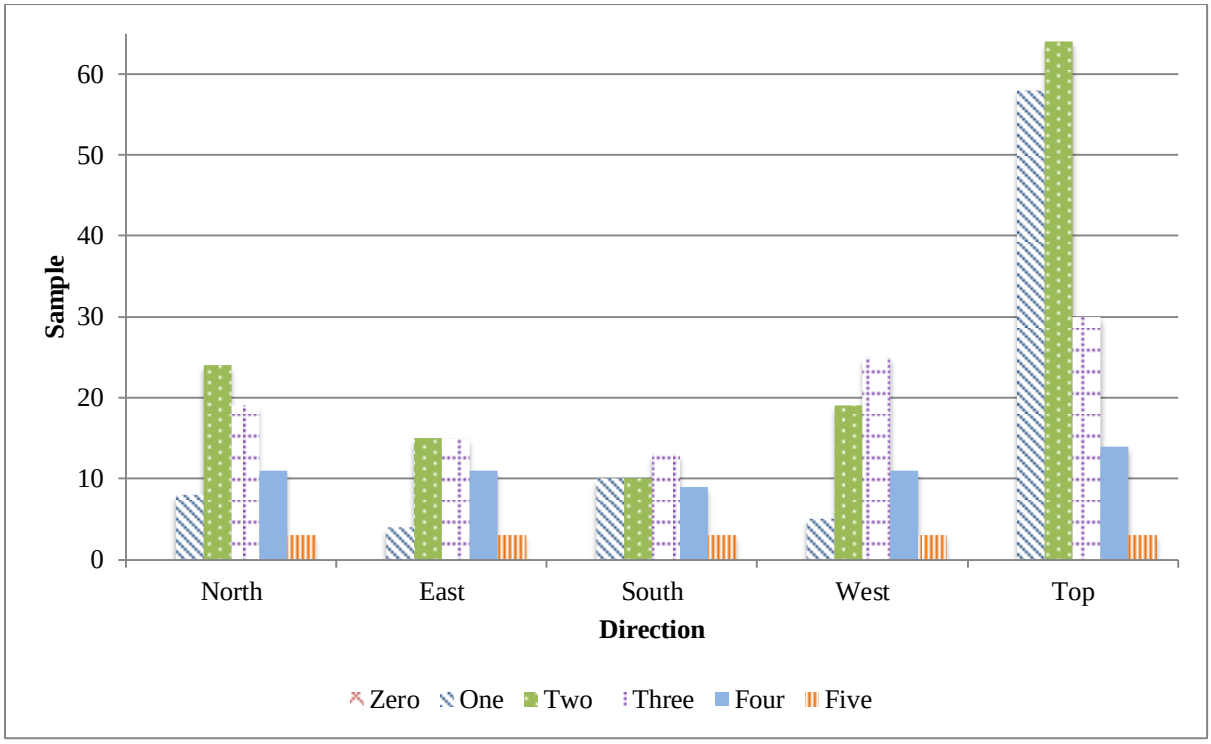

Figure 54: Column graph of the number of pitted sides observed for clasts across the study site, grouped into five aspects (north-, east-, south-, west-, top-facing sides).

Weathering pits are small and fairly shallow for clasts investigated. The mean diameter calculated for weathering pits on 20 clasts equals 6.71 mm (Table 28, pg. 95). This suggests that pitting is not very advanced for the study site. Maximum and minimum a-axis measurements (33.64 mm and 2.92 mm respectively) suggest a large range of pitting sizes. The average Cailleux' Flatness Index for the 200 sample pits equals 214.25. This value is close to the minimum flatness index of 100.00. Overall, weathering pits were found to be near cubic, with the highest flatness index calculated to be 723.00. The range for the flatness indices is also narrow (613.22) and the variance fairly low (s = 82.38; c = 38.45%), indicating cubic, shallow and elongated (mean Krumbein's Sphericity Index of 0.66) pitting for sample clasts. Weathering pits, therefore, occur in the top-most layer on the surface of clasts. Furthermore, the small and shallow pitting suggests a surface that has been exposed to weathering processes only recently. Please refer to Rock Hardness: Schmidt Hammer and Equotip Methods (pg. 101) and Particle Size Analysis (pg. 134) for a discussion on the estimated age of the surface of the blocky deposit. Axes measurements also show a similar coefficient of variation (c) between 35.00% and 40.00% (38.36%, 34.49% and 36.83% for a-axes, b-axes and c-axes measurements respectively), indicating similar variation for the different parameter distributions. All data (axes) distributions are positively skewed, with b- and c-axes distributions very positively skewed and the a-axis distribution highly positively skewed. These values suggest a tail toward greater axes lengths.

Table 28: Descriptive statistics for weathering pitting observed for sample clasts (n = 20). A-, b-, c- axes as well as mean clast diameter are measured in centimetres (cm).

	A-axis	**B-axis**	**C-axis**	**Mean Diameter**	**Sphericity Index**	**Flatness Index**
Min	2.92	2.74	1.00	2.65	0.28	109.78
Max	33.64	19.20	10.28	20.20	0.94	723.00
Range	30.72	16.46	9.28	17.55	0.66	613.22
Mean	9.72	6.38	4.03	6.71	0.66	214.25
Median	9.21	6.20	3.82	6.48	0.66	194.98
Mode	7.96	5.40	2.16	6.67	None	None
Skewness	1.75	1.36	1.13	1.57	-0.08	2.14
s	3.73	2.20	1.48	2.16	0.12	82.38
c	38.36	34.49	36.82	32.13	18.46	38.45

An analysis on which aspect exhibits the highest amount of pitting within each classification (the number of sides having pitting per clast) is shown in Table 29. Nearly 70% (68.24%) of top-facing sides show pitting (for one side exhibiting pitting per clast). Analyses of clasts having two sides pitted show the majority of top-facing sides (96.97%) exhibiting pitting. The north- and west-facing sides show evidence of pitting at 36.36% and 28.79% respectively. Approximately 90% of top-facing sides (88.24%) exhibit pitting amongst clasts when three sides show evidence of pitting. West- and north-facing sides have the next two highest percentage values (73.53% and 55.88% respectively). All top-facing aspects, as well as 78.57% of the north-, east- and west-facing sides, show weathering pits amongst clasts with four sides pitted.

Table 29: Amounts and percentage of clasts exhibiting pitting on one, two, three, four or all of their faces (n = 260).

	Faces					
Pitted Surfaces	North	East	South	West	Top	**Total Clasts**
Zero	0	0	0	0	0	58
% of Total	20	20	20	20	20	100
One	8	4	10	5	58	85
% of Total	9.41	4.71	11.76	5.88	68.24	100
Two	24	15	10	19	64	66
% of Total	36.36	22.73	15.15	28.79	96.97	100.00
Three	19	15	13	25	30	34
% of Total	55.88	44.12	38.24	73.53	88.24	100.00
Four	11	11	9	11	14	14
% of Total	78.57	78.57	64.29	78.57	100.00	100.00
Five	3	3	3	3	3	3

	Faces					
Pitted Surfaces	North	East	South	West	Top	**Total Clasts**
% of Total	100.00	100.00	100.00	100.00	100.00	100.00

Overall, the top-facing sides exhibit the highest amount of pitting, with east-facing sides the least. This is of interest, as the eastern-facing aspects face the dominant winds, suggesting wind is not a driving factor in the development of weathering pits. Instead the leeward western side consistently places in the top third of pitting observed amongst sides. This suggests snow deposition on the leeward side, and the melting thereof during the diurnal and seasonal cycle, may contribute to the development of pitting on clast surfaces for the study site. A summary of a-axes and top-face orientations of clasts is shown in Table 30.

Table 30: Orientations of a-axis and top-facing sides observed for samples, grouped into 20° classes ranging from north to south (n = 260; n = 258 respectively).

	ORIENTATION (°)								
	0-20	**21-40**	**41-60**	**61-80**	**81-100**	**101-120**	**121-140**	**141-160**	**161-180**
A-Axis	37	26	36	29	28	24	24	29	27
% of Total	14.23	10.00	13.85	11.15	10.77	9.23	9.23	11.15	10.38
Top-Face	36	24	29	32	31	22	27	32	25
% of Total	13.95	9.30	11.24	12.40	12.02	8.53	10.47	12.40	9.69

The majority of a-axes orientations for clasts hold a bearing between 0° and 20° (north to north-north-east), similar to that observed for top-face orientations (13.95%). The next largest class is that of 41°-61° (north-east to east-north-east). Clasts, therefore, appear to have a bi-modal orientation for a-axes, similar to openwork block accumulations found in the Lesotho Highlands of southern Africa (Boelhouwers *et al.*, 2002). Rose diagrams for a-axes and top-facing side orientations are shown in Figure 55 (pg. 97) and Figure 56 (pg. 97) respectively.

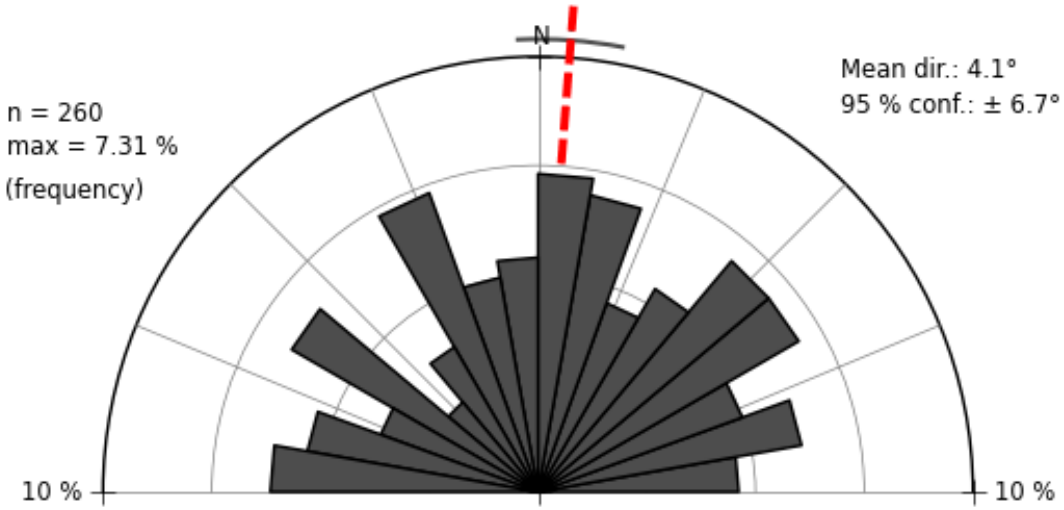

Figure 55: Rose diagram of a-axis orientations for samples for the study site (n = 260). The dashed line indicates the sample mean. The maximum frequency is 10% and diagonals represent 22.5° segments.

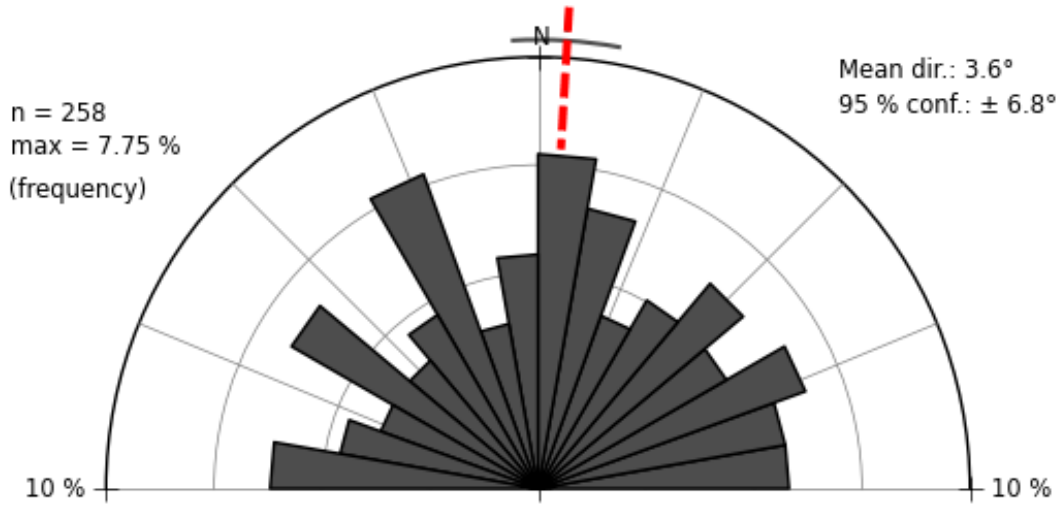

Figure 56: Rose diagram of top-facing side orientations (n = 258). The dashed line indicates the sample mean. The maximum frequency is 10% and diagonals represent 22.5° segments.

Contrary to these values, the dominant orientation for both a-axes and top-facing sides is not in a northern direction. Calculations for von Mises distribution for the study site indicate a mean orientation vector of 90.00° (Table 31 [pg. 98]; n = 260) for both a-axes and top faces orientations (Table 32 [pg. 98]; n = 258). This, as discussed under Blockfield Survey, (pg. 76) equates to an easterly direction. Values for *s* (mean angular deviation) show that approximately four fifths ($\frac{4}{5}$) of the a-axis orientation angular measurements lie within an angle of 90.00° (90.00°±79.30°; Table 31 [pg. 98]). Similarly, approximately three quarters (¾) of the top-facing side orientation angular

measurements lie within an angle of 90.00° (90.00°±76.30°; Table 32). Coefficients of variation are 88.11% and 84.78% for a-axes and top faces orientations respectively, indicating comparability amongst populations.

Table 31: Von Mises distribution calculations for determining preferential orientation among a-axis orientations (n = 260).

Parameter	Value
$\bar{x}$	-0.04
$\bar{y}$	0.02
r	0.04
$cos\bar{\theta}$	-0.91
$sin\bar{\theta}$	0,42
μ_0 ($\bar{\theta}$)	**90.00**
s	79.30
k	0.44
c	88.11
n	260

Table 32: Von Mises distribution calculations for determining preferential orientation among top-facing side orientations (n = 258).

Parameter	Value
$\bar{x}$	-0.11
$\bar{y}$	0.04
r	0.11
$cos\bar{\theta}$	-0.93
$sin\bar{\theta}$	0.36
μ_0 ($\bar{\theta}$)	**90.00**
s	76.30
k	0.44
c	84.78
n	258

Bar graphs showing a-axes and top-face orientations are drawn for Figure 57 and Figure 58 below. Similarity of class sizes suggests similar populations. The distributions also approximate near-symmetrical distributions. Pie charts depicting the grouping within classes may be viewed in Appendix E: Pie Charts Accompanying Statistical Analyses of Clast Characterisation, Figure 94 and Figure 95 (pg. 177) for a-axes and top-face orientations respectively.

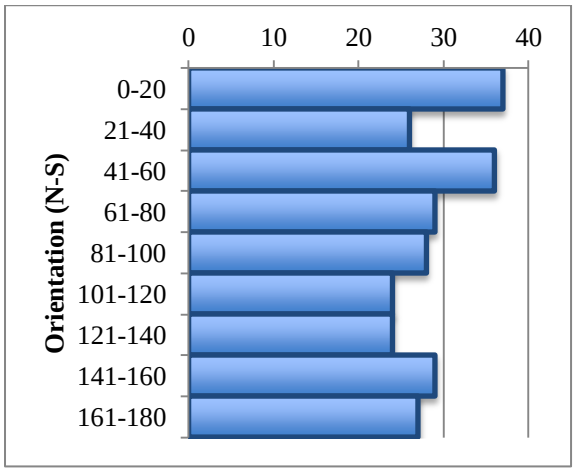

Figure 57: Bar graph of a-axis orientations, ranging from north to south, arranged in 20° intervals (n = 260).

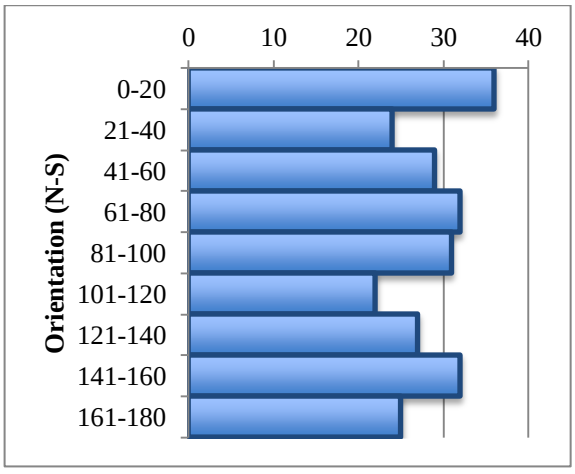

Figure 58: Bar graph of the top aspect orientation, ranging from north to south with 20° intervals (n = 258)

Dip calculations are shown in Table 33. Top-facing sides have a predominantly horizontal position, with the majority of samples (108 out of 140) at an inclination of less than 20°. In contrast, the remaining sides (remaining four aspect-facing sides) have a predominantly vertical inclination (dip of approximately 90°). In certain incidences, the dip of sides exceeds 90°. These values show that clasts are predominantly found to be lying in the horizontal (parallel to the ground surface), as already indicated on pg. 83, with clast sides near perpendicular to the top face. Figure 59 (pg. 100) gives a visual description of dip observed per aspect amongst clasts for the study site, showing the approximate parallel position of the top-facing sides. Similarly, the clustering of bars around 90° suggests clasts sides' perpendicular to top-facing sides.

Table 33: Calculations for inclination of sides (dip) per aspect for all samples (n = 260). Dip is measured in degrees (°).

	Faces				
Dip	North	East	South	West	Top
0-10	1	0	0	0	60
11-20	0	1	0	0	48
21-30	0	0	0	1	24
31-40	2	2	1	0	4
41-50	4	1	3	5	1
51-60	6	7	7	9	1
61-70	10	10	13	12	0
71-80	24	19	23	26	0
81-90	26	37	39	24	1
91-100	28	28	23	34	1
101-110	18	18	17	14	0
111-120	9	6	4	1	0
121-130	0	5	0	1	0
131-140	0	1	0	0	0
n	128	135	130	127	140

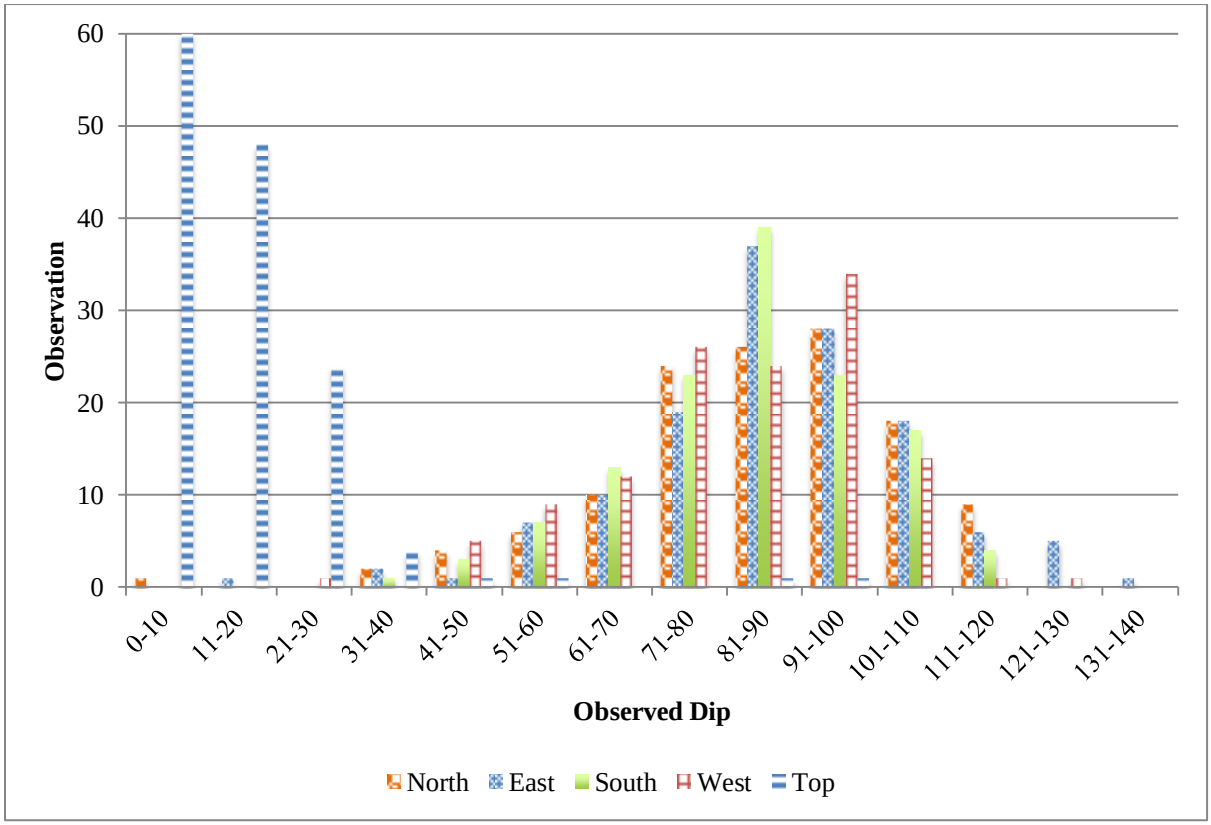

Figure 59: Column chart of dip observed per aspect (north-, east-, south-, west-, top-facing sides) amongst clasts for the study site (n = 140).

Figure 60 (pg. 101) provides a visual representation of sample clasts on slope (in degrees) for the study site. Arrows indicate the orientation of the a-axis. It becomes clear from the figure that samples are predominantly randomly orientated, with the exception of when clasts align to an increase in slope gradient across the Northern Buttress. The dotted red line indicates a break in slope with the area to the west fairly gentle, and the area to the east becoming steeper. The figure shows that the a-axes (long axes) of samples to the west of this line exhibit a random orientation. In contrast, a-axes orientations to the east of this line seem to follow the orientation of the slope more closely. The dotted arrows indicate the dominant wind direction out of the east. Although the deposit may be described as autochthonous, as discussed above, clasts do appear to be slightly influenced by topographic change, *i.e.* slope gradient. The steepest change in slope for the study site occurs in a general north-easterly direction, although change in slope is also observed for the east-north-east and east. An increase in slope gradient is, therefore, observed in a generally easterly direction. Since clast orientation is approximately 90°, the primary alignment of clasts appears to be moderately influenced by the change in slope for the blockfield. This parallel alignment of clasts to slope gradient is comparable to that of clasts found on blockfields in the Lesotho Highlands (Boelhouwers *et al.*, 2002). These findings show that although the blockfield is autochthonous, micro-scale changes in topography do affect changes in

clast characteristics. Furthermore, where a change in slope is observed, clast orientation becomes less random.

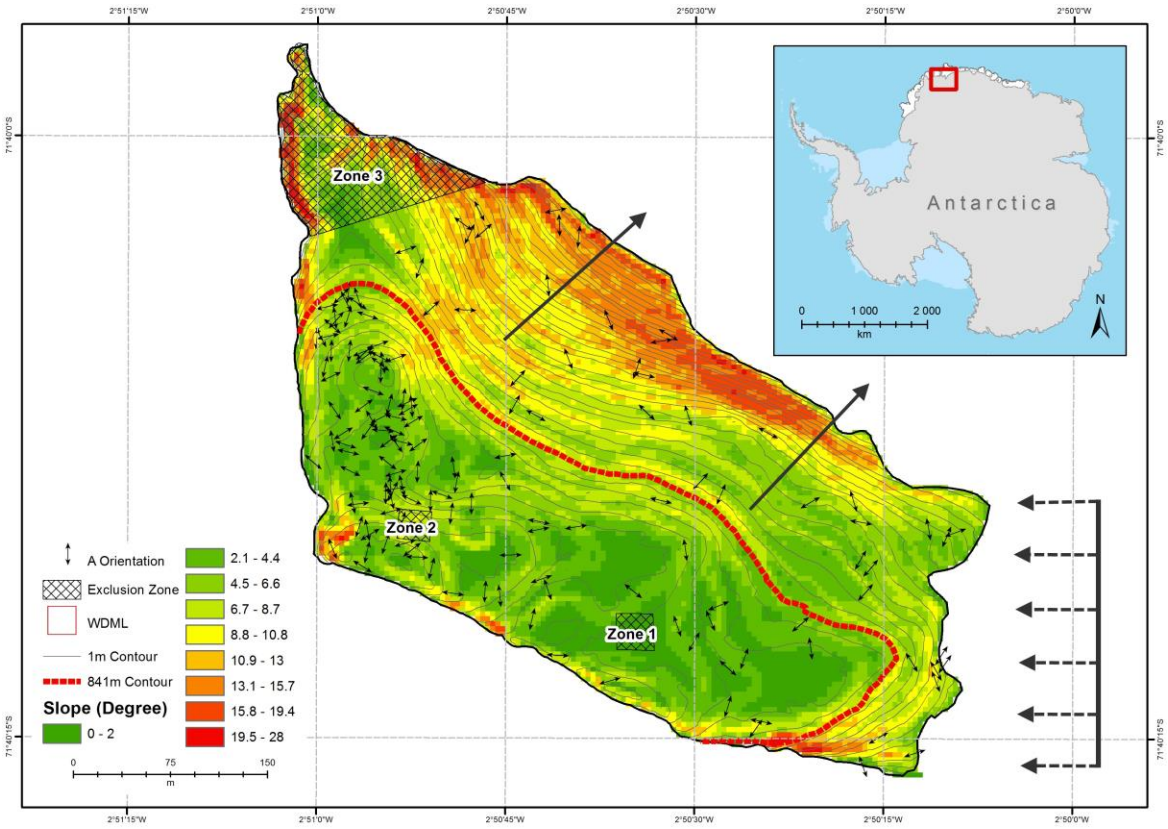

Figure 60: Slope (in degrees) compared to sample clast a-axis (long axis) orientations. Orientation is indicated by black arrows. Two long solid arrows indicate changes in slope (downslope), whereas dotted arrows indicate the dominant wind direction from the east. The dotted red line indicates the 841m contour.

4.3 Rock Hardness: Schmidt Hammer and Equotip Methods

Summary statistics for SH readings for the five clast faces being investigation are shown in Table 34 (pg. 102). The highest mean *R*-values are observed for the south-, west- and top-facing sides at 33.45, 33.06 and 32.5 respectively. The east-facing sides exhibit the lowest observed mean *R*-value of 31.13. As discussed in Rock Hardness: Schmidt Hammer and Equotip Methods (pg. 35), the south-facing aspect in the southern hemisphere receives less solar radiation than the northern aspect. The maximum *R*-value (62) is observed for the south-facing sides. The high mode (34) and median values (33) for the southern sides also clearly show that the rock surfaces of these sides are the hardest, *i.e.* least weathered. This is mirrored by lowest mode (28) and median values (30) for the east-facing sides, showing the lowest rock hardness values and the most weathered surface. The high *R*-values recorded for the southern aspect suggest solar radiation plays a role in rock surface weathering for the study site. The highest range of *R*-values is observed for the south-facing sides, with the smallest range occurring for the east-facing aspects. However, the highest coefficient of variation is observed for the top-facing sides (26.15%), with the lowest *c* calculated for the eastern sides. Consequently, the

sample *s* for the eastern aspect is only 24.70% of the sample mean. Standard errors are low and centring on 0.70% of population means. Data distributions for all aspects are positively skewed (0.3-1.0 skewness value), with very platykurtic kurtosis values (< 0.67). Consequently, data distributions are peaked with a tail to the right (high *R*-values).

Table 34: Summary statistics for SH readings for five treatments (north-, east-, south-, west- and top-facing sides).

	North	**East**	**South**	**West**	**Top**
Mean	32.312	31.13	33.45	33.06	32.50
Standard Error	0.23	0.21	0.23	0.23	0.23
% of Mean	0.71	0.67	0.69	0.70	0.71
Median	32	30	33	32	32
Mode	30	28	34	30	26
s	8.25	7.69	8.56	8.56	8.50
c	25.53	24.70	25.59	25.89	26.15
Sample Variance	68.12	59.15	73.21	73.19	72.25
Kurtosis	-0.45	-0.41	-0.49	-0.36	-0.40
Skewness	0.35	0.44	0.34	0.47	0.39
Range	44	43	48	45	44
Minimum	14	14	14	16	14
Maximum	58	57	62	61	58
Sum	43 460	42 984	47 936	43 971	44 851
Count	1345	1381	1433	1330	1380

Similar to SH readings, the highest mean L-value for Equotip values is recorded for the south-facing sides (399.81). Summary statistics for Equotip readings for the five faces under investigation are shown in Table 35 (pg. 103). The next highest mean L-values are observed for the west-facing sides (398.06), followed by the east-, north- and top-facing aspects at 380.28, 374.64 and 369.00 respectively. In contrast to SH readings, the lowest average values recorded using the Equotip occur for the top-facing sides at 369.00, followed by the north-facing sides (374.65). The highest (407.00) median values are observed for the south-facing sides. These values agree with those calculated for SH readings. Furthermore, the second lowest median values (380.00) are observed for the eastern aspect (compared to the lowest median values observed for the eastern aspect for SH readings). In contrast to SH readings, the highest range of rock hardness rebound values is observed for the east-facing sides (894.00). However, with the smallest range in rock hardness rebound values occurs for the north-facing aspects (810.00), agreeing with SH findings. The highest *c* is observed for the east-facing sides (43.33%), with the lowest *c* calculated for the south-facing sides (41.12%). Consequently, the sample *s* is only 41.12% of the sample mean, indicating less variability for this aspect. Standard

errors are low, falling between 0.60-0.73 percent of population means, almost identical to those calculated for SH observations. Data distributions for all aspects are finely positively skewed (0.13 to 0.26 skewness value), with platykurtic kurtosis values (0.67-0.90). Consequently, data distributions are peaked. Kurtosis values are also similar to those calculated for SH readings.

Table 35: Summary statistics for Equotip readings for five treatments (north-, east-, south-, east- and top-facing sides).

	North	**East**	**South**	**West**	**Top**
Mean	374.65	380.28	399.81	398.06	369.00
Standard Error	2.64	2.71	2.58	2.92	2.25
% of Mean	0.70	0.71	0.65	0.73	0.61
Median	373.00	380.00	407.00	402.50	368.00
Mode	204.00	195.00	437.00	482.00	191.00
s	158.12	164.78	163.99	165.43	157.96
c	42.21	43.33	41.12	41.45	42.81
Sample Variance	25 002.47	27 153.47	26 893.72	27 365.61	24 950.66
Kurtosis	0.76	0.79	0.79	0.74	0.79
Skewness	0.25	0.23	0.13	0.18	0.26
Range	810.00	894.00	857.00	836.00	877.00
Minimum	30.00	5.00	11.00	38.00	6.00
Maximum	840.00	899.00	868.00	874.00	883.00
Sum	1 345 736.00	1 404 751.00	1 611 185.00	1 276 976.00	1 814 756.00
Count	3 592	3 694	4 040	3 200	4 918

Consistently high rock hardness values observed for the south-facing sides using both the SH and Equotip suggest that these sides are the least weathered. These faces receive a smaller annual incident solar radiation budget, which influences thermal regimes and processes such as freeze-thaw cycles. The lower likelihood of snow or ice-melt being available for chemical weathering for the south-facing aspects may be the reason for the highest rock surface hardness values being recorded for these aspects. In comparison, the consistently low mean *R*- and L-values for the north-facing sides for both SH and Equotip in turn suggest that this aspect is the most weathered. These sides receive the highest annual solar radiation budget, increasing the availability of snowmelt and a more dynamic thermally driven weathering regime. Differential surface weathering due to thermal fatigue may play an important role in aspect control on weathering of clast surfaces across the blockfield.

The various outputs of ESDA are shown in Figure 61 to Figure 63 (pg. 104). Only the histogram, QQ plot and trend analysis for mean L-values of the east-facing sides of clasts, measured using the

Equotip are shown since ESDA analyses conducted for the other indicators of weathering yielded similar results. Figure 61 shows the distribution of the data, where the majority of data points fall within a short distance of the arithmetic mean, suggesting a normal distribution. This is confirmed by Figure 62, which shows the QQ plot of the data. The data is plotted in a straight line, indicating that the distribution of the particular dataset follows a normal distribution. Figure 63 shows that there is no apparent trend inherent in the dataset under investigation. Predictor lines are straight and horizontal, clearly showing the lack of a trend amongst data points. Consequently, GIS analyses support classical statistical analyses. Furthermore, the lack of an inherent trend confirms IDW as the preferred method of interpolation.

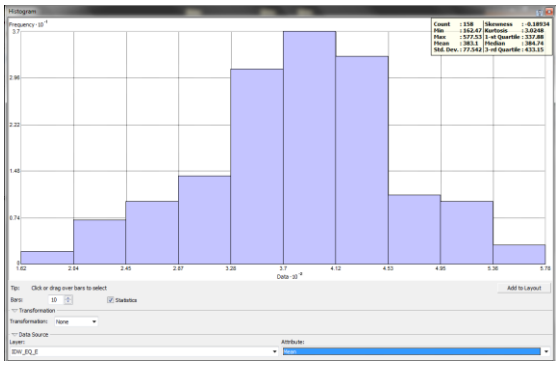

Figure 61: A histogram determined for mean L-values for the east-facing sides of samples, measured using the Equotip. The histogram was created using ESDA in GIS.

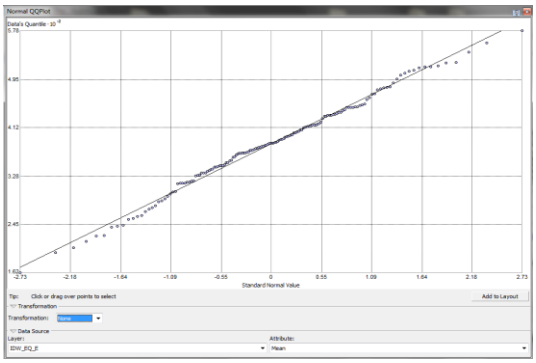

Figure 62: A QQ plot determined for mean L-values for the east-facing sides of clasts, measured using the Equotip. The QQ plot was created using ESDA in GIS.

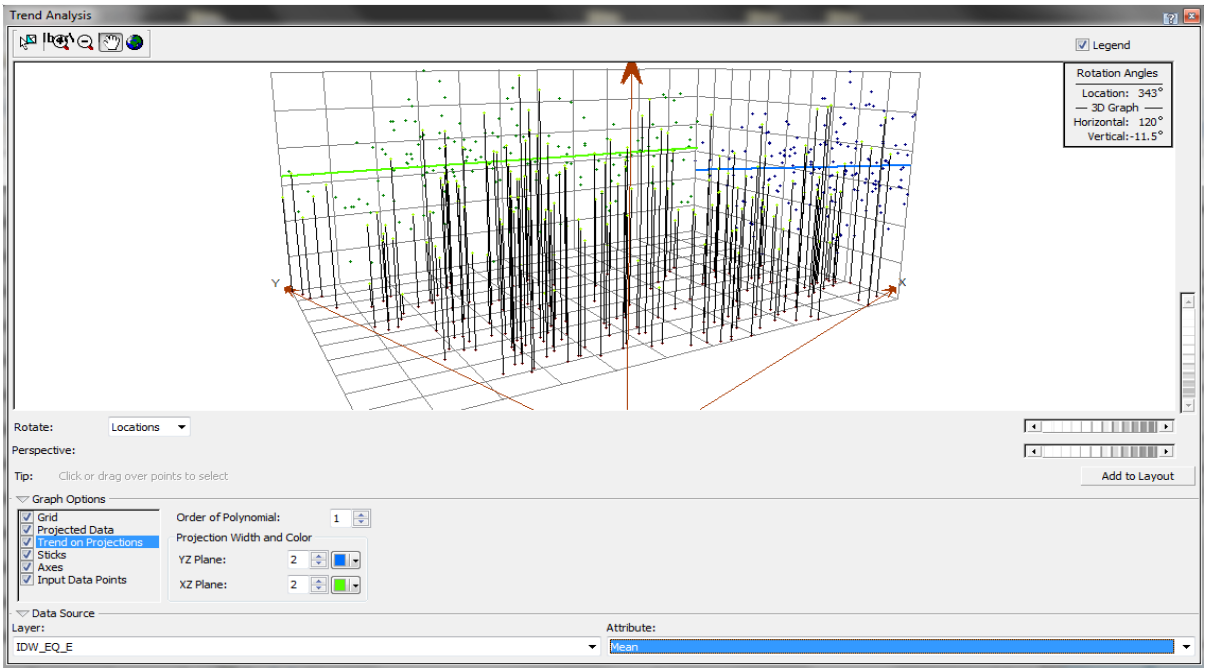

Figure 63: The result of trend analysis done in GIS using ESDA. Trend analysis on mean L-values for east-facing sides of samples, measured using the Equotip, are shown. No trend is apparent, as seen by the straight predictor lines drawn through the data.

Sample variances for SH and Equotip values are 65.42 and 26 860.13 respectively. SH readings are consequently used as the denominator and Equotip readings as the nominator when calculating the *F* test statistic. The null and alternate hypotheses of the *F*-test are given below.

H_0 = *SH and Equotip populations have the same variances*

H_a = *SH and Equotip variances are not the same*

A more detailed explanation of the *F*-test and its application in the current context is given under Rock hardness: Schmidt Hammer and Equotip methods (pg. 64 onwards). *F*-test calculations show that the SH data distribution has a similar variance to the Equotip data distribution. H_0 can, therefore, not be rejected at a 99% level of confidence ($\alpha = 0.01$; $p < 0.01$), indicating similarities in variances. Subsequent to the *F*-test, the *t*-test was run to determine the comparability of the two data series. The null and alternate hypotheses of the *t*-test are given below.

H_0 = *SH and Equotip measurements are comparable to each other,* i.e. $\mu_1 = \mu_2 = \ldots = \mu_i$

H_a = *SH and Equotip measurements are drawn from different populations and are not comparable to each other,* i.e. $\mu_1 \neq \mu_2 \neq \ldots \neq \mu_i$

A more detailed explanation of the *t*-test and its application in the current context is given under Rock hardness: Schmidt Hammer and Equotip methods (pg. 64 onwards). Results of the *t*-test show that H_0 is rejected at the 99% level of confidence ($\alpha = 0.01$; $p < 0.01$). SH and Equotip readings are, therefore, not statistically comparable, agreeing with the findings of Viles *et al.* (2011). The two data series should not be used for direct comparison of data values. Differing lowest average *R*- and L-values for SH and Equotip readings, as discussed above, already indicated this. Furthermore, the low Pearson's correlation coefficient of 0.12 indicates no or next-to-no relationship apparent between the two data sets. The two scales of measurement (0-100 for the SH; 0-1 000 for the Equotip) would suggest that ten units of the SH are equal to 100 units for the Equotip. However, the results of the *t*-test clearly show that such a comparison may not be drawn. This was already indicated by a comparison of mean rock hardness rebound values recorded for the two instruments (Table 34, pg. 102 and Table 35, pg. 103). Although values appear similar (differing by a factor of ten), SH readings are lower than those of the Equotip. Furthermore, populations for SH readings are positively skewed whereas Equotip populations are negatively skewed. These findings support results of the *t*-test and the non-comparability of the two instruments. However, kurtosis values are similar for both instruments, as are median values recorded. Standard errors make up similar percentage values of the respective population means and *c* values are similar. Although SH and Equotip readings are not comparable, they do exhibit some similarities in population parameters. Furthermore, the *F*-test shows that

population variances are similar. Greater care when taking measurements in the field, for example taking Equotip and SH readings on the same spot, may allow for the direct comparison of these data series. The Inferential statistics results, displayed in tabular format, are shown in Appendix G: Inferential Statistics for Rock Hardness Rebound Values (pg. 189), for the *F*-test (Table 84) and *t*-test (Table 85) respectively. Calculations for Pearson's correlation coefficient are shown in Table 86 (pg. 189).

ANOVA was calculated for SH and Equotip readings for five (north-, east-, south-, west- and top-facing sides) and four treatments (north-, east-, south-, and west-facing sides). Furthermore, ANOVA was run for the five treatments for the presence of lichen, flaking, weathering pitting and the roughest observable face. The null and alternate hypotheses of ANOVA for these tests are given below.

H_0 = *mean rock hardness rebound values/lichen presence/flaking/weathering pitting/roughest observable clast face are similar for all aspects*
H_a = *mean rock hardness rebound values/lichen presence/flaking//weathering pitting/roughest observable clast face is different for all aspects*

A more detailed explanation of the ANOVA and its application in the current context is given under Rock hardness: Schmidt Hammer and Equotip methods (pg. 64 onwards). The result of the test shows H_0 being rejected at a level of significance of $\alpha = 0.01$ ($p < 0.01$) and a level of confidence of 99%. Similar analyses for ANOVA for four treatments (north-, east-, south-, and west-facing sides) result in H_0 being rejected for SH readings ($\alpha = 0.01$; $p < 0.01$). H_0 for Equotip readings for the same number of treatments could only be rejected at a level of significance of $\alpha = 0.05$ ($p < 0.05$). Although this confidence level is less than ANOVA for five treatments, it is nonetheless within the specified 95% level of confidence appropriate for physical geographical sciences (please refer to Statistical Analyses and Preparation, pg. 57). The difference in results may be applied to the Equotip being more sensitive to surface irregularities than the SH. Tabular output of ANOVA tests are shown in Appendix G: Inferential Statistics for Rock Hardness Rebound Values, pgs. 190-191 [Table 87 (SH five treatments); Table 88 (SH four treatments); Table 89 (Equotip five treatments); Table 90 (Equotip four treatments)].

ANOVA conducted for lichen presence for all aspects, as well as evidence of flaking, pitting and the roughest observable face shows H_0 being rejected in all instances (Appendix G: Inferential Statistics for Rock Hardness Rebound Values, pgs. 191-192 for tabular ANOVA output). Evidence of flaking, pitting and the roughest observable face are significant at $\alpha = 0.01$ ($p < 0.01$). In contrast, ANOVA for

lichen presence shows a confidence interval larger than the required 95% ($\alpha = 0.05$, $p < 0.05$) for physical sciences. H_0 is rejected for lichen presence at $\alpha = 0.10$ ($p < 0.10$), indicating α is larger than realistic level of uncertainty observed in physical geography. Table 36 (pg. 107) provides a summary of the various ANOVA test run and the respective levels of confidence associated with each test. With the exception of lichen presence, all parameters investigated support a rejection of H_0 at a 99% level of confidence.

Table 36: Summary of ANOVA tests for rock hardness rebound values for the SH and Equotip, lichen presence, flaking, pitting and the roughest observable face for samples from the study site.

Investigation	**Level of Confidence**	**Level of Significance (α)**	**Rejection of H_0**	**Significant for $p < 0.05$**
Rock Hardness: SH	99%	0.01	Yes	Yes
Rock Hardness: Equotip	99%	0.01	Yes	Yes
Lichen Presence	90%	0.10	Yes	No
Flaking	99%	0.01	Yes	Yes
Pitting	99%	0.01	Yes	Yes
Roughest Observable Face	99%	0.01	Yes	Yes

The rejection of H_0 at a 99% level of confidence for SH and Equotip rock hardness rebound values signifies population means across samples are not equal. Aspect, therefore, exerts a control on weathering for blockfield samples across the study site, when using rock hardness as an indicator of weathering. Similarly, additional indicators of weathering (evidence of flaking, pitting and the roughest observable face) support these findings. The results agree with studies by Hall (1999 in Goudie, 2006) and Waragai (1999 in Goudie, 2006). However, lichen presence is not within the required 95% level of confidence for physical geography, as suggested by Briggs (1977a). The lower level of confidence calculated for lichen presence may be due to lichen colonising sheltered locations. Since certain parameters, such as jointing of clasts, are controlled by the lithology and geology of the study site (Weinert 1980) and not necessarily by weathering processes, lichen analyses may not be the best indicator for aspect control. The result of the *t*-test shows that SH and Equotip measurements are not comparable. Nevertheless, statistical analyses conducted on the two separate data series confirm each other's findings (ANOVA yields a rejection of H_0 in all instances, indicating aspect control), further supported by the parameters of flaking, pitting and the roughest observable face. A reason for the non-comparable nature of SH and Equotip readings may be attributed to SH readings not being taken on the exact same point of the clast surface as Equotip readings. Furthermore, studies by Aoki and Matsukura (2007) show that the thickness of the material being tested may impact the rebound value of the Schmidt Hammer, indicating that the rebound value represents the weathered surface as well as internal non-weathered material. In comparison, the Equotip records rock hardness in a narrow

surface zone. Consequently, small differences in grains, micro-fissures and other surface irregularities yield statistically different rock hardness rebound values. In addition, SH and Equotip measurements were taken by different two people, introducing a margin of error into observations.

Following ANOVA analyses, Fisher's LSD tests were conducted to determine similarity of variance for individual data series pairings. The null and alternate hypotheses for this statistical test are given below.

H_0 = *the two population variances are equal,* i.e. $\mu_1 = \mu_2$

H_a = *the two population variances are not equal,* i.e. $\mu_1 \neq \mu_2$

A more detailed explanation of Fisher's LSD test and its application in the current context is given under Rock hardness: Schmidt Hammer and Equotip methods (pg. 64 onwards). Results of Fisher's LSD tests on SH readings are given in Table 37. Table 38 shows Fisher's LSD results for Equotip readings. H_0 is accepted for three out of the ten paired comparisons of SH readings. Similarly, three out of ten of the paired comparisons for Equotip readings yield an acceptance of H_0. For SH readings, the only aspects exhibiting similar populations are the top-facing with north-facing pairing, top-facing with west-facing pairing and south-facing with west-facing pairing. All other paired SH comparisons exhibit dissimilar populations. The top-facing with north-facing pairing and the south-facing with west-facing pairing also show similar populations for Equotip readings. In contrast, the north-facing with east-facing pairing is dissimilar to Fisher's LSD tests for the SH. Nevertheless, all other pairings yield a rejection of H_0, signifying dissimilar populations, *i.e.* rock hardness rebound values are dissimilar for those aspect pairings, suggesting aspect control on weathering.

Table 37: Results of Fisher's LSD tests on paired aspects ($\alpha = 0.05$, $p < 0.05$) of SH readings, in order to determine which aspects are different. The critical value (*t*-value) for each comparison is 1.961.

	Top vs. N	**Top vs. E**	**Top vs. S**	**Top vs. W**	**N vs. E**	**N vs. S**	**N vs. W**	**E vs. S**	**E vs. W**	**S vs. W**
t-Statistic	0.587	4.458	2.956	1.710	3.886	3.568	2.303	7.576	6.200	1.199
P two-tail	0.557	8.59E-06	3.15E-03	8.75E-02	1.04E-04	3.66E-04	2.13E-02	4.82E-14	6.52E-10	0.231
Accept H_0	Yes	No	No	Yes	No	No	No	No	No	Yes

Table 38: Results of Fisher's LSD tests on paired aspects ($\alpha = 0.05$, $p < 0.05$) of Equotip measurement, in order to determine which aspects are different. The critical value (*t*-value) for each comparison is 1.961.

	Top vs. N	**Top vs. E**	**Top vs. S**	**Top vs. W**	**North vs. E**	**N vs. So**	**N vs. W**	**E vs. S**	**E vs. W**	**S vs. W**
t-Statistic	1.628	3.218	8.734	8.221	1.488	6.533	6.213	4.952	4.710	0.063

	Top vs. N	Top vs. E	Top vs. S	Top vs. W	North vs. E	N vs. So	N vs. W	E vs. S	E vs. W	S vs. W
P two-tail	0.104	0.001	2.89E-18	2.32E-16	0.137	6.85E-11	5.50E-10	7.51E-07	2.53E-06	0.949
Accept H_0	Yes	No	No	No	Yes	No	No	No	No	Yes

The acceptance of H_0 of the top-facing with north-facing pairing, south-facing with west-facing pairing and top-facing with west-facing pairing for the SH readings as well as the top-facing with north-facing pairing, south-facing with west-facing pairing and north-facing with east-facing pairing for the Equotip readings indicate that these pairings (populations) are not aspect controlled. In particular the top-facing with north-facing and south-facing with west-facing pairings appear similar (population variances are similar) for both SH and Equotip observations. The similarity of mean *R*- and L-values, standard errors, *s*, and *c* values (see Table 34, pg. 102 and Table 35, pg. 103 for SH and Equotip respectively) of these pairings supports this conclusion. Furthermore, as discussed previously (see Rock Hardness: Schmidt Hammer and Equotip Methods, pg. 35) north-facing sides are exposed to higher amounts of solar radiation than southern sides. GIS calculations, shown in Table 39, show that the highest amount of solar radiation received throughout the year is for the northern aspect at 716 859 $WH.m^{-2}$. Similarly, top-facing sides receive the next greatest amount of solar radiation (686 885 $WH.m^{-2}$). The southern aspect receives the lowest amount (647 341 $WH.m^{-2}$) of solar radiation annually.

Table 39: Average solar radiation ($WH.m^{-2}$) received per aspect for the study site. Summary solar radiation values are determined using GIS.

Aspect	Average Solar Radiation Received
North	716 859
East	666 152
South	607 341
West	624 444
Top	686 885

Larger amounts of solar energy received yield greater likelihood of freeze-thaw cycles occurring, as well as promoting a more thermally driven regime. Since moisture availability influences weathering rates, it can be argued that these aspects, receiving higher levels of solar irradiation, would be exposed to similar weathering processes and rates, suggesting similarity in populations. Similarly, south- and east-facing sides receive less solar irradiation (607 341 $WH.m^{-2}$ and 624 444 $WH.m^{-2}$ respectively), resulting in less snow and ice melt and slowed chemical weathering rates. Consequently, these aspects should yield similar populations, as shown by Fisher's LSD tests. Differences in acceptance of hypotheses for the third pairing (top-west for SH; north-east for Equotip) may be ascribed for the greater sensitivity to surface irregularities of the Equotip compared to the SH.

The results of Fisher's LSD tests are confirmed by GIS analyses. Zonal statistics for slope classes are shown in Table 40. More gentle slopes (0-12º) have higher median and maximum *R*- and L-values (less weathered), with steeper slopes yielding lower *R*- and L-values (more weathered). Gentler slopes also have smaller ranges in mean *R*- and L-values than steeper slopes. These findings are the same for both SH and Equotip readings and suggest that gentler slopes influence weathering rates, with softer (more weathered) surfaces found on steeper slopes.

Table 40: Zonal statistics per slope class for SH and Equotip mean rock hardness rebound values. Slope is measured in degrees (°) and zonal statistics are determined using GIS.

Schmidt Hammer							
Slope	Max	Min	Range	Average	Mode	Minority	Median
0-6	40-45	20-25	35-40	30-35	30-35	20-25	30-35
6-12	40-45	20-25	35-40	30-35	30-35	40-45	30-35
12-18	35-40	25-30	45-50	30-35	25-30	35-40	25-30
18-24	35-40	25-30	45-50	25-30	25-30	35-40	25-30
> 24	35-40	25-30	45-50	30-35	30-35	35-40	30-35
Equotip							
Slope	Max	Min	Range	Average	Mode	Minority	Median
0-6	500-550	200-250	450-500	350-400	350-400	500-550	350-400
6-12	500-550	250-300	500-550	350-400	350-400	500-550	350-400
12-18	450-500	250-300	550-600	350-400	350-400	250-300	350-400
18-24	450-500	250-300	550-600	350-400	300-350	450-500	300-350
> 24	400-450	300-350	650-700	350-400	300-350	350-400	300-350

Zonal statistics for slope classes are shown in Table 41 (pg. 111). The higher the amount of solar radiation received, the lower the *R*- and L-values calculated, *i.e*. the more weathered the clast surface. The lowest mean *R*- and L-values are observed for areas receiving the highest amount of annual solar radiation, as are the highest ranges, median and modal values observed. Interestingly, maximum *R*- and L-values are not calculated for these zones, but rather those areas receiving between 650 600 – 723 200 $WH.m^{-2}$ for the SH, and 650 600 – 578 000 $WH.m^{-2}$ for the Equotip. Nevertheless, these findings suggest areas receiving higher annual solar radiation exert a control on mean rock hardness rebound values. Furthermore, the relationship between the two parameters appears to be inverse in nature, *i.e*. the higher the amount of solar radiation received, the lower the rock hardness rebound values recorded in the field. This is expected as solar radiation received contributes toward the melting of snow and ice, yielding a more dynamic thermally driven environment. In addition, processes such as freeze-thaw cycles are enhanced, contributing to the weathering of clast surfaces.

Table 41: Zonal statistics per class of annual solar radiation ($WH.m^{-2}$) received for SH and Equotip mean rock hardness rebound values. Zonal statistics are determined using GIS.

Schmidt Hammer							
Radiation	Max	Min	Range	Average	Mode	Minority	Median
723 200 - 795 800	35-40	25-30	45-50	25-30	25-30	35-40	25-30
650 600 - 723 200	40-45	20-25	35-40	30-35	25-30	40-45	30-35
578 000 - 650 600	35-40	20-25	40-45	30-35	35-40	20-25	30-35
505 500- 578 000	35-40	25-30	45-50	30-35	35-40	25-30	30-35
432 900 - 505 500	35-40	25-30	45-50	30-35	30-35	25-30	30-35
Equotip							
Radiation	Max	Min	Range	Average	Mode	Minority	Median
723 200 - 795 800	450-500	250-300	550-600	350-400	350-400	450-500	350-400
650 600 - 723 200	500-550	200-250	450-500	350-400	350-400	200-250	350-400
578 000 - 650 600	500-550	300-350	550-600	400-450	400-450	500-550	400-450
505 500- 578 000	450-500	300-350	600-650	350-400	400-450	350-400	400-450
432 900 - 505 500	400-450	300-350	650-700	350-400	400-450	350-400	400-450

Zonal statistics for snow cover classes are shown in Table 42. Snow cover, determined by local climate and topography, has been shown to influence weathering rates (see Weathering and Erosion, pg. 15 onwards). The least common *R*- and L-values for areas of less snow cover are in the higher ranges. Consequently, high *R*- and L-values occur less often for areas of low to medium snow cover. Similarly, higher modal and median *R*- and L-values are observed for areas of high snow cover. Higher *R*- and L-values occur in areas of high snow cover. The opposite also applies, although the difference between low and medium snow cover is less pronounced than the difference between high and low and high and medium snow cover. When an analysis focuses on only high and low snow cover areas, it becomes clear that less snow cover yields lower *R*- and L-values, *i.e.* more weathered clast surfaces. These findings suggest that snow cover influences rock hardness rebound values.

Table 42: Zonal statistics for SH and Equotip mean rock hardness rebound values per snow zone (low, medium, high). Zonal statistics are determined using GIS.

Snow Zone	**Max**	**Min**	**Range**	**Average**	**Mode**	**Minority**	**Median**
Schmidt Hammer							
Low	35-40	25-30	45-50	30-35	25-30	30-35	30-35
Medium	40-45	20-25	35-40	25-30	25-30	40-45	25-30
High	35-40	25-30	45-50	30-35	30-35	25-30	30-35
Equotip							
Low	450-500	300-350	600-650	350-400	300-350	450-500	350-400
Medium	450-500	300-350	600-650	350-400	350-400	450-500	350-400
High	400-450	300-350	650-700	350-400	350-400	400-450	350-400

4.4 Near-Surface Ground Temperature Dynamics

Average ambient wind speeds recorded, seasonal minimum and maximum as well as seasonal ranges are shown in Table 43. The lowest average wind speeds occur for the summer months (8.0 ms^{-1}), with the autumn months recording the highest average wind speeds of 12.2 ms^{-1}. However, the highest average maximum speeds are observed during spring (39.5 ms^{-1}). The highest gust of wind (50.5 $m.s^{-1}$) also occurs for spring. This is the equivalent of 181.8 $km.h^{-1}$ or 98.172 kn (1 ms^{-1} = 1.944 kn = 3.6 $km.s^{-1}$).

Table 43: Average, minimum, maximum values as well as ranges observed for wind speed ($m.s^{-1}$) for the Vesleskarvet Nunataks, grouped by season.

Season	Average	Min	Max	Range
Autumn	12.2	0	34.8	34.8
Winter	11.0	0	34.4	34.4
Spring	11.3	0	39.5	39.5
Summer	8.0	0	31.0	31.0
Annual	10.6	0	39.5	39.5
n = 2 years; 14 months				

The dominant wind direction for the study site is slightly south of east, at approximately 100°. Table 44 depicts wind direction averages, minimum and maximum values recorded, as well as ranges and modal wind directions. Although wind directions occur for the entire wind rose (the whole circle of 360°), the main and dominant wind direction is an easterly one (see Table 3, pg. 48 for classifications of wind direction). The modal wind direction for the study site is 120°, 80°, 70° and 100° for autumn, winter, spring and summer respectively, ranging from east-north-east to east-south-east. This average easterly wind direction falls comfortably within the observed modal values. The summer months, with an average temperature of 98° and a mode of 100° are of interest, as iButtons recorded data during January and February.

Table 44: Average, minimum, maximum, range and modal values for the dominant wind direction (degrees clockwise from north) observed at SANAE IV, grouped by season.

Season	Average	Minimum	Maximum	Range	Mode
Autumn	100	0	360	360	120
Winter	100	0	360	360	80
Spring	103	0	360	360	70
Summer	98	0	360	360	100
Annual	100.3	0	360	360	90
n = 12 years; 128 months					

Calculations for average temperatures throughout the year for the study site are shown in Table 45. The lowest average temperature observed for the study site occurs during the winter months (-21.9℃); the highest average temperatures occur during summer (-8.3℃). All average seasonal temperature values are well below 0℃. Autumn and winter, although exhibiting different average minimum and maximum values, have the same range of 14.9℃. The highest range (21.1℃) in observed average hourly temperature values occurs during the spring months. The summer months, in contrast, show the lowest observed range of 13.1℃. The summer months, with an average temperature of -8.3℃ and a range of 13.1℃ are of interest, as iButtons recorded data during January and February.

Table 45: Mean, average maximum and average minimum values observed for ambient temperature (℃) for the Vesleskarvet Nunataks, grouped by season.

Season	**Average**	**Maximum**	**Minimum**	**Range**
Autumn	-17.4	-10.0	-24.9	14.9
Winter	-21.9	-13.9	-28.8	14.9
Spring	-17.8	-6.7	-27.8	21.1
Summer	-8.3	-2.2	-15.3	13.1
Annual	-16.4	-2.2	-27.8	-25.6
n = 12 years; 131 months				

The study site exhibits similar relative humidity values throughout the year, with Austral winter and summer seasons only differing by a few percentage values. Values for relative humidity are shown in Table 46. All seasons show average relative humidity values in the 60s; however, summer has the highest relative humidity with a value of 66%. In contrast, spring has the highest maximum value recorded (100%) as well as the highest range in observed relative humidity (74%). Autumn shows the lowest relative humidity value at 26%. The summer months, with an average relative humidity of 66% and a range of 57% are of interest, as iButtons recorded data during January and February.

Table 46: Mean, average maximum and average minimum values observed for relative humidity (%) for the Vesleskarvet Nunataks, grouped by season.

Season	**Average**	**Maximum**	**Minimum**	**Range**
Autumn	62	88	26	62
Winter	63	87	31	56
Spring	61	100	26	74
Summer	66	93	36	57
Annual	63	100	26	74
n = 12 years; 131 months				

Similarly to relative humidity, average pressure for the study site shows a similarity in values across the seasons. Values for observed pressure are shown in Table 47. Low-pressure systems are more favourable to precipitation events. Since Antarctica receives very little precipitation annually, as discussed in Study Site (pg. 6 onwards) and Weathering and Erosion (pg. 15 onwards), high average pressures are expected for the study site. All seasons show fairly high average pressure values, with minimum pressure values approximating 865 mb for all seasons. The highest average pressure occurs during the winter months (890.5 mb), with the lowest average value observed during spring (878.0 mb). The low average value for spring is mirrored by the lowest maximum pressure value observed also occurring during the spring months (895.3 mb). In addition, spring exhibits the highest range in observed pressure values at 132.7 mb. Autumn and summer exhibit near-identical maximum pressure observations at 992.5 mb and 992.3 mb respectively. The summer months, with an average pressure of 888.1 mb and a range of 122.4 mb are of interest, as iButtons recorded data during January and February.

Table 47: Mean, average maximum and average minimum values observed for pressure (mb) for the Vesleskarvet Nunataks, grouped by season.

Season	**Average**	**Maximum**	**Minimum**	**Range**
Autumn	890.5	992.5	865.5	127.0
Winter	884.4	986.7	864.3	122.4
Spring	878.0	895.3	862.6	132.7
Summer	888.1	992.3	869.9	122.4
Annual	885.3	992.3	862.6	129.7
n = 12 years; 131 months				

Table 48 (pg. 115) lists the number of freeze-thaw cycles observed for the study site for a number of thresholds during 2010-1012. Frozen and melted hours are also indicated, as is the average for the three years. Furthermore, exotherms and endotherms have been observed in data collected for the site (Meiklejohn, unpublished data). An average of 40 and 59 freeze-thaw cycles is observed for the three years using the -2.5°C and 0°C thresholds respectively. The higher the number of melted hours, the higher the number of cycles observed. This is to be expected as freezing and thawing requires the availability of moisture. There are also a higher number of frozen hours observed for the 0°C than the -2.5°C threshold. The 0°C threshold is of particular interest as 8480 frozen hours are observed, equating to 96.81% of available hours in a year (8760 hours [365*24]). In comparison, 94.11% of annual hours represent frozen hours at the -2.5°C threshold. In terms of melted hours, 2.27% and 4.97% of annual hours are observed for the 0°C and -2.5°C thresholds respectively.

Table 48: The number of freeze-thaw cycles, melted hours and frozen hours observed for various thresholds for three years (2010-2012) for the study site.

Description	**2010**	**2011**	**2012**	**Average**
Freeze-Thaw data using -0°C as boundary	44	33	44	40
Freeze-Thaw data using -2.5°C as boundary	82	44	51	59
Melted Hours using -0°C as boundary	185	182	230	199
Melted Hours using -2.5°C as boundary	505	360	441	435
Frozen Hours using -0°C as boundary	8571	8578	8291	8480
Frozen Hours using -2.5°C as boundary	8251	8400	8080	8244

Table 49 provides an overview of freeze-thaw cycles observed for the study site during the 2009/10, 2010/11, and 2011/12 summer Austral seasons using a variety of thresholds. The average number of cycles observed for the three summer seasons is 36 and 59 for the -2.5°C and 0°C thresholds respectively. It is also clear from the table that the higher the number of melted hours, the higher the number of cycles, similar to values shown in Table 48 (pg. 115). This again highlights the role of moisture, stressing the limiting role that moisture has on freeze-thaw cycles. As expected, the number of frozen hours is high, with more frozen hours observed for the 0°C than for the -2.5°C threshold. In comparison, more freeze-thaw cycles are observed for the 0°C than that observed for the -2.5°C threshold. An average of one cycle occurs every 2.5 days. This clearly shows that the number of freeze-thaw cycles observed is not high. Nevertheless, the data show that freezing and thawing does occur for the study site and that this process may not be discounted in geomorphic processes active in the area. Furthermore, 36 of the 40 observed mean cycles occur during the summer months. This is to be expected as higher temperatures and incoming solar radiation are observed during the summer months.

Table 49: Freeze-thaw cycles observed for various thresholds during the Summer austral seasons of 2009/10, 2010/11, and 2011/12.

Description	**2009/10**	**2010/2011**	**2011/2012**	**Average**
Freeze-Thaw data using -0°C as boundary	39	43	26	36
Freeze-Thaw data using -2.5°C as boundary	74	67	36	59
Melted Hours using -0°C as boundary	202	218	76	165
Melted Hours using -2.5°C as boundary	549	457	187	398
Frozen Hours using -0°C as boundary	4162	4150	4053	4122
Frozen Hours using -2.5°C as boundary	3815	3911	3942	3889

Summary statistics for iButton data from the 2010/11 and 2011/12 field season are shown in Table 50 and Table 51 (pg. 117). Data for the 2010/11 field season show that T1 and T5 are symmetrical, T2, and the average global data series (iB Mean 2011) finely positively skewed and T6 finely negatively skewed. T3, T7 and the PACE XR5 logger have positively skewed distributions. All iButton data for the 2011/12 field season, with the exception of sample 17 (iB17; highly positively skewed) are positively skewed. Similarly, the global data set (iB Mean 2012; n = 64 306) is positively skewed at 0.76 with a kurtosis value near zero (0.01). Skewness values are sufficiently low to allow for standardisation of values and assuming normal or near-normal distributions. Please refer to Appendix B: Statistical Descriptions, Ranges and Classes, Table 74 (pg. 167) for a description of terms used. Skewness values for 2010/11 range from -0.14 (T6) to 0.55 (PACE XR5). In 2011/12, skewness values range from 0.38 (iB7) to 1.04 (iB17). Data show that for the two field seasons, average, median and modal GST is generally below 0°C. During 2010/11, the lowest mean temperature occurs for the PACE XR5 logger (-2.03°C). In comparison, the highest mean temperature is observed for T7 (1.54°C), yielding a range of 3.57°C. In 2011/12, the lowest mean temperature is observed for iB14 (-3.86°C) with the highest mean temperature observed for iB5 (-0.10°C). This gives an overall maximum range of 29.64°C. Median temperature values during 2010/11 range from -2.40°C to 0.11°C for the PACE XR5 logger and T1 respectively. In comparison, for the 2011/12 field season GST range from -5.00°C for iB14 to -0.94°C for iB7. It is apparent that mean, median and modal temperatures for the first field season are higher than mean, median and modal temperatures for the second field season. This difference in modal and mean values may be ascribed to GST recorded for only ten days in 2010/11, compared to 30 days during 2011/12. In addition, a storm event occurred during the second field season, decreasing average GST recorded while also introducing variability into the data set. This increased variability is reflected by the *s* and sample variance values calculated for the second field season. Variability for the total dataset for 2011/12 is 28.78 with an *s* of ±5.37°C. In comparison, the sample variance for the global data set for the first field season is 10.07 with an *s* of ±3.17°C. Overall, standard errors are low for all sample sites for both field seasons.

Table 50: Summary statistics calculated on GST (°), soil moisture and ambient temperature (°C) for each iButton sample site and the PACE XR5 data logger, during the 2010/11 field season.

	PACE Logger	T1	T2	T3	T5	T6	T7	iB Mean 2011	Soil Moisture	Ambient Temperature
Mean	-2.03	-0.35	-2.61	-1.03	-0.99	-0.91	1.54	-0.58	3.17	-3.28
Standard Error	0.24	0.25	0.22	0.27	0.16	0.10	0.27	0.20	0.15	0.17
Median	-2.40	0.11	-2.42	-1.41	-0.94	-0.69	0.59	-0.88	2.62	-3.57
Mode	-3.67	0.61	-6.45	-4.92	-0.44	-0.46	-1.92	N/a	0.58	-2.57
s	3.73	3.64	3.40	3.97	2.34	1.29	3.93	3.17	2.38	2.71
Sample Variance	13.94	13.26	11.53	15.78	5.47	1.67	15.45	10.07	5.68	7.36
Kurtosis	-0.45	-0.97	-1.14	-1.15	-0.88	-0.55	-1.02	-1.02	-1.57	0.22
Skewness	0.55	0.04	0.14	0.33	0.09	-0.14	0.48	0.18	0.27	0.74
Range	16.25	14.08	12.59	13.56	8.56	5.03	13.55	14.96	7.27	13.46
Minimum	-7.68	-7.45	-8.47	-6.94	-4.97	-3.48	-4.43	-6.39	0.44	-8.10
Maximum	8.57	6.64	4.12	6.62	3.59	1.55	9.11	8.57	7.70	5.36
Sum	-491.68	-74.99	-613.68	-231.13	-225.57	-159.66	327.55	-139.17	767.10	-794.15
Count	242	216	235	224	227	176	213	240	242	242

Table 51: Summary statistics calculated on GST (°) for each iButton sample site, as well as the global data series, observed during the 2011/12 field season.

	iB1	iB2	iB3	iB4	iB5	iB6	iB7	iB8	iB9	iB10	iB11	iB13	iB14	iB15	iB16	iB17	iB Mean 2012
Mean	-0.74	-1.71	-1.21	-2.16	-0.10	-2.47	-1.27	-2.02	-3.53	-1.84	-3.26	-2.02	-3.68	-1.31	-0.92	-1.94	-1.88
Standard Error	0.10	0.07	0.09	0.07	0.09	0.09	0.07	0.08	0.08	0.09	0.06	0.08	0.07	0.08	0.10	0.09	0.07
Median	-1.70	-1.84	-1.72	-2.47	-1.17	-3.72	-0.94	-2.04	-4.61	-2.85	-3.79	-2.25	-5.00	-1.42	-1.97	-3.53	-2.59
Mode	-7.24	-7.63	-7.57	-7.76	0.21	-7.99	-0.06	0.16	-8.26	-7.81	-7.31	0.20	-7.71	0.27	-8.14	-7.11	-7.63
s	6.15	4.73	5.54	4.65	6.03	6.00	4.71	5.30	4.95	5.48	3.72	4.81	4.24	5.24	6.19	5.91	5.37
Sample Variance	37.81	22.35	30.72	21.65	36.31	35.96	22.17	28.05	24.45	30.04	13.83	23.18	18.00	27.46	38.27	34.98	28.78
Kurtosis	-0.21	-0.41	-0.74	-0.14	-0.15	-0.16	-0.52	-0.35	-0.33	-0.32	-0.26	-0.35	0.18	-0.44	-0.50	0.29	0.01
Skewness	0.72	0.51	0.46	0.66	0.83	0.77	0.38	0.55	0.68	0.70	0.61	0.55	0.96	0.57	0.65	1.04	0.76
Range	27.24	21.56	22.94	21.24	26.70	26.74	21.57	24.27	22.82	24.97	17.16	22.87	18.43	23.77	25.99	25.43	29.64
Minimum	-10.63	-9.15	-9.84	-9.52	-8.83	-11.77	-8.91	-10.74	-11.54	-10.77	-9.32	-10.50	-9.41	-9.77	-10.28	-10.13	-11.77
Maximum	16.61	12.41	13.10	11.72	17.87	14.97	12.66	13.53	11.28	14.20	7.84	12.38	9.02	14.00	15.72	15.30	17.87
Count	4 033	4 012	4 033	4 008	4 033	4 033	4 033	4 033	3 986	4 033	3 932	4 016	4 022	4 033	4 033	4 033	64 306

Eleven of the sample sites for 2011/12 (iB1-4, 6, 9-11, 14, 16-17), as well as the global data series show modal temperature values between -7°C to -8°C. The remaining sample sites (iB5, 8, 13, 15) yield modal temperatures just above 0°C. The difference in modal temperatures is of interest, as samples 7, 13 and 15 all occur in close proximity to each other toward the western section of the blockfield, supporting the contention that topography exerts a control on ground temperature regimes. Nevertheless, temperatures recorded are fairly variable with temperatures as high as 17.87°C recorded for iB5. iB11 exhibits the lowest maximum temperature of 7.84°C. This site also has the lowest range in temperatures at 17.16°C. The largest range (27.24°C) is observed for iB1. The large ranges displayed by all samples, with temperatures reaching as high as 17.87°C indicate that, in the presence of sufficient moisture, near-surface temperature dynamics for the study site should promote micro-scale landforms consistent to a diurnal frost environment. The variability in observed temperatures indicate an active layer in which weathering and soil formation may be enhanced, taking the dry, cold and desert environment of the continent into consideration. Summary statistics for the climate parameters of wind speed and direction, ambient temperature, relative humidity and pressure for the month under investigation are shown in Table 52.

Table 52: Summary statistics for the climate parameters of wind speed ($m.s^{-1}$) and direction (°), ambient temperature (°C), relative humidity (%) and pressure observed for the study site during the 2011/12 field season.

	Wind Speed	**Wind Direction**	**Ambient Temperature**	**Relative Humidity**	**Pressure**
Mean	7.10	131.01	-8.23	67.69	878.42
Standard Error	0.07	1.12	0.04	0.27	0.08
Median	6.20	104.10	-8.40	66.40	878.50
Mode	4.70	76.10	-9.00	93.30	877.60
s	4.17	70.12	2.48	16.71	4.76
Sample Variance	17.41	4916.78	6.15	279.15	22.68
Kurtosis	0.43	-0.06	-0.18	-0.74	0.35
Skewness	0.96	1.11	0.23	-0.05	-0.18
Range	19.60	340.10	13.70	72.50	25.80
Minimum	0.00	0.00	-14.40	24.80	864.20
Maximum	19.60	340.10	-0.70	97.30	890.00
Count	3587	3943	3565	3798	3893

Adlam *et al.* (2010) suggest that wind direction and ambient temperature exert the greatest influence on the active layer, *i.e.* GST dynamics. Ishikawa (2003) also stresses the impact of air temperature on GST. As such, the following discussion focuses on these climate parameters. Ambient temperature is finely positively skewed compared to the highly positively skewed distribution of wind direction. Wind speed exhibits a positively skewed distribution. The final climate parameters of relative humidity and pressure have symmetrical and finely negatively skewed distributions respectively.

Similar to iButton measurements, skewness values, medians and mean of these climate parameters are sufficiently low and similar in values to allow for standardisation of raw data (assuming normal distributed data series). The modal wind speed for the days under investigation is 4.7 $m.s^{-1}$, below the average of 7.1 $m.s^{-1}$. This average wind speed is less than the calculated annual average of 10.6 $m.s^{-1}$, but approximates the 8.0 $m.s^{-1}$ calculated for the summer months (please refer to Table 43, pg. 112). The maximum speed recorded is 19.60 $m.s^{-1}$, yielding a range of almost 20 $m.s^{-1}$. Further similarities occur for relative humidity and pressure for long-term climate data and weather observed for the period under investigation. Average relative humidity for the period under investigation is 67.69%, close to the average summer relative humidity of 66% (please refer to Table 46, pg. 113). Average pressure observed is 878.42 mb, compared to the average summer pressure of 888.10 mb. Please refer to Table 47 (pg. 114) for a listing on annual and seasonal observed pressure for the study site. Wind direction is, as expected, highly variable, as indicated by a high variance of 4916.78 and a relatively high standard error of 1.12 (Table 52, pg. 118). However, the median wind direction of 104.10° agrees with the long-term analyses of climate data for the area, which shows that the dominant wind direction is out of a generally eastern direction (please refer to Table 44, pg. 112). The lowest ambient temperature recorded is -14.40°C while the highest temperature is -0.70°C. This yields a range of 13.80°C. Average, median and modal temperatures recorded (-8.23°C, -8.40°C and -9.00°C respectively) fall within a 0.77°C to each other. Average ambient temperatures are, therefore, lower than average near-surface temperatures recorded. Nevertheless, modal temperature values approximate each other. Ambient temperatures do not pass the 0°C mark and the lowest recorded temperature is more than 2°C below the lowest temperature recorded with an iButton during the period under investigation. In contrast, iButtons recorded temperatures are well above 0°C, indicating a more variable and dynamic regime of GST compared to ambient temperatures. Discussions on the role that solar radiation received has on weathering across the blockfield (please refer to Rock Hardness: Schmidt Hammer and Equotip Methods, pg. 101 onwards) may be applied to ground temperatures as well, as suggested by Adlam *et al.* (2010).

A graph of averages taken for all sample sites for each data point recorded and combined into one global data series is shown in Figure 64 (pg. 120). The trendline is indicated by a dashed line, as is the equation ($y = -0.0015x + 1.2502$) of the trendline. The 13th, 14th, 17th-19th of January was warm and calm, in contrast to the 15th and 16th of January when drifting snow conditions were observed. Between the 20th and 25th the region experienced a storm with whiteout conditions (high wind speeds, low temperatures). Near-surface temperatures appear to follow ambient temperature conditions, although a time lag of approximately 12-24 hours is observed. This agrees with findings of Adlam *et al.* (2010), who suggest that soil temperatures respond to ambient temperatures within a 24-hour period. The storm event occurred from the 20th-25th of January and near-surface temperatures dip

noticeably from the 21st-26th of January. Similarly, a peak in temperatures is observed between the 14th and 15th of January, approximately a day after the study site experienced calm and warm conditions. The same applies to the 17th to 19th of January, where higher peaks on the graph occur around the 18th to 20th of January. Ambient temperature and near-surface temperatures, therefore, appear to be related with ground temperatures influenced by ambient temperatures. Near-surface temperatures also appear less variable, *i.e.* stable during the time of the storm event, similar to the stability of moisture samples discussed in Rock Properties and Moisture Uptake (pg. 130 onwards). This supports findings by *e.g.* Ishikawa (2003), Hedding (2008), and Grab *et al.* (2012) who suggest that snow cover has an insulating effect on GST. In addition, during the storm event GST are low and do not surpass the 0°C mark.

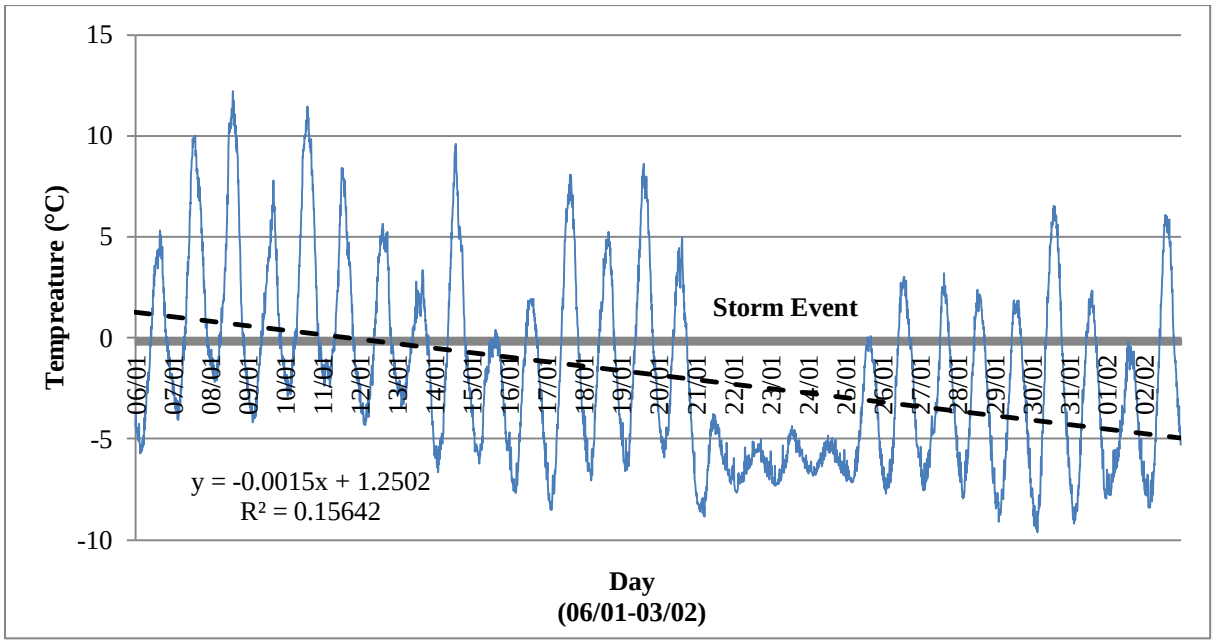

Figure 64: Temperature graph of combined GST observed for the study site for the 2011/12 field season. The storm even of the 20th to the 25th of January can be clearly identified from the graph. A dashed line indicates the trendline. The equation of the trendline and R^2-statistic are also indicated.

Analyses of GST recorded using the PACE XR5 logger and six iButtons during the 2010/11 field season show that ambient temperatures influence soil moisture and GST. Pearson's correlation coefficients for these parameters are shown in Table 53 (pg. 121). Soil moisture and temperatures have a strong and positive relationship at 0.67, which is significant at 99%. Similarly, GST and ambient temperatures show a strong positive relationship at 0.84, at 99% significance. This correlation is higher than that calculated for the 2011/12 field season (see discussion below). This may be ascribed to ambient temperatures being recorded by the PACE XR5 logger and not the SAWS station located at SANAE IV, on the Southern Buttress of the Vesleskarvet Nunataks. The PACE XR5 logger records temperature values at the same location it records GST and soil moisture. This should yield higher correlation coefficients, as shown by Table 53 (pg. 121). Findings for the study

site support the argument of Adlam *et al.* (2010), that soil moisture increases active layer depths through heat transfer and thermal conductivity (please see discussion under Near-Surface Ground Temperature Dynamics, pg. 41-44). The high correlation coefficient calculated between soil moisture and average GST suggests that greater amounts of moisture yield higher temperatures observed in the ground, *i.e.* a deeper active layer. Soil moisture and ambient temperatures yield the lowest correlation coefficient. Nevertheless, the correlation coefficient calculated between these two parameters is fairly strong and positive, at a 99% confidence level.

Table 53: Pearson's correlation coefficient matrix calculated between ambient temperature (°C), soil moisture and average GST (°C) observed during the 2010/11 field season. All coefficients are significant at 99% (α = 0.01, $p < 0.01$).

	Soil Moisture	**iB Mean 2011**	**Ambient Temperature**
Soil Moisture	1		
iB Mean 2011	0.67	1	
Ambient Temperature	0.56	0.84	1

The strength of these relationships is reflected on Figure 65, where ambient temperature, average GST and soil moisture follow the same general curve, *i.e.* peaks and troughs are similar. One can, however, notice that soil moisture lags behind ambient temperatures. This is similar to the lag-effect noticed between GST and ambient temperatures (discussed above). The lower than expected correlation coefficient calculated for these two parameters may be partly ascribed to the observed lag-effect.

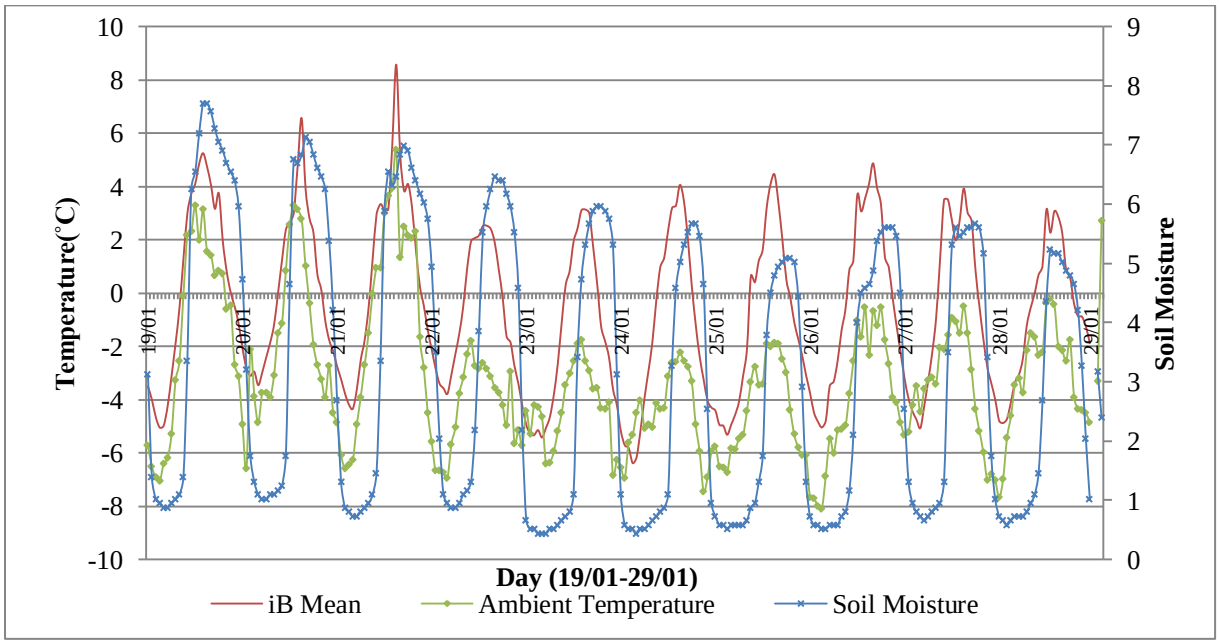

Figure 65: Soil moisture, average GST and ambient temperature observed for ten days from the 19th to 29th of January 2011. Soil moisture never dips below zero. Ambient temperature tends to stay below 0°C with average GST yielding higher temperatures.

In order to determine possible relationships between the five climate parameters of wind direction and speed, ambient temperature, relative humidity and pressure with GST, Pearson's correlation coefficients are shown in Table 54. All calculated coefficients are significant at 99% ($\alpha = 0.01$, $p < 0.01$). Near-surface temperatures show a negative (inverse) relationship to wind speed and relative humidity. The other parameters of wind direction, ambient temperature and pressure show a positive (direct) relationship to average GST. Ambient temperature has the highest correlation coefficient of 0.62), indicating a strong positive relationship to average GST. This agrees with findings of Ishikawa (2003) and Adlam *et al.* (2010), who suggest that temperature exerts the greatest influence on active layer dynamics, with higher ambient temperatures resulting in deeper active layers. Furthermore, it supports the earlier finding of ambient temperature affecting near-surface temperatures, albeit with a lag effect (see Figure 65, pg. 121). In contrast, wind direction is weakly (0.18) related to near-surface temperatures. Although the influence of wind direction appears negligible, strong winds are known to influence ground response to ambient temperatures. Wind strength has a positive correlation to active layer depths (Adlam *et al.*, 2010) and wind speed for the study site shows a fairly strong negative correlation (-0.44) to average GST. Consequently, it may be argued that an increase in wind speed yields a decrease in ground temperatures. Similarly, an increase in relative humidity yields a decrease in near-surface temperatures, as can be deduce from the negative correlation coefficient of -0.30. In contrast, an increase in pressure yields an increase in ground temperatures (correlation coefficient of 0.31). In particular, the combination of low temperatures and high wind speeds, as observed during storm conditions, would yield low GST, as already indicated on Figure 64 (pg. 120).

Table 54: Pearson's correlation coefficient matrix calculated between individual climate parameters and average GST (°C) for the 2011/12 field season. Climate parameters consist of wind speed ($m.s^{-1}$) and direction (°), ambient temperature, relative humidity (%) and pressure (mb). All coefficients are significant at 99% ($\alpha = 0.01$, $p < 0.01$).

Parameters	**iB Mean 2012**	**Wind Speed**	**Wind Direction**	**Ambient Temperature**	**Relative Humidity**	**Pressure**
iB Mean 2012	1.00					
Wind Speed	-0.44	1.00				
Wind Direction	0.18	-0.33	1.00			
Ambient Temperature	0.62	-0.42	0.10	1.00		
Relative Humidity	-0.30	0.61	-0.38	-0.29	1.00	
Pressure	0.31	-0.39	0.52	0.19	-0.20	1.00

Temperature surfaces are created in GIS by interpolating sample temperature data across the blockfield. Universal Kriging with a linear semivariogram model (using quadratic drift) is employed. Nugget, lag sizes, major ranges and partial sills are calculated separately for each data series, using the method described in Interpolation and geostatistical data analyses (pg. 72). Figure 66 (pg. 124)

shows selected GST observed for midnight and midday from the 6th to 8th of January. The 6th, 7th and 8th of January were calm and warm, yielding highly variable GST. This variability is reflected on Figure 66 (pg. 124). Midday temperatures consistently measure higher than midnight temperatures. Furthermore, the western and northern areas of the study site show higher temperatures during the day. Similar trends are observed for night temperatures. The amount of red shown on the map for the 8th of January (midday) suggests this is the warmest day for the three days investigated. A peak for the 8th, shown on Figure 64 (pg. 120) supports this finding. GIS analyses, therefore, corroborate results of classical statistics. Figure 67 (pg. 125) shows midday and midnight GST observed for sample sites for the 20th to 22nd of January. These days mark the onset of a storm with whiteout conditions experienced for the study site. As discussed above and shown in Figure 64 (pg. 120), GST during the storm event is less variable and more stable. These characteristics are reflected on Figure 67 (pg. 125). The range of colours is less, *i.e.* colours are more often yellow and blue than red, suggesting smaller absolute ranges between day and night observed temperatures.

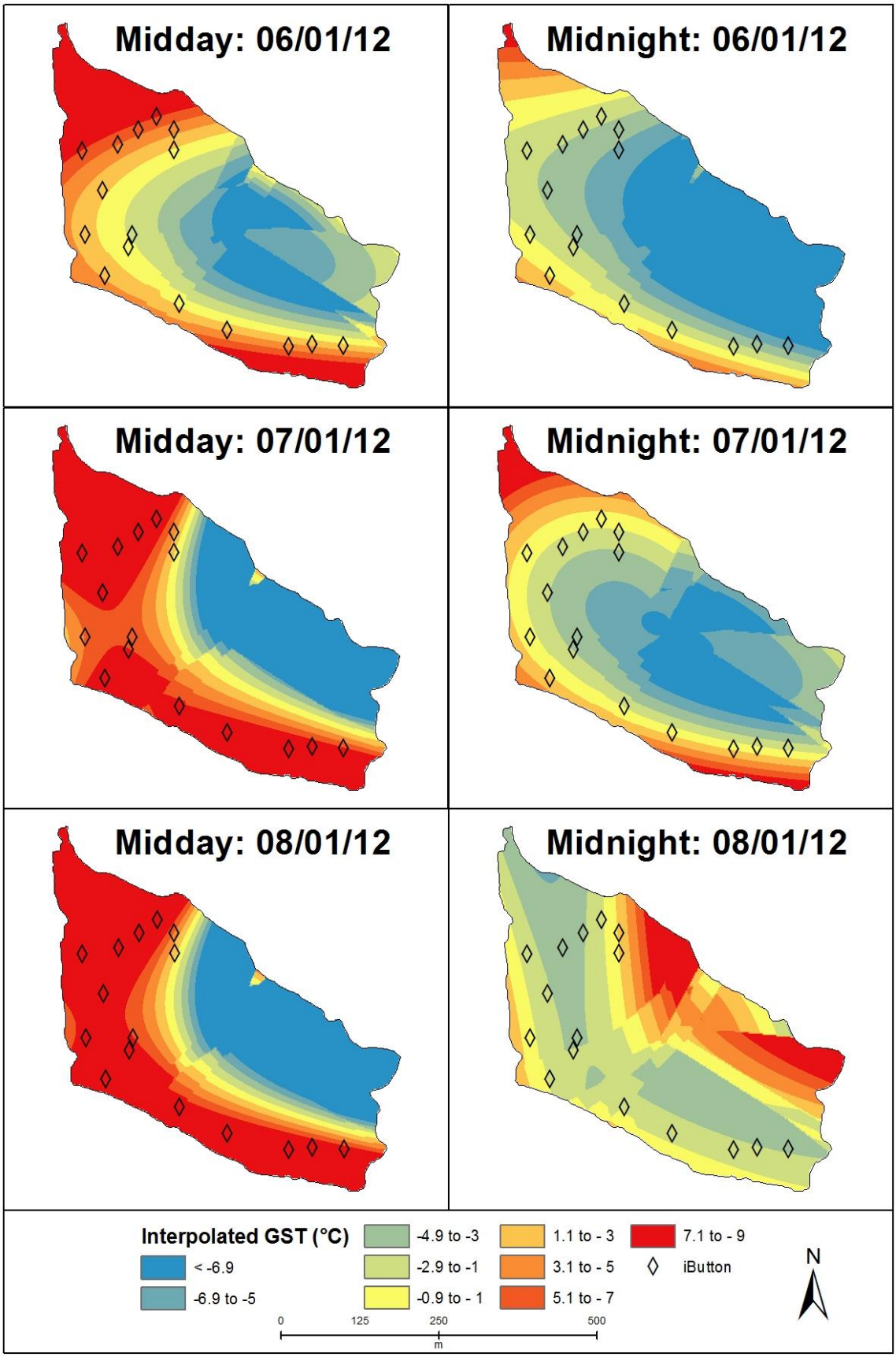

Figure 66: GST interpolated for sample sites across the study using Universal Kriging. Midday and midnight temperatures for the 6th to the 8th of January are indicated. Colours toward the red portion of the spectrum indicate higher temperatures; lower temperatures are shown by blue hues.

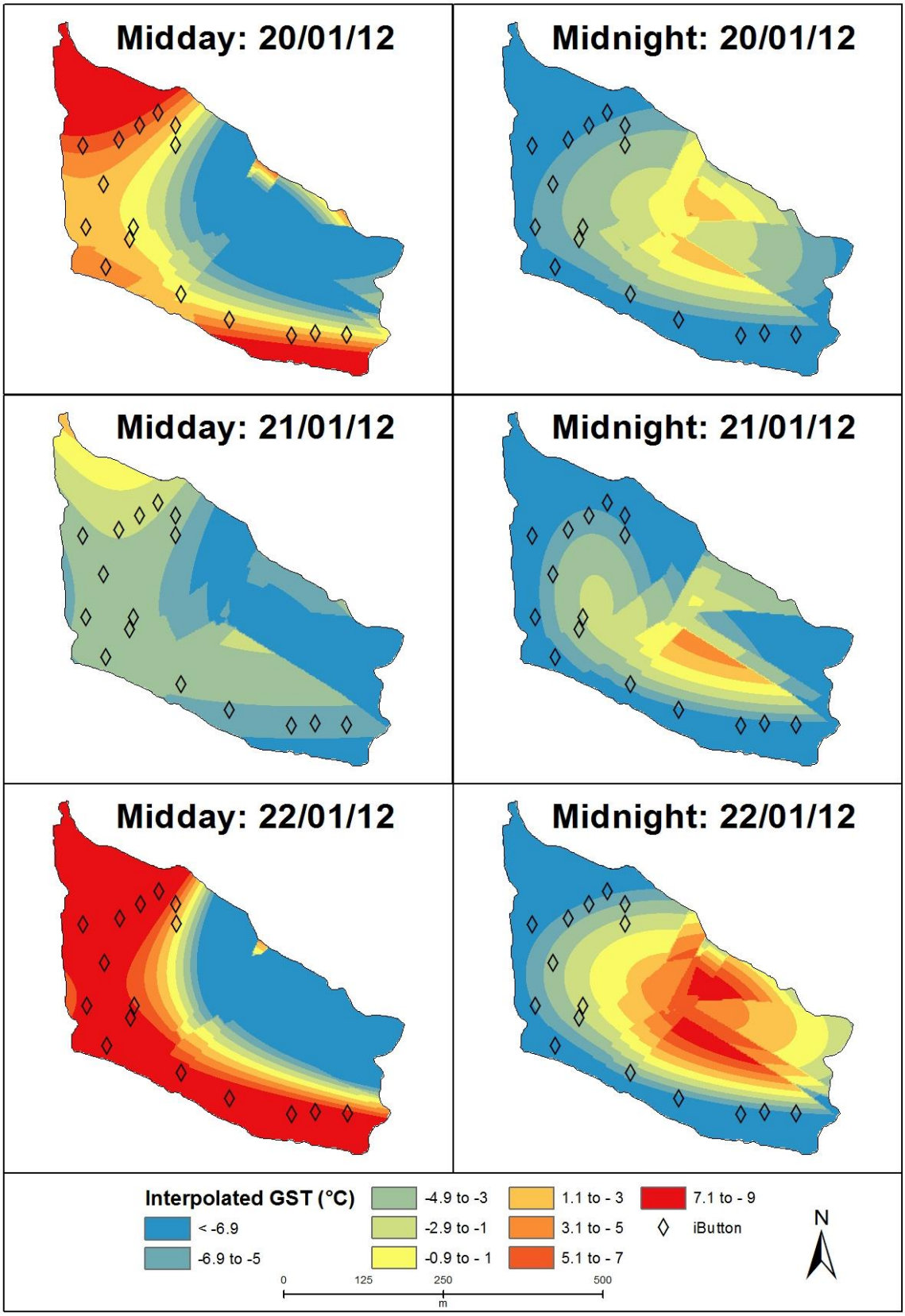

Figure 67: GST shown for selected days from the 20th to 22nd of January. GST is shown for midday and midnight for the days under investigation. Colours toward the red portion of the spectrum indicate higher temperatures; lower temperatures are shown by blue hues.

Trendline equations and R^2 for the different climate parameters are shown in Table 55. R^2 values are low overall, ranging from 0.00163 (relative humidity) to 0.15642 (near-surface temperature data). Consequently, in no instance is more than 16% of the total variance of each specific parameter explained by a linear relationship through the indices of that specific data series. In particular, only 0.2% of the variability of relative humidity may be explained by the linear relationship drawn through the data series. Data, therefore, do not follow linear patterns. Graphs showing average GST compared to the various climate parameters, as well as their concomitant trendlines and equations, are shown in Appendix F: Climate Parameters, pg. 179 onwards. Figure 96 (pg. 179) shows wind speed compared to average GST, whereas Figure 97 (pg. 180) depicts wind direction compared to average GST. Figure 98 (pg. 180), Figure 99 (pg. 181) and Figure 100 (pg. 181) show ambient temperatures, relative humidity and pressure compared to average GST respectively.

Table 55: Trendline equations and R^2-statistics calculated for climate parameters and the global average GST (°C) data series for the 2011/12 field season. Climate parameters include wind speed ($m.s^{-1}$) and direction (°), ambient temperature (°C), relative humidity (%) and pressure (mb).

Parameter	**Trendline Equation**	**R^2**
iB Mean 2012	y = -0.0015x + 1.2502	R^2 = 0.15642
Wind Speed	y = 0.0003x + 6.4746	R^2 = 0.00817
Wind Direction	y = -0.0091x + 149.55	R^2 = 0.02317
Ambient Temperature	y = -0.0007x - 6.7771	R^2 = 0.11865
Relative Humidity	y = -0.0006x + 68.84	R^2 = 0.00163
Pressure	y = -0.0013x + 881.05	R^2 = 0.10409

In the presence of topographic control, samples in similar topographic settings should relate to each other. Pearson's correlation coefficient calculated for the different sample sites (Table 56, pg. 128) show that iB13 and iB14 have negative and weak relationship to the other sample series'. iB13 is of interest as this data series also yields modal temperatures slightly above 0°C. However, the correlation coefficient does not conclusively show that samples differ significantly, nor does it shed light on whether or not topographic control on GST dynamics exists. ANOVA calculations, as well as Fisher's LSD tests are more appropriate to determining similarities or differences in populations. The null and alternate hypotheses of ANOVA are given below.

H_0 = ground temperature values are similar for all sample points

H_a = ground temperature values vary across the nunatak

Following ANOVA calculations, Fisher's LSD tests were run on individual data series to determine similarity of variances. The null and alternate hypotheses of Fisher's LSD for these tests are given on the following page.

H_0 = *the two population variances are equal,* i.e. $\mu_1 = \mu_2$

H_a = *the two population variances are not equal,* i.e. $\mu_1 \neq \mu_2$

A more detailed explanation of both statistical tests mentioned above and their applications in the current context is given under Near-surface ground temperature dynamics (pg. 67 and pg. 68 respectively). ANOVA calculations for the 2010/11 field season sample sites, as well as the PACE XR5 data logger are shown in Appendix F: Climate Parameters Graphs and Inferential Statistics on Near-Surface Temperature Dynamics, Table 79 (pg. 182). Similarly, ANOVA calculations for all sample sites, as well as the average global population for the 2011/12 field season are shown in Table 80 (pg. 182). For both ANOVA analyses the test statistics exceed critical values, yielding a rejection of H_0 at 99% ($\alpha = 0.01$; $p < 0.01$). Sample temperature population variances are, therefore, dissimilar. Fisher's LSD results for the 2010/11 and 2011/12 field season are shown in Table 81 and Table 82 in Appendix F: Climate Parameters Graphs and Inferential Statistics on Near-Surface Temperature Dynamics (pgs. 183 and 184 respectively). A summary of Fisher's LSD tests for the 2010/11 and 2011/12 field seasons are given in Table 57 and Table 58 (pg. 128).

Six out of the possible 21 pairings for the 2010/11 field season show similarities in population variances. These pairings occur for the PACE XR5 logger with T2; T1 with T3; T1 with T6; T3 with T5; T3 with T6 and T5 with T6. Fifteen (15) out of a possible 120 pairings for the 2011/12 field season exhibit similar populations. Similar population variances occur for the pairings of iB1 with iB16; iB2 with iB10; iB3 with iB7 and iB15; iB4 with iB8, iB13 and iB17; iB7 with iB15; iB8 with iB10, iB13 and iB17; iB9 with iB14; iB10 with iB13 and iB17 and iB13 with iB17. All other pairwise comparisons are dissimilar. ANOVA and Fisher's LSD tests suggest that external parameters such as topography (slope gradient and aspect) and solar radiation received (for the period under investigation) may influence site-specific GST. Snow cover may be excluded in these analyses as snow cover has an insulating effect on ground temperatures and data loggers were placed in snow free areas and cleared of snow.

Table 56: Correlation matrix calculated for the different 2011/12 field season iButton sample sites.

Sample	iB1	iB2	iB3	iB4	iB5	iB6	iB7	iB8	iB9	iB10	iB11	iB13	iB14	iB15	iB16	iB17
iB1	1.00															
iB2	0.96	1.00														
iB3	0.97	0.95	1.00													
iB4	0.92	0.95	0.93	1.00												
iB5	0.94	0.91	0.95	0.90	1.00											
iB6	0.96	0.96	0.95	0.93	0.89	1.00										
iB7	0.93	0.96	0.92	0.92	0.92	0.89	1.00									
iB8	0.93	0.97	0.94	0.94	0.91	0.94	0.96	1.00								
iB9	0.92	0.95	0.92	0.94	0.88	0.96	0.91	0.96	1.00							
iB10	0.92	0.93	0.94	0.97	0.92	0.92	0.94	0.95	0.94	1.00						
iB11	0.91	0.89	0.93	0.89	0.90	0.89	0.82	0.84	0.87	0.87	1.00					
iB13	-0.28	-0.29	-0.30	-0.29	-0.26	-0.28	-0.28	-0.29	-0.29	-0.28	-0.40	1.00				
iB14	0.12	0.13	0.13	0.14	0.10	0.13	0.12	0.13	0.13	0.12	0.17	-0.35	1.00			
iB15	0.96	0.97	0.95	0.94	0.93	0.93	0.98	0.97	0.94	0.96	0.85	-0.29	0.13	1.00		
iB16	0.98	0.97	0.98	0.94	0.94	0.97	0.93	0.94	0.93	0.94	0.92	-0.29	0.12	0.96	1.00	
iB17	0.91	0.89	0.91	0.88	0.93	0.90	0.90	0.91	0.91	0.93	0.86	-0.25	0.11	0.93	0.93	1.00

Table 57: Summary of acceptance or rejection of H_0, following Fisher's LSD tests, for the 2010/11 field season GST sample sites.

Pairs	*t*-Statistic	P Two-Tail	Accept H_0	Number of Pairs	Percentage of Total
PACE&T2; T1&T(3,6); T3&T(5, 6); T5&T6	> 1.97	> 0.05	Yes	6	28.6%
All other combinations	< 1.97	< 0.05	No	21	71.4%

Table 58: Summary of acceptance or rejection of H_0, following Fisher's LSD tests, for the 2011/12 field season GST sample sites.

Pairs	*t*-Statistic	P Two-Tail	Accept H_0	Number of Pairs	Percentage of Total
iB1&iB16; iB2&iB10; iB3&iB(7,15); iB4&iB(8,13,17); iB7&iB15; iB8&iB(10, 13, 17); iB9&iB14; iB10&iB(13, 17); iB13&iB17	>1.96	> 0.05	Yes	15	12.5%
All other combinations	< 1.96	< 0.05	No	105	87.5%

Results of GIS analyses (sample sites overlain with aspect; slope gradient, elevation and solar radiation received) are shown in Appendix F: Climate Parameters Graphs and Inferential Statistics on Near-Surface Temperature Dynamics, Table 83 (pg. 187). Table 59 provides a brief summary of similarities or differences observed for aspect orientation, slope gradient, elevation and mean solar radiation received for the period under investigation for the various sample sites. Pairings yielding an acceptance of H_0 for Fisher's LSD tests show similar mean solar radiation received (96% similarity), as well as similarities in elevation (83% similarity). Slope gradient shows a similarity value of 63%. Aspect does not appear to play a significant role (33% similarity) on GST dynamics. This is in contrast to findings on aspect control on weathering, discussed under Rock Hardness: Schmidt Hammer and Equotip Methods (pg. 101 onwards). The scarcity of soil, especially on steeper slopes, decreases the weighting of slope gradient on GST dynamics. Furthermore, the range of elevation values is not great for the study site, decreasing the importance of this parameter on ground temperature dynamics. Nevertheless, topography and relief are known to influence active layer dynamics (Weinert, 1980; Vieira *et al.*, 2010; Grab *et al.*, 2012), as reflected by the similarity of elevation values for these pairings. Findings suggest that mean summer solar radiation received exerts the greatest control on GST. This is in agreement to Adlam *et al.* (2010), who argue the importance of summer radiation received on active layer dynamics.

Table 59: Summary of similarities and differences between sample sites in terms of aspect (north, east, south, west, top), slope gradient (°), elevation (MASL) and mean solar radiation ($WH.m^{-2}$) received for the period under investigation.

Pairing	**Aspect**	**Slope**	**Elevation**	**Mean Solar Radiation**
PACE-T2	No	Yes	Yes	Yes
T1-T2	Yes	Yes	Yes	Yes
T1-T3	No	Yes	Yes	Yes
T1-T6	No	Yes	Yes	Yes
T3-T5	Yes	Yes	Yes	Yes
T3-T6	No	Yes	Yes	Yes
T5-T6	No	Yes	Yes	Yes
iB1-iB16	No	No	No	Yes
iB2-iB10	No	No	Yes	No
iB3-iB7	No	No	No	Yes
iB3-iB15	No	No	No	Yes
iB4-iB8	No	Yes	Yes	Yes
iB4-iB13	No	Yes	Yes	Yes
iB4-iB17	Yes	No	Yes	Yes
iB7-iB15	Yes	Yes	Yes	Yes
iB8-iB10	No	No	Yes	Yes
iB8-iB13	Yes	Yes	Yes	Yes

Pairing	Aspect	Slope	Elevation	Mean Solar Radiation
iB8-iB17	No	No	Yes	Yes
iB9-iB14	No	Yes	No	Yes
iB10-iB13	No	No	Yes	Yes
iB10-iB17	Yes	Yes	Yes	Yes
iB13-iB17	No	No	Yes	Yes

4.5 Rock Properties and Moisture Uptake

A linear graph depicting average percentage weight gain or loss for samples within each group is shown on Figure 68. Large variability in series movements is observed for the 13th to 19th of January. As discussed in Near-Surface Ground Temperature Dynamics (pg. 112 onwards), the 13th, 14th, 17th-19th of January was warm and calm, providing ideal situations for snow or ice melt during the day and freezing of snowmelt at night. The 15th and 16th experienced drifting snow conditions. The warm and fairly wind still days, interspersed by windier and colder days provided variable climate conditions to the study site. This variability is reflected in the series' curves on Figure 68.

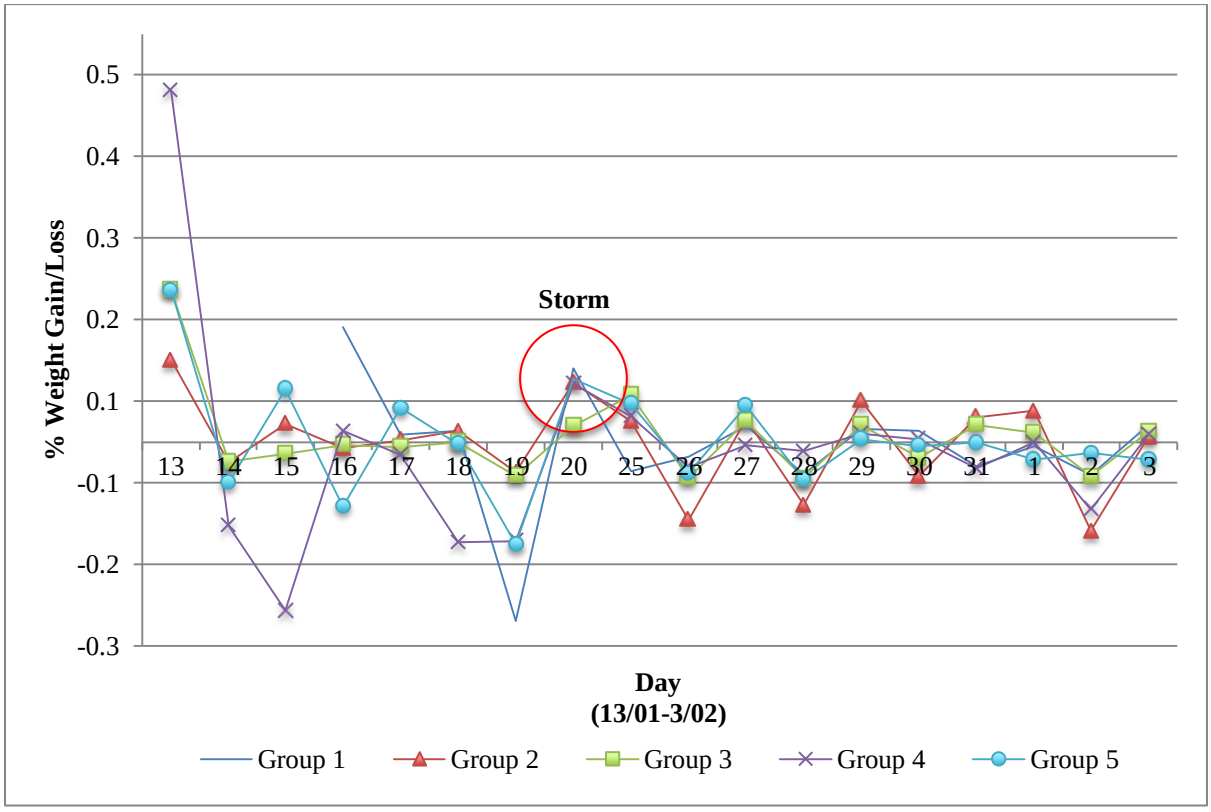

Figure 68: Average percentage weight gain or loss (over each 24-hour period) for grouped samples. Group 1 (ice) is indicated by a solid line; Group 2 (rock) by a solid line interspersed by a triangular marker; Group 3 (soil) by a solid line with a rectangular marker; Group 4 (placed on snow) by a solid line with a cross as a marker and Group 5 (buried in snow) by a solid line with a circular marker. A red circle indicates the storm event.

Between the 20th and 25th the region experienced a storm with whiteout conditions. During this time samples are fairly stable in terms of weight gain or loss (please refer to Figure 68 and the storm event indicated on it). This decrease in variability and apparent stability mirrors that of near-surface temperature data recorded by iButtons (please refer to Near-Surface Ground Temperature Dynamics, pg. 120). This is to be expected; as for these days weather conditions remained the same (high wind speeds and relative humidity, low temperatures and pressure) throughout the diurnal cycle. Please refer to Table 60 for calculated weather parameters. On the days following drifting snow or storm events, samples show a loss in weight, *i.e.* moisture was lost. This may be explained by the warm and calm days having the lowest relative humidity and greatest amount of solar radiation received per unit area, compared to storm or drifting snow events. Groups 1, 2 and 4 show the greatest crests and depressions overall, suggesting the greatest variability amongst data. This visual observation is confirmed by calculating *s* for all groups, discussed in greater detail below.

Table 60: Weather conditions for the study site for the duration of samples remaining in the field. Wind speed ($m.s^{-1}$), ambient temperature (°C), relative humidity (%) and pressure (mb) are indicated.

Description	**Days**	**Wind Speed**	**Ambient Temperature**	**Relative Humidity**	**Pressure**
Calm, Warm	13, 14, 17-19, 2	4.99	-7.82	68.42	883.07
Storm	20-25	12.15	-9.38	78.49	874.00
Drifting Snow	15, 16, 27, 1	9.33	-8.10	74.52	879.96

Averages and *s* for percentage weight gain or loss for each group are listed in Table 61 (pg. 132). Samples placed on bare rock and on top of snow show a loss of weight on average, whereas samples placed on ice, buried in snow and placed on soil show a gain in weight on average. The highest variation within a population is observed for samples of Group 4 (placed on snow), with the least variation observed for samples of Group 3 (placed on soil). The next lowest *s* is observed for samples of Group 5 (buried in snow). These samples are less exposed to external climate parameters and should, therefore, exhibit less variable measurements, reflecting the insulating properties of snow cover (Hedding, 2008). The highest average percentage weight gain is observed for Group 3 (placed on soil), followed by Group 5 (buried in snow). Soil retains moisture more easily than bare rock, allowing for easier uptake of moisture by clasts. Samples placed on ice, in contrast, exhibit the least average percentage weight gain; suggesting moisture becomes less readily available in these environmental settings. Samples placed on bare rock show negligible gain and loss of weight, retaining an approximately stable weight. This is to be expected, since the lack of ice or snow removes a source of moisture to the samples. Furthermore, precipitation to the region is negligible, removing precipitation as a source of moisture to these samples. Interestingly, Group 4 (samples placed on top of snow) shows a loss of percentage weight on average. This is counterintuitive to the

argument (see Rock Properties and Moisture Uptake, pg. 49) that snow becomes a source of free moisture, especially during the Austral summer.

Table 61: Average sample weight gain or loss, as well as *s* or all samples within each separate grouping, is expressed as a percentage (%).

Group	**Mean**	***s***
1 (Placed on Ice)	0.0026	0.0856
2 (Placed on Rock)	-0.0003	0.0813
3 (Placed on Soil)	0.0065	0.0617
4 (Placed on Top of Snow)	-0.0090	0.1557
5 (Buried in Snow)	0.0033	0.0754

Although mean values calculated are similar, this does not conclusively show that populations are statistically similar. Instead, ANOVA were calculated for the five different groupings to determine similarity of populations. The null and alternate hypotheses of ANOVA are given below.

H_0 = samples are similar for P/M/WA/S/% saturation and can be used comparatively

H_a = samples represent different populations and should be excluded from the study

A more detailed explanation of the ANOVA and its application in the current context is given under Rock properties and Moisture Uptake (pg. 69). ANOVA for rock properties (P, M, WA, S or % saturation) yields an acceptance of H_0 in all instances. ANOVA results may be viewed in Appendix H: Inferential Statistics for Sample Moisture Gain or Loss, Table 95 to Table 99 (pgs. 194-195). Samples per grouping, therefore, are comparable, represent similar populations and individual samples are not expected to skew field moisture gain or loss observation. Levels of confidence calculated during ANOVA analyses for porosity, microporosity, water absorption capacity, saturation coefficient and percentage saturation are shown in Table 62.

Table 62: Levels of confidence calculated for all samples for porosity (P), microporosity (M), water absorption capacity (WA), saturation coefficient (S) and percentage saturation, following ANOVA analyses.

Investigation	**Level of Confidence**	**Level of Significance (α)**	**Rejection of H_0**	**Significant for $p < 0.05$**
Porosity	90%	0.10	No	No
Microporosity	26%	0.74	No	No
Water Absorption Capacity	91%	0.09	No	No
Saturation Coefficient	63%	0.37	No	No
Percentage Saturation	61%	0.39	No	No

Average rock property values for the 20 samples are shown in Table 63 . As expected, P and WA of samples are low (0.60% and 0.57% respectively) with M high (82.06%). Less than one percentage (1%) of clasts represents pore space. Similarly less than one percentage (1%) of water is absorbed by clasts within one 24-hour period. The low P values also make clasts stronger and less frost susceptible (Whalley, 1981; Ballantyne, 2010), having implications on weathering and blockfield development. The saturation coefficient is high at 0.94, as is the percentage saturation (84.16%). Since rock weathering is directly proportional to M, P and WA (see discussion under see Rock Properties and Moisture Uptake, pg. 48), it is expected that weathering occurs at slow rates and clay minerals (discussed under Particle Size Analysis, pg. 134), if present, are expected to be scarce for the study site (taking parameters such as length of surface exposure and climate into consideration).

Table 63: Average rock property values for all samples (n = 20).

	Porosity (P)	**Water Absorption Capacity (WA)**	**Microporosity (M)**	**Saturation Coefficient (S)**	**% Saturation**
Average	0.60	0.57	82.06	0.94	84.16
Median	0.53	0.51	84.62	0.94	84.00
s	0.22	0.24	8.63	0.04	9.35

In order to determine whether or not the access to moisture and the environmental setting influences the moisture absorption of samples, ANOVA was calculated for five treatments. The null and alternate hypotheses of ANOVA are given below.

H_0 = moisture uptake is similar for all clasts for all environmental settings

H_a = environmental setting does influence moisture uptake of clasts

A more detailed explanation of the ANOVA and its application in the current context is given under Rock properties and Moisture Uptake (pg. 69). Results of ANOVA show that the different treatments represent the same grouping, *i.e.* for sample within each grouping show that all sample weight gain or loss data (within each grouping) represent the same population. Consequently, sample variances for each sample within each grouping are similar. H_0 cannot be rejected for samples within and between the five groupings at a 95% level of confidence ($\alpha = 0.05$; $p < 0.05$). Environmental setting in terms of moisture availability, therefore, does not have a statistically significant impact on moisture gain or loss for samples across the study site. Table 64 (pg. 134) lists levels of confidence calculated during ANOVA analyses for samples within and between each grouping. ANOVA results may be viewed in Appendix H: Inferential Statistics for Sample Moisture Gain or Loss, Table 100 to Table 105 (pgs. 196-198).

Table 64: Levels of confidence calculated for the samples within each separate group, as well as on the combined group data, following ANOVA analyses.

Investigation	**Level of Confidence**	**Level of Significance (α)**	**Rejection of H_0**	**Significant for $p <$ 0.05**
Samples within Group 1	15%	0.85	No	No
Samples within Group 2	10%	0.90	No	No
Samples within Group 3	2%	0.98	No	No
Samples within Group 4	16%	0.84	No	No
Samples within Group 5	2%	0.98	No	No
Amongst Groups	18%	0.82	No	No

Individual samples as well as groupings exhibit similarities in population variances. The highest level of confidence calculated is 18%, well below the statistically significant one of 95% for physical geographical sciences. Assuming similarities in external parameters such as geology, time of exposure and climate exist, the type of available moisture (snow or ice or none) does not statistically influence moisture absorption of samples. This is in contrast to findings of Lee *et al.* (2013), who suggest that moisture availability is largely influenced by microclimate. The consistent decrease of weight following drifting snow or storm events, as discussed above (pg. 130), suggests that regional climate parameters, such as relative humidity, exert a greater influence on clast moisture content, supporting the assertions of Briggs (1977a), who suggests that rock moisture content is influenced by large-scale environmental conditions. It must further be noted that samples were only observed in the field for a period of approximately a month. A longer observation period will more conclusively show the influence that environmental setting and concomitant available moisture have on moisture uptake of clasts in the field. As such, although results indicate the environmental setting does not play the dominant role when moisture uptake is concerned, a longer observation period (through all seasons) may alter the results.

4.6 Particle Size Analysis

Mineral soils have a bulk density between 1.0-2.0 $g.cm^{-3}$. The estimated bulk density of all three samples collected for the study site fall within this specified range (Table 65, pg. 135). As described under Particle Size Analysis (pg. 54), mineral soils should have a bulk density of 1.25 $g.cm^{-3}$. As organic content causes bulk density to decrease, the higher than expected bulk density indicates the lack of organic content in the soil. As discussed in Weathering and Erosion (pg. 15), this could indicate that the study site was in fact recently covered by glacial ice. The retreat of the ice only 8 000

years BP implies that the study site would have been stripped by the ice mass, removing organic-rich soil. In addition, the recent exposure of the surface does not provide sufficient time for the local environment to produce organic-rich soil.

Table 65: Values required for determining bulk density, as well as bulk density per sample (S1, S2, S3) are indicated: h = height of the sample in centimetres; π = radius of beaker; R^2 = radius of the beaker squared; V = volume of sample in centimetres squared; W = weight of the sample in grams; D_b = the bulk density of the sample in grams per cubic centimetres.

Sample	**h (cm)**	**π**	**R^2**	**V (cm^2)**	**W (g)**	**D_b ($g.\ cm^{-3}$)**
S1	11.3	3.14	39.06	1 386.72	2 552.29	1.84
S2	8.0	3.14	39.06	981.75	1 957.84	1.99
S3	6.4	3.14	39.06	785.40	1 507.14	1.92

Sieving the ground samples leads to a proportion of the sample being lost, *i.e.* the original total weight of the sample is more than the total weight of the sample after sieving. However, this loss is small (less than 1% of total weight for each sample) and not significant. The three samples (S1, S2, and S3) lost 0.24%, 0.63% and 0.29% of their total weight respectively. Particle size dry mass proportions for each sample are presented in Table 66 below. Values represent sieving analyses only. Sample proportions following SediGraph analyses are discussed at a later stage.

Table 66: Particle size proportions, excluding proportions of the fine earth fraction, for each sediment sample site (S1, S2, and S3) are indicated.

Size (µm)	**Phi (Φ) Size**	**S1**	**% Weight**	**S2**	**% Weight**	**S3**	**% Weight**
8 000	-3	260.11	10.19	265.15	13.55	270.56	17.96
4 000	-2	376.61	14.76	295.74	15.11	287.21	19.06
2 000	-1	666.73	26.13	432.74	22.11	336.32	22.32
1 000	0	712.68	27.93	476.75	24.36	296.99	19.71
500	1	381.49	14.95	250.54	12.80	204.06	13.54
250	2	119.44	4.68	90.32	4.61	74.12	4.92
125	3	28.75	1.13	58.69	3.00	20.48	1.36
63	4	3.92	0.15	47.05	2.40	8.23	0.55
< 63	> 4	2.32	0.09	40.23	2.06	8.88	0.59
Total		2 552.05	100	1 957.21	100	1 506.85	100

The largest proportion in terms of weight of particles for S1 is for coarse sand, particles between 1 000 µm and 2 000 µm (27.93%). The next greatest proportion is for fine gravel, particles between 2 000 µm and 4 000 µm (26.13%). Together these proportions account for more than half the weight of the sample (54.06%). Similar values are observed for S2, with the largest weight proportion occurring for particles between 1 000 µm and 2 000µm, with the next largest proportion occurring for particles between 2 000 µm and 4 000µm (24.36% and 22.11% respectively, amounting to 46.47%). S3

exhibits slightly different proportion (largest and next-largest proportions being reversed), as the largest weight proportion is observed for fine gravel, particles ranging from 2 000-4 000 µm (22.32%). The next largest proportion is observed for coarse sand, particles smaller than 2 000 µm but greater than 1 000 µm (19.71%). Together these proportions amount to 42.03%. The lowest value for particle smaller than 63 µm (as a percentage of total weight) is observed for S1 (0.09%), with the highest observed for S2 (2.06%). S3 shows 0.59% for this fraction. Figure 69 shows bar graphs of the dry mass proportions per sample, expressed as a percentage of total sample weight. As can be seen from the figure all samples recorded the majority of their weight for coarse sand and fine gravel. All three samples follow a similar curve (Figure 70, pg. 137) in terms of their particle size distribution, indicating that all samples may represent the same population. This is investigated by inferential statistics (Kolmogorov-Smirnov test). Results of the Kolmogorov-Smirnov test are discussed on pg. 143.

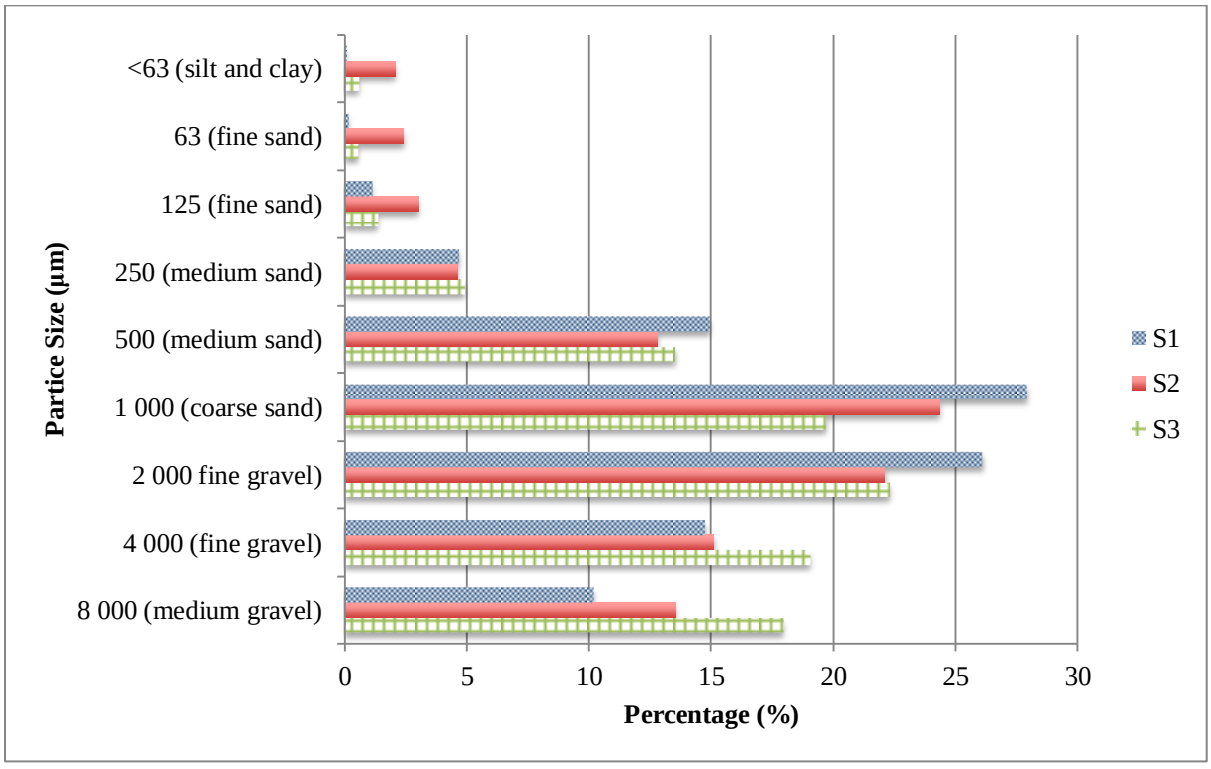

Figure 69: Bar graph of the dry mass per particle size, expressed as a percentage of total mass. Percentage values are indicated for all sediment samples (S1, S2, and S3).

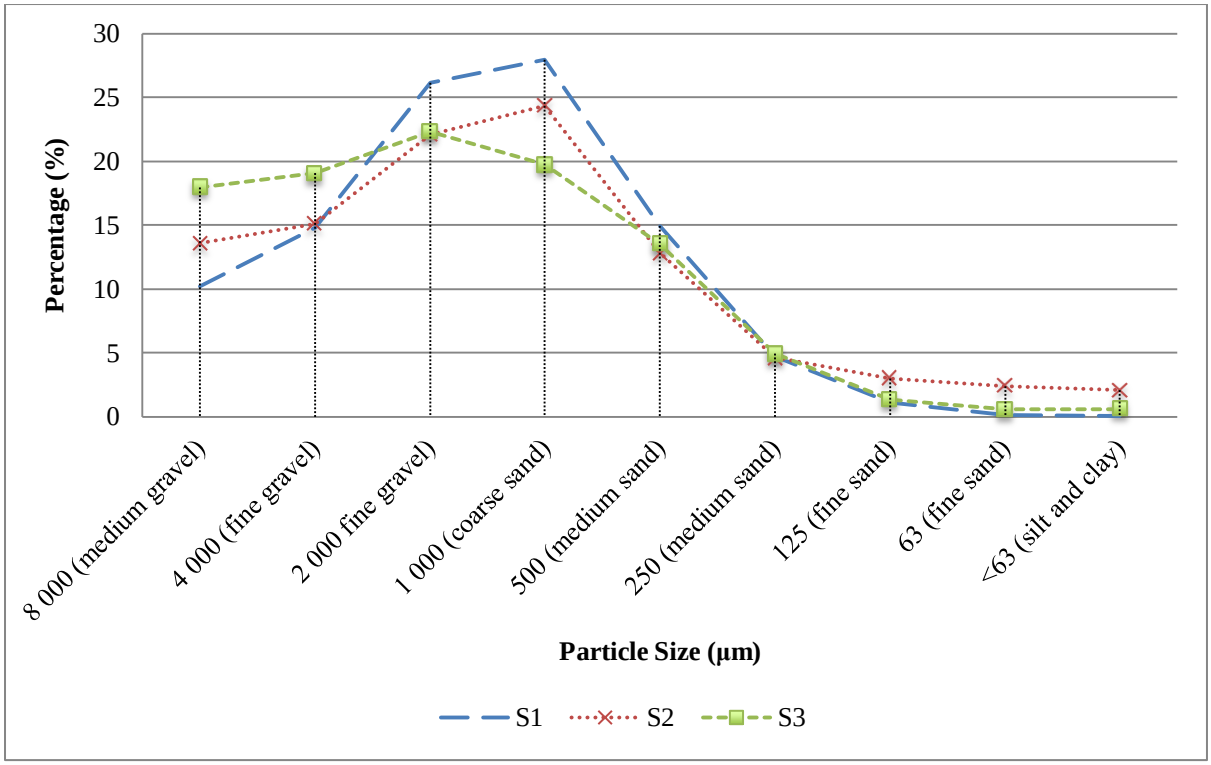

Figure 70: Particle size distribution per sample, expressed as a percentage of total weight. A blue dashed line indicates S1; S2 is shown as a red dotted line with a cross marker; and S3 is drawn as a green dashed line with a square marker.

The cumulative percentage graph (Figure 71, pg. 138) for the three samples also shows the expected shape associated with fine fraction analyses. The graph lines climb most steeply between fine gravel and coarse sand, indicating the largest proportion of dry mass between these two grades. Furthermore, the graph clearly shows the small proportion of sediment smaller than fine sand. This is expected for the study site, assuming mineral soils lacking organic content and minimal decomposition of material. This is, furthermore, corroborated when assigning samples to a soil texture class. All three samples have a sand proportion greater that 95% (comparing the sand, silt and clay fractions). Consequently, according to Briggs' (1977a) soil texture diagram (Appendix B: Statistical Descriptions, Ranges and Classes, Figure 76, pg. 168), the textural class of the soil is sandy.

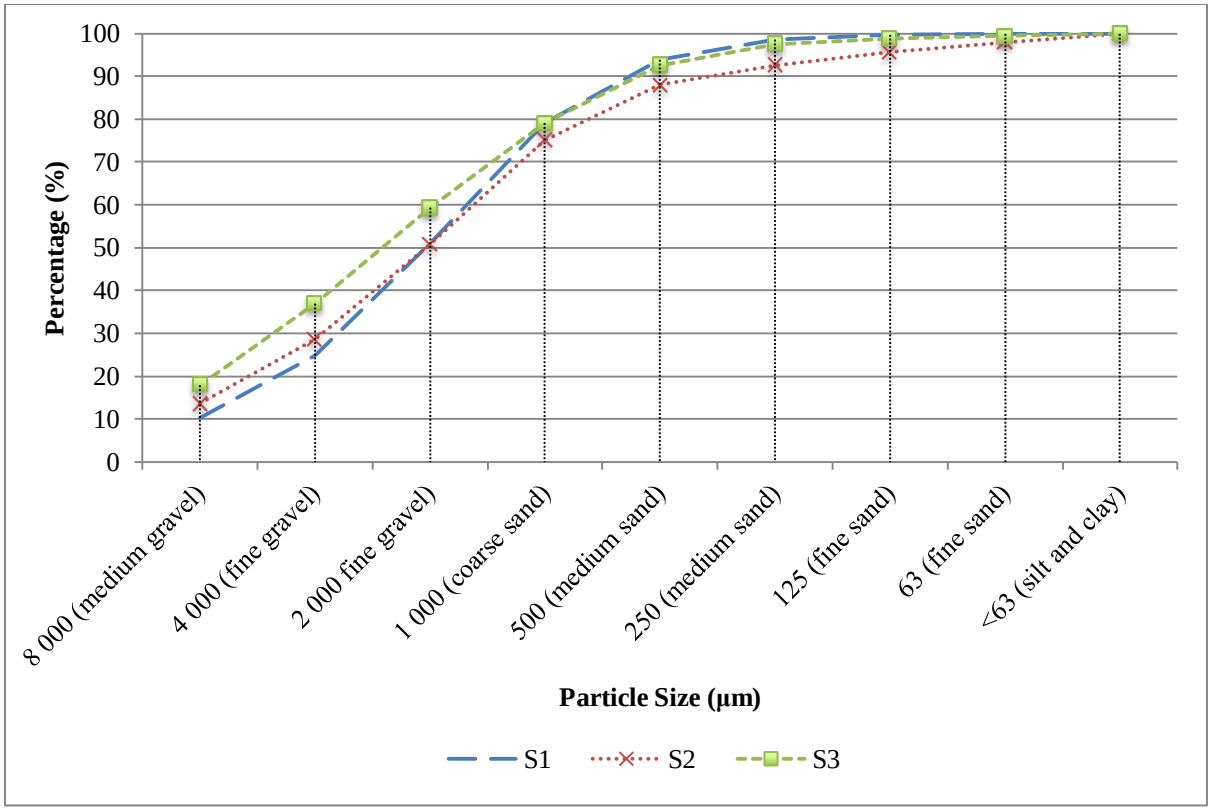

Figure 71: Cumulative percentage (%) of particle proportions for all sediment samples, ranging from coarse to fine portions. A blue dashed line indicates S1; S2 is shown as a red dotted line with a cross marker; and S3 is drawn as a green dashed line with a square marker.

SediGraph analyses show that all three samples have a clay proportion of at least 15%. Values are shown in Table 67 (pg. 139). These values reflect percentage proportions following SediGraph analyses only. Sample particle size proportions following sieving are given in Table 66 (pg. 135). S2 shows the greatest portion of clay particles (20.7%), followed by S1 (15.1%) and S2 (10.8%). S2 also has the largest portion of silt particles (medium and fine silt), equalling almost 45% (44.9%). S1 exhibits the largest sand particles per sample (56.8%), followed by S3 (52.5%) and S1 (34.3%). The SediGraph analysed a total of one gram of sediment per analysis run. According to Table 66 (pg. 135), S1 contains 0.09% particles smaller than 63 µm. SediGraph analysis shows that of that portion, only 15.1% represents clay particles. Consequently, only 0.01% of S1 are clay particles. S2 and S3 contain 0.43% and 0.06% clay particles respectively. Overall, sediment from the study site contains less than half a percent of clay particles. Figure 72 (pg. 139) shows bar graphs of the mass proportions per sample, expressed as a percentage of total sample weight. Figure 73 (pg. 140) shows the equivalent proportions in terms of cumulative percentage. S1 and S3 follow the most similar curve, with S2 deviating slightly. This is due to S2 having a smaller fine sand proportion than S1 and S3.

Table 67: Percentages (%) for particle sizes (ranging from clay to sand) for each sediment sample (S1, S2, S3) are indicated. Particle proportions are determined during sedimentary analyses using the SediGraph 5100.

Description	Percentage		
	S1	S2	S3
Sand	56.8	34.4	52.5
Coarse Silt	10.2	19.4	21.5
Medium and Fine Silt	17.9	25.5	15.2
Clay	15.1	20.7	10.8

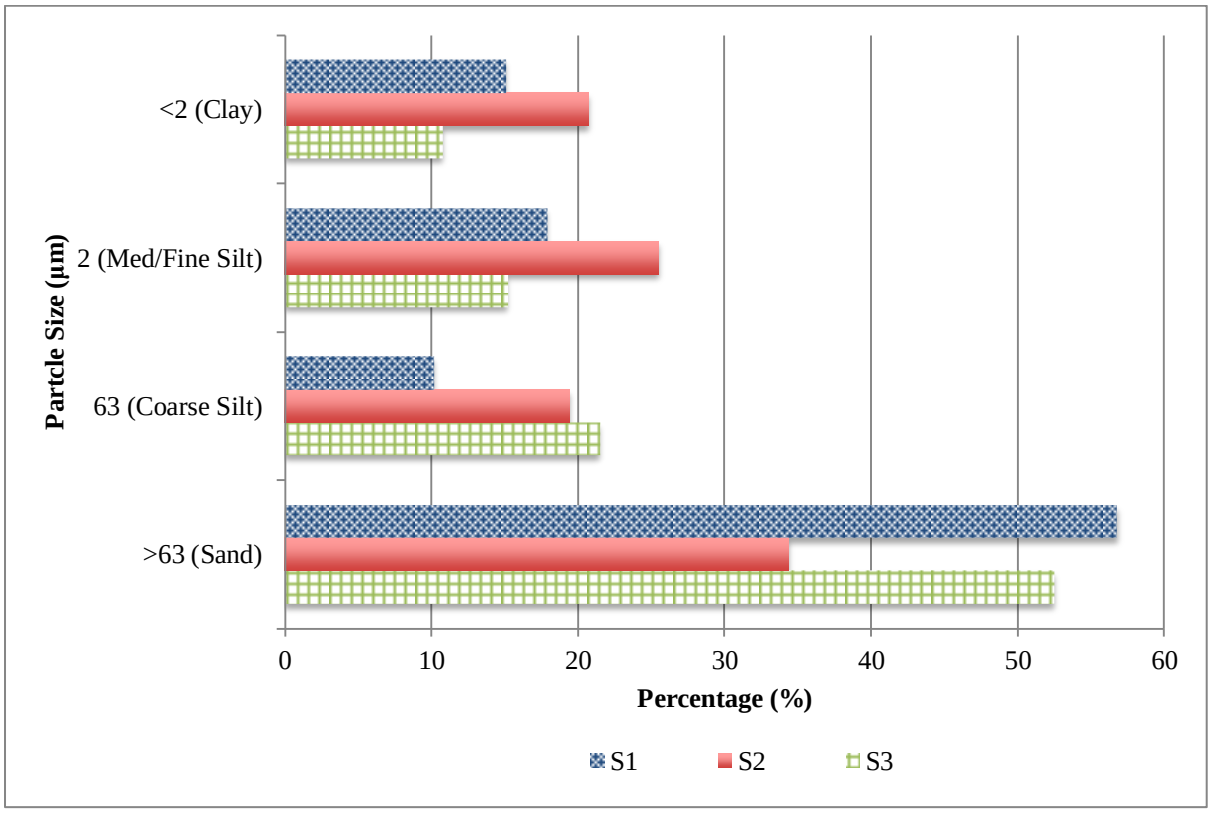

Figure 72: Bar graph of particle mass expressed as a percentage of the analysed sediment sample. Percentage values are indicated for all sediment samples (S1, S2, and S3) following SediGraph 5100 analyses.

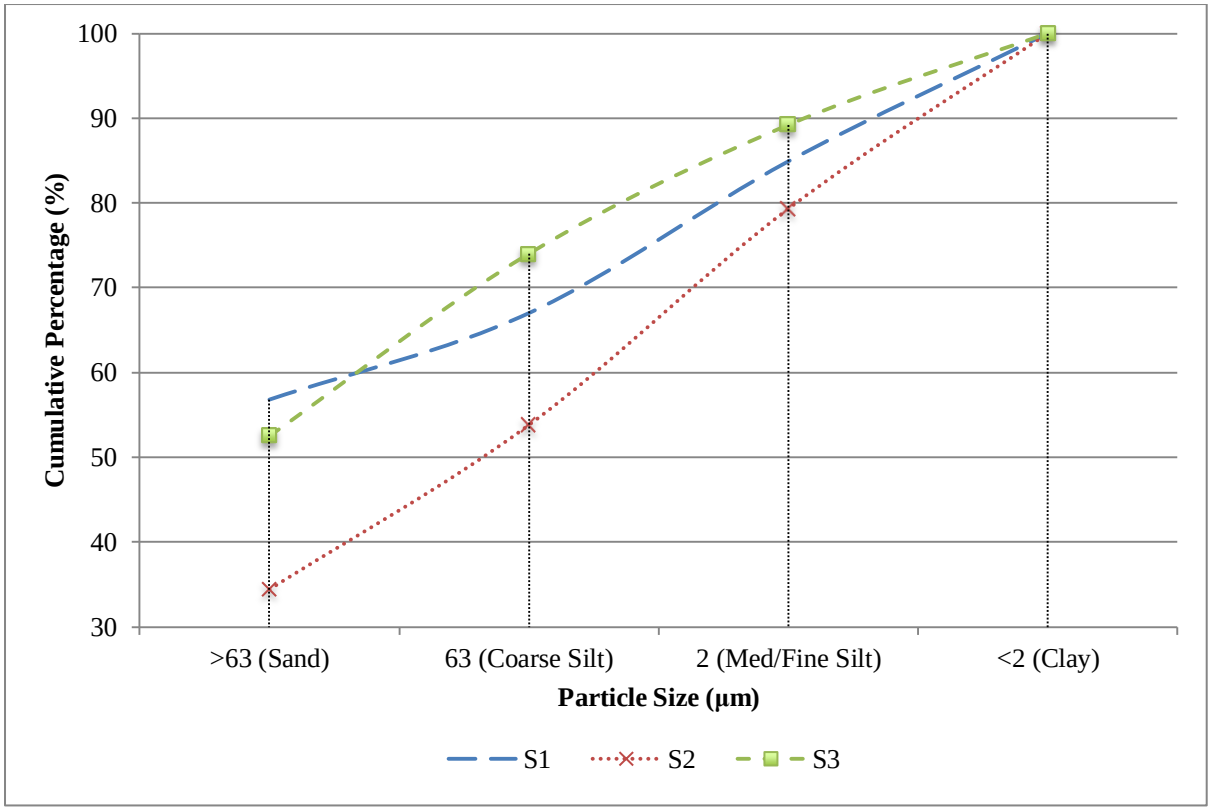

Figure 73: Cumulative percentage (%) of sample proportions for particles less than 63 µm in diameter. Percentage values are indicated for all sediment samples (S1, S2, and S3). A blue dashed line indicates S1; S2 is shown as a red dotted line with a cross marker; and S3 is drawn as a green dashed with a square marker.

These small percentages suggest minimal decomposition of the source rock into clay particles, signifying limited chemical weathering. This agrees with earlier findings of low porosity and water absorption capacity values for clasts (see Table 63, pg. 133). Furthermore, Type I blockfield matrices have low clay proportions, as discussed in Study Site (pg. 10). The small proportions of clay particles found for sediment samples following laboratory analyses support the earlier finding that the blockfield represents an openwork deposit on a Type I matrix (see Blockfield Survey, pg. 79). If the blockfield remained intact under a cold-based glacier, a possibility discussed under Blockfields (pg. 10 onwards), evidence in terms of pre-Holocene weathering should have been retained in the soil. Since clay proportions are very low it can be suggested that the blockfield is of Holocene origin. Consequently, the deposit falls within the periglacial model of blockfield development. However, clay minerals may not be seen as a conclusive indicator for dating a deposit (*e.g.* Meiklejohn and Hall, 1997; Andre, 2003; Boelhouwers, 2004; Ballantyne, 2010). Although the lack of clay minerals does point to the blockfield falling within the periglacial model, radioisotope and similar dating methods should be considered to conclusively determine the age of the surface of the deposit. Furthermore, Holmlund and Näslund (1994) argue that the Maudheimvidda ice sheet in DML is cold-based and frozen to the substrate. Consequently, blockfields may have remained intact during glaciation and pre-date glaciation for the region, suggesting a pre-Holocene age.

Descriptive statistics calculated for sediment samples may be seen in Table 68 below.

Table 68: Descriptive statistics, including mean, median, skewness, kurtosis and sorting values for soil samples (S1, S2, and S3) are shown.

Phi (ϕ)	**S1**	**S2**	**S3**
Mean	-1	-1	-1.5
Median	-1	-1	-2
Skewness	-0.1	0.1	0.2
Kurtosis	1.20	1.14	1.26
Sorting	1.6	1.8	2.0

The Phi (ø) median value for S1 and S2 centres on -1 (2 000 μm), whereas S3 has a Phi (ø) median value of -2 (4 000 μm). Although the Phi (ø) median value of S3 is different to that of S1 and S2, it remains classed as fine gravel. Phi (ø) mean values for all samples are close to Phi (ø) median values calculated, with S1, S2 and S3 having Phi (ø) mean values of approximately -1, -1 and -1.5 respectively (all classed as fine gravel on the Wentworth grade, see Appendix B: Statistical Descriptions, Ranges and Classes, Table 73, pg. 166). Samples S1 and S2 exhibit symmetrical distributions with Phi (ø) skewness values centring on zero. Unlike S2 and S3, S1 has a Phi (ø) skewness value of -0.1, signifying a distribution with coarser particles in its tail. S3 exhibits a positively skewed distribution (fine particles in its tail) with a Phi (ø) skewness value of 0.2. High Phi (ø) sorting values indicate that sediment is poorly sorted (S1 and S2) and very poorly sorted (S3) for the study site. This is to be expected for the region, as glacial deposits tend to have a large mixture of particle sizes (Briggs, 1977a). Phi (ø) kurtosis values indicate leptokurtic distributions for all samples. This signifies normal (as seen by skewness values centring on zero, indicating symmetric distributions) and fairly peaked (positive kurtosis values) distributions. The peaked distribution signifies that the majority of data fall around the mean. The leptokurtic distributions are in contrast to Briggs (1977a), who suggests poorly sorted sediment (as indicated by sorting values of two) should by platykurtic. Bivariate scatterplots of Phi (ø) kurtosis vs. Phi (ø) skewness and Phi (ø) sorting vs. Phi (ø) mean values are shown in Figure 74 and Figure 75 on pg. 142. Figure 74 shows the predominantly normal yet peaked distribution of the samples, with two of the three samples exhibiting a tail in the fine fraction. This signifies a population of predominantly fine gravel (coarse sediment), with a small sub-population of fine sediment. Figure 75 shows the poorly sorted and coarse nature of the sediment, indicating glacial or periglacial deposits. The clustering of S1 and S2 on both graphs also indicates, graphically, their similarity in populations. This similarity is calculated, using inferential statistics, in the discussion following on pg. 143.

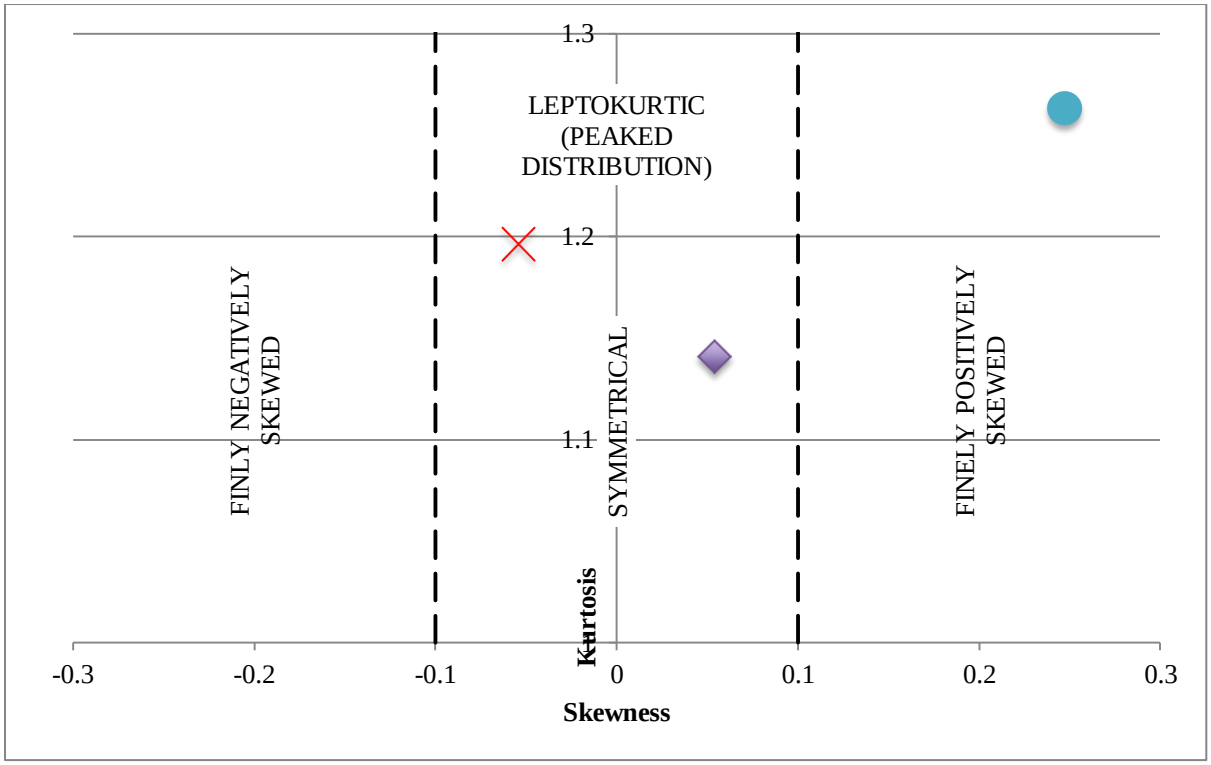

Figure 74: Bivariate scatterplot of Phi (ø) kurtosis values vs. Phi (ø) skewness values. The cross represents S1, the diamond S2 and the circle S3. The scatterplot shows that S2 and S3 have similar Phi (ø) skewness and Phi (ø) kurtosis values.

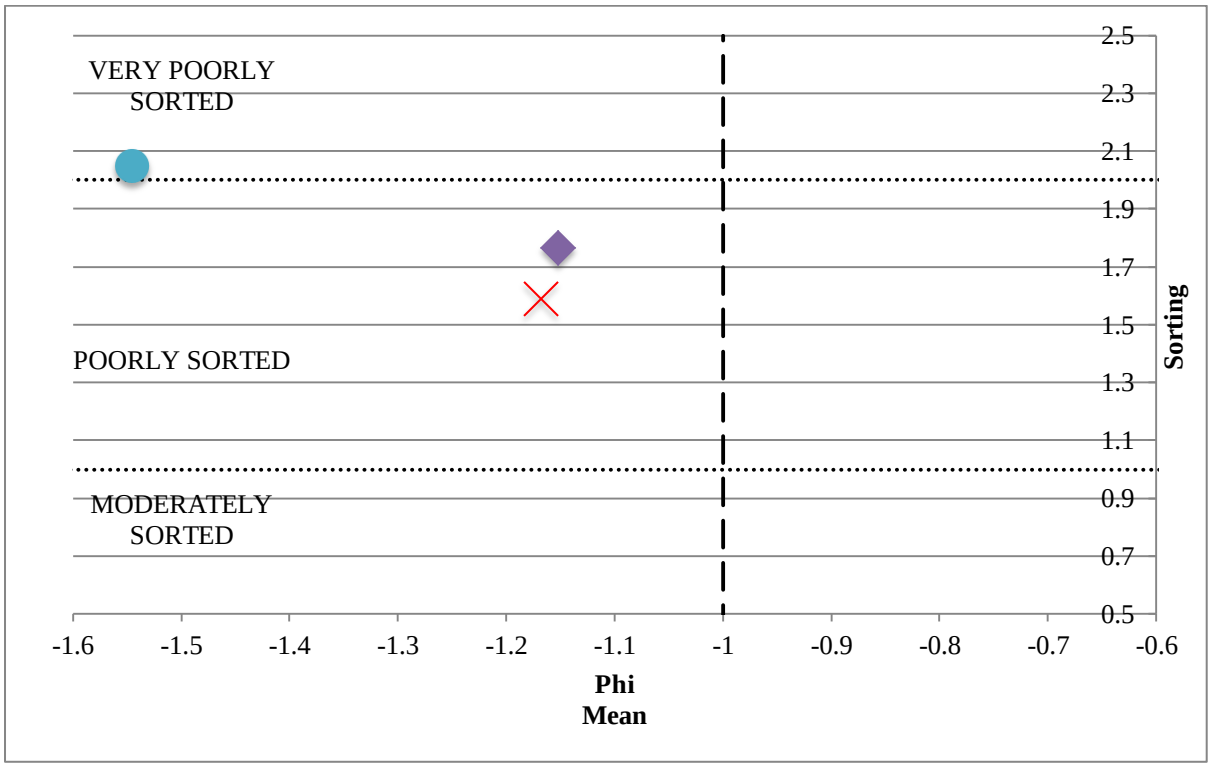

Figure 75: Bivariate scatterplot of Phi (ø) sorting values vs. Phi (ø) mean values. The cross represents S1, the diamond S2 and the circle S3. The scatterplot shows that S2 and S3 have similar Phi (ø) sorting and Phi (ø) mean values.

The Kolmogorov-Smirnov test allows for the statistical comparison of individual data series. This test was run comparing S1&S2, S1&S3, as well as S23. The null and alternate hypotheses for this test are given below.

H_0 = particle size fractions are similar for two sample locations
H_a = particle size fractions are different for two sample locations

A more detailed explanation of the Kolmogorov-Smirnov test and its application in the current context is given under Particle size analysis (pg. 71). Results of the Kolmogorov-Smirnov test following sieve-stack and SediGraph analyses (Table 69) show that S2 and S3 are statistically different, as is S1 compared to S3. For these two comparisons H_0 may be rejected. In contrast to this is the comparison of S1 and S2, which shows statistically that the two samples represent the same population. For this comparison H_0 cannot be rejected. This agrees with the particle size proportion analyses, discussed above, where S1 and S2 have approximately 50% of their particle sizes falling between 1 000 μm and 4 000μm. Furthermore, S1 and S2 are symmetrical (Figure 74, pg. 142) and have similar sorting values (Figure 75, pg. 142), with S3 positively skewed and exhibiting less sorting of particles than the other two samples.

Table 69: Calculations and results of the Kolmogorov-Smirnov test determined for the sediment samples (S1&S2, S1&S3, and S2&S3).

		Cumulative Percentage (%)			**Comparison**		
Size (μm)	**Phi (Φ) Size**	**S1**	**S2**	**S3**	**S1 vs. S2**	**S1 vs. S3**	**S2 vs. S3**
8 000 (medium gravel)	-3	10.19	13.55	17.96	3	8	4
4 000 (fine gravel)	-2	24.95	28.66	37.02	4	12	8
2 000 fine gravel)	-1	51.07	50.77	59.34	0	8	9
1 000 (coarse sand)	0	79.00	75.13	79.04	4	0	4
500 (medium sand)	1	93.95	87.93	92.59	6	1	5
250 (medium sand)	2	98.63	92.54	97.51	6	1	5
125 (fine sand)	3	99.76	95.54	98.86	4	1	3
63 (fine sand)	4	99.96	98.65	99.72	1	0	1
23 (coarse silt)	> 4	99.97	99.05	99.85	1	0	1
2 (medium/fine silt)	9	99.99	99.58	99.94	0	0	0
< 2 (clay)	> 9	100.00	100.00	100.00	0	0	0
Maximum Comparison D					6	12	9
Calculated D (n = 11)					7	7	7

The test suggests that local conditions, such as slope, aspect, exposure and even length of exposure must be taken into consideration when analysing samples. GIS analyses in terms of aspect, slope,

elevation and annual solar radiation received are shown in Table 70. The concomitant GIS model is shown in Appendix D: GIS Models as Figure 86 (pg. 175). These values show that, when comparing S1 with S3, aspect, slope and elevation are different. This suggests possible control of these parameters on sediment populations. However, a comparison of S2 with S3 shows that both sample sites exhibit the same values for aspect, slope and elevation, suggesting that these parameters do not exert any particular control on sediment populations. It can, therefore, not conclusively be stated that aspect, slope and elevation influence sediment populations to the extent that the populations become statistically different. However, the calculated D for the comparison of S2 and S3 is much lower than that of S1 vs. S3. S1 and S3 also have markedly different aspect, slope and elevation values. Consequently, a tentative conclusion is that when these parameters are markedly different, populations will differ significantly.

Table 70: GIS analyses for the three sample sites (S1, S2, and S3) in terms of aspect (north, east, south, west, top), slope gradient (°), elevation (MASL) and annual solar radiation received ($WH.m^{-2}$).

Sample	**Aspect**	**Slope**	**Elevation**	**Solar Radiation**
S1	East	12-18	820-830	650 602-723 169
S2	North	0-6	840-850	650 602-723 169
S3	North	0-6	840-850	650 602-723 169

Adlam *et al.* (2010) argue that incoming annual solar radiation does not significantly affect active layer depth, as discussed in Near-Surface Ground Temperature Dynamics (pg. 41). The freeze-thaw cycle occurring in the active layer contributes and accelerates sediment supply and soil development. GIS analyses show that incoming solar radiation does not affect sediment properties, and supports the findings of Adlam *et al.* (2010). Consequently incoming solar radiation may be excluded as an external control parameter on sediment properties, whereas aspect, slope and elevation should be investigated further in order to conclusively determine the role these parameters play on sediment populations.

CHAPTER 5: Considerations and Recommendations

This chapter details considerations and limitations to the study, as well as recommendations and further areas of research. Limitations of four of the six objectives of the project are considered. Please refer to Aims and Objectives (pg. 9), for a list of objectives. Furthermore, the implications on each objective are addressed. Further avenues of research and recommendations are discussed under Recommendations and Further Areas of Research (pg. 149 onwards).

5.1 Considerations

The nature of the project, difficulties in access of the study site and the variety of objectives to be achieved yielded a few problems encountered in the field and during statistical analyses. These are discussed below. It must be noted, however, that none of the considerations adversely affected the outcome of any of the objectives.

5.1.1 Rock Hardness: Schmidt Hammer and Equotip and Methods

The following discusses problems encountered when conducting fieldwork for Objective 3 (pg. 9). Equotip readings were found to be fairly variable but this variability did not negatively affect the results of statistical analyses. High variability within recorded Equotip rebound values reflects the susceptibility of the instrument to micro-scale variations in surface roughness (Viles *et al.*, 2011). SH readings showed lower than expected *R*-values. Mean recorded *R*-values for diorite and dolerite should be 61.1 and 64 respectively (Goudie, 2006). However, the mean *R*-value for the total recorded values was 32.5, approximately half that of the expected value. The lower-than-average readings recorded in the field may be due to the N-type instead of L-type hammer having been used. Although the N-type is less influenced by surface irregularities, the L-type hammer is best used when examining weathered surfaces. This is due to only 0.735 $N.m^{-1}$ being exerted upon impact, compared to the 2.207 $N.m^{-1}$ of the N-type (Basu and Aydin, 2004; Goudie, 2006; Aydin, 2008). Surface roughness has also been shown to influence rebound values (Ericson, 2004). Additional factors that influence rebound values are: 1) the relative strength of coarse grains compared to the local matrix, 2) and moisture content, and 3) anisotropy (lamination, foliation, schistosity, lineation) (Goudie, 2006; Aydin, 2008; Viles *et al.*, 2011). Grains equal in size to the plunger tip may skew rebound values. Weathering leads to microstructural changes of the rock and yield significantly different rebound values (Aydin, 2008). Weathered surfaces also absorb more of the applied energy than non-weathered surfaces, decreasing rebound values and introducing errors into the data set (Ericson, 2004; Basu and Aydin, 2004). Moisture content leads to inter-grain sliding and a softening of grains,

decreasing rebound values. Anisotropic planes significantly reduce rebound values. Differences in the elastic and elastoplastic response across the surface in response to the impact device may also yield highly scattered values (Aydin, 2008). Rebound values on weathered surfaces should, therefore, yield lower rebound values than on non-weathered surfaces (Ericson, 2004; Aydin, 2008). Another consideration is that rebound values for nunataks above historical glacial extent will have lower rock rebound values due to periglacial weathering (Goudie, 2006). SH readings are also higher for younger sites than relict sites (Sumner *et al.*, 2002). Matthew and Owen (2008) argue that rock exposed for approximately 10 000 years on a glacier in Norway, shows a decrease of *R*-values of 20 units. Furthermore, Shakesby *et al.* (2006) show a mean *R*-value 41.6 ±1.4 for Preboreal surfaces exposed 9700 years BP. The lithology is similar to that found at the study site (granodioritic) and occurs in a similar periglacial environment. The lower-than-expected *R*-values, when adjusted for deglaciation in the Holocene, fall within the expected range of 60 units. The effect of moisture on rock hardness values (Sumner and Nel, 2002) can be excluded as a reason for low *R*-values, as rock surfaces were allowed to surface dry before measurements were taken. Samples were also exposed to similar climatic conditions throughout the field season, making micro-scale moisture variations negligible. This argument is supported by the discussion under Rock Properties and Moisture Uptake (pg. 130), which argues that different environmental settings do not influence the moisture absorption capability and weathering of clasts.

The k-value (rebound value over maximum rebound value) may be used as an indication of compressive strength loss (Equation 9). It varies between samples and is calculated by dividing the mean of the values (L_s) by the mean of the maximum three recorded values (L_{Max}) (Aoki and Matsukura, 2007).

Equation 9: k-Value calculation after Aoki and Matsukura (2007).

$$k = \frac{L_s}{L_{Max}}$$

The k-value was determined for Sample 13, and SH readings taken on weathered and non-weathered surfaces. The calculation may be viewed in Table 71 below.

Table 71: k-Value calculations for Sample 13 on weathered vs. non-weathered surfaces. The weathered surface yields a lower k-value to the non-weathered surface of the clast.

	FIELD VALUES		**STANDARDISED VALUES**	
Sample	**Weathered**	**Non-weathered**	**Weathered**	**Non-weathered**
1	26	28	-1.43561	
2	30	36	-0.99388	-1.89197
3	34	38	-0.55216	-0.88292

	FIELD VALUES		STANDARDISED VALUES	
Sample	**Weathered**	**Non-weathered**	**Weathered**	**Non-weathered**
4	34	40	-0.55216	0.12613
5	36	40	-0.33129	0.12613
6	40	40	0.11043	0.12613
7	42	40	0.33129	0.12613
8	42	42	0.33129	1.13518
9	50	42	1.21475	1.13518
10	56	50	1.87734	
Minimum	26	36	-1.43561	-1.89197
Maximum	56	42	1.87734	1.13518
Average	39	39.75	0.00000	0.00000
Median	38	40	-0.11043	0.12613
s	9.05539	1.98206	1	1
Top 3 Mean	47.5	40.7		
n	10	8	10	8
Indicates outlier				
k-Value	**Weathered**		**Non-weathered**	
	0.82		0.98	

The comparison of these values indicates the degree of weathering of the surfaces. A comparison of a weathered vs. non-weathered surfaces yields a value of 0.82 vs. 0.98. The non-weathered surface, therefore, reflects a harder surface, with the weathered surface exhibiting only 84% of the non-weathered rock hardness. This implies lower median rebound values for weathered clasts. In addition, it must be noted that the *s* of values recorded on the non-weathered surface is much lower than that of the weathered surface. This agrees with Aydin (2008) that weathered surfaces yield more scattered rock rebound values. Ericson (2004) shows that the hardest granite surfaces are those polished by fluvial, aeolian or glacial action whereas the softest surfaces are highly weathered ones. This has implications for rebound values in the field and must be considered when conducting analyses. Consideration must also be given to case hardening of clast surfaces. Mol and Viles (2012) show that case hardening influence the internal moisture regime of a clast, reducing the effect of moisture in weathering. In the absence of a protective crust, moisture evaporates more quickly from the surface, possibly increasing weathering and weakening of the rock (Mol and Viles, 2012). Instrument errors and age are also of concern (Ericson, 2004; Goudie, 2006; Shakesby *et al.*, 2006). The plunger becomes rougher with repeated impacts and may yield lower rebound values in the field (Aydin, 2008). However, this deterioration of the plunger won't necessarily be noticed during calibration (Aydin, 2008), introducing an additional margin of error into field observations.

5.1.2 Near-Surface Ground Temperature Dynamics

This section discusses problems encountered when conducting fieldwork in order to achieve Objective 4 (pg. 9). Measurements on GST were limited to seven sites during the 2010/11 field season and 17 for the 2011/12 field season. The scarcity of soil on the blockfield made finding suitable sample points challenging. The short field season also meant GST dynamics, when using iButtons, were recorded for a maximum of one month during the Austral summer. The difference in mean, median and modal temperatures for the two field seasons show that the length of investigation is crucial. Longer-term data allow the incorporation of the variable weather parameters found at the study site. Consequently, longer-term data collection is preferred over short-term data collection. Nevertheless, data recorded during the period under investigation show the expected variability of GST during the summer months. The data may, therefore, be seen as representative of summer GST across the blockfield.

5.1.3 Rock Properties and Moisture Uptake

The following section discusses problems encountered when conducting fieldwork in order to achieve Objective 5 (pg. 9). Rock properties were calculated for samples less than 320g in weight. Furthermore, samples were rounded and exhibited well-developed weathering rinds. These samples, therefore, represent already weathered material. Consequently, rock properties calculated for the purpose of this study represent overestimations of actual rock properties expected for the majority of clasts on the study site. However, the more weathered samples were more suited to the moisture uptake experiment, as more weathered material should be able to absorb moisture with greater ease than non-weathered material. Furthermore, rock properties calculated were as expected for the type of rock found at the study site.

5.1.4 Particle Size Analysis

Problems encountered when conducting laboratory work in order to achieve Objective 6 (pg. 9) are discussed in this section. Sediment samples were initially sieved in a sieve stack. That portion of the samples less than 63 µm in diameter subsequently underwent SediGraph analyses. Results of the SediGraph show that some of the portion analysed was larger than 63 µm. The largest particle size measured by the SediGraph equalled approximately 65 µm. The sieve of the sieve stack, therefore, shows slight variations to the specified 63 µm web size. However, the observed error was taken into account when analysing samples and observed percentages (proportions) adjusted accordingly.

5.1.5 GIS Analyses Methods

The following discusses considerations when conducting geostatistics and geographical analyses. This applies to methods used throughout the project, in particular Objectives 4 (pg. 9). One of the considerations of GIS is the uncertainty of error propagation in modelling of spatial data (Atkinson, 1999). Geostatistical techniques such as Kriging, however, incorporate this uncertainty and allow the user to generate error maps (Burrough, 2001). In addition, the variance-covariance matrix used during Kriging analyses predicts unsampled values with a high degree of accuracy (Griffith, 2005), minimising error propagation throughout the model. As such, error propagation was minimised using the tools at hand and did not adversely affect the geostatistical and geographical output.

5.2 Recommendations and Further Areas of Research

At present there are three recognised matrices for openwork block deposits: Type I, II and III (Ballantyne, 1998). However, the interlaced ice in the matrix found at the study site points to an additional matrix yet to be described. This matrix would consist of a clast-supported deposit, consisting of jointed bedrock, occurring in a periglacial environment. In these environments seasonal and diurnal freezing and thawing of ice and snow has the potential to exert a significant control on blockfield development. Ice fills available joints and cracks of the underlying clastic matrix. The diurnal and seasonal freezing of ice and snow leads to clasts of the overlying deposit being heaved up and/or outward, similar to permafrost heave. In turn, seasonal ice and snow melt leads to subsidence. Movement of clasts may, therefore, be attributed to the ice-rich matrix and this scenario warrants further investigation. Blockfields found in WDML would provide ideal study sites these investigations and the result of such studies would further our understanding of openwork deposits.

Clast dimensions and orientations, historical climate analyses and sediment analyses all suggest a blockfield of periglacial and recent (10 000 BP) development. Clast supply, in particular the angular nature of clasts, may be ascribed to the pre-existing jointed nature of the hypabyssal and plutonic doleritic and dioritic intrusion. The retreat of the Antarctic ice sheet during the LGM meant an unloading of the surface, subsequent pressure release and fracturing of bedrock. However, this mechanism is likely not the only one in terms of block supply. Thermal fatigue and stress, as discussed under Weathering and Erosion (pg. 15 onwards), may lead to further weakening of clasts along areas of weakness and concomitant block supply. An investigation into thermal properties of clasts, rock mineralogy and climatic variability (temperature and moisture) will provide insight into the development of blockfields found in these settings. It is suggested that thermal temperature regimes for clast surfaces are examined, especially during the Austral summer season. It is also recommended that quantitative dating analyses, such as cosmogenic or radioisotope analyses

(Cockburn and Summerfield, 2004), are conducted for the blockfield surface. In particular, cosmogenic isotope dating may be used to identify the time a surface has been exposed (Cockburn and Summerfield, 2004), *i.e.* surface age of the deposit as opposed to geological age.

Friedmann (1986) suggests that lichen and microorganisms may colonise a sharply defined sub-surface zones. These organisms play a significant role in biogenic weathering of rock in extreme climates (Matthews and Owen, 2008; Mol and Viles, 2012). Matthews and Owen (2008) show that in the initial stages of endolithic lichen colonisation, rock surface strength decreases rapidly. Lichen is effective at penetrating and weakening rock surface layers, resulting in flaking and exfoliation (Friedmann, 1086; Matthews and Owen, 2008). The role these organisms have in the weathering of rock surfaces and landform development should, therefore, be investigated for the region. In particular, studies should look at the effect microorganisms have on exfoliation weathering and granular disintegration, as suggested by Friedmann (1986). Nearby nunataks in WDML such as Robertskollen, should provide ideal study sites for this type of investigation.

Pearson's product-moment coefficient of linear correlation and a coefficient matrix were used during GST analyses to determine the relative influence the specific climate parameters and the parameters of aspect, slope gradient, elevation and mean solar radiation received have on GST dynamics. It is suggested that PCA (Principal Component Analysis) is used to further define these relative relationships and to identify the role of other parameters not considered during the analyses, such as hours of sunshine received or cloud cover. PCA is used to remove noise or redundancy in data in order to identify the principal causation factor(s) (Doornkamp and King, 1971). Applying PCA reduces many variables to a few, essentially summarising the data (Doornkamp and King, 1971). It is often difficult, if not impossible to isolate individual processes from and their influence on the landscape (Church, 2010). Any landscape is the product of synergistic (additive or amplifying) and competing processes, acting on various spatial and temporal scales (Church, 2010). Processes may interact in a non-linear way to result in chaotic (spatially diffuse) effects (Murray *et al*., 2009). PCA may be applied to identify synergistic processes and remove these from the data set. During PCA the correlation matrix is replaced by a factor-loading matrix (Doornkamp and King, 1971). The factor-loading matrix calculates which variables load highly on which factor. In addition, variability in the original data is explained by the importance of each factor (eigenvalue). Only factors with an eigenvalue greater than one are considered in analyses (Doornkamp and King, 1971) Consequently, PCA would be appropriate to identify all climate parameters and the role each plays on soil temperature regimes across the surface of the Northern Buttress.

CHAPTER 6: Conclusion

This chapter concludes the dissertation. The six objectives of the project (Aims and Objectives, pg. 9) are summarised, as well as whether or not the objective has been achieved. Furthermore, the role these findings may have in furthering our understanding of blockfields, their development and the processes acting on these in addressed.

The first objective required whether or not the deposit is autochthonous or allochthonous in nature, as well as the type of matrix found on the deposit. Since an autochthonous deposit consists of clasts that weather *in situ* and that show no preferential orientation and/or dip, the deposit was found to be autochthonous. This is indicated by statistical analyses of clast orientations as well as dip. Furthermore, the fact that clasts overly the same lithology and that slope gradient is predominantly less than 25° supports this argument. However, although the blockfield is autochthonous small changes in topography, such as increase in slope gradient, effect clast characteristics, in particular clast orientation and dip. This is most noticeable on the steeper northeast-facing slopes. Analyses of clast support, sediment and the fact that clasts are poorly disassociated from the underlying bedrock suggests a Type I matrix for the deposit. However, fines are rare and ice prevalent, suggesting a new type of matrix. Please refer to Recommendations (pg. 149) for a discussion on this. Clasts are predominantly of rod index and highly variable in mean diameter. Sphericity indices are similar to the expected indices of sedimentary particles. Furthermore, sphericity and flatness indices are variable, conforming to indices of a possible glacial deposit. However, the lack of a mixed and varied lithology for the study site makes a glacially derived deposit unlikely. Instead, the predominantly rod-shaped clasts are due to weathering along pre-existing lines of weakness, such as jointing, present in the deposit. Furthermore, the jointed nature of the doleritic and dioritic intrusion yields angular and elongated blocks and block supply is predominantly influenced by the jointed nature of the intrusion. Homogeneous indications in terms of angularity and roughness, furthermore, suggest a common source and *in situ* weathering of the deposit. These values, therefore, corroborate the conclusion reached above (that the deposit is autochthonous).

The second objective investigated the morphology and characteristics of clasts found across the blockfield. Data on clast dimensions, axes orientations, evidence of pitting or flaking, lichen presence and if lichen was sheltered, whether or not the clast was block, ice or block/ice supported as well as snow show a number of interesting characteristics. Lichen prefers the more sheltered west-facing aspect, with the least lichen observed for the eastern-facing and wind-exposed sides. Flaking, pitting as well as the roughest observable face is most likely found on top-facing and least for south-facing

sides, suggesting aspect control on weathering. Weathering pitting occurs on the majority of two or three sides of each clast, with pits fairly shallow and elongated in nature. Furthermore, weathering pits occur only in the top-most layer of clast surfaces, suggesting the blockfield has been exposed to weathering processes only fairly recently and that weathering occurs at slowed rates. In general, clasts are resting in a horizontal position (top surface parallel to the ground; clast sides' perpendicular to clast top aspects). Furthermore, the predominant orientation of clasts is in an easterly direction and is influenced by an increase in slope toward the east and north-east. The third objective aimed to investigate the role that aspect has on weathering for the study site. Using clast surface hardness as an indicator of weathering, aspect was found to exert a significant control on weathering of clast surfaces. Additional indicators, such as weathering pitting, flaking and the roughest observable face per clast further support aspect control of weathering for the study site. In contrast, due to a lower confidence interval, lichen presence is not considered as an indicator for aspect control. Lichen appears to prefer sheltered locations and is sparse across the study site. As such, lichen may be seen as an indicator of weathered surfaces but not as an agent of weathering. For both the SH and Equotip the southern aspect exhibits the highest mean *R*- and L-values, followed by the west-facing sides. Consistently low mean *R*- and L-values observed for the north-facing sides suggest these sides are the most weathered. Analyses of the SH and Equotip data series shows that the two instrument are not directly comparable. Nevertheless, similarities in recorded rebound populations and ANOVA results are apparent. For both the SH and Equotip Fisher's LSD tests show that north-top and south-west pairings are similar. Similarities in the population pairings may be attributed to similarities in annual solar radiation received. A higher annual radiation budget coupled with slope gradients, orientation and snow cover drives thermal regimes and weathering rates, leading to differential weathering per clast orientation and aspect. Zonal statistics suggest that lower *R*- and L-values are observed for areas on steeper slopes, low snow cover and receiving higher amounts of solar radiation annually. Snow cover, as a proxy for moisture availability, and thermal fatigue of rock surfaces is thought to play important roles in the weathering across the blockfield.

The fourth objective focused on soil moisture and temperature regimes across the blockfield and the influence that snow cover, slope, aspect and solar radiation have on these regimes. Objective 5 in turn asked the question whether or not the environmental setting and the availability of moisture to each clast influenced the absorption of moisture of each clast. Ambient temperatures and wind speeds were found to influence GST; with ambient temperatures having the greatest impact on GST. An increase in ambient temperature leads to an increase in GST and soil moisture dynamics. In contrast, an increase in wind speed leads to a decrease in GST. The presence of snow also leads to more stable GST. Relative humidity and pressure cause GST to decrease and increase respectively. As has been found in other studies, a lag occurs between ambient and ground temperatures. For both GST and soil

moisture a time lag of approximately 12-24 hours is observed. Other parameters such as topography and mean summer solar radiation received also exert a control on GST dynamics. In contrast, slope orientation (aspect) and wind direction do not appear to influence GST to any great extent. GIS analyses confirm classical statistical analyses, illustrating the advantage of using a combination of classical and geostatistical methods when analysing spatial data. The availability of snow and ice to clasts does not significantly affect clast moisture uptake or loss. Instead, large-scale climate parameters such as relative humidity appear to override any control the micro-scale environment has on moisture uptake or loss. Ambient temperatures and humidity, therefore, influence not only GST but also the moisture absorption rates of clasts across the study site.

The sixth and final objective investigated the possible physical and chemical weathering processes active on the blockfield, as well as the age of the surface of the landform. Using indicators of age, such as clay mineral proportions in the fine earth fraction, as well as surface hardness, the blockfield is thought to have only been recently exposed following deglaciation. *R*-values, supported by fine sediment analyses, suggest the blockfield has been exposed for a duration of approximately 10 000 years. Soil is scarce for the study site and sediment analyses yield only small portions (< 1% per analysed sample) of clay particles, as suggested by low sample porosities and water absorption capacities of sample clasts. Furthermore, high microporosities and saturation coefficients are observed among samples. These values suggest a resistance to chemical weathering, making clasts less frost susceptible. Bulk densities of sediment suggest mineral soils with no (or virtually no) organic content. Although chemical weathering is present (as indicated by the presence of clay particles) the small proportion of these particles suggests decomposition occurs at a slowed rate. Instead, physical weathering processes such as thermal fatigue, thermal stress, and freeze-thaw are thought to play a more dominant role. Incoming solar radiation does also not exert an apparent control on sediment populations. Nevertheless, there are indications that marked differences in aspect, slope and elevation may contribute to statistically different sediment populations. The lack of significant proportions of clay, the lack of fines and the mineral nature of the soil suggest the study site has only recently been exposed, *i.e.* approximately 8 000-10 000 years. These findings are supported by low SH readings, shallow weathering pits, poorly disassociated clasts from the underlying bedrock and the Type I matrix. A Neogene or pre-Pleistocene origin of the blockfield is, therefore, unlikely. It is suggested that the retreat of the Antarctic ice sheet during the last LGM led to unloading of the surface, dilatation, subsequent fracturing of the bedrock along pre-existing joints and clast supply. Subsequent weathering and erosion along other points or lines of weakness then yielded fines and slight edge rounding of clasts. The blockfield under investigation may be described as an openwork autochthonous deposit of the periglacial model of blockfield development and findings suggest it is of recent (Holocene) origin.

References

Adlam, L.S., Balks, M.R., Seybold, C.A. and Campbell, D.I. 2010. Temporal and spatial variation in active layer depth in the McMurdo Sound Region, Antarctica. *Antarctic Science*, 22: 45-52.

Alsharhan, A.S. and El-Sammak, A.A. 2004. Grain-size analysis and characterisation of sedimentary environments of the United Arab Emirates coastal area. *Journal of Coastal Research*, 20: 464-477.

Anderson, M.G. and Burt, T.P. 1981. Part One: Introduction. *In* Goudie, A. (ed.). *Geomorphological Techniques*. London: George Allen & Unwin. pp. 3-25.

André, M.-F. 2002. Rates of postglacial rock weathering on glacially-scoured outcrops (Abisko-Riksgränsen area). *Geografiska Annaler, Series A,* 84: 139-150.

André, M.-F. 2003. Do periglacial landscape evolve under periglacial conditions? *Geomorphology*, 52: 149-164.

André, M.-F., Hall, K., Bertran, P. and Arocena, J. 2008. Stone runs in the Falkland Islands: Periglacial or tropical? *Geomorphology*, 95: 524-543.

Aoki, H. and Matsukura, Y. 2007. A new technique for non-destructive field measurement of rock-surface strength: an application of the Equotip hardness tester to weathering studies. *Earth Surface Processes and Landforms*, 32: 1759-1769.

Ashcroft, M.B. and Gollan, J.R. 2012. Fine-resolution (25 m) topoclimatic grids of near-surface (5 cm) extreme temperatures and humidities across various habitats in a large (200 × 300 km) and diverse region. *International Journal of Climatology*. 32: 2134-2148 .

Atkinson, P.M. 1999. Geographical information science: Geostatistics and uncertainty. *Progress in Physical Geography*, 23: 134-142.

Atkinson, P.M. 2001. Geographical information science: GeoComputation and nonstationarity. *Progress in Physical Geography*, 25: 111-122.

Atkinson, P.M., German, S.E., Sear, D.A. and Clark, M.A. 2003. Exploring the Relations Between Riverbank Erosion and Geomorphological Controls Using Geographically Weighted Logistic Regression. *Geographical Analysis*, 35: 58-82.

ATS. 1959. *The Antarctic Treaty*. Washington, D.C.: Secretariat of the Antarctic Treaty, December 1 1959.

Aydin, A. 2008. ISRM suggested method for determination of the Schmidt Hammer rebound hardness: Revised version. *International Journal of Rock Mechanics & Mining Sciences*, 46: 627-634.

Ballantyne, C.K. 1984. The late Devensian periglaciation of upland Scotland. *Quaternary Science Reviews*, 3: 311-343.

Ballantyne, C.K. 1998. Age and significance of mountain-top detritus. *Permafrost and Periglacial Processes*, 9: 327-345.

Ballantyne, C.K. 2002. Paraglacial geomorphology. *Quaternary Science Reviews*, 21: 1935-2017.

Ballantyne, C.K. 2010. A general model of autochthonous blockfield evolution. *Permafrost and Periglacial Processes*, 21: 289-300.

Ballantyne, C.K. and Matthews, J.A. 1982. The development of sorted circles on recently deglaciated terrain, Jotunheimen, Norway. *Arctic and Alpine Research*. 14: 341-354.

Basu, A. and Aydin, A. 2004. A method for normalization of Schmidt Hammer rebound values. *International Journal of Rock Mechanics & Mining Sciences*, 41: 1211-1214.

Boelhouwers, J.C. 1993. A discussion regarding weathering in the Western Cape mountains, South Africa: Implications for Pleistocene cryoclastic debris production. *South African Geographical Journal*, 75: 46-52.

Boelhouwers, J.C. 1995. Present day soil frost activity at the Hex River Mountains, Western Cape, South Africa. *Zeitschrift für Geomorphologie*, 39: 237-248.

Boelhouwers, J.C. 1999. Block deposits in southern Africa and their significance to periglacial autochthonous blockfield development. *Polar Geography*, 23: 12-22.

Boelhouwers, J.C. 2004. New perspectives on autochthonous blockfield development. *Polar Geography*, 28: 133-146.

Boelhouwers, J.C., Holness, S., Meiklejohn, I. and Sumner, P. 2002. Observations on a blockstream in the vicinity of Sani Pass, Lesotho Highlands, southern Africa. *Permafrost and Periglacial Processes*, 13: 251-257.

Boelhouwers, J.C., Holness, S. and Sumner, P.D. 2003. The sub-Antarctic: a distinct periglacial environment. *Geomorphology*, 52: 39-55.

Boelhouwers, J.C. and Meiklejohn, K.I. 2002. Quaternary periglacial and glacial geomorphology of southern Africa: review and synthesis. *Periglacial Research*, 98: 47-55.

Boelhouwers, J.C., Meiklejohn, K.I., Holness, D. and Hedding, D.W. 2008. Geology, geomorphology and climate change. *In* Chown, S.I. and Froneman, P.W. (eds.). *The Prince Edward Islands: Land-Sea Interactions in a Changing Ecosystem*. Stellenbosch: Sun Press. pp. 65-96.

Boelhouwers, J.C. and Sumner, P.D. 2003. *The palaeoenvironmental significance of southern African blockfields and blockstreams. In* Phillips, M., Springman, S.M. and Arenson, L.U. (eds.). *Permafrost*. Lisse, Netherlands: Swets and Zeitlinger. pp. 73-78.

Briggs, D. J. 1977a. Sources and Methods in Geography – Soils. London: Butterworths & Co. Ltd.

Briggs, D. J. 1977b. Sources and Methods in Geography – Sediments. London: Butterworths & Co. Ltd.

Brunsdon, C., Fotheringham, A. and Charlton, M. 1998. Geographically Weighted Regression-Modelling Spatial Non-Stationarity. *Journal of the Royal Statistical Society. Series D (The Statistician)*, 47: 431-443.

Büdel, B., Weber, B., Kühl, M., Pfanz, H. and Wessels, D. 2004. Reshaping of sandstone surfaces by cryptoendolithic cyanobacteria: bioalkalisation causes chemical weathering in arid landscapes. *Geobiology*, 2: 261-268.

Burrough, P.A. 2001. GIS and geostatistics: Essential partners for spatial analysis. *Environmental and Ecological Statistics*, 8: 361-377.

Caine, N. 1983. *The Mountains of Northeastern Tasmania. A Study of Alpine Geomorphology*. Australia: Balkema.

Chang, K-T. 2012. *Introduction to Geographic Information Systems* (6ed.). New York: McGraw-Hill.

Charlton, M., Fotheringham, A. and Brunsdon, C. 2006. *Geographically Weighted Regression*. ESRC National Centre for Research Methods, NCRM Methods Review Papers, NCRM/006.

Church, M. 2010. The trajectory of geomorphology. *Progress in Physical Geography*, 34: 265-286.

Cockburn, H.A.P. and Summerfield, M.A. 2004. Geomorphological applications of cosmogenic isotope analysis. *Progress in Physical Geography*, 28: 1-42.

Cooke, R.U. 1979. Laboratory simulation of salt weathering processes in arid environments. *Earth Surface Processes and Landforms*, 4: 347-359.

Cramp, A., Lee, S.V., Herniman, J., Hiscott, R.N., Manley, P.L., Piper, D.J.W., Deptuck, M., Johnston, S.K. and Black, K.S. 1997. Interlaboratory comparison of sediment grain-sizing techniques: data from Amazon fan upper levee complex sediment. *In* Flood, R.D., Piper, D.J.W., Klaus, A., and Peterson, L.C. (eds.), *Proceedings of the Ocean Drilling Program, Scientific Results, Volume 155*. College Station, TX (Ocean Drilling Program). pp. 217-228.

Doornkamp, J.C. and King, C.A.M. 1971. *Numerical analysis in geomorphology – an introduction*. London: Butler & Tanner Ltd.

Dredge, L. A. 1992. Breakup of limestone bedrock by frost shattering and chemical weathering, eastern Canadian Arctic. *Arctic and Alpine Research*, 24: 314-323.

Ericson, K. 2004. Geomorphological surfaces of different age and origin in granite landscapes: an evolution of the Schmidt Hammer test. *Earth Surface Processes and Landforms*, 29: 495-509.

ESRI. 2012. *ArcGIS Resource Centre – How Create Random Points Works.* [Online]. Available: http://help.arcgis.com/en/arcgisdesktop/10.0/help/index.html#/How_Create_Random_Points_works/0017000000t4000000/. [22/05/2012].

Fahey, B.D. 1973. An Analysis of Diurnal Freeze-Thaw and Frost Heave Cycles in the Indian Peak Region of the Colorado Front Range. *Arctic and Alpine Research*. 5: 269-281.

Forbes, K. 2007. *Calibration, recognition and shape from silhouettes of stones*. Cape Town: University of Cape Town (PhD thesis) [pdf].

Fraser, J.K. 1959. Freeze-thaw frequencies and mechanical weathering in Canada. *Artic*, 12: 40-53.

French, H.M. 1996. *The Periglacial Environment* (2e). Harlow: Addison Wesley Longman Ltd.

French, H.M. 2011. Periglacial. *In* Singh, V.P., Singh, P. and Haritashya, U.K. (eds.). *Encyclopedia of Snow, Ice and Glaciers*. Dordrecht: Springer. pp. 827-841.

Friedmann, E.I. 1986. The Antarctic cold desert and the search for traces of life on Mars. *Advanced Space Research*, 6: 265-268.

Gibbard, P.L., Head, M.J., Walker, M.J.C. and The Subcommission on Quaternary Stratigraphy. 2010. Formal ratification of the Quaternary System/Period and the Pleistocene Series/Epoch with a base at 2.58 Ma. *Journal of Quaternary Science*, 25: 96-102.

Goodfellow, B.W., Fredin, I.O., Derron, M.-H. and Stroeven, A.P. 2008. Weathering processes and Quaternary origin of an alpine blockfield in Arctic Sweden. *Boreas*, 38: 379-398.

Goudie, A.S. 2006. The Schmidt Hammer in geomorphological research. *Progress in Physical Geography*, 30: 703-718.

Grab, S.W. 1997. Annually re-forming miniature sorted patterned ground in the high Drakensberg, southern Africa. *Earth Surface Processes and Landforms*, 22: 733-745.

Grab, S.W. 1999. Block and debris deposits in the high Drakensberg, Lesotho, southern Africa: implications for high altitude slope processes. *Geografiska Annaler, Series A*, 81: 1-16.

Grab, S.W. 2005. Earth hummocks (thúfur): new insights to their thermal characteristics and development in eastern Lesotho, southern Africa. *Earth Surface Processes and Landforms,* 30: 541-555.

Grab, S.W. 2007. Near-surface rockwall temperatures in the high Drakensberg basalt: spatio-temporal differences and possible implications for weathering. *Zeitschrift für Geomorphologie*. 51 (Supplement 1): 103-113.

Grab, S.W., Mills, S.C. and Carr, S.J. 2012. Periglacial and glacial geomorphology. *In* Holmes, P. and Meadows, M. (3ds). *Southern African Geomorphology: Recent Trends and New Directions*. Bloemfontein: SUN MeDIA. pp. 233-267.

Griffith, D.A. 2005. *Spatial Autocorrelation.* Syracuse: University of Syracuse.

Grosch, E.G., Bisnath, A., Frimmel, H.E. and Board, W.S. 2007. Geochemistry and tectonic setting of mafic rocks in Western Dronning Maud Land, East Antarctica: implications for the geodynamic evolution of the Proterozoic Maud Belt. *Journal of the Geological Society, London*. 164: 465-475.

Grotzinger, J., Jordan, T.H., Press, F. and Siever, R. 2007. *Understanding Earth* (5ed). New York: W. H. Freeman and Company.

Gupta, V., Sharma, R. and Sah, M. P. 2009. An evaluation of surface hardness of natural and modified rocks using Schmidt Hammer: study from northwestern Himalaya, India. *Geografiska Annaler, Series A*, 91: 179-188.

Hall, A.M. and Phillips, W.M. 2006. Glacial modification of granite tors in the Cairngorms, Scotland. *Journal of Quaternary Science*, 21: 811-830.

Hall K.1983. Observations of some periglacial features and their palaeoenvironmental implications on sub-Antarctic islands Marion and Kerguelen. *South African Journal of Antarctic Research.* 13: 35-40.

Hall, K.I. 1997: Rock temperatures and implications for cold region weathering. I: New data from Viking Valley, Alexander Island, Antarctica. *Permafrost and Periglacial Processes* 8: 69-90.

Hall, K.I. 1999. The role of thermal stress fatigue in the breakdown of rock in cold regions. *Geomorphology*, 31: 47-63.

Hall, K.I. 2002. Review of present and quaternary periglacial processes and landforms of the maritime sub-Antarctic. *South African Journal of Science*. 98: 71-81.

Hall, K.I., Thorn, C.E., Matsuoka, N. and Prick, A. 2002. Weathering in cold regions: some thoughts and perspectives. *Progress in Physical Geography*, 26: 577-603.

Harris, S.A. and Pedersen, D.E. 1998. Thermal regimes beneath coarse blocky materials. *Permafrost and Periglacial Processes*, 9: 107-120.

Hedding, D.W. 2008. Spatial inventory of landforms in the recently exposed central highland of sub-Antarctic Marion Island. *South African Journal of Geographers*, 90: 11-21.

Holcombe, R. 2011. *Structural Geology-Mapping/GIS Software*. [Online] Available: http://www.holcombe.net.au/software/rodh_software_georient.htm. [02/08/2013].

Holmlund, P. and Näslund, J-O. 1994. The glacially sculptured landscape in Dronning Maud Land, Antarctica, formed by wet-based mountain glaciation and not by the present ice sheet. *Boreas*, 23: 139-148.

Ishikawa, M. 2003. Thermal regimes at the snow-ground interface and their implications for permafrost investigation. *Geomorphology*, 52: 105-120.

ISRM (International Society for Rock Mechanics). 1978: Commission on standardization of laboratory and field tests. Suggested methods for determining hardness and abrasiveness of rocks. *International Journal of Rock Mechanics and Mining Sciences Geomechanical Abstracts* 15: 89-97.

Katz, O., Reches, Z. Roegiers, J.-C. 2000: Evaluation of mechanical rock properties using a Schmidt Hammer. *International Journal of Rock Mechanics and Mining Sciences* 37: 723-28.

Kitching, R. and Tate, N.J. 2000. *Conducting Research in Human Geography: theory, methodology and practice*. Edinburgh: Pearson Education Limited.

Klein, C. and Dutrow, B. 2008. *The 23rd Edition of the Manual of Mineral Science* (23ed). USA: John Wiley & Sons, Ltd.

Kleman, J. and Glasser, N. 2007. The subglacial thermal organization (STO) of ice sheets. *Quaternary Science Reviews*, 25: 585-597.

Kompatscher, M., 2004: Equotip-rebound hardness testing after D. Leeb. In: *Proceedings, Conference on Hardness Measurements Theory and Application in Laboratories and Industries*. pp. 11-12.

Lara, O.G. and Matthes, W.J. 1986. The SediGraph as an alternative to the pipet. *In Proceedings of the 4th Federal Interagency Sedimentation Conference*. *Subcommittee on Sedimentation of the Interagency Advisory Committee on Water Data, Volume 1*. Las Vegas, Nevada, March 24-27th, 1986. pp. 1-1 – 1.12.

Lee, J.E., le Roux, P.C., Meiklejohn, K.I. and Chown, S.L. 2013. Species distribution modelling in low-interaction environments: Insights from terrestrial Antarctic system. *Austral* Ecology, 38: 279-288.

Lozinski, W. 1909. Über die mechanische Verwitterung der Sandsteine im Gemässigten Klima. *Bulletin International de l'Académie des Sciences de Cravocie class des Sciences Mathématiques et Naturelles*, 1: 1 – 25.

Marquette, G.C., Gray, J.T., Gosse, J.C., Courchesne, F., Stockli, L., Macpherson, G. and Finkel, R. 2004. Felsenmeer persistence under non-erosive ice in the Torngat and Kaumajet mountains, Quebec and Labrador, as determined by soil weathering and cosmogenic nuclide exposure dating. *Canadian Journal of Earth Sciences*, 41: 19-38.

Matsuoka, N. 2008. Frost weathering and rockwall erosion in the southeastern Swiss Alps: long-term observations. *Geomorphology*, 99: 353-368.

Matthews, J.A. and Owen, G. 2008. Endolithic lichens, rapid biological weathering and Schmidt Hammer *R*-values on recently exposed rock surfaces: Storbreen glacier foreland, Jotunheimen, Norway. *Geografiska Annaler, Series A*, 90: 287-297.

Matthews, J.A. and Shakesby, R.A. 1984: The status of the 'Little Ice Age' in southern Norway: relative- age dating of Neoglacial moraines with Schmidt Hammer and lichenometry. *Boreas* 13: 333-46.

McCarthy, T. and Rubidge, B. 2005. *The Story of Life and Earth: A southern African perspective on a 4/6-bilion-year journey*. Cape Town: Struik Nature.

Meiklejohn, K.I. 2007. [Photograph]. Personal Communication. May 2011.

Meiklejohn, K.I. 2012. Initial Environmental Evaluation – Landscape Processes in Antarctic Ecosystems. Department of Environmental Affairs, South Africa.

Meiklejohn, K.I. 2012. Professor, Department of Geography, Rhodes University. Personal Communication. June 2012.

Meiklejohn, K. I. and Hall, K. 1997. Aqueous geochemistry as an indicator of chemical weathering on southeastern Alexander Island, Antarctica. *Polar Geography*, 21: 100-112.

Micromeritics, 2012. *SediGraph III Technique Overview*. [Online]. Available: http://micromeritics.com/Repository/Files/SEDIGRAPH_III_5120_TECHNIQUE_OVEVIEW.pdf. [20/11/2012].

Middleton, G.V. 1965. The Tukey Chi-square test. *The Journal of Geology*, 73: 547-549.

Miller, J.A. 2012. Species distribution models: Spatial autocorrelation and non-stationarity. *Progress in Physical Geography*, 36: 681-692.

Mol, L. and Viles, H. 2012. The role of rock surface hardness and internal moisture in tafoni development in sandstone. Earth Surface Processes and Landforms, 37: 301-314.

Mulder, N. and Grab, S.W. 2002. Remote sensing for snow cover analysis along the Drakensberg escarpment. *South African Journal of Science*, 98: 213-217.

Murray, A.B., Lazarus, E., Ashton, A., Baas, A., Coco, G., Coulthard, T., Fonstad, M., Haff, P., McNamara, D., Paola, C., Pelletier, J. and Reinhardt, L. 2009. Geomorphology, complexity, and the emerging science of the Earth's surface. *Geomorphology*, 103: 496-505.

Murton, J.B., Peterson, R. and Ozouf, J.-C. 2006. Bedrock fracture by ice segregation in cold regions. *Science*, 314: 1127-1129.

Nesje, A., Dahl, S.O., Anda, E. and Rye, N. 1988. Block fields in southern Norway: significance for the Late Weichselian ice sheet. *Norsk Geologisk Tidsskrift*, 68: 149-169.

Niedzielskie, T., Migoń, P. and Placek, A. 2009. A minimum sample size required from Schmidt Hammer measurements. *Earth Surface Processes and Landforms*, 34: 1713-1725.

Onuigbo, E.N., Okoro, A. U., Obiadi, I.I., Akpunonu, E.O., Okeke, H.C. and Maduewesi, V.U. 2012. Tide-generated sedimentary structures, lithofacies and particle size distribution: proxies to the depositional setting of the Ajali sandstone in the Anambra basin, southeastern Nigeria. *Journal of Natural Sciences Research*, 2: 2224-3186.

Instituto de Geociências – Universidade de São Paulo. 2010. *OpenStereo*. [Online]. Available: http://www.igc.usp.br/index.php?id=391. [02/08/2013].

Paasche, Ø., Strømsøe, J.R., Dahl, S.O. and Linge, H. 2006. Weathering characteristics of arctic islands in northern Norway. *Geomorphology*, 82: 430-452.

PermaNet (Permafrost Monitoring Network), 2011. *Guidelines for Monitoring GST – Ground surface temperature (v3)*. [Online]. Available: www.permanet-alpinespace.eu/archive/pdf/GST.pdf [24/11/2012].

Ravindra, R. and Chaturvedi, A. 2011. Antarctica. *In* Singh, V.P., Singh, P. and Haritashya, U.K. (eds.). *Encyclopedia of Snow, Ice and Glaciers*. Dordrecht: Springer. pp. 45-54.

Rea, B.R. 2007. Blockfields. *In* Elias, S. (ed.). *Encyclopaedia of Quaternary Science*, Elsevier. pp. 2225-2236.

Rea, B.R., Whalley, W.B., Rainey, M.M. and Gordon, J.E. 1996. Blockfields, old or new? Evidence and implications from some plateaus in northern Norway. *Geomorphology*, 15: 109-121.

Reijmer, C. H. and van den Broeke, M. R. 2001. Moisture source of precipitation in Western Dronning Maud Land, Antarctica. *Antarctic Science,* 13: 210-20.

Republic of South Africa. 1981. *Reconnaissance Geological Map of the Ahlmannryggen Area, Western Dronning Maud Land, Antarctica*, SR29-30/15 (part) and SR29-30/16 1: 250 000 Sheet 1. Pretoria, South African Scientific Committee for Antarctic Research.

Richter, D. and Simmons, G. 1974. Thermal expansion behaviour on igneous rocks. *International Journal of Rock Mechanics and Mining Science and Geomechanics Abstracts*. 11: 403-411.

SANAP. 1992. *South African National Antarctic Program (SANAP) Antarctic Field Manual*. Pretoria: Department of Environmental Affairs.

SANAP. 2009. *South African National Antarctic Program (SANAP) Safety Manual for Participants*. Pretoria: Department of Environmental Affairs.

SANAP. 2012a. *About Sanap*. [Online]. Available: http://www.sanap.org.za/about_sanap/about_sanap.html. [22/05/2012].

SANAP. 2012b. *Sanae base – History*. [Online]. Available: http://www.sanap.org.za/sanap_sanae/sanae_history.html. [22/05/2012].

SANAP. 2012c. *Sanap – Research*. [Online]. Available http://www.sanap.org.za/sanap_research/sanap_research.html. [22/05/2012].

SCAR. 2010. [Online]. *Scientific Committee on Antarctic Research.* [Online]. Available: http://www.scar.org/about/. [22/05/2012].

Serrano, E. and López-Martínez, J. 2000. Rock glaciers in the South Shetland Islands, Western Antarctica. *Geomorphology*. 35: 145 – 162.

Shakesby, R.A., Matthews, J.A. and Owen, G., 2006. The Schmidt Hammer as a relative-age dating tool and its potential for calibrated-age dating in Holocene glaciated environments. *Quaternary Science Reviews*, 25: 2846-2867.

Small, E.E., Anderson, R.S. and Hancock, G.S. 1999. Estimates of the rate of regolith production using 10Be and 26Al from an alpine hillslope. *Geomorphology*, 27: 131-150.

Stein, R. 1985. Rapid grain-size analyses of clay and silt fraction by SediGraph 500D: comparison with Coulter Counter and Attenberg methods. *Journal of Sedimentary Petrology*, 55: 590-593.

Stewart, J. 2011. *Antarctica – An Encyclopedia* (2e). London: McFarland & Company, Inc.

Stone P. 1974. Physiography of the north-east coast of South Georgia. *British Antarctic Survey Bulletin.* 38: 17-36.

Sumner, P.D. 2004. Geomorphic and climatic implications of relict openwork block accumulations near Thabana-Ntlenyana, Lesotho. *Geografiska Annaler, Series A*, 3: 289-302.

Sumner, P.D., Hall, K.J., Van Rooy, L. and Meiklejohn, K.I. 2009. Rock weathering on the eastern mountains of southern Africa: Review and insights from case studies. *Journal of African Earth Sciences*, 55: 236-244.

Sumner, P.D. and Meiklejohn, K.I. 2004. On the development of autochthonous blockfields in the grey basalts of sub Antarctic Marion Island. *Polar Geography*, 28: 20-32.

Sumner, P.D. and Nel, W. 2002. The effect of rock moisture on Schmidt Hammer rebound: tests on rock samples from Marion Island and South Africa. *Earth Surface Processes and Landforms*, 27: 1137-42.

Sumner, P.D., Nel, W. and Hedding, D.W. 2004. Thermal attributes of rock weathering: zonal or azonal? A comparison of rock temperatures in different environments. *Polar Geography*. 28: 79-92.

Sumner, P.D., Nel, W., Holness, S. and Boelhouwers, J. 2002. Rock weathering characteristics as relative-age indicators for glacial and post-glacial landforms on Marion Island. *South African Geographical Journal*. 84: 153-157.

Thorn, C.E., 1992. Periglacial Geomorphology: What, Where, When? *In* Dixon, J.C., Abrahams, A.D. (eds.), *Periglacial Geomorphology, The Binghampton Symposia in Geomorphology: International Series*. Wiley, Chichester, West Sussex, UK; Hoboken, NJ, pp. 1–31.

Till, R. 1985. *Statistical Methods for the Earth Scientist – an introduction*. London: MacMillian Education Ltd.

Van den Berg, L. 2012. [Photograph]. Personal Communication. January 2012.

Van der Merwe, B. 2012. Lecturer, Department of Geography, Geoinformatics and Meteorology. University of Pretoria. Personal Communication. January 2012.

Vieira, G., Bockheim, J., Guglielmin, M., Balks, M., Abramov, A.A., Boelhouwers, J., Cannone, N., Ganzert, L., Gilichinsky, D.A., Goryachkin, S., López-Martínez, J., Meiklejohn, I., Raffi, R., Ramos, M., Schaefer, C., Serrano, E., Simas, F., Sletten, R. and Wagner, D. 2010. Thermal state of permafrost and active-layer monitoring in the Antarctic: advances during the International Polar Year 2007-2009. *Permafrost and Periglacial Processes*, 21: 182-197.

Viles, H., Goudie, A., Grab, S. and Lalley, J. 2011. The use of the Schmidt Hammer and Equotip for rock hardness assessment in geomorphology and heritage science: a comparative analysis. Earth Surface Processes and Landforms, 36: 320-333.

Waragai, T. 1999. Weathering processes on rock surfaces in the Hunza Valley, Karakoram, North Pakistan. *Zeitschrift für Geomorphologie Supplementband*, 119: 119-36.

Washburn, A.L., 1980. *Geocryology: a survey of periglacial processes and environments*. Wiley, New York.

Weaver, A.v.B. and Grobler, D.C. 1981. An evaluation of the SediGraph as a standard method of sediment particle size analysis. *Water SA*, 7: 79-87.

Weinert, H.H. 1980. *The Natural Road Construction Materials of Southern Africa*. Pretoria: H&R Academia (Pty.) Ltd.

Whalley, W.B. 1981. Part Three: Material Properties. *In* Goudie, A. (ed.). *Geomorphological Techniques*. London: George Allen & Unwin. pp. 79-104.

Whalley, W.B., Rea, B.R. and Rainey, M.M. 2004. Weathering, blockfields and fracture systems and the implications for long-term landscape formation: some evidence from Lyngen and Øksfordjøkelen areas in north Norway. *Polar Geography*, 28: 93-119.

Whalley, W.B., Rea, B.R., Rainey, M.M. and McAlister, J.J. 1997. Rock weathering in blockfields: some preliminary data from mountain plateaus in North Norway. *Geological Society, London, Special Publication*, 120: 133-145.

Williams. T.A., Sweeney. D.J. and Anderson. D.R. 2006: *Contemporary Business Statistics with Microsoft® Excel*. Mason: Thomson South-Western.

Wilson, P. 2007. Block/Rock Streams. *In* Elias, S. (ed.). *Encyclopaedia of Quaternary Science.* Elsevier. pp. 2217-2225.

Yong, C. and Wang, C. 1980. Thermally-induced acoustic emission in westerly granite, *Geophysical Research letters*, 7: 1089-1092.

Appendix A: Instruments

A variety of instruments were used both during the course of fieldwork, laboratory analyses as well as during data analyses. The list below details instruments used for each data requirement.

Table 72: Table of instruments used for the duration of the project during the fieldwork, as well as laboratory component.

Instrument/Tool	Accuracy/Resolution	Comment
GPSmart 60CSx GARMIN GPS	3 m	Clast characterisation
Proceq N-34 Schmidt Hammer	Two units	Clast characterisation
Proceq Equotip hardness tester	4HL	Clast characterisation
SONY Cyber-shot digital camera	14.1 megapixels	Clast characterisation
WEBCO measuring tapes	3 m, 5 m, 50 m	Clast characterisation
Clino Master clinometer	0.25°	Clast characterisation
SILVA Sight Master magnetic compass	0.5°	Clast characterisation
Eastwing geological hammer	N/a	Clast characterisation
Labcon Forced Circulation Oven FSOE	Min. 0°C; max. 250°C	Clast characterisation
Scaltec Instruments scale	Maximum of 320 g; resolution of 0.001g	Soil moisture and temperature regimes
IncoTherm Labotec oven	Min. 0°C; max. 250°C	Soil moisture and temperature regimes
XR5-SE/PACE data logger	0.15°C	Soil moisture and temperature regimes
Fairbridge Technologies (Pty) Ltd iButton Thermochrons® Type DS1922L	0.0625°C	Soil moisture and temperature regimes
Endecott test sieve shaker	Sieve sizes: 8 000-63 µm	Particle size analyses
Mettler PF3000 scale	Resolution of 0.00 g	Particle size analyses
SediGraph 5100	125-0.18 µm	Particle size analyses
Labotec Ultrasonic LC130H	N/a	Particle size analyses
Esri ArcGIS Suite of Products	N/a	Clast characterisation; soil moisture and temperature regimes
Microsoft® EXCEL	N/a	Clast characterisation; soil moisture and temperature regimes
OpenStereo; GEOrient 9.5.0	N/a	Clast characterisation

Appendix B: Statistical Descriptions, Ranges and Classes

Terms used throughout statistical and laboratory analyses often need to be defined and assigned to classes, in order to standardise all terms used. Tables below show terms, such as 'negatively skewed', and their specific range of values. Furthermore, particle size classes are indicated as well as an example of a soil texture diagram.

Table 73: Size grades of sedimentary particles (Briggs, 1977a).

Phi Size (ø) ($ø = -log_2 d$)	**Millimetres (mm)**	**Micrometres (µm)**	**Wentworth Grade**
-6.0	64	64 000	Cobbles ------- 60.0 mm -------
-5.5	44.8	44 800	
-5.0	32	32 000	Coarse gravel
-4.5	22.4	22 400	------- 20.0 mm -------
-4.0	16	16 000	
-3.5	11.2	11 200	Medium gravel
-3.0	8	8 000	------- 6.0 mm -------
-2.5	5.6	5 600	
-2.0	4	4 000	Fine gravel
-1.5	2.8	2 800	
-1.0	2	2 000	------- 2.0 mm -------
-0.5	1.4	1 400	
0.0	1	1 000	Coarse sand
0.5	0.71	710	------- 0.6 mm -------
1.0	0.5	500	
1.5	0.355	355	Medium sand
2.0	0.25	250	------- 0.2 mm -------
2.5	0.18	180	
3.0	0.125	125	Fine sand
3.5	0.090	90	
4.0	0.063	63	------- 0.06 mm -------
4.5	0.045	45	
5.0	0.032	32	Coarse silt
5.5	0.023	23	------- 0.02 mm -------
6.0	0.016	16	
6.5	0.011	11.0	Medium silt
7.0	0.008	8.0	------- 0.006 mm -------

Phi Size (ø) ($ø = -log_2 d$)	Millimetres (mm)	Micrometres (µm)	Wentworth Grade
7.5	0.0055	5.5	
8.0	0.004	4.0	Fine silt
8.5	0.00275	2.75	------- 0.002 mm -------
9.0	0.002	2.0	
9.5	0.00138	1.38	Clay
10.0	0.001	1.0	

Table 74: Descriptive terms and ranges used for skewness classes (adapted from Briggs, 1977a and Williams *et al.*, 2006).

Description	Range
Highly negatively skewed	< -1.62
Negatively skewed	-1.0 – -1.62
Moderately negatively skewed	-0.3 – -1.0
Finely negatively skewed	-0.3 – -0.1
Symmetrical	-0.1 – 0.1
Finely positively skewed	0.1 – 0.3
Positively skewed	0.3 –1.0
Very positively skewed	1.0 – 1.62
Highly positively skewed	> 1.62

Table 75: Descriptive terms and ranges used for sediment sorting classes (Briggs, 1977a).

Description	Range
Very well sorted	< 0.35
Well sorted	0.35 – 0.50
Moderately well sorted	0.50 – 0.70
Moderately sorted	0.70 – 1.00
Poorly sorted	1.00 – 2.00
Very poorly sorted	2.00 – 4.00
Extremely poorly sorted	> 4.00

Table 76: Descriptive terms and ranges used for kurtosis classes (Briggs, 1977a).

Description	Range
Very platykurtic	< 0.67
Platykurtic	0.67-0.90
Mesokurtic	0.90-1.11

Description	Range
Leptokurtic	1.11-1.50
Very leptokurtic	1.50-3.00
Extremely leptokurtic	> 3.00

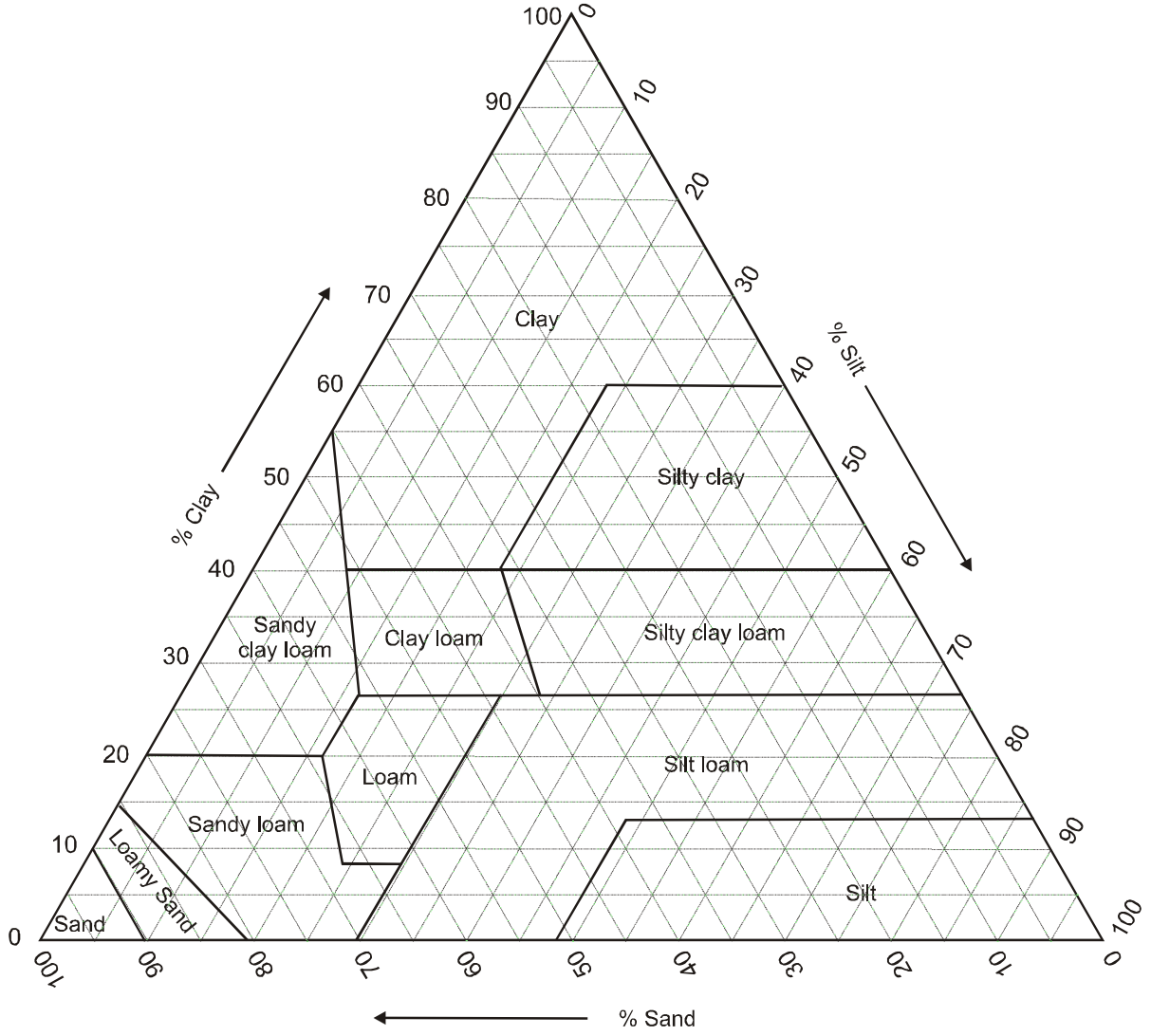

Figure 76: Soil texture diagram, based on sand, silt and clay content (Briggs, 1977b).

Appendix C: SediGraph 5100 Settings

Tables contained within this appendix detail analysis settings for the SediGraph 5100, as used during fine earth fraction analyses. A graph depicting the result of the baseline sample test (executed before SediGraph analyses test runs) is also shown.

Table 77: Baseline test-run settings of the SediGraph 5100. The baseline test is run on the prepared sodium hexametaphosphate solution (0.1%). Results of the test are used to calibrate subsequent analysis results.

Parameter	Value
Temperature	32°C ± 0.2°C
X-Ray Intensity	Normal
Pump Control	Auto
Sample Amount	50 ml
Analysis Runs (Number of Tests)	One
Analysis Liquid	Sodium hexametaphosphate ($NaPO_4$) in deionised water at 0.1%

Table 78: SediGraph 5100 settings. Three samples were analysed with three tests run per sample. Consequently, nine tests were run in total (three per sediment sample).

Parameter	Value
Temperature	32°C ± 0.2°C
X-Ray Intensity	Normal
Pump Control	Auto
Sample Amount	50 ml
Analysis Runs (Number of Tests)	Three
Sample Material	Sediment densities of 1.257 $g.ml^{-1}$ (S1), 1.142 $g.ml^{-1}$ (S2) and 1.321 $g.ml^{-1}$ (S3).
Starting Diameter	63 µm
End Diameter	0.5 µm
Analysis Liquid	Water
Analysis Type	Standard
Rinse after Analysis	Yes (two rinses; pump speed of five)
Distribution Type	Mass
Test	Average
Full Scale Mass Percentage	100
Reporting Option	Full report set: – Cumulative Finer Mass Percentage vs. Diameter – Mass Frequency vs. Diameter

Parameter	Value
	– Rosin Rammler Graph – X-Ray Intensity vs. Cell Position – Cumulative Surface Area Coarser vs. Diameter – Surface Area Population vs. Diameter – Cumulative Particle Number Coarser vs. Diameter – Particle Number Populations vs. Diameter – Log Probability Graph

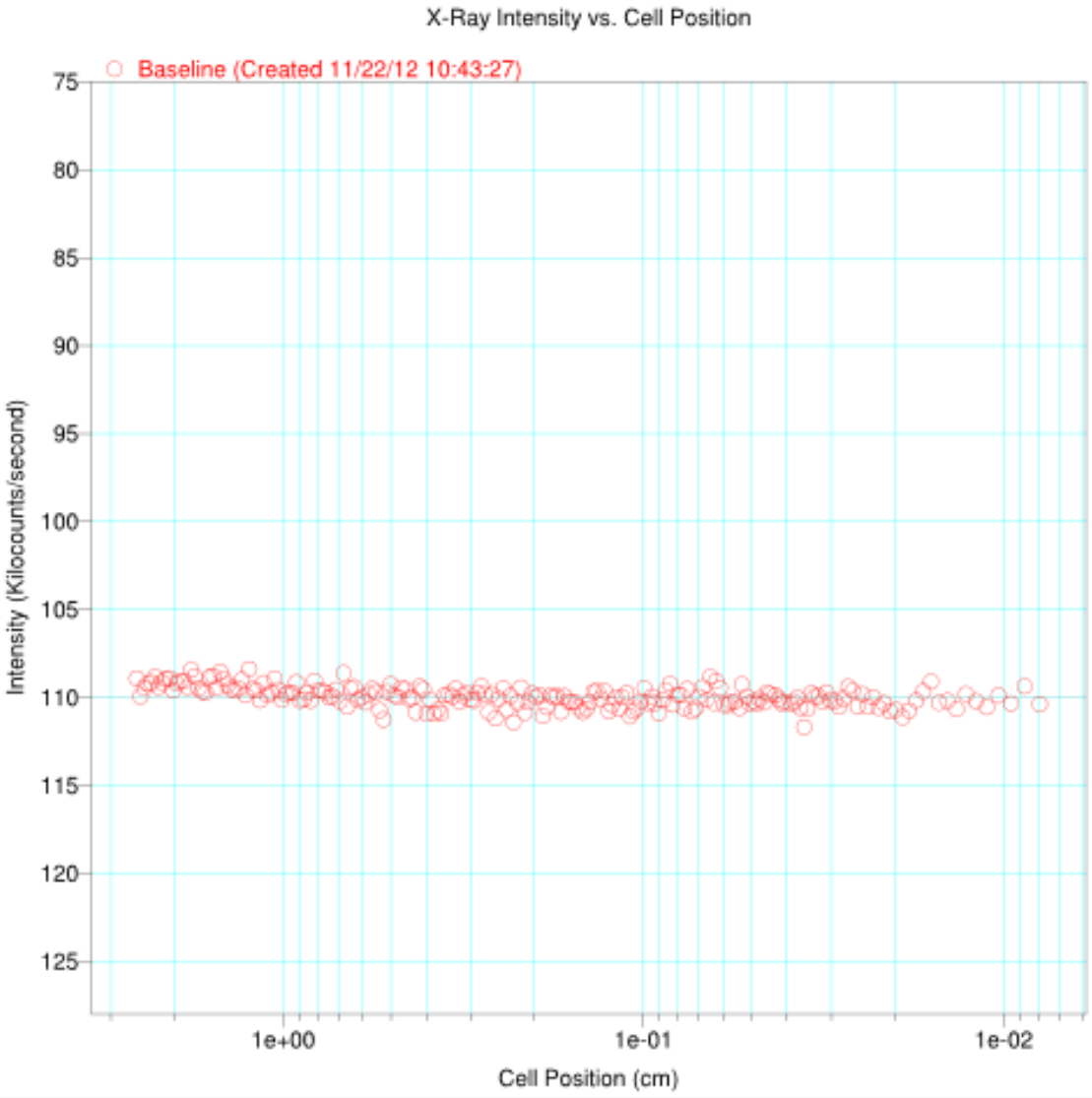

Figure 77: Graph of the result of the baseline test run on the SediGraph 5100, using a 0.1% sodium hexametaphosphate solution.

Appendix D: GIS Models

This appendix illustrates models created in Model Builder™ of ArcGIS®. Models were created for easy re-use in GIS analyses.

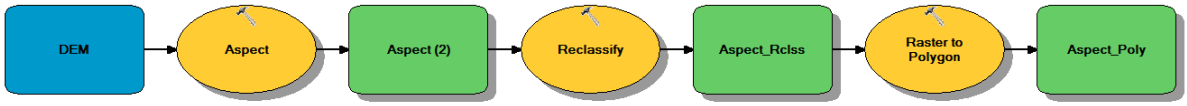

Figure 78: GIS model to calculate aspect (north, east, south, west, top) across the study site.

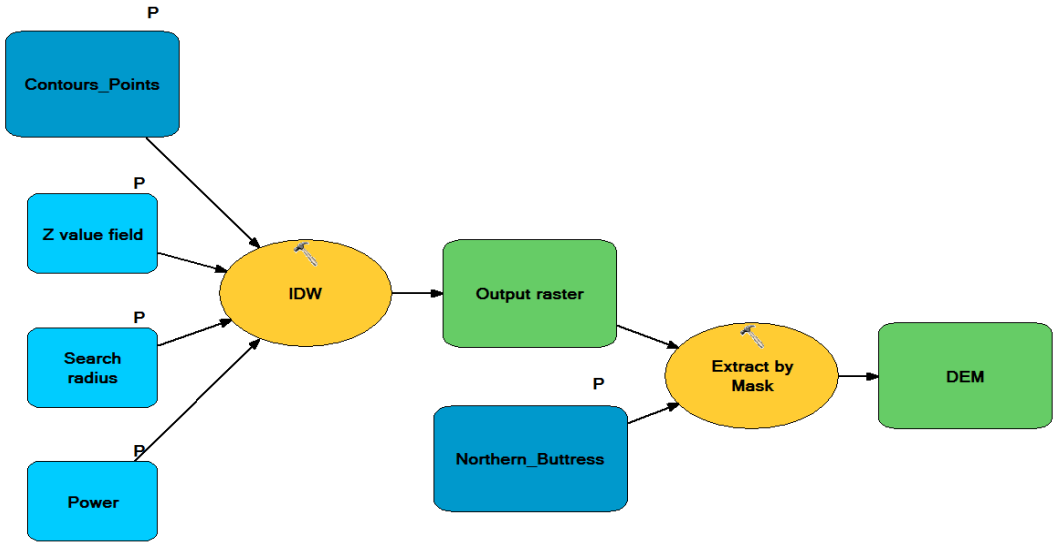

Figure 79: GIS model to calculate slope gradient (percentage and degree) across the study site.

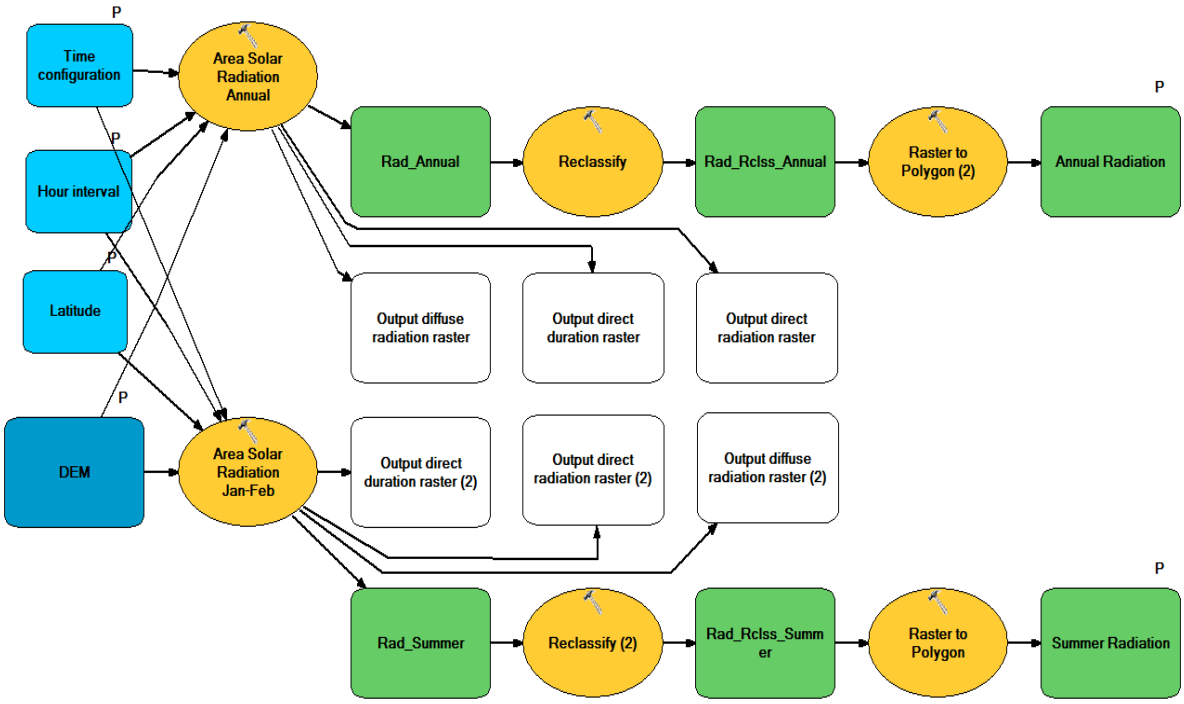

Figure 80: GIS model for calculating solar radiation ($WH.m^{-2}$). Solar radiation is calculated for the full solar year (365 days) as well as January/February 2012. These radiation surfaces are used during analyses on rock hardness rebound values and GST dynamics respectively.

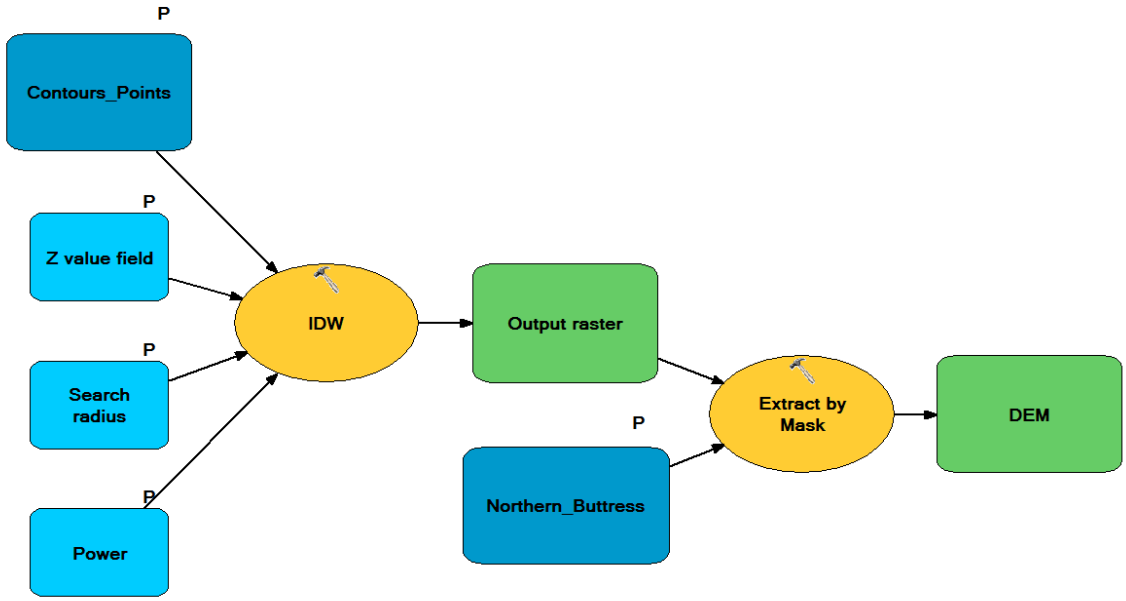

Figure 81: GIS model for interpolating contour values to a DEM.

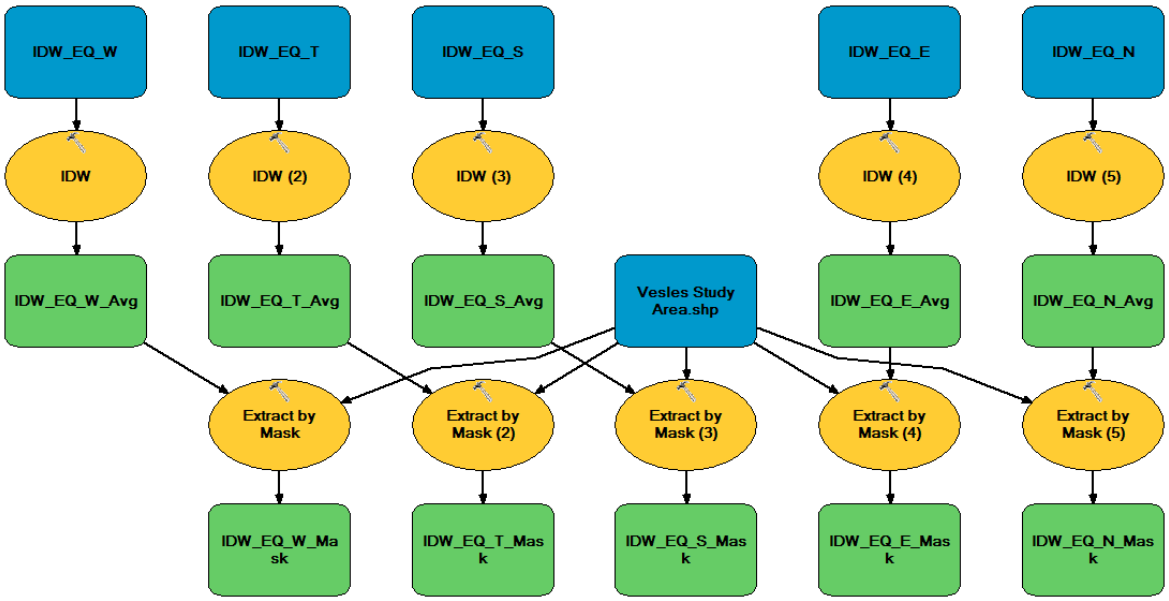

Figure 82: The process followed during GIS analyses for interpolating Equotip rock hardness rebound values per aspect across the study site. Average rock hardness rebound values are used as input to the model. The same process is followed for SH values.

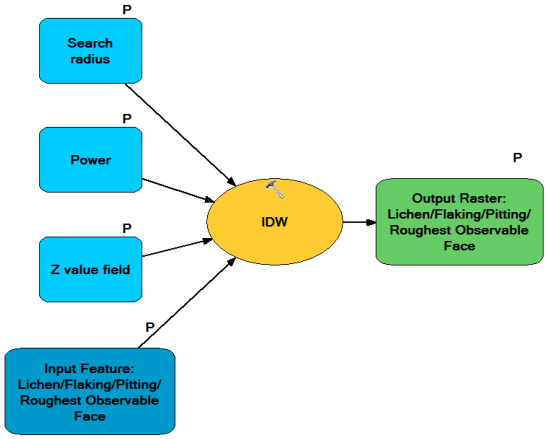

Figure 83: Interpolating weathering indicators (roughest observable face, weathering pitting, flaking and lichen presence) for each aspect (north-, east-, south-, west-, top-facing sides) across the study site.

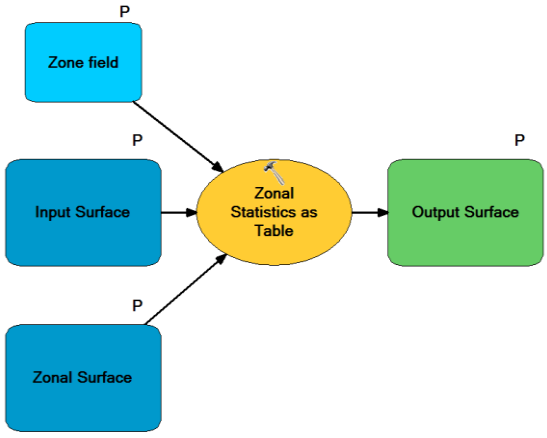

Figure 84: GIS model for conducting zonal statistics for mean rock hardness rebound values per aspect (north, east, south, west, top), slope gradient (°), snow cover (low, medium, high) and solar radiation ($WH.m^{-2}$).

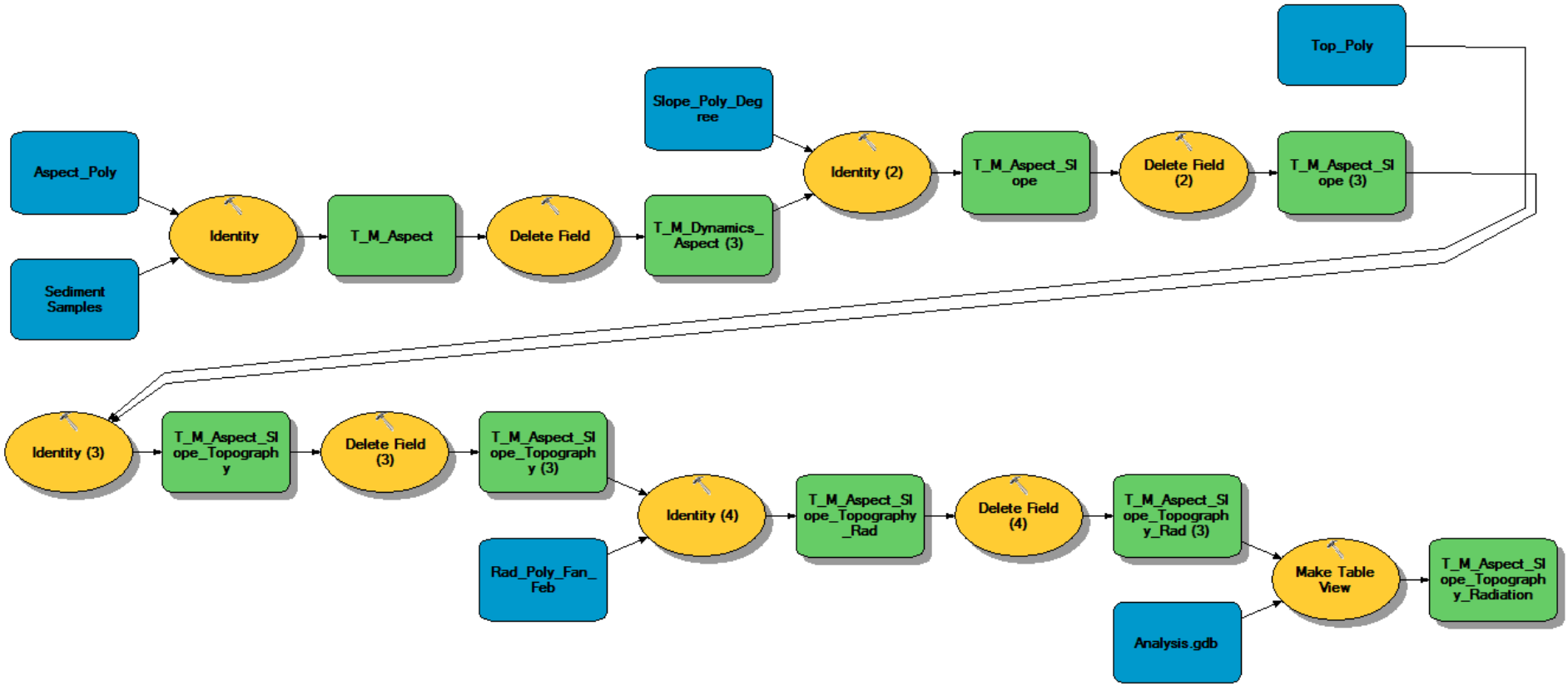

Figure 85: A graphical depiction of the process followed during GIS analyses to determine similarities in aspect (north, east, south, west, top), slope gradient (°), elevation (MASL) and solar radiation ($WH.m^{-2}$) received for GST sample sites for the period under investigation.

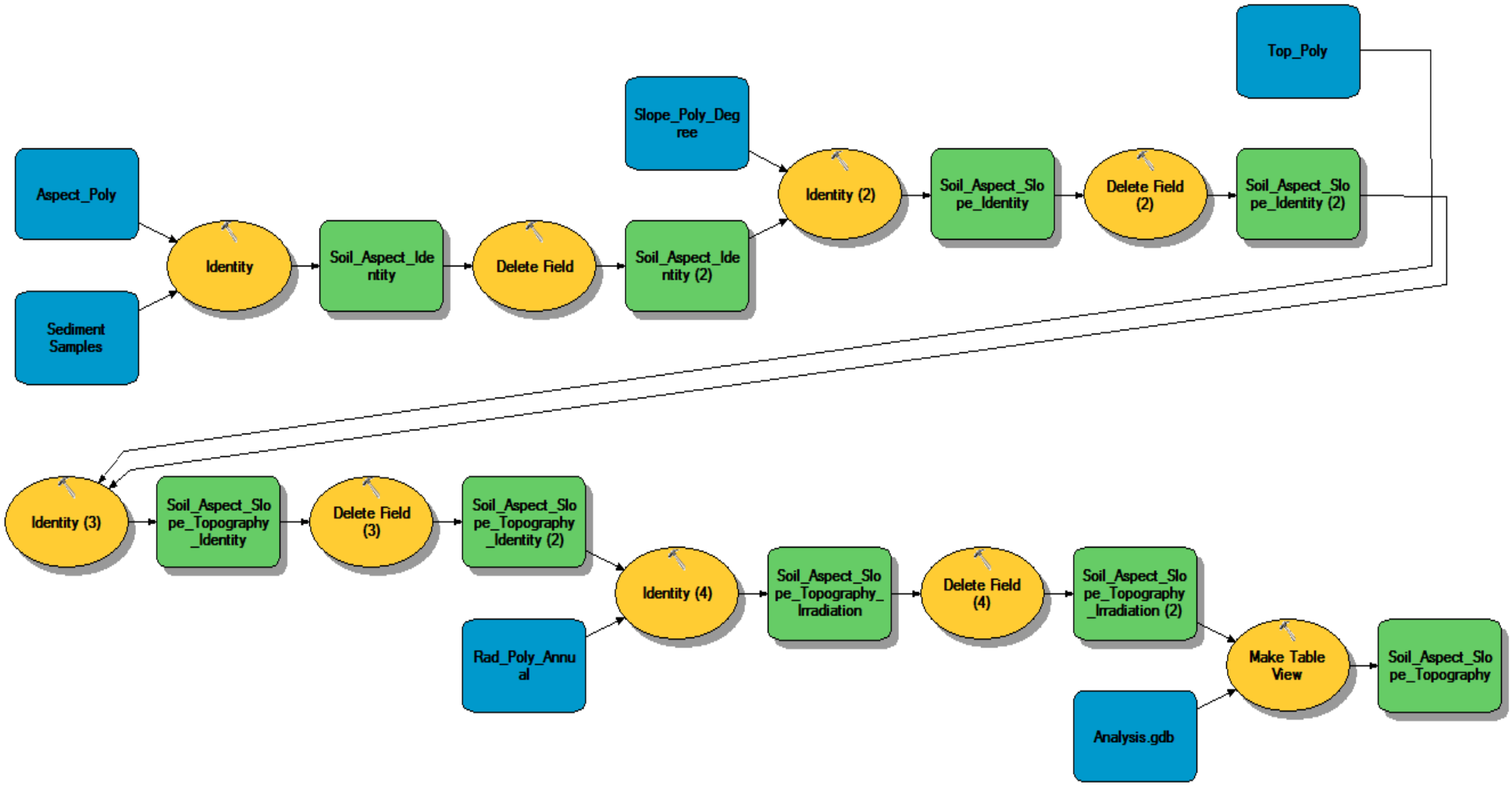

Figure 86: A graphical depiction of the process followed during GIS analyses to determine similarities in aspect (north, east, south, west, top), slope gradient (°) and elevation (MASL) for sediment samples (S1, S2, S3).

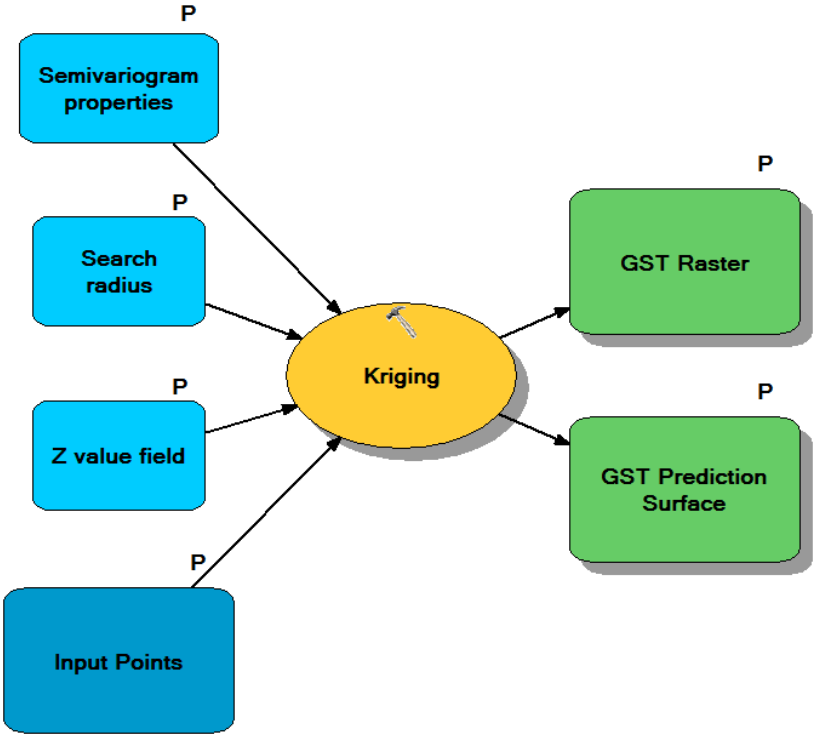

Figure 87: A graphical description of the GIS process followed when interpolating values to a surface using Universal Kriging.

Appendix E: Pie Charts Accompanying Statistical Analyses of Clast Characterisation

Pie charts on a variety of parameters investigated during clast characterisation analyses are indicated. These parameters include the nature of clast support (block, ice or ice and block), the plane (ab, ac, bc) representing the top-facing sides of clasts, lichen presence per clast side, flaking and weathering pits observed for clasts, the roughest face, as well as a-axis and top-facing side orientations. Proportions are expressed as a percentage (%).

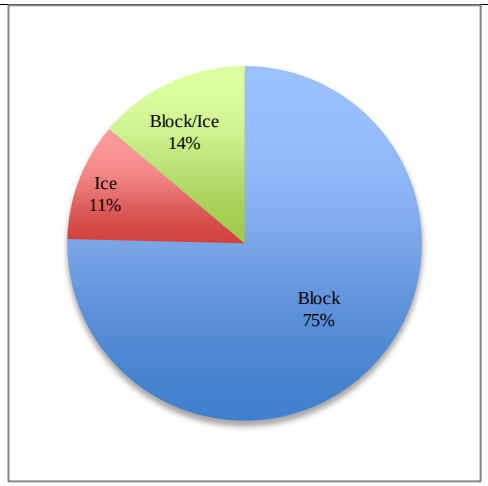

Figure 88: Percentage values (%) of clasts either block supported, ice supported or supported by a combination of block and ice (n = 260).

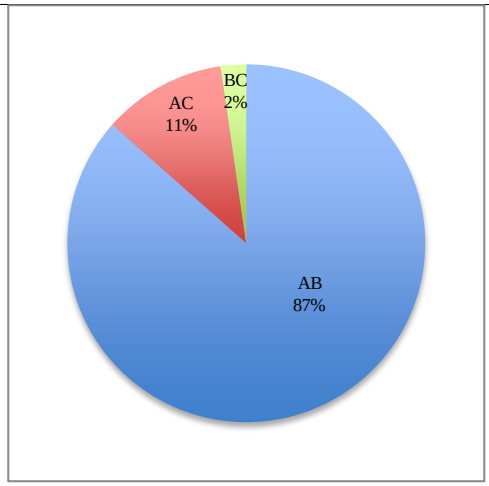

Figure 89: Top face plane per aspect (ab, ac, bc), expressed as a percentage (%) (n = 260).

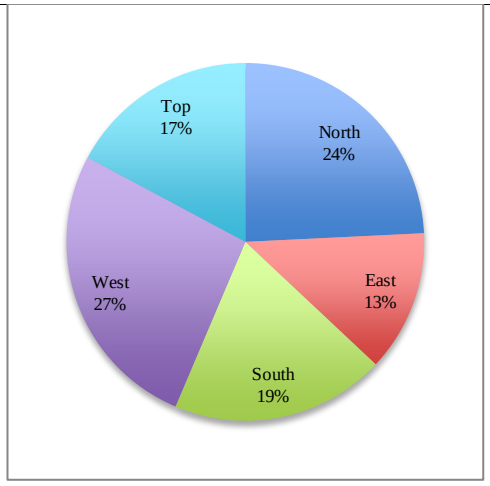

Figure 90: Percentage values (%) of lichen presence, grouped per aspect (n = 260).

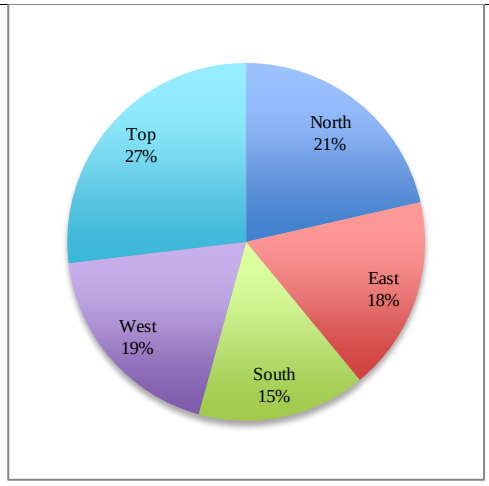

Figure 91: Percentage values (%) of flaking of clast surfaces, grouped per aspect (n = 260; number of faces exhibiting flaking = 420).

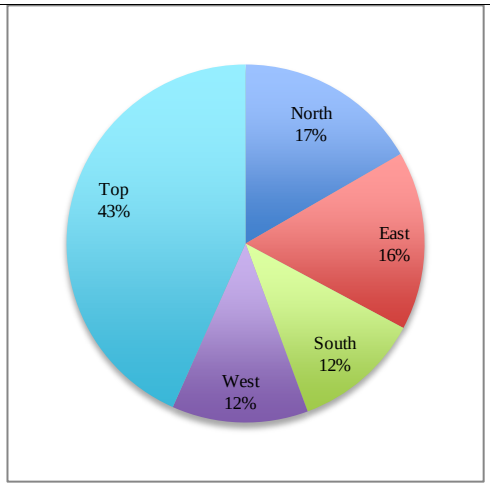

Figure 92: Weathering pits observed per clast face, expressed as a percentage (%) and grouped per aspect.

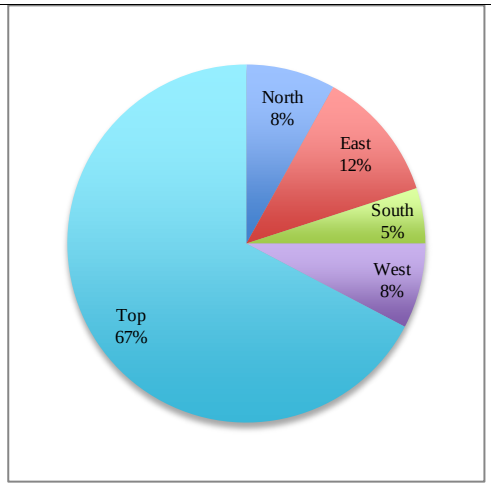

Figure 93: Roughest observable face, expressed as a percentage (%) and grouped per aspect (n = 260).

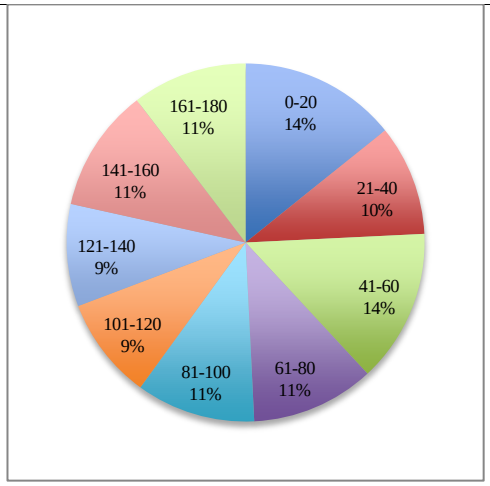

Figure 94: A-axis orientations ranging from north to south, expressed as a percentage (%) (n = 260).

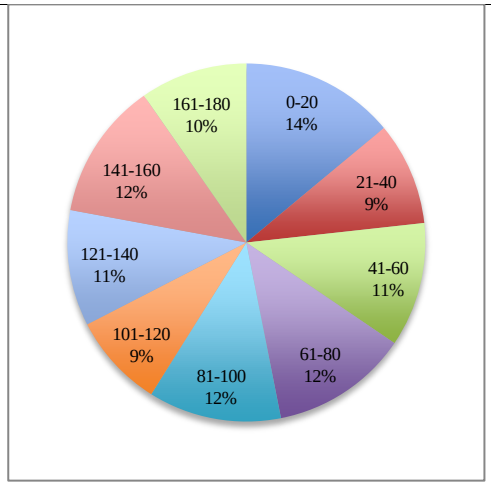

Figure 95: Top face orientation of clasts, ranging from north to south, expressed as a percentage (%) (n = 258).

Appendix F: Climate Parameters Graphs and Inferential Statistics on Near-Surface Temperature Dynamics

This appendix contains graphs, trendlines and the calculated R^2-statistics for the climate parameters of wind direction and speed, ambient temperature, relative humidity and pressure for the study site from the 6th of January to the 3rd of February 2012. Inferential statistics (ANOVA; Fisher's LSD test) are also shown for GST for the 2010/11 and 2011/12 field seasons.

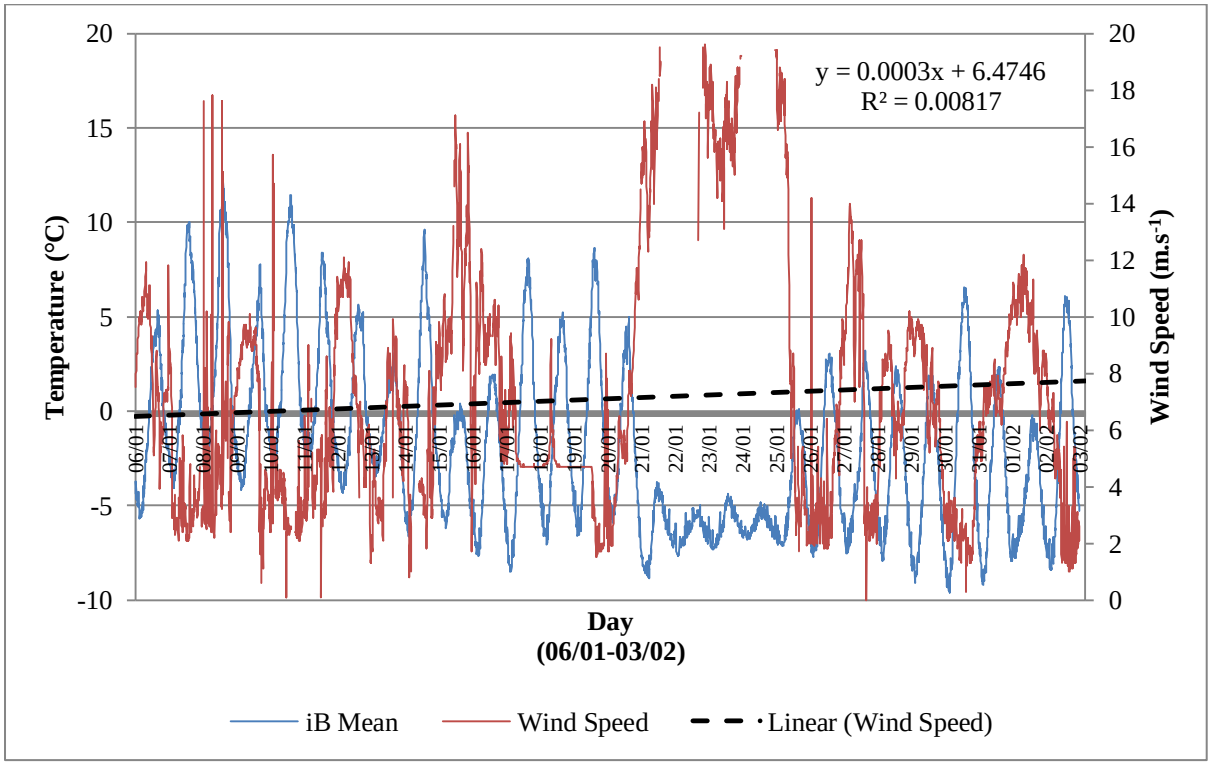

Figure 96: Wind speed, measured in meters per second (m.s-^{1}), compared to average GST observed for the study site from the 6th of January to 3rd of February 2012. The trendline for wind speed is indicated as a dashed line. The equation of the trendline and the R^2-statistic are also indicated.

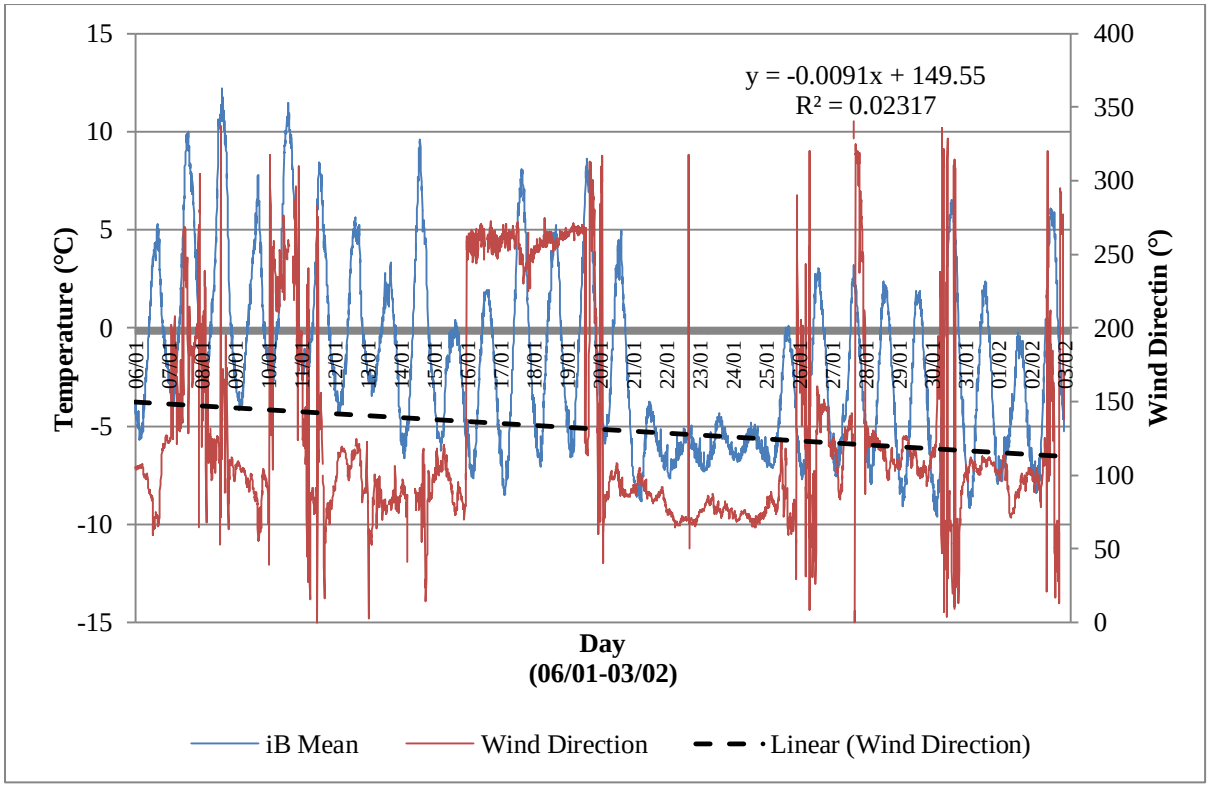

Figure 97: Wind direction, measured in degrees from 0-360, compared to average GST for the study site from the 6th of January to 3rd of February 2012. The trendline of wind direction is indicated as a dashed line. The equation of the trendline and the R^2-statistic are also indicated.

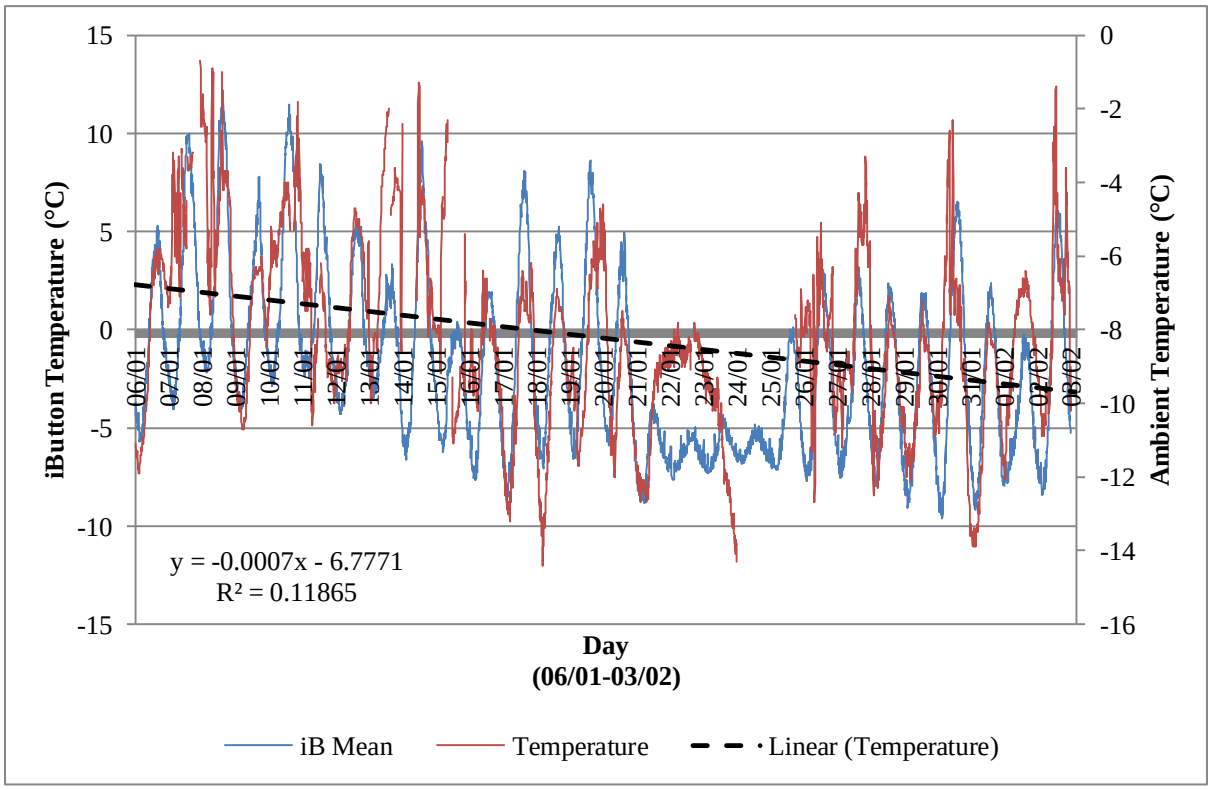

Figure 98: Ambient temperature, measured in degrees Celsius (°C), compared to average GST for the study site from 6th of January to 3rd of February 2013. The trendline of ambient temperature is indicated as a dashed line. The equation of the trendline and the R^2-statistic are also indicated.

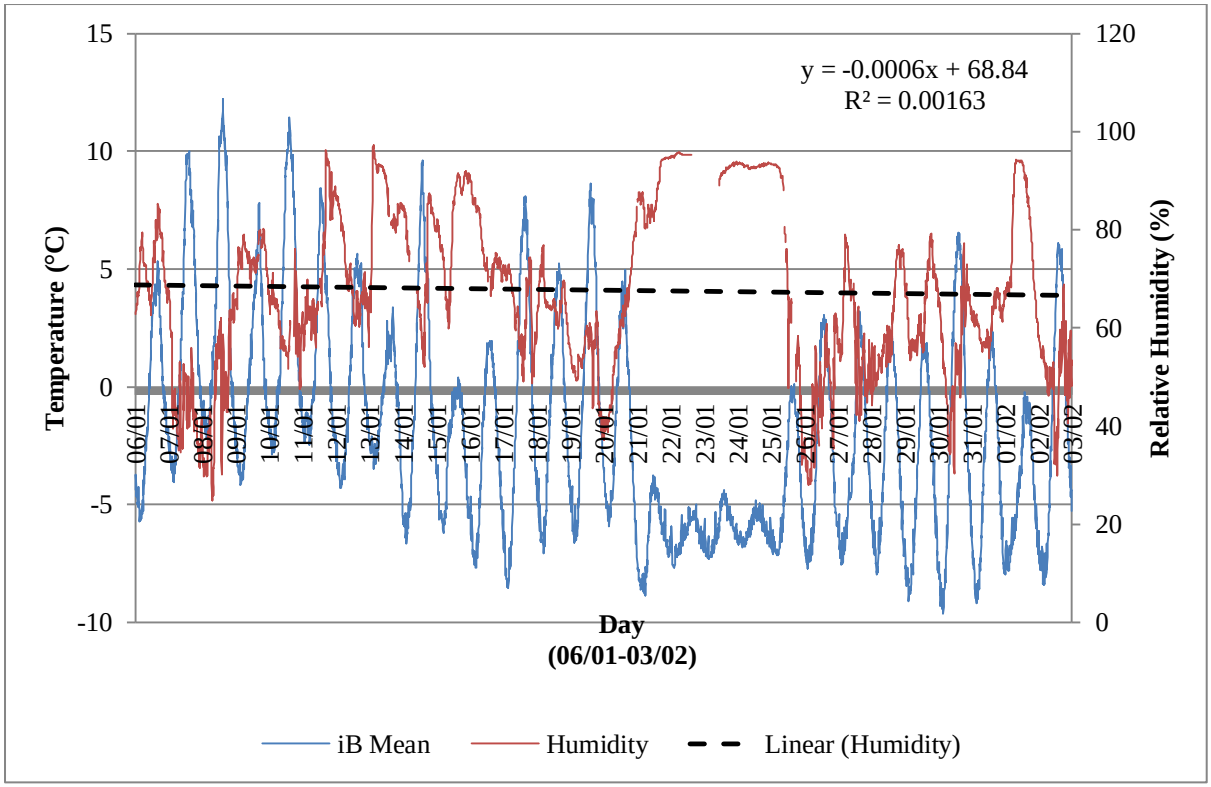

Figure 99: Relative humidity, measured in percentage (%), compared to average GST for the study site from the 6th of January to the 3rd of February 2012. The trendline of relative humidity is indicated as a dashed line. The equation of the trendline and the R^2-statistic are also indicated.

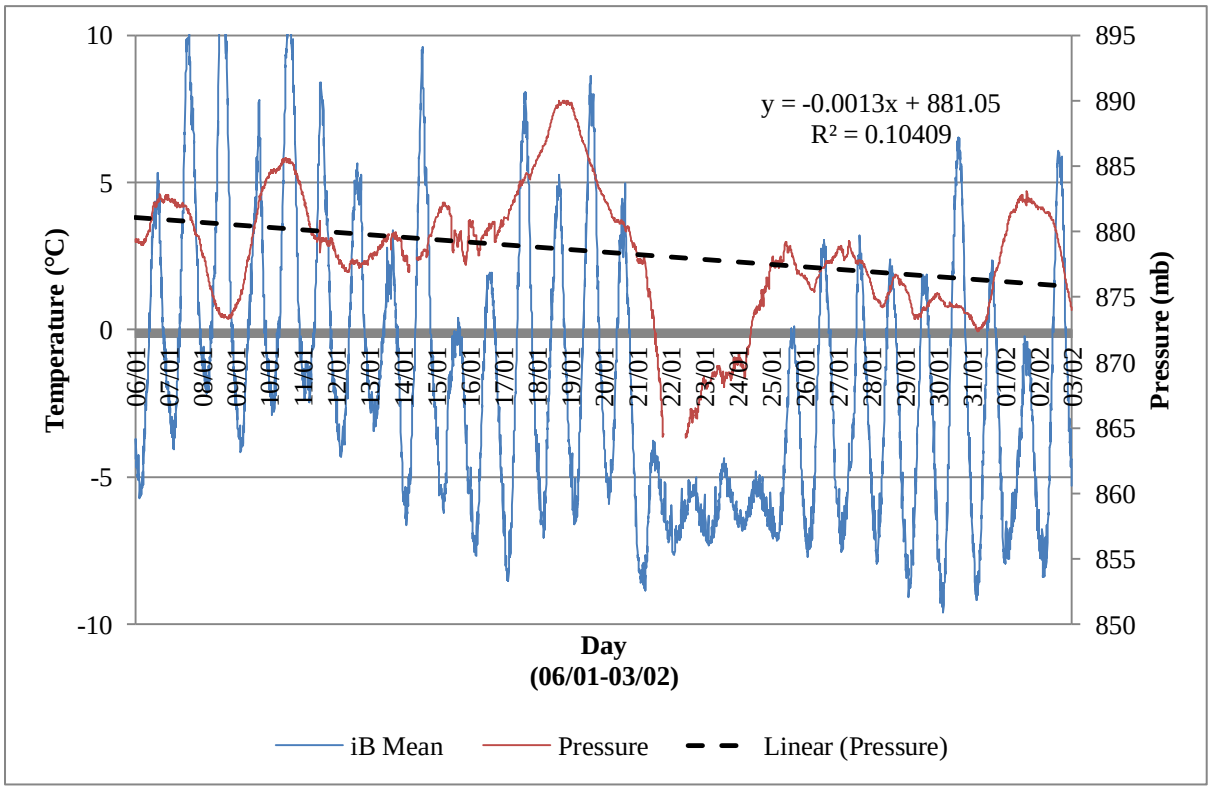

Figure 100: Pressure, measured in millibar (mb), compared to average GST for the study site from the 6th of January to the 3rd of February 2012. The trendline of pressure is indicated as a dashed line. The equation of the trendline and the R^2-statistic are also indicated.

Table 79: Single factor ANOVA ($\alpha = 0.01$, $p < 0.01$) results for GST dynamics, using six sample sites and the PACE XR5 data logger, for the 2010/11 field season. Location is the factor and the various sample locations the treatments.

SUMMARY				
Groups	*Count*	*Sum*	*Average*	*Variance*
PACE Logger	242	-491.6756	-2.0317	13.9360
T1	216	-74.9923	-0.3472	13.2622
T2	235	-613.6832	-2.6114	11.5270
T3	224	-231.1266	-1.0318	15.7848
T5	227	-225.5689	-0.9937	5.4650
T6	176	-159.6557	-0.9071	1.6729
T7	213	327.5475	1.5378	15.4519

ANOVA						
Source of Variation	*SS*	*df*	*MS*	*F*	*P-value*	*F crit*
Between Groups	2330.7494	6	388.4582	34.4025	0.0000	2.1045
Within Groups	17230.9258	1526	11.2916			
Total	19561.6751	1532				

Table 80: Single factor ANOVA ($\alpha = 0.01$, $p < 0.01$) on GST dynamics, using 16 sample sites and a global average data series for the 2011/12 field season. Location is the factor and the various sample locations the treatments.

SUMMARY				
Groups	*Count*	*Sum*	*Average*	*Variance*
iB1	4033	-2991.46	-0.74	37.81
iB2	4012	-6844.34	-1.71	22.35
iB3	4033	-4870.77	-1.21	30.72
iB4	4008	-8660.32	-2.16	21.65
iB5	4033	-397.14	-0.10	36.31
iB6	4033	-9950.79	-2.47	35.96
iB7	4033	-5103.79	-1.27	22.17
iB8	4033	-8154.47	-2.02	28.05
iB9	3986	-14055.12	-3.53	24.45
iB10	4033	-7436.13	-1.84	30.04
iB11	3932	-12820.37	-3.26	13.83
iB13	4016	-8130.66	-2.02	23.18
iB14	4022	-14815.16	-3.68	18.00
iB15	4033	-5295.66	-1.31	27.46
iB16	4033	-3691.89	-0.92	38.27
iB17	4033	-7824.08	-1.94	34.98

SUMMARY				
Groups	*Count*	*Sum*	*Average*	*Variance*
iB Mean	4033	-7454.49	-1.85	20.46

ANOVA						
Source of Variation	*SS*	*df*	*MS*	*F*	*P-value*	*F crit*
Between Groups	59814.34	16	3738.40	136.32	0	1.64
Within Groups	1873583.84	68322	27.42			
Total	1933398.18	68338				

Table 81: Results of Fisher's LSD tests ($\alpha = 0.05$, $p < 0.05$) for 21 possible pairings for the 2010/11 field season sample sites. The critical value for all pairings is 1.97. A test statistic greater than this value yields a rejection of the H_0.

Pairing	**t-Statistic**	**P Two Tail**	**Accept H_0**
PACE-T1	-4.88	1.49E-06	No
PACE-T2	1.77	7.69E-02	Yes
PACE-T3	-2.80	5.31E-03	No
PACE-T5	-3.58	3.77E-04	No
PACE-T6	-3.83	1.47E-04	No
PACE-T7	-9.93	3.79E-21	No
T1-T2	6.83	2.72E-11	No
T1-T3	1.88	6.05E-02	Yes
T1-T5	2.23	2.60E-02	No
T1-T6	1.94	5.28E-02	Yes
T1-T7	-5.15	3.92E-07	No
T2-T3	-4.59	5.84E-06	No
T2-T5	-5.95	5.46E-09	No
T2-T6	-6.32	6.72E-10	No
T2-T7	-11.98	6.98E-29	No
T3-T5	-0.12	9.01E-01	Yes
T3-T6	-0.40	6.89E-01	Yes
T3-T7	-6.79	3.62E-11	No
T5-T6	-0.44	6.59E-01	Yes
T5-T7	-8.27	1.63E-15	No
T6-T7	-7.90	2.84E-14	No

Table 82: Results of Fisher's LSD tests ($\alpha = 0.05$, $p < 0.05$) for the 120 possible pairings for the 2011/12 field season sample sites. The critical value for all pairings is 1.96. A test statistics greater than this value yields a rejection of H_0.

Pairing	***t*-Statistic**	**P Two Tail**	**Accept H_0**
iB1-iB2	7.88	3.66E-15	No
iB1-iB3	3.57	3.53E-04	No
iB1-iB4	11.66	3.50E-31	No
iB1-iB5	-4.74	2.12E-06	No
iB1-iB6	12.76	6.31E-37	No
iB1-iB7	4.29	1.77E-05	No
iB1-iB8	10.02	1.75E-23	No
iB1-iB9	22.33	3.41E-107	No
iB1-iB10	8.50	2.30E-17	No
iB1-iB11	22.05	1.19E-104	No
iB1-iB13	10.42	2.98E-25	No
iB1-iB14	24.98	9.49E-133	No
iB1-iB15	4.49	7.19E-06	No
iB1-iB16	1.26	2.06E-01	Yes
iB1-iB17	8.92	5.74E-19	No
iB2-iB3	-4.34	1.47E-05	No
iB2-iB4	4.34	1.43E-05	No
iB2-iB5	-13.31	5.59E-40	No
iB2-iB6	6.32	2.72E-10	No
iB2-iB7	-4.19	2.86E-05	No
iB2-iB8	2.82	4.78E-03	No
iB2-iB9	16.83	1.87E-62	No
iB2-iB10	1.21	2.27E-01	Yes
iB2-iB11	16.27	1.48E-58	No
iB2-iB13	2.99	2.79E-03	No
iB2-iB14	19.73	1.13E-84	No
iB2-iB15	-3.53	4.18E-04	No
iB2-iB16	-6.44	1.28E-10	No
iB2-iB17	1.96	5.00E-02	No
iB3-iB4	8.35	8.13E-17	No
iB3-iB5	-8.60	9.18E-18	No
iB3-iB6	9.80	1.57E-22	No
iB3-iB7	0.50	6.14E-01	Yes
iB3-iB8	6.74	1.64E-11	No
iB3-iB9	19.76	7.30E-85	No

Pairing	*t*-Statistic	P Two Tail	Accept H_0
iB3-iB10	5.18	2.25E-07	No
iB3-iB11	19.36	1.26E-81	No
iB3-iB13	7.06	1.84E-12	No
iB3-iB14	22.50	8.02E-109	No
iB3-iB15	0.88	3.80E-01	Yes
iB3-iB16	-2.23	2.55E-02	No
iB3-iB17	5.74	9.98E-09	No
iB4-iB5	-17.17	6.50E-65	No
iB4-iB6	2.56	1.05E-02	No
iB4-iB7	-8.57	1.18E-17	No
iB4-iB8	-1.25	2.12E-01	Yes
iB4-iB9	12.71	1.12E-36	No
iB4-iB10	-2.79	5.21E-03	No
iB4-iB11	11.62	5.81E-31	No
iB4-iB13	-1.29	1.98E-01	Yes
iB4-iB14	15.32	2.88E-52	No
iB4-iB15	-7.67	1.94E-14	No
iB4-iB16	-10.20	2.88E-24	No
iB4-iB17	-1.86	6.30E-02	Yes
iB5-iB6	17.70	8.91E-69	No
iB5-iB7	9.69	4.34E-22	No
iB5-iB8	15.23	1.25E-51	No
iB5-iB9	27.83	9.46E-163	No
iB5-iB10	13.61	1.05E-41	No
iB5-iB11	28.10	1.06E-165	No
iB5-iB13	15.84	1.18E-55	No
iB5-iB14	30.86	8.56E-198	No
iB5-iB15	9.66	5.91E-22	No
iB5-iB16	6.01	1.97E-09	No
iB5-iB17	13.85	3.93E-43	No
iB6-iB7	-10.01	1.88E-23	No
iB6-iB8	-3.54	4.09E-04	No
iB6-iB9	8.62	7.94E-18	No
iB6-iB10	-4.87	1.11E-06	No
iB6-iB11	7.07	1.64E-12	No
iB6-iB13	-3.65	2.62E-04	No
iB6-iB14	10.50	1.20E-25	No

Pairing	*t*-Statistic	P Two Tail	Accept H_0
iB6-iB15	-9.20	4.29E-20	No
iB6-iB16	-11.44	4.52E-30	No
iB6-iB17	-3.98	7.07E-05	No
iB7-iB8	6.78	1.30E-11	No
iB7-iB9	20.97	4.63E-95	No
iB7-iB10	5.08	3.81E-07	No
iB7-iB11	20.95	6.69E-95	No
iB7-iB13	7.15	9.40E-13	No
iB7-iB14	24.21	4.85E-125	No
iB7-iB15	0.43	6.68E-01	Yes
iB7-iB16	-2.86	4.25E-03	No
iB7-iB17	5.67	1.51E-08	No
iB8-iB9	13.14	4.82E-39	No
iB8-iB10	-1.48	1.38E-01	Yes
iB8-iB11	12.05	3.75E-33	No
iB8-iB13	0.02	9.81E-01	Yes
iB8-iB14	15.54	1.18E-53	No
iB8-iB15	-6.04	1.59E-09	No
iB8-iB16	-8.63	7.39E-18	No
iB8-iB17	-0.66	5.12E-01	Yes
iB9-iB10	-14.43	1.36E-46	No
iB9-iB11	-2.70	6.99E-03	No
iB9-iB13	-13.76	1.32E-42	No
iB9-iB14	1.53	1.26E-01	Yes
iB9-iB15	-19.45	2.45E-82	No
iB9-iB16	-20.86	3.81E-94	No
iB9-iB17	-13.02	2.29E-38	No
iB10-iB11	13.47	7.01E-41	No
iB10-iB13	1.57	1.16E-01	Yes
iB10-iB14	16.84	1.41E-62	No
iB10-iB15	-4.44	8.91E-06	No
iB10-iB16	-7.13	1.06E-12	No
iB10-iB17	0.76	4.49E-01	Yes
iB11-iB13	-12.79	4.38E-37	No
iB11-iB14	4.72	2.35E-06	No
iB11-iB15	-19.08	1.99E-79	No
iB11-iB16	-20.44	1.48E-90	No

Pairing	*t*-Statistic	P Two Tail	Accept H_0
iB11-iB17	-11.89	2.39E-32	No
iB13-iB14	16.39	2.08E-59	No
iB13-iB15	-6.34	2.39E-10	No
iB13-iB16	-8.97	3.51E-19	No
iB13-iB17	-0.70	4.82E-01	Yes
iB14-iB15	-22.31	5.05E-107	No
iB14-iB16	-23.41	2.43E-117	No
iB14-iB17	-15.20	1.89E-51	No
iB15-iB16	-3.12	1.85E-03	No
iB15-iB17	5.04	4.79E-07	No
iB16-iB17	7.60	3.23E-14	No

Table 83: Results of GIS analyses to determine aspect (north, east, south, west, top), slope gradient (°), elevation (MASL) and average solar radiation ($WH.m^{-2}$) received for the period under investigation for the various sample sites.

Sample	Aspect	Slope	Elevation	Mean Solar Radiation Received
T-1	Top	0-6	840-853	114 136.20
T-2	Top	0-6	840-853	114 136.20
T-3	East	0-6	840-853	114 136.20
T-4	North	0-6	840-853	114 136.20
T-5	East	0-6	840-853	114 136.20
T-6	North	0-6	840-853	114 136.20
T-7	East	6-12	830-840	114 136.20
iB1	East	6-12	830-840	114 136.20
iB2	South	0-6	840-853	104 673.54
iB3	East	6-12	820-830	114 136.20
iB5	East	6-12	820-830	114 136.20
iB4	North	0-6	840-853	114 136.20
iB6	South	0-6	840-853	114 136.20
iB7	North	0-6	840-853	114 136.20
iB8	East	0-6	840-853	114 136.20
iB9	South	6-12	840-853	104 673.54
iB10	North	6-12	840-853	114 136.20
iB11	East	6-12	830-840	114 136.20
iB13	East	0-6	840-853	104 673.54
iB14	North	6-12	820-830	114 136.20
iB15	North	0-6	840-853	114 136.20

Sample	Aspect	Slope	Elevation	Mean Solar Radiation Received
iB16	South	0-6	840-853	104 673.54
iB17	North	6-12	840-853	114 136.20
PACE XR5	North	0-6	840-853	114 136.20

Appendix G: Inferential Statistics for Rock Hardness Rebound Values

This appendix contains inferential statistical output calculated for SH and Equotip rock hardness rebound values, as well as lichen presence, observable weathering pitting and flaking on clast surfaces as well as clast's roughest observable side.

Table 84: Results for the two-sample for variance *F*-test ($\alpha = 0.01$, $p < 0.01$). The *F*-test is performed on SH and Equotip rock hardness rebound values to determine equality of variances.

	SH	**EQ**
Mean	32.34	421.77
Variance	65.42	26 860.13
Observations	3149	4789
df	3148	4788
F		0.002
P(*F* <= f) one-tail		0
F Critical one-tail		0.949

Table 85: Results of a two sample Student's *t*-test ($\alpha = 0.01$, $p < 0.01$), assuming equal variances for SH and Equotip readings.

	SH	**EQ**
Mean	32.34	421.77
Variance	65.42	26 860.13
Observations	3149	4789
Pooled Variance		16 231.38
Hypothesized Mean Difference		0
df		7 936
t Stat		-133.231
P(T <= t) one-tail		0
t Critical one-tail		1.645
P(T <= t) two-tail		0
t Critical two-tail		1.960

Table 86: Frequency distribution for the SH and Equotip. Pearson's correlation coefficient is also indicated.

***R*-value**	**Schmidt Hammer**	***R*-value**	**Equotip**
0-20	142	0-200	519
21-30	1321	201-300	593
31-40	1171	301-400	958

***R*-value**	**Schmidt Hammer**	***R*-value**	**Equotip**
41-50	551	401-500	1165
51-60	63	501-600	868
> 61	1	> 601	686
Count	3248		4789
Correlation			**0.12**

Table 87: Results for single factor ANOVA ($\alpha = 0.01$, $p < 0.01$) for five treatments (north-, east-, south-, east- and top-facing sides) for SH rock hardness rebound values.

SUMMARY						
Groups	*Count*	*Sum*	*Average*	*Variance*		
Top	1380	44851	32.50	72.25		
North	1345	43460	32.31	68.12		
East	1381	42984	31.13	59.15		
South	1433	47936	33.45	73.21		
West	1330	43971	33.06	73.19		
ANOVA						
Source of Variation	*SS*	*df*	*MS*	*F*	*P-value*	*F crit*
Between Groups	4372.89	4	1093.22	15.80	7.05469E-13	3.32
Within Groups	474930.12	6864	69.19			
Total	479303.0112	6868				

Table 88: Results for single factor ANOVA ($\alpha = 0.01$, $p < 0.01$) for four treatments (north-, east-, south- west-facing sides) for SH rock hardness rebound values.

SUMMARY						
Groups	*Count*	*Sum*	*Average*	*Variance*		
North	1345	43460	32.31227	68.1167		
East	1381	42984	31.12527	59.15314		
South	1433	47936	33.4515	73.21011		
West	1330	43971	33.0609	73.19493		
ANOVA						
Source of Variation	*SS*	*df*	*MS*	*F*	*P-value*	*F crit*
Between Groups	4372.814	3	1457.605	21.30325	1.03E-13	2.606528
Within Groups	375293.1	5485	68.4217			
Total	379665.9	5488				

Table 89: Results for single factor ANOVA ($\alpha = 0.01$, $p < 0.01$) using five treatments (north-, east-, south-, east- and top-facing sides) for Equotip rock hardness rebound values.

SUMMARY						
Groups	*Count*	*Sum*		*Average*	*Variance*	
North	3 592	1 345 736		374.6481	25 002.4710	
East	3 694	1 404 751		380.2791	27 153.4680	
South	4 040	1 611 185		399.8082	26 893.7178	
West	3 200	1 276 976		398.0550	27 365.6125	
Top	4 918	1 814 756		369.0028	24 950.6581	
ANOVA						
Source of Variation	*SS*	*df*	*MS*	*F*	*P-value*	*F crit*
Between Groups	3 073 795.853	4	768 448.963	29.35267	2.26318E-24	2.37239
Within Groups	508 910 337.1	19 439	26 179.862			
Total	511 984 132.9	19 443				

Table 90: Results for single factor ANOVA ($\alpha = 0.05$, $p < 0.05$) for four treatments (north-, east-, south- west-facing sides) for Equotip rock hardness rebound values.

SUMMARY						
Groups	*Count*	*Sum*		*Average*	*Variance*	
North	3592	1345736		374.6481	25002.47096	
East	3694	1404751		380.2791	27153.46798	
South	4040	1611185		399.8082	26893.71783	
West	3200	1276976		398.0550	27365.61248	
ANOVA						
Source of Variation	*SS*	*df*	*MS*	*F*	*P-value*	*F crit*
Between Groups	1723133.732	3	574377.9108	21.5963552	0.018	3.79
Within Groups	386227951.1	14522	26596.05778			
Total	387951084.8	14525				

Table 91: Results for single factor ANOVA ($\alpha = 0.10$, $p < 0.10$) for five treatments (north-, east-, south-, east- and top-facing sides) for lichen presence observed for samples.

SUMMARY				
Groups	*Count*	*Sum*	*Average*	*Variance*
North	141	56	0.397163	5.641135
East	141	20	0.141844	0.765451
South	141	40	0.283688	2.918946

SUMMARY						
Groups	*Count*	*Sum*		*Average*		*Variance*
West	141	62		0.439716		6.890983
Top	141	44		0.312057		3.516211
ANOVA						
Source of Variation	*SS*	*df*	*MS*	*F*	*P-value*	*F crit*
Between Groups	7.512057	4	1.878014	0.475863	0.753487	1.952907
Within Groups	2762.582	700	3.946545			
Total	2770.094	704				

Table 92: Results for single factor ANOVA ($\alpha = 0.01$, $p < 0.01$) for five treatments (north-, east-, south-, east- and top-facing sides) for flaking observed for clasts for the study site.

SUMMARY						
Groups	*Count*	*Sum*		*Average*		*Variance*
North	260	90		0.346154		0.227205
East	260	74		0.284615		0.204396
South	260	64		0.246154		0.186279
West	260	79		0.303846		0.21234
Top	260	113		0.434615		0.246674
ANOVA						
Source of Variation	*SS*	*df*	*MS*	*F*	*P-value*	*F crit*
Between Groups	5.392308	4	1.348077	6.259101	5.48E-05	1.949205
Within Groups	278.9154	1295	0.215379			
Total	284.3077	1299				

Table 93: Results for single factor ANOVA ($\alpha = 0.01$, $p < 0.01$) for five treatments (north-, east-, south-, east- and top-facing sides) for pitting observed amongst clasts for the study site.

SUMMARY						
Groups	*Count*	*Sum*		*Average*		*Variance*
North	260	65		0.25		0.188224
West	260	63		0.242308		0.184304
South	260	45		0.173077		0.143674
East	260	48		0.184615		0.151114
Top	260	169		0.65		0.228378
ANOVA						
Source of Variation	*SS*	*df*	*MS*	*F*	*P-value*	*F crit*
Between Groups	41.01538	4	10.25385	57.2397	1.63E-44	1.949205
Within Groups	231.9846	1295	0.179139			
Total	273	1299				

Table 94: Results for single factor ANOVA ($\alpha = 0.01$, $p < 0.01$) for five treatments (north-, east-, south-, east- and top-facing sides) for the roughest observable face for sample clasts for the study site.

SUMMARY						
Groups	*Count*	*Sum*		*Average*	*Variance*	
North	260	21		0.080769	0.074532	
East	260	31		0.119231	0.10542	
South	260	13		0.05	0.047683	
West	260	20		0.076923	0.07128	
Top	260	175		0.673077	0.220894	
ANOVA						
Source of Variation	*SS*	*df*	*MS*	*F*	*P-value*	*F crit*
Between Groups	73.36923	4	18.34231	176.4328	1.1E-120	1.949205
Within Groups	134.6308	1295	0.103962			
Total	208	1299				

Appendix H: Inferential Statistics for Sample Moisture Gain or Loss

This appendix contains inferential statistical output calculated on sample rock properties (P, M, WA, S and % saturation), on percentage weight gain or loss for samples within groupings, as well as on the five groups taken together.

Table 95: Single factor ANOVA ($\alpha = 0.05$, $p < 0.05$) for sample porosity, using five treatments (Groups 1-5).

SUMMARY						
Groups	*Count*		*Sum*	*Average*		*Variance*
1-4	4		1.610	0.402		0.009
5-8	4		2.202	0.551		0.049
9-12	4		3.920	0.980		0.045
13-16	4		2.532	0.633		0.070
17-20	4		4.033	1.008		0.438
ANOVA						
Source of Variation	*SS*	*df*	*MS*	*F*	*P-value*	*F crit*
Between Groups	1.151	4	0.288	2.356	0.101	3.056
Within Groups	1.832	15	0.122			
Total	2.983	19				

Table 96: Single factor ANOVA ($\alpha = 0.05$, $p < 0.05$) for sample microporosity, using five treatments (Groups 1-5).

SUMMARY						
Groups	*Count*		*Sum*	*Average*		*Variance*
1-4	4		355.021	88.755		330.081
5-8	4		346.032	86.508		68.183
9-12	4		320.916	80.229		48.995
13-16	4		319.193	79.798		134.787
17-20	4		339.530	84.883		43.878
ANOVA						
Source of Variation	*SS*	*df*	*MS*	*F*	*P-value*	*F crit*
Between Groups	246.211	4	61.553	0.492	0.742	3.056
Within Groups	1877.774	15	125.185			
Total	2123.985	19				

Table 97: Single factor ANOVA ($\alpha = 0.05$, $p < 0.05$) for sample water absorption capacity, using five treatments (Groups 1-5).

SUMMARY						
Groups	*Count*		*Sum*	*Average*		*Variance*
1-4	4		1.667	0.417		0.006
5-8	4		2.140	0.535		0.045
9-12	4		3.764	0.941		0.027
13-16	4		2.418	0.605		0.052
17-20	4		3.730	0.933		0.339
ANOVA						
Source of Variation	*SS*	*df*	*MS*	*F*	*P-value*	*F crit*
Between Groups	0.911	4	0.228	2.423	0.094	3.056
Within Groups	1.410	15	0.094			
Total	2.322	19				

Table 98: Single factor ANOVA ($\alpha = 0.05$, $p < 0.05$) for sample saturation coefficients, using five treatments (Groups 1-5).

SUMMARY						
Groups	*Count*		*Sum*	*Average*		*Variance*
1-4	4		4.190	1.048		0.007
5-8	4		3.894	0.974		0.006
9-12	4		3.891	0.973		0.013
13-16	4		3.874	0.968		0.003
17-20	4		3.743	0.936		0.001
ANOVA						
Source of Variation	*SS*	*df*	*MS*	*F*	*P-value*	*F crit*
Between Groups	0.027	4	0.007	1.143	0.374	3.056
Within Groups	0.089	15	0.006			
Total	0.116	19				

Table 99: Single factor ANOVA ($\alpha = 0.05$, $p < 0.05$) for sample percentage saturation, using five treatments (Groups 1-5).

SUMMARY				
Groups	*Count*	*Sum*	*Average*	*Variance*
1-4	4	434.518	108.630	862.444
5-8	4	453.783	113.446	605.295
9-12	4	354.558	88.639	20.562

SUMMARY						
Groups	*Count*		*Sum*	*Average*		*Variance*
13-16	4		401.101	100.275		383.212
17-20	4		359.396	89.849		315.151
ANOVA						
Source of Variation	*SS*	*df*	*MS*	*F*	*P-value*	*F crit*
Between Groups	1949.194	4	487.299	1.114	0.386	3.056
Within Groups	6559.991	15	437.333			
Total	8509.185	19				

Table 100: Single factor ANOVA ($\alpha = 0.05$, $p < 0.05$) for samples within Group 1 using sample percentage weight gain or loss as input values. There are four treatments: Samples 1-4.

SUMMARY						
Groups	*Count*		*Sum*	*Average*		*Variance*
1	16		0.01	0.001		0.005
2	16		0.23	0.014		0.007
3	16		-0.19	-0.012		0.014
4	16		0.12	0.007		0.004
ANOVA						
Source of Variation	*SS*	*df*	*MS*	*F*	*P-value*	*F crit*
Between Groups	0.006	3	0.002	0.265	0.850	2.758
Within Groups	0.456	60	0.008			
Total	0.462	63				

Table 101: Single factor ANOVA ($\alpha = 0.05$, $p < 0.05$) for samples within Group 2 using sample weight gain or loss as input values. There are four treatments: Samples 17-20.

SUMMARY						
Groups	*Count*		*Sum*	*Average*		*Variance*
17	18		0.115	0.006		0.001
18	18		0.035	0.002		0.007
19	18		-0.235	-0.013		0.019
20	18		0.062	0.003		0.001
ANOVA						
Source of Variation	*SS*	*df*	*MS*	*F*	*P-value*	*F crit*
Between Groups	0.004	3	0.001	0.198	0.897	2.740
Within Groups	0.465	68	0.007			
Total	0.469	71				

Table 102: Single factor ANOVA ($\alpha = 0.05$, $p < 0.05$) for samples within Group 3 using sample percentage weight gain or loss as input values. There are four treatments: Samples 13-16.

SUMMARY						
Groups	*Count*		*Sum*	*Average*		*Variance*
13	18		0.029	0.002		0.001
14	18		0.175	0.010		0.004
15	18		0.167	0.009		0.010
16	18		0.095	0.005		0.001
ANOVA						
Source of Variation	*SS*	*df*	*MS*	*F*	*P-value*	*F crit*
Between Groups	0.001	3	0.000	0.066	0.978	2.740
Within Groups	0.270	68	0.004			
Total	0.270	71				

Table 103: Single factor ANOVA ($\alpha = 0.05$, $p < 0.05$) for samples within Group 4 using sample percentage weight gain or loss as input values. There are four treatments: Samples 9-12.

SUMMARY						
Groups	*Count*		*Sum*	*Average*		*Variance*
9	18		0.119	0.007		0.009
10	18		-0.653	-0.036		0.063
11	18		-0.245	-0.014		0.017
12	18		0.130	0.007		0.011
ANOVA						
Source of Variation	*SS*	*df*	*MS*	*F*	*P-value*	*F crit*
Between Groups	0.023	3	0.008	0.305	0.821	2.740
Within Groups	1.698	68	0.025			
Total	1.721	71				

Table 104: Single factor ANOVA ($\alpha = 0.05$, $p < 0.05$) for samples within Group 5 using sample percentage weight gain or loss as input values. There are four treatments: Samples 5-8.

SUMMARY				
Groups	*Count*	*Sum*	*Average*	*Variance*
5	18	0.147	0.008	0.003
6	18	0.098	0.005	0.006
7	18	0.005	0.000	0.007
8	18	-0.012	-0.001	0.008

The table continues on the following page (pg. 198)

ANOVA						
Source of Variation	*SS*	*df*	*MS*	*F*	*P-value*	*F crit*
Between Groups	0.001	3	0.000	0.054	0.984	2.740
Within Groups	0.403	68	0.006			
Total	0.404	71				

Table 105: Single factor ANOVA ($\alpha = 0.05$, $p < 0.05$) for all groups, *i.e.* environmental settings, using five treatments (Groups 1-5).

SUMMARY					
Groups	*Count*	*Sum*	*Average*		*Variance*
Group 1	63	0.152	0.002		0.007
Group 2	71	-0.121	-0.002		0.007
Group 3	71	0.367	0.005		0.004
Group 4	71	-0.938	-0.013		0.023
Group 5	71	0.074	0.001		0.005
ANOVA					
Source of Variation	*SS*	*df*	*MS*	*F*	*P-value*	*F crit*
Between Groups	0.014	4	0.004	0.383	0.820	2.398
Within Groups	3.191	342	0.009			
Total	3.206	346				